AN ABSTRACT OF THE THESIS OF

Edward D. Zaron for the degree of Doctor of Philosophy in Oceanography

presented on August 25, 1995.

Title: The Time-Averaged Circulation of the North Pacific Ocean:

An Analysis Based on Inverse Methods.

Redacted for Privacy

Abstract approved: _____

Andrew F. Bennett

The time-averaged velocity field in the North Pacific was estimated in two sets of inverse calculations. The planetary geostrophic equations were the basis for dynamical models of the flow in each case. The inverse estimates of the circulation were obtained by minimizing a positive-definite cost function, which measured the inconsistency of the model's predictions against a set of observations comprised of a large, high-quality hydrographic data set, and surface fluxes of heat, fresh water, and momentum.

In the first part of this work, four solution methods for the generalized inverse of a linear planetary geostrophic model of the North Pacific are compared. A conjugate gradient solver applied to the equation for the generalized inverse, expressed in terms of a representer expansion, was the most computationally efficient solution method. The other methods, in order of decreasing efficiency, were, a conjugate gradient descent solver (preconditioned with the inverse of the model operators), a direct solver for the representer coefficients, and a second conjugate gradient descent solver (preconditioned so that the diagonal elements of the cost

function Hessian were unity). All but the last method were successful at minimizing the penalty function.

Inverse estimates of the circulation based on the linear planetary geostrophic model were stable to perturbations in the data, and insensitive to assumptions regarding the model forcing and boundary condition uncertainties. A large calculation, which involved approximately 18,000 observations and 60,000 state variables, indicated that the linear model is remarkably consistent with the observations.

The second part of this work describes an attempt to use a nonlinear planetary geostrophic model (which included realistic bottom topography, lateral momentum mixing, out-cropping layers, and air-sea fluxes of heat, freshwater, and momentum) to assimilate the same hydrographic data set as above. Because of the nonlinearity in the model, descent methods (rather than a representer-based method) were used to solve the inverse problem. The nonlinearity of the model and the poor conditioning of the cost function Hessian confounded the minimization process. A solver for the tangent-linearization of the planetary geostrophic system should be used as a preconditioner if calculations of this type are attempted in the future.

The Time-Averaged Circulation of the North Pacific Ocean: An Analysis Based on Inverse Methods

by

Edward D. Zaron

A THESIS

submitted to

Oregon State University

in partial fulfillment of
the requirements for the
degree of

Doctor of Philosophy

Completed August 25, 1995
Commencement June 1996

Doctor of Philosophy thesis of Edward D. Zaron presented on August 25, 1995

APPROVED:

Redacted for Privacy

Major Professor, representing Oceanography

Redacted for Privacy

Dean of College of Oceanic and Atmospheric Sciences

Redacted for Privacy

Dean of Graduate School

I understand that my thesis will become part of the permanent collection of Oregon State University libraries. My signature below authorizes release of my thesis to any reader upon request.

Redacted for Privacy

Edward D. Zaron, Author

ACKNOWLEDGEMENTS

This work would never have been completed without the support and encouragement of my advisor, Andrew Bennett. I have also benefited greatly from discussions with Li Yuan, a post-doctoral scientist visiting my advisor's group.

The Reid-Mantyla hydrographic data set used in this study was originally provided by the NCAR Data Services Division. I would like to thank Joe Reid for providing me with an updated version of this data set.

The computations reported in Chapters 2 and 3 were performed on the computer facilities provided by the College of Oceanic and Atmospheric Sciences at Oregon State University. I am grateful to the College for the access I was allowed to the College's Connection Machines and IBM cluster.

From 1990 through 1993 I was supported by a NASA Global Change Research Fellowship. I would like to extend my appreciation to Dr. Ghassem Asrar, the NASA administrator supervising the Fellowship, for his actions on my behalf.

TABLE OF CONTENTS

TABLE OF CONTENTS (Continued)

TABLE OF CONTENTS (Continued)

LIST OF FIGURES

LIST OF FIGURES (Continued)

Figure | Page

LIST OF FIGURES (Continued)

LIST OF TABLES

The Time-Averaged Circulation of the North Pacific Ocean: An Analysis Based on Inverse Methods

1. INTRODUCTION

1.1. Introduction

Understanding the circulation and water masses of the oceans is the task of physical oceanographers. As we have come to appreciate the role of the oceans in the maintenance of the Earth's climate, oceanographers have sought to explain the temporally and spatially averaged circulation, the general circulation, as the dynamic response of the ocean to the fluxes of momentum, heat, and mass across its boundaries. As a scientific discipline, the central expression of this understanding is in the creation of models to explain oceanic observations.

Although the laws of continuum mechanics are quite accurate, it is beyond our present capabilities to model the general circulation, say, by numerically integrating the Navier-Stokes equations. Consequently, models of the general circulation must include numerous approximations and parameterizations for sub-grid scale phenomena.

More importantly, the forcing functions and boundary conditions for general circulation models are contaminated with error. Typical models require air-sea fluxes of heat, fresh water, and momentum as boundary conditions at the ocean surface. Estimates for each type of flux may contain complex sources of error, and the large-scale climatologies, which are often used for model boundary conditions, may

contain large-scale systematic errors of as much as 20% (e.g., Schmitt et al., 1989; Böning et al., 1991).

The time-averaged circulation is exceedingly difficult to measure directly because of the intensity and time-scales of transient motions relative to the mean (Flierl and McWilliams, 1977). As a consequence, simplified forms of tracer conservation and momentum balance are invoked to indirectly estimate the general circulation. The "core method" and the "dynamic method" (Pickard and Emery, 1982) are the two approaches historically used to infer the large-scale velocity field. The hydrographic data on which these inferences are based are often sparse in space and time owing to the great expense required for their acquisition. Because of this paucity of observations and errors in model boundary conditions, it has proved difficult to test models of the general circulation conclusively.

The World Ocean Circulation Experiment, hereafter referred to as WOCE, has as one of its goals the development of models for the prediction of climate change (U.S. WOCE, 1989). A necessary step toward this goal is the development and testing of ocean models for the present-day climate. The purpose of this thesis is to explore the issues involved with "testing" an ocean model; in practice, this involves comparing the prediction from such a model with observations of the predicted variables. Systematic procedures for making such comparisons are part of the theory of hypothesis testing, statistical estimation, and inverse methods.

In order to answer the question: "Is the general circulation, as observed with hydrographic measurements, in accord with theory?" this study used inverse methods to assimilate a large hydrographic data set into a model of the North Pacific general circulation. There were three specific goals:

1. To examine whether the hypothetical dynamics are consistent with the observations;

2. To produce an objectively smoothed ocean circulation as a plausible climatology for the North Pacific; and,

3. To estimate the errors in the proposed climatology in order to understand what questions can be addressed with hydrographic data.

The North Pacific ocean was chosen as the location for this study primarily because it is free of deep convection (Warren, 1983), which other inverse studies have found to play havoc with their solution methods (Tziperman et al., 1992b; Marotzke and Wunsch, 1992). In addition, there are large discrepancies between different estimates of the air-sea heat flux in the North Pacific (Talley, 1984). These discrepancies are believed to be caused by systematic errors in the bulk flux formulae on which these estimates are based, and which, when integrated over the large area of the North Pacific, lead to significant errors in the zonally integrated, meridional heat transport of the North Pacific. This work is based on the assumption that an inverse study, which used hydrographic data scattered throughout the North Pacific, would be able to constrain the surface heat flux better than estimates from bulk formulae alone.

In the future, this same methodology should be applicable towards creating the global "snapshot" envisioned by WOCE. Attaining this goal will require the generalized inverse of a nonlinear, global, general circulation model. Significant work still remains in the development of a practical solution method for such a model.

1.2. Literature Survey

The intent of this brief overview is to establish a context for the technical issues involved in using inverse methods to estimate the general circulation. There

are a number of good texts and reviews which consider the broader applications of inverse methods within oceanography and geophysical sciences in general. Tarantola (1987), Bennett (1992), and Parker (1994) cover inverse methods as applied to geophysical data smoothing, prediction, observing system analysis, and model testing, among other topics. The texts by Thiebaux and Pedder (1987) and Daley (1991) emphasize operational meteorological data assimilation. In addition to the aforementioned texts, there is a vast literature on engineering control theory and statistical estimation methods. A number of anthologies concerning oceanographic data assimilation have appeared, namely, the special volume of *Dynamics of Atmospheres and Oceans* (Ghil, 1989), and the collections edited by Bengtsson et al. (1981), Anderson and Willebrand (1989), and Desaubies et al. (1990). Review articles such as Ghil et al. (1981), Ghil (1989), Miller and Ghil (1990), and Ghil and Malanotte-Rizzoli (1991) emphasize time-dependent assimilation problems and, in particular, Kalman filtering. Government panel summaries of inverse methods (National Research Council, 1991 and 1993) present an institutional perspective.

The remainder of this section emphasizes the use of inverse methods for estimating the general circulation.

Inferences about the ocean circulation that are based on hydrographic data typically involve a number of assumptions regarding the motion. The "dynamic method" is motivated by the scale analysis which suggests that, for small Rossby number, the momentum equations simplify to hydrostatic and geostrophic balance (Pedlosky, 1979). Given a section of hydrographic data, the dynamic method is useful for calculating the geostrophic transport between station pairs, relative to some unknown transport. For many purposes this calculation is adequate, since the deep flows are generally small, and the absolute transport can be estimated by assigning zero velocity at some depth.

The pioneering work of Wunsch (1978) and Stommel and Schott (1977) attempted to remove or reduce the indeterminacy of the velocity field inherent in the dynamic method. The so-called "β-spiral" calculation (Stommel and Schott, 1977) used conservation statements, in their differential form, to over-determine the absolute transport. Alternately, Wunsch (1978) used the integral form of a conservation law to partially remove the indeterminacy of the absolute transport through a section of hydrographic casts. The historical importance of Wunsch (1978) lies in its thoughtful analysis of the structure of the problem from the point of view of linear operator theory (Lanczos, 1961). It was Davis (1978) who first stated the dynamical equivalence of the approaches in Stommel and Schott (1977) and Wunsch (1978).

Many researchers have extended the research program initiated by these papers. Olbers et al. (1985) applied a β-spiral formulation to estimate the general circulation of the North Atlantic from a portion of the Levitus (1982) hydrographic atlas. The three-dimensional velocity field and turbulent diffusivities they estimated are plausible; however, because the β-spiral calculation is based on local differential relations, the final velocity field is non-physical in the sense that it violates the elementary constraint of incompressibility. Olbers et al. acknowledged this as a major weakness in the assumptions on which the β-spiral calculation is based. Roemmich and McAllister (1989) applied the methods developed in Wunsch (1978) to determine the general circulation of the North Pacific; however, their approach is limited because one obtains information regarding only the component of the flow which is normal to the hydrographic sections used in the method. The culmination of this work has been in the development and implementation of inverse methods for incorporating observations into three-dimensional general circulation models.

Contemporary work has sought to formulate the problem of estimating the general circulation as a minimization problem in the context of "control theory"

(Tziperman and Thacker, 1989). Given a three-dimensional, general circulation, ocean model, what are the values of the model control parameters[1] (e.g., air-sea fluxes of heat, fresh water, and momentum) which will bring the model state variables (e.g., temperature, salinity, and velocity) into congruence with a set of observations? Letting u denote the state variable (a vector field in general), the optimal control problem is formulated by defining a penalty function, the value of which would be zero if the model and observations were in complete agreement:

$$\mathcal{J}(u) = \mathcal{J}_{\text{dyn}}(u) + \mathcal{J}_{\text{data}}(u). \tag{1.1}$$

As discussed in many texts (e.g., Tarantola, 1987), the relative sizes of the two terms, $\mathcal{J}_{\text{dyn}}(u)$ and $\mathcal{J}_{\text{data}}(u)$, express the tradeoff between errors in the model (i.e., adjustments to the control parameters), and fidelity to the data. The optimal estimate of the state, u, is defined as that value, u_{min}, which minimizes $\mathcal{J}$. In all of the cases considered herein, $\mathcal{J}_{\text{dyn}}$ and $\mathcal{J}_{\text{data}}$ are both quadratic functions of the model and data misfits, respectively.

The same formulation also provides the basis for "model testing." One can determine whether the estimated state u_{min} is plausible by inspecting the residuals in the fit of u_{min} to both the model equations and the observations. In particular, if the errors in the model and the observations are normally distributed with known covariances, then the expected value of $\mathcal{J}(u_{\text{min}})$ is a χ^2-variable with M degrees of freedom (where M is the number of measurements). A test of the model (i.e., the

---

[1]The partitioning between state variables and control parameters is not unique. In the models used here, the control parameters are the models' inhomogeneities, and they can be diagnosed by substituting the state variables into the model equations. Therefore, the optimal control problems will be posed in terms of the state variables alone.

consistency of the model, observations, and their respective errors) is then provided by the value of the χ^2-variable.

Bogden (1991) applied this formalism to assimilate hydrographic data into a linear model of the North Atlantic. To the constraints from the dynamic method (geostrophic and hydrostatic balance) were added incompressibility and linearized conservation of (approximate) potential density. The Levitus (1982) climatology was the source of observations, and it also provided the field about which the potential density conservation equation was linearized. Boundary conditions on the flow were provided by specifying the wind-driven Ekman pumping, the barotropic transport into the eastern boundary, and no-normal-flow at the bottom. In a series of experiments, Bogden minimized the penalty function

$$\mathcal{J}(\Psi_{\text{eb}}, \rho) = \mathcal{J}_{\text{dyn}}(\Psi_{\text{eb}}, \rho) + \mathcal{J}_{\text{data}}(\rho), \tag{1.2}$$

where

$$\mathcal{J}_{\text{dyn}}(\Psi_{\text{eb}}, \rho) = \int_D \text{f}^2 \left[\mathbf{u} \cdot \nabla \hat{\rho} + w \frac{\partial \hat{\rho}}{\partial z} \right]^2 dA \tag{1.3}$$

penalized the deviation of of the predicted flow field from a minimum-mixing ideal (at 1000m depth), and

$$\mathcal{J}_{\text{data}}(\rho) = \lambda \int_D \int_{-H}^{0} [\rho - \rho_{\text{obs}}]^2 \, dA dz \tag{1.4}$$

penalized the misfit of the density from the observations, ρ_{obs}. The minimum-mixing criterion, equation 1.3, used $\hat{\rho} = \rho_{\text{obs}} - g\rho_o z/c^2$ as an approximation to potential density (ρ_o and c, a reference density and the speed of sound, were taken to be constants). The velocity field, (u, v, w) or $(\mathbf{u}, w)$, is implicitly a function of density, ρ, and the value of the barotropic streamfunction on the eastern boundary, Ψ_{eb}, through the relations provided by the hydrostatic equation, geostrophic balance, and incompressibility. The parameter λ was chosen to control the tradeoff

between "mixing," as measured by $\mathcal{J}_{\text{dyn}}$, and infidelity to the data, as measured by $\mathcal{J}_{\text{data}}$. The Coriolis parameter, f, was used in equation 1.3 to reduce the relative strength of the mixing penalty near the equator.

Bogden (1991) proceeded by minimizing $\mathcal{J}$ with respect to Ψ_{eb} and with respect to certain classes of ρ adjustments. The dimension of the problem was small enough that direct matrix methods could be used to solve the equations for the extremum of $\mathcal{J}$. He obtained a plausible circulation that deviated acceptably from the observations, and which, over-all, had a plausible transport into the eastern boundary. By allowing for errors in the density data and the eastern boundary condition on the barotropic flow, Bogden overcame the primary inadequacy which arises when the geostrophic velocity field is diagnosed from density data, namely, the large, unrealistic flows driven by vortex stretching from cross-isobath flow (e.g., Sarkisyan, 1977; Sarmiento and Bryan, 1982; and Fujio and Imasoto, 1991). Bogden's approach ameliorated many of these difficulties, because his minimum-mixing criterion was effectively a minimum w criterion.

The most recent work has sought to estimate the time-averaged general circulation by assimilating data into nonlinear general circulation models. Tziperman et al. (1992b and 1992c) is typical of this work, in which a penalty function is composed of two terms, a steadiness penalty and a data misfit penalty. The steadiness term penalizes the difference between the model's prognostic variables between two times, say, $t = 0$ and $t = T$. In the case of Tziperman et al., temperature, θ, and salinity, S, were the prognostic variables; the velocity field was diagnosed from θ, S, and the surface wind stress. The data misfit penalty consisted of two sets of terms, those which measured the misfit between θ and S at $t = 0$ and the corresponding observations, and those terms which measured the departure of the surface fluxes from observations. The ocean model entered the problem by providing the constraints

which relate the prognostic variables at the two times with the air-sea fluxes; these constraints were appended to the penalty function with time-dependent Lagrange multipliers, and the entire penalty function was minimized using a descent method.

Tziperman et al. (1992c) considered the North Atlantic in an application of their methodology. They encounted numerous difficulties with the convergence of the descent method. The difficulty was attributed to the poor conditioning of the Hessian (the matrix of second derivatives) of the cost function, and to nonlinearity, which entered their model in the convection terms and in the vertical convective mixing scheme in the heat and salt conservation equations. They illustrated both of these problems by plotting the penalty function along sections of state space.

Marotzke and Wunsch (1992) used the same inverse formulation as in Tziperman et al. (1992b and 1992c), with the benefit of the preconditioning algorithm discussed in Marotzke (1992). The descent algorithm performed much better than in the previous studies, and Marotzke and Wunsch were able to draw some tentative conclusions regarding the ability of the nonlinear model to reconcile hydrographic data (taken from Fukumori and Wunsch, 1991) with air-sea fluxes. They found that the best-fit fields differed systematically from the data, with a tendency for the estimated surface fluxes to adjust toward winter conditions. In effect, the surface forcing fields were adjusted in order to support the steady-state generation of extreme water masses. Marotzke and Wunsch suggested that the era of inverse studies of the general circulation based on steady models is over, and that future inverse studies should be time-dependent, and include open boundary conditions as parameters in the inverse calculation so that the appropriate water masses can be advected into the model domain.

In spite of its success, the descent calculations of Marotzke and Wunsch (1992) are computationally intensive. If one counts each time-step of their

forward-backward integration as one model "substitution" (see Chapter 3), then the number of model substitutions in Marotzke and Wunsch's inverse calculation is equal to roughly half the number of state variables. The $2° \times 1°$ by 14-level model has roughly 85,000 state variables. Clearly there is more work to be done towards preconditioning these very large inverse calculations.

To date, researchers have tended to focus on somewhat idealized problems in which hydrographic observations are provided at every model grid point, and the weights used in the penalty function are each diagonal. The use of diagonal weights is equivalent to the assumption that the errors are uncorrelated, and their use may introduce spurious spatial structure in the solution of the inverse problem (Bennett and Budgell, 1987). Schlitzer (1993) is an exception to the use of diagonal weights; he used nondiagonal weights to enforce the smoothness of his solution in a formulation which is a nonlinear generalization of the approach in Wunsch (1978).

Despite these most recent advances, the central problem of estimating the general circulation is still with us. The most recent approaches, which are based on assimilating data into nonlinear, three-dimensional general circulation ocean models, are technically complex endeavors which require expertise in the design and implementation of the ocean model, its adjoint (which is used to compute the gradient of the penalty function), and large-scale minimization methods. We are still far from realizing the primary goal of WOCE, "...to develop models useful for predicting climate change...", if we regard this as predicated upon models which can reproduce present-day climate.

1.3. Overview

The chapters that follow use the planetary geostrophic equations (Pedlosky, 1979) as the basis for a dynamical description of the general circulation of the North Pacific. This system is a simplification of the primitive equations which effectively filters out inertial waves and dispersive Rossby waves. The planetary geostrophic system was first suggested by Hasselmann (1982) as the appropriate system for use in climate change studies, as the fast waves are effectively filtered out by the approximation. This system was used in an idealized geometry (a rectangular basin) by Colin deVerdiere (1988a and 1988b) to study the nonlinear interaction of thermohaline and wind-driven flows, and it is the basis of the Hamburg general circulation model (Maier-Reimer and Hasselmann, 1987). In addition, the planetary geostrophic balances explain many of the results of non-eddy-resolving primitive-equation models, such as that of Bryan and Lewis (1979).

In order to distinguish efficiently between diabatic and adiabatic mixing processes, the planetary geostrophic system is formulated using potential temperature as the vertical coordinate. Such an approach is based on the work of Bleck (1973) with atmospheric models. This choice of coordinate simplifies the representation of adiabatic flow at the expense of complicating the surface and bottom boundary conditions.

This study shares much with those already mentioned: the mid-ocean dynamics are geostrophic and hydrostatic, and a conservation equation is used. This approach differs from β-spiral calculations in that the circulation is governed by nonlocal dynamics. Similarly, it differs from the studies following Wunsch (1978) in that the three-dimensional circulation is sought, not just the component normal to

a hydrographic section. Furthermore, the hydrographic data are assumed to contain errors.

The present formulation of the inverse problem builds on the work of Tziperman et al. (1992c) and Marotzke and Wunsch (1992). An ocean circulation scheme is sought which is simultaneously consistent with an ocean model and a data set. The problem is significantly complicated by assimilating unsmoothed hydrographic data; a consequence of this is that nondiagonal weights are necessary in the definition of the penalty function.

Two planetary geostrophic models are used in the course of this study, a linearized model (Chapter 2), and a nonlinear model, which includes the effects of layer outcropping, lateral eddy mixing, and bottom topography (Chapter 3). Chronologically, the nonlinear calculations were performed prior to the linear calculations; however, for logical clarity the linear analysis is presented first.

The linear model permits a complete analysis via the "representer expansion" (explained in the following chapter). Assimilation experiments are performed to assess the efficacy of hydrographic measurements for improving estimates of air-sea fluxes. A number of solution methods for the generalized inverse are compared with this model, and a large, high-quality, hydrographic data set (Reid and Mantyla, 1988), with approximately 18,000 measurements, is assimilated into the model.

The nonlinear planetary geostrophic system discussed in Chapter 3 presents a much more complicated problem. Conservation equations for both heat and salt, and their respective air-sea fluxes, are used as constraints. The convective nonlinearity in the model, and the absence of a viable solver for the linearized system, make it necessary to use a substituting method. Several descent methods (for obtaining the best-fit solution), and several Monte Carlo methods (for obtaining a posteriori

errors) are used, but none prove adequate. The success of future attempts to estimate the general circulation will hinge on the development of efficient solvers for the quasi-steady general circulation. Once such a solver is available, all of the solution methods discussed in Chapter 2 will be applicable. Furthermore, the development of such a solver would resolve the long-standing "spin-up," or initialization problem for general circulation ocean models.

2. ARRAY ANALYSIS AND DATA ASSIMILATION WITH A LINEARIZED PLANETARY GEOSTROPHIC MODEL

2.1. Introduction

In this chapter, a linearized planetary geostrophic model is used to examine the usefulness of hydrographic data for determining the general circulation of the oceans. A representer expansion is the fundamental analytical tool.

The planetary geostrophic system is a simplified description of the large-scale ocean dynamics. The linearization used in this chapter eliminates layer outcropping at the ocean surface. The effects of irregular bathymetry and friction are also neglected; hence, the model cannot support a western boundary current. These significant simplifications allow us to examine some of the fundamental issues involved in estimating the general circulation, aside from complications arising from nonlinearity.

The model was formulated using potential temperature as the vertical coordinate. This choice was made in order to facilitate the modeling of approximately adiabatic dynamics, which govern the ocean away from its boundaries. In the present linearized system, the coordinate has no intrinsic advantage; it was used to make the results comparable with those from the nonlinear model discussed in the next chapter.

The model and its inverse formulation are discussed in Section 2.2. Section 2.3 is a brief review of solution methods for the generalized inverse. The generalized inverse is then used to study the efficacy of hydrographic data at determining the general circulation for two observing arrays: a set of scattered thermocline depth

measurements (Section 2.4), and a zonal section of hydrographic casts (Section 2.5); in both cases, the various solution methods outlined in Section 2.3 are compared. In Section 2.6 the model is used to assimilate a large hydrographic data set to estimate the North Pacific circulation, and the results are compared with a conventional objective analysis of the same data.

2.2. Model and Inverse Formulation

2.2.1. Model Formulation

The ocean model is similar to that used by Pedlosky (1992) to study the baroclinic structure of the abyssal circulation. Unlike Pedlosky, the present model uses potential temperature, denoted by θ, as the vertical coordinate (Bleck, 1978).

The model describes the steady, geostrophic motion of a layer of fluid on the surface of the Earth. Motion is driven by heat fluxes and isotherm depth variations at the top and bottom boundaries, and the velocity normal to the boundary is specified at the eastern boundary. It is assumed that Fick's law provides an adequate description of turbulent mixing. The mean stratification (about which the model is linearized) is maintained by a small amount of uniform upwelling, which is determined by the global balance of deep-water production.

The reader is referred to Pedlosky (1979) for a detailed derivation of the planetary geostrophic system. The equations will simply be quoted below.

Spherical coordinates are used, with latitude λ, longitude ϕ, and potential temperature θ as the local vertical coordinate. The total velocity vector is (u, v, ω), where the velocity components are defined by

$$u = r_o \cos\phi \frac{d\lambda}{dt}, \tag{2.1}$$

$$v = r_o \frac{d\phi}{dt}, \tag{2.2}$$

$$\omega = \frac{d\theta}{dt}, \tag{2.3}$$

and r_o denotes the radius of the Earth. The along-isotherm (adiabatic) velocity vector is denoted $\mathbf{u} = (u, v)$. Note that the conventional vertical velocity is

$$\frac{dz}{dt} = z_t + \mathbf{u} \cdot \nabla z + \omega z_\theta, \tag{2.4}$$

rather than ω, which is used here. Overbar indicates mean fields which define the linearization, and the perturbation quatities are denoted *without* primes. For example, the height of an isotherm, a function of λ, ϕ, and θ, is given by $\overline{z}(\theta) + z(\lambda, \phi, \theta)$, where $\overline{z}(\theta)$ is the mean depth profile. Buoyancy $\rho g/\rho_o$, is denoted by b, and is determined from a linear equation of state: $\rho = \rho_o(1 - \alpha\theta)$, with $\alpha = 0.2 \times 10^{-3}(^oC)^{-1}$. B is a Bernoulli function which is related to pressure, buoyancy and z by $B = p/\rho_o + \overline{b}z$, while f is the Coriolis parameter. The operators ∇ and $\nabla\cdot$ are, respectively, the horizontal gradient and divergence operators in spherical polar coordinates.

The model equations are as follows:

(the horizontal momentum equations)

$$\mathrm{f}\hat{k} \times \mathbf{u} = -\nabla B, \tag{2.5}$$

(hydrostatic balance)

$$\overline{b}_\theta z = B_\theta, \tag{2.6}$$

(the continuity equation)

$$\nabla \cdot (\mathbf{u}\overline{z}_\theta) + (\omega \overline{z}_\theta)_\theta = 0, \tag{2.7}$$

and (the energy equation)

$$\omega\overline{z}_\theta = -\left(\frac{K_V}{\overline{z}_\theta^2} z_\theta\right)_\theta . \tag{2.8}$$

Boundary conditions are specified at θ_B, the bottom isotherm:

$$z = z_B, \tag{2.9}$$

$$\omega\overline{z}_\theta = w_B, \tag{2.10}$$

at θ_T, the top isotherm:

$$z = z_T, \tag{2.11}$$

$$\omega\overline{z}_\theta = w_T, \tag{2.12}$$

and at $\lambda = \lambda_E$, the eastern boundary:

$$z = z_E, \tag{2.13}$$

$$B(\lambda_E, \theta_B) = B_E. \tag{2.14}$$

Note that B_E is a function of ϕ, z_E is a function of ϕ and θ, while z_B, z_T, w_B, and w_T are functions of λ and ϕ. Lower-case Greek characters which appear as subscripts denote partial derivatives; Roman character subscripts are part of the variables' names.

The mean profile cannot be specified arbitrarily. In order for the mean profile to be a solution of the nonlinear equations, the mean state must have a nondivergent vertical heat transport. In other words, the vertical velocity of the mean, $\overline{w} = \overline{\omega z}_\theta$, is a constant. If this were not the case, the perturbation equations would be forced by a source term from the mean state. Assuming that the diabatic mixing ω obeys a Fick's law relationship with θ, then the mean state has an upwelling velocity given by

$$\overline{w} = \left(\frac{K_V}{\overline{z}_\theta}\right)_\theta . \tag{2.15}$$

Therefore, the mean profile and diffusivity are related by

$$\frac{K_V}{\overline{z}_\theta} = \overline{w}\theta + C, \tag{2.16}$$

for constants $\overline{w}$ and C. In the present calculation, K_V is chosen to be a constant, hence

$$\overline{z} = L_{TC} \log\left(\frac{\theta + \theta_{TC}}{\theta_B + \theta_{TC}}\right) + \overline{z}(\theta_B), \tag{2.17}$$

where the thermocline length and temperature scales are $L_{TC} = K_V/\overline{w}$ and $\theta_{TC} = C/\overline{w}$, respectively.

The parameters defining the mean state, K_V, L_{TC}, and $\overline{w}$, are not determined by the model equations; they must be specified. The turbulent diffusivity, K_V, is set to the canonical value of $1\text{cm}^2/\text{sec}$ (Munk, 1966); this value is five to ten times larger than that inferred from tracer release studies (Ledwell et al., 1993), and orders of magnitude larger than the turbulent diffusivity inferred from microstructure measurements (Gregg, 1987). The thermocline length scale, L_{TC}, is determined by an L_1-norm fit (least-absolute-values) of $\overline{z}$ to the observations (Tarantola, 1987). That is, L_{TC} is determined by minimizing

$$\mathcal{J}_{TC}(L_{TC}) = \sum_{i=1}^{M} |\overline{z}(\theta_i) - z_i(\lambda_i, \phi_i, \theta_i)|, \tag{2.18}$$

in which $\overline{z}$ is given by equation 2.17. The absolute value norm is used to reduce the sensitivity of the L_{TC} estimate to outliers. The mean upwelling velocity cannot be specified independently of K_V and L_{TC}; in this case, it corresponds to a global deep-water production rate of roughly 20 Sverdrups ($1\text{ Sverdrup} = 10^6\text{m}^3/\text{sec}$). The physical parameters used in the linear model are summarized in Table 2.1.

Solutions of this system can be regarded as the steady response of damped-baroclinic Rossby waves to forcing imposed at the upper, lower, and eastern bound-

TABLE 2.1. Physical Parameters

Parameter	Value
r_o, Earth's radius	6×10^3 km
T_{day}, length of day	8.64×10^4 s
g, gravitational acceleration	9.8m/s^2
K_V, vertical diffusivity	$1 \times 10^{-4}\text{m}^2/\text{s}$
L_{TC}, vertical length scale	538m
$\overline{w}$, mean upwelling	5.8m/yr

aries. Pedlosky (1992) sought to explain the vertical layering of the abyssal circulation by considering the response of the planetary geostrophic system to surface Ekman pumping. It is clear that both surface and bottom Ekman pumping and isotherm depth variations are capable of generating motion. As an aside, spatial variability of K_V would also be capable of generating motion.

The advantage of this linearized system, relative to the full planetary geostrophic equations, lies in the simplicity with which it can be solved. This permitted the comparison of a number of solution methods and the examination of the conditioning of the inverse in much more detail than would have been possible otherwise. It should be kept in mind that the nonlinear system differs from the linearization primarily through the advection of the mass field. At mid-latitudes, the lowest-order long Rossby wave speed is roughly 1.5cm/sec, so the quantitative validity of the linear model is dubious, especially in the thermocline, where one expects the advecting velocity to be comparable to the Rossby wave speed.

To summarize, a model of the North Pacific was built for the purpose of estimating the general circulation from hydrographic data. Possibly significant effects caused by salinity, bottom topography, and the convective nonlinearity were

neglected. The linear system nonetheless was a tractable alternative to the full model, and it was amenable to the linear analysis afforded by the construction of the generalized inverse using a representer expansion.

2.2.2. Inverse Formulation

The inverse formulation is based on minimizing a penalty function.[1] The inverse, or best-fit solution is that set: $\mathbf{u}$, ω, z, and B, which most nearly satisfies the model, equations 2.5–2.14, and which most nearly fits a data set. The penalty function and the Euler-Lagrange system for the model system, 2.5–2.14, are written in full in Appendix 4.3.

The best-fit solution solves the set of Euler-Lagrange equations for the extremum of the penalty function. The best-fit solution is an optimal (maximum likelihood) estimate for the state in the event that one has correct prior knowledge of the uncertainties in the model, boundary conditions, and data. In the presence of an inaccurate statistical description of these errors, the best-fit is simply one of many estimates for the true state; information regarding the plausibility of the best-fit can be obtained by comparing the residual misfits to the a priori uncertainties. These facts are reviewed in any text on inverse methods (e.g., Tarantola, 1987; Bennett, 1992; Parker, 1994).

---

[1]In general, the penalty function may be a *functional*, i.e., a function of a function; however, all of the numerical methods that are used below rely on approximating the original functions on finite lattices: the penalty *functional* is approximated with a penalty *function*. In particular, the solution methods are explained using a notation that is most suggestive of a the finite-dimensional formulation. Hence, the expression *penalty function* is used rather than *penalty functional*.

It is assumed that the measurements to be assimilated are those which are available from typical hydrographic casts: measurements of temperature, salinity, and pressure. For the purpose of assimilating data into the planetary geostrophic model, these are regarded as measurements of depth at potential temperature levels. The measurements consist of a set,

$$\{z_i\}_{i=1}^{M}, \tag{2.19}$$

where z_i is an observed value of $z(\mathbf{x}_i)$, and $\mathbf{x}_i = (\lambda_i, \phi_i, \theta_i)$ denotes the measurement location. Each measurement may be contaminated by error ζ_i, therefore

$$z_i = z(\mathbf{x}_i) + \zeta_i. \tag{2.20}$$

Using the language of functional analysis, one would say that the measurement operator is a delta function, i.e.,

$$\mathcal{L}_i \circ_3 z = \int_D \delta(\mathbf{x} - \mathbf{x}_i) z(\mathbf{x}) d\mathbf{x}, \tag{2.21}$$

where $\mathcal{L}_i$ is the measurement functional, D is the three-dimensional domain on which z is defined, and δ is the delta function (a distribution or generalized function; Lighthill, 1958). The symbol $\circ_3$ is used to denote integration over a three-dimensional domain.

The weights in the penalty function are specified next. In statistical estimation, each weight is the inverse of a corresponding error covariance. There exists only one realization of the general circulation; therefore, the prior error *covariances* are prior *uncertainties*, i.e., the weights are based on uncertainty in our state of knowledge rather than variability in a random variable. For convenience, the terms "uncertainty" and "covariance" will be used interchangeably; however, it should be understood that *statistical estimation is not implied.* The following discussion starts by specifying the prior data covariance and then proceeds through the prior model covariances. Table 2.2 summarizes the covariance information.

TABLE 2.2. Prior Covariance Values

Covariance	L_{corr}	θ_{corr}	Fractional Error
C^z	500km	2°C	0.20
C^{z_T}	250km	na	0.20
C^{w_T}	1000km	na	0.20
C^{z_B}	250km	na	0.20
C^{w_B}	500km	na	0.20
C^{z_E}	250km	2°C	0.20

2.2.2.1. Data Errors

Each measurement z_i is related to the true time-averaged isotherm depth by

$$z_i = z_{\text{true}}(\mathbf{x}_i) + \zeta_i, \tag{2.22}$$

where ζ_i denotes the measurement error. The measurement error consists of a sum of instrumentation error, errors introduced by converting the raw hydrographic measurements to isotherm depth measurements, and errors of representativeness.

The uncertainty in individual temperature, salinity, and pressure measurements is assumed to be negligible. Presumably these measurements contain both random and systematic errors caused by equipment malfunction, finite-volume averaging (to remove salt-spikes or sample water volumes), calibration errors, and operator error. The raw hydrographic data base (Reid and Mantyla, 1988), which consists of roughly 1300 stations and 38,000 individual measurements, was processed to remove gross outliers (based on two passes of a three standard deviation test for temperature and salinity separately), and to remove unsuitable data (stations which sampled statically unstable profiles, and thermally inverted profiles were excluded). Finally, the acceptable hydrographic data were converted to (potential) isotherm depth measurements by cubic spline interpolation.

Errors of representativeness are likely to be the dominant source of error. A particular cast can be used to estimate an isotherm depth quite accurately; however, this depth is likely to be the result of motion on a number of time scales, none of which are adequately sampled.

As a rough estimate, the measurement error variance was estimated as 1/8 of the spatial variance of the isotherm depth. Multiple observations at a site were assumed to be independent and reduce the error variance accordingly. Values for the standard deviation of the data error range from roughly 50m to 100m.

2.2.2.2. Model Errors

The linear planetary geostrophic system, equations 2.5–2.14, neglects a number of processes which are likely to be important in the real ocean. The principal approximations are the neglect of the convective nonlinearity, and the crude mixing closure. The error covariances are characterized by a spatially inhomogeneous variance, horizontal and vertical correlation scales, and a spectral form describing the asymptotic roll-off rate.

The principal error in the horizontal momentum equations arises from the neglect of the advection terms. This error is proportional to the Rossby number for the flow (Pedlosky, 1979), which should be no more than 10^{-2}. Likewise, thickness-weighted Reynolds averages have also been neglected (DeSzoeke and Bennett, 1993); it is difficult to estimate the magnitude of these, but they should be no more than the conventional Reynolds flux, which also scales like the Rossby number. Errors caused by the Boussinesq approximation are also negligible. The total fractional uncertainty in the momentum equations is small compared to other errors, so the horizontal momentum equation errors were neglected.

The vertical momentum equation is simply hydrostatic balance. Nonlinear terms were neglected by virtue of the small Rossby number and aspect ratio. Larger sources of error are caused by the linearization and neglect of (thickness-weighted) Reynolds averages. These are potentially significant sources of error in the deep geostrophic velocity (e.g., McDougall, 1987); however, for simplicity, and because the hydrostatic relation is used in the coordinate transformation, the error in hydrostatic balance was neglected.

Using thickness-weighted Reynolds averages, the continuity equation is an exact relation expressing conservation of volume (DeSzoeke and Bennett, 1993). The planetary geostrophic system used here is linearized; hence, the continuity equation may have significant errors caused by the neglected nonlinear terms. These errors were retained as the only significant source of error in the planetary geostrophic system (excluding the boundary conditions). These errors were assumed to have a 500km horizontal correlation scale, a 2°C vertical correlation scale, and a magnitude (standard deviation) equal to 20% of the horizontal standard deviation of $\nabla \cdot (\mathbf{u}\overline{z}_\theta)$ computed from the first-guess solution (the first-guess solution is explained in section 2.3 below).

Errors in the energy equation, which defines the diabatic velocity ω, are attributed to errors in the turbulent-mixing closure. The terms neglected in the linearization may also be significant. It is difficult to estimate the uncertainty in the closure scheme; not only may the diffusion coefficient be wrong, but the concept of a local closure by down-gradient diffusion may be incorrect. One could include the parameters from the mixing parameterization as further unknowns to be estimated by the inverse method; however, given the extreme simplicity of the model, and the evidence that inverse-estimated mixing coefficients are indistinguishable from noise (Tziperman, 1988), energy equation errors were not considered.

2.2.2.3. Boundary Condition Errors

The boundary conditions consist of three pairs of conditions at the top, bottom, and eastern boundaries. The data for each boundary condition was assumed to contain error.

The eastern boundary conditions derive from specifying the geostrophic velocity normal to the boundary. Equivalently, B at the bottom and z are specified; these conditions determine B on the eastern boundary (from hydrostatic balance), which then determines the normal geostrophic velocity. Errors in the eastern boundary condition are caused by uncertainty in the first-guess z and bottom B fields, the former was specified by an objective analysis of the interior hydrographic data, and the latter was set to zero (no normal-flow at the bottom).

An analysis of the Euler-Lagrange system for equations 2.5 (Appendix 4.3) shows that hydrographic measurements are incapable of altering the eastern boundary condition on the bottom value of B. In other words, the bottom-eastern boundary value of B is unobservable with hydrographic observations. Hence, the error covariance for this boundary condition is immaterial; it was taken to be zero. The unobservability of the eastern boundary condition is a consequence of the decoupling of the barotropic and baroclinic dynamics in this model; irregular bottom topography could be incorporated to recouple the dynamics.

Boundary conditions on z at the eastern boundary were assumed to have a 250km meridional correlation scale, a 2°C vertical correlation scale, and a standard deviation of 20% of the meridional standard deviation of the first-guess field (the first-guess field is described in more detail below). The standard deviation of the eastern boundary condition error ranges in value from roughly 30m at the bottom to 50m at mid-depth.

The top and bottom boundary conditions contain errors caused by errors in the boundary data itself, and by linearization. The top and bottom isotherms are not material surfaces; the z and $\omega\overline{z}_\theta$ boundary conditions are analogous to the boundary conditions on temperature and vertical velocity used by Pedlosky (1992).

The top isotherm is regarded as the surface on which wind-driven Ekman pumping is applied. It is apparent that the top, 15°C, isotherm is not at or even immediately below the surface mixed layer over much of the North Pacific. This isotherm intersects the ocean surface at approximately 40°N and deepens to roughly 300m at lower latitudes. Another source of error in the surface boundary condition is the neglect of the "adiabatic component" of the Ekman pumping. In other words, the un-approximated boundary condition at θ_T relating ω to the Ekman pumping is

$$w_{\text{Ekman}} = \mathbf{u} \cdot \nabla z + \omega z_\theta, \tag{2.23}$$

but because the motion is linearized about a state of rest, the first nonlinear term (i.e., the adiabatic component of the Ekman pumping) was completely omitted. In any case, the errors in z_T were assigned a horizontal correlation scale of 250km and a standard deviation equal to 20% of the spatial standard deviation of the z_T data itself. The error in the surface Ekman pumping was assigned a length scale of 1000km (to reflect the larger scale of the atmospheric forcing), and a standard deviation equal to 20% of the observed spatial standard deviation (Böning et al., 1991).

Similar considerations apply to the bottom boundary conditions. The bottom isotherm depth was assigned a horizontal correlation scale of 250km and a standard deviation of 20m. The bottom vertical velocity boundary condition was assigned a horizontal correlation scale of 500km and a standard deviation of 20% of the mean vertical velocity, $\overline{\omega z}_\theta$.

The facts concerning all of the prior error covariances are summarized in Table 2.2. The implementation of these (non-diagonal) covariances is discussed in Appendix 4.3.

The prior error covariances, as illustrated in Figures 2.1 and 2.2, are neither homogeneous nor isotropic in spherical polar coordinates. The asymptotic spectral forms of the zonal, meridional, and vertical correlation structure functions were chosen so that the inverse problem generated a reproducing kernel Hilbert space (Bennett and McIntosh, 1982); this insured that the solution was a physically realizable field that did not contain delta functions or other singularities. The technical details regarding reproducing kernel Hilbert spaces may be found in Wahba (1990).

This representation of the error structure of the model was intended to be provisional. It is precisely the virtue of formal inverse methods that they make the choices for these error covariances explicit; they are entirely open for discussion. With the possible exception of the Ekman pumping boundary condition at the upper surface, it is difficult to assign values for either the length scales or the standard deviations of any of the errors. Rather than regarding the covariances as descriptions of random variables, they should be regarded as descriptions of uncertainty in our state of knowledge.

2.2.2.4. Summary

With the three pieces of information now specified: the model equations, the observations, and their respective uncertainties, the equations for the generalized inverse of system 2.5–2.14 can now be stated. The system is written in terms of the state variables, (u, v, ω, z, B), and the so-called "adjoint variables," $(\mu, \nu, \gamma, \alpha, \epsilon)$. Since the momentum, hydrostatic, and thermodynamic equations are exact con-

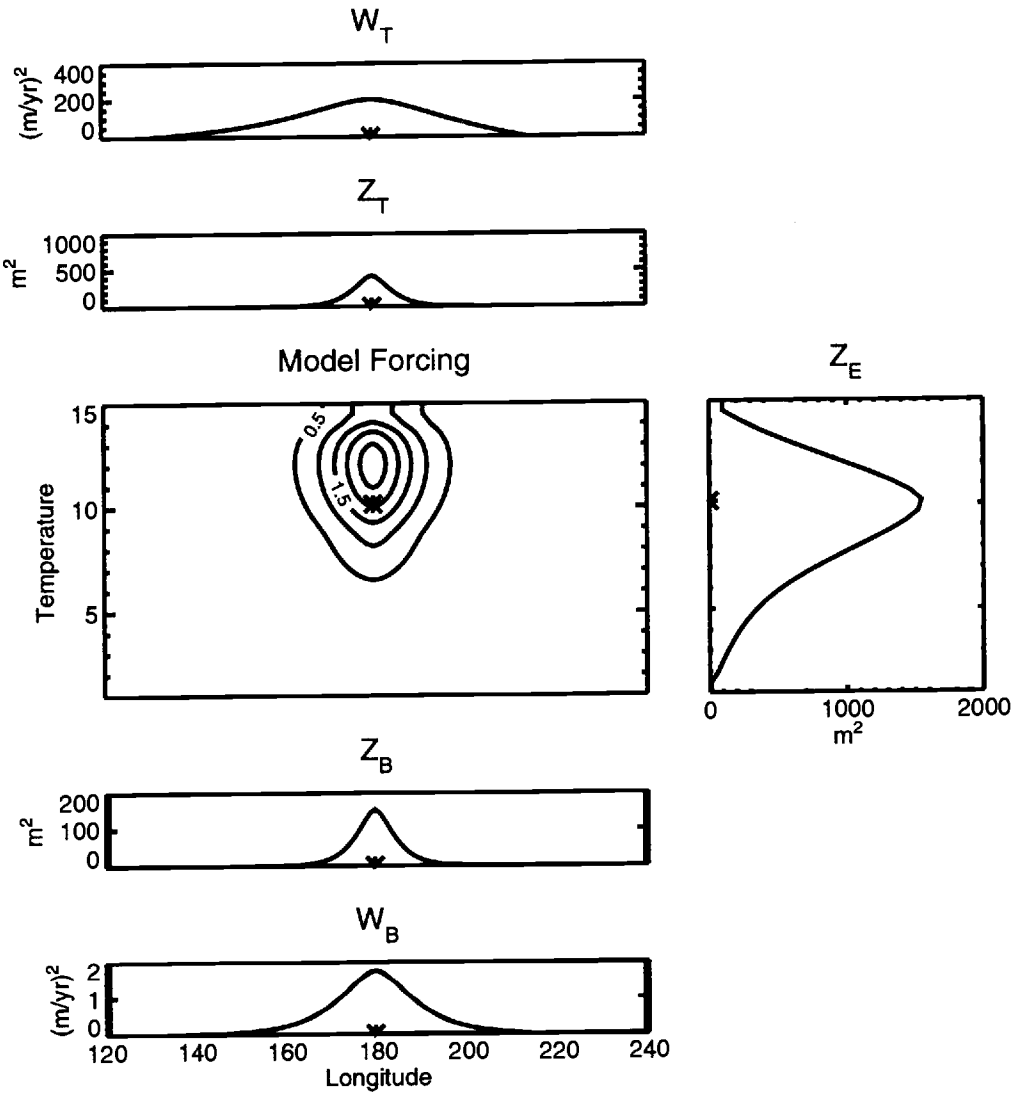

FIGURE 2.1. Prior forcing covariances: zonal section.

The prior model forcing error covariances at 25°N are shown. Each panel shows the covariance of the field with respect to the point marked with the astericks (*). Units of $m^2(yr\ °C)^{-2}$ are used in the central panel entitled "Model Forcing."

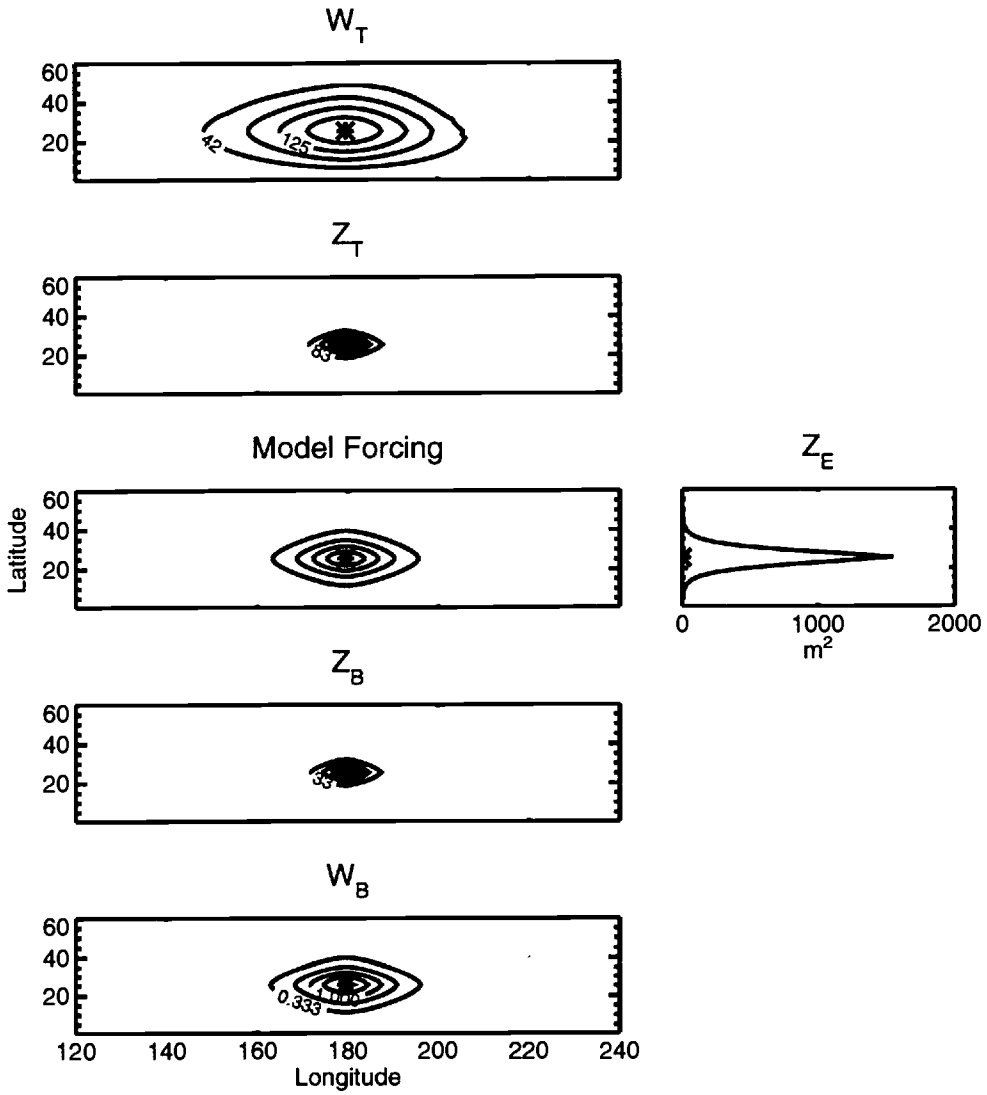

FIGURE 2.2. Prior forcing covariances: plan view.

The prior model forcing error covariances are shown in plan view. The units of the contoured fields are the same as those used in the previous figure. Once again, each panel shows the covariance of the field with respect to the point marked with the astericks (*).

straints, the variables μ, ν, γ, and α are Lagrange multipliers; $C^z \circ_3 \epsilon$ is the only model residual. The $\circ$ symbols denote inner products which are defined in Appendix 4.3, where the full penalty function is written out, and the Euler-Lagrange system is derived. The Euler-Lagrange equations for the proposed problem are as follows:

$$\mathrm{f}\hat{k} \times \mathbf{u} = -\nabla B \tag{2.24}$$

$$\overline{b}_\theta z = B_\theta \tag{2.25}$$

$$\nabla \cdot (\mathbf{u}\overline{z}_\theta) + (\omega \overline{z}_\theta)_\theta = C^z \circ_3 \epsilon \tag{2.26}$$

$$\omega \overline{z}_\theta = -\left(\frac{K_V}{\overline{z}_\theta^2} z_\theta\right)_\theta, \tag{2.27}$$

with boundary conditions at θ_B, the bottom isotherm,

$$z = z_B - C^{z_B} \circ_2 \frac{K_V}{\overline{z}_\theta^2} \epsilon_{\theta\theta}, \tag{2.28}$$

$$\omega \overline{z}_\theta = w_B - C^{w_B} \circ_2 \epsilon, \tag{2.29}$$

at θ_T, the top isotherm,

$$z = z_T + C^{z_T} \circ_2 \frac{K_V}{\overline{z}_\theta^2} \epsilon_{\theta\theta}, \tag{2.30}$$

$$\omega \overline{z}_\theta = w_T + C^{w_T} \circ_2 \epsilon, \tag{2.31}$$

and at the eastern boundary, $\lambda = \lambda_E$,

$$z = z_E - C^{z_E} \circ_{2E} \overline{b}_\theta \int_\theta^{\theta_T} \epsilon \frac{\beta}{\mathrm{f}^2} \overline{z}_\vartheta (1,0) \cdot \mathbf{n} d\vartheta, \tag{2.32}$$

$$B(\lambda_E, \theta_B) = B_E. \tag{2.33}$$

The so-called "adjoint equations" are as follows (where the notation $\mathbf{v} = (\mu, \nu)$ is used):

$$-\mathrm{f}\hat{k} \times \mathbf{v} = \overline{z}_\theta \nabla \epsilon \tag{2.34}$$

$$\gamma = \epsilon_\theta \tag{2.35}$$

$$-\nabla \cdot \mathbf{v} + \alpha_\theta = 0 \tag{2.36}$$

$$-\bar{b}_\theta \alpha + \left(\frac{K_V}{\bar{z}_\theta^2} \gamma_\theta \right)_\theta = -\sum_{i=1}^{M} \mathcal{L}_i \sigma_i^{-2} \left(\mathcal{L}_i \circ_3 z - z_i \right) \tag{2.37}$$

with homogeneous boundary conditions at θ_B and θ_T,

$$\alpha = 0, \tag{2.38}$$

$$\gamma = 0, \tag{2.39}$$

and at the western boundary,

$$\epsilon = 0. \tag{2.40}$$

The above system was solved numerically using standard finite-difference methods. The parameters used to define numerical model are listed in Table 2.3. The numerical method is discussed in more detail in Appendix 4.3.

TABLE 2.3. Numerical Model Parameters

Parameter	Value
D, model domain	North Pacific, 1^o to 60^oN 120^oE to 60^oW
$\Delta\lambda$, zonal resolution	1^o (approx.)
$\Delta\phi$, meridional resolution	2^o (approx.)
$\Delta\theta$, vertical resolution	0.5^oC (approx.)
nx, zonal grid-points	128
ny, meridional grid-points	32
n, vertical grid-points	32
θ_B, bottom temperature	1^oC
θ_T, top temperature	15^oC

For the purpose of discussing solution methods, it is helpful to represent the above system in compressed notation by representing the planetary geostrophic

system (including boundary conditions) as the action of a linear operator L, on a vector field u:

$$Lu = C\lambda + f. \tag{2.41}$$

In this terse notation, u denotes $(\mathbf{u}, \omega, B, z)$, λ denotes $(\mathbf{v}, \gamma, \alpha, \epsilon)$, $C\lambda$ represents the inner products of the covariances on the adjoint variables, and f stands for the model forcings (including the boundary conditions). In similarly terse notation, let the adjoint planetary geostrophic system be written

$$L^T\lambda = -HW(H^Tu - m), \tag{2.42}$$

where L^T represents the adjoint dynamical operator (including boundary conditions), H^Tu represents the inner products M measurement operators on the state variable, and m is an $M \times 1$ vector of observations. The matrix W is diagonal with ordered entries σ_i^{-2} on the diagonal.

This terse notation succinctly compresses the Euler-Lagrange equations for the planetary geostrophic system. It, equally well, represents the finite-difference approximation to this system, for which solutions were actually obtained. If equations 2.41 and 2.42 are regarded as a matrix system, then u is the $N \times 1$ vector of state variables, λ is the $N \times 1$ vector of adjoint variables, L is an $N \times N$ matrix (and L^T is its transpose), C is an $N \times N$ positive-definite-symmetric matrix, and H is an $N \times M$ matrix. L is of full rank because the model is well-posed. Each measurement operator, $\mathcal{L}_i \circ_3 z$, is represented with the dot product h_i^Tu, where h_i is an $N \times 1$ column of H. It is implied that the appropriate area elements have been absorbed into L, C, W, and H, so that the inner products are correctly weighted for spherical polar coordinates.

Lastly, the penalty function in this terse notation is

$$\mathcal{J}(u) = (Lu - f)^T Q(Lu - f) + (H^T u - m)^T W(H^T u - m), \tag{2.43}$$

where Q is the $N \times N$ inverse of C. The Euler-Lagrange system, 2.41–2.42, expresses the condition that

$$\frac{1}{2}\nabla_u \mathcal{J}(u) = 0, \tag{2.44}$$

where ∇_u denotes the gradient operator with respect to the $N \times 1$ elements of u.

For future reference, the $N \times N$ matrix of second derivatives of $\mathcal{J}$, with respect to u, is called called the *Hessian* of $\mathcal{J}$. Let S denote the Hessian, then

$$S = \frac{\partial^2 \mathcal{J}}{\partial u \partial u^T}, \tag{2.45}$$

or

$$S = \nabla_{u^T}(\nabla_u \mathcal{J}). \tag{2.46}$$

The terse notation defined in this section simplifies the explication of solution methods, presented below, by hiding an enormous amount of extraneous detail.

2.3. Solution Methods

The solution of inverse problems based on realistic ocean models is a demanding computational task. The linear planetary geostrophic model consists of roughly 60,000 unknowns; the nonlinear model in the next chapter has over 200,000 unknowns. Because there is no unequivically "best" method for solving very large inverse problems, four methods are compared in sections 2.4 and 2.5.

There are two, formally equivalent, approaches to the problem of minimizing $\mathcal{J}$ in equation 2.43. The first approach, *direct minimization*, seeks to use any

number of minimization methods (steepest descent, conjugate gradients, Newton's method, etc.) to minimize the cost function. In order to use these methods, it is necessary to evaluate the cost function, and a means of computing the gradient of the cost function is also helpful. When direct minimization methods are used, the data assimilation method is referred to as "the adjoint method" (Tziperman and Thacker, 1989), because operators "adjoint" to the original model operators are used to compute the gradient of the cost function efficiently.

The other approach to minimizing the cost function is to solve the Euler-Lagrange equations for the extrema of $\mathcal{J}$. If $\mathcal{J}$ is a convex function of the state variables, then there is a unique extremum of $\mathcal{J}$ at its minimum value. Conventional objective analysis (Bretherton et al., 1976) can be interpreted as a solution procedure for an Euler-Lagrange system. Likewise, the "representer expansion" is another solution procedure for an Euler-Lagrange system. This class of solution methods will be called *Euler-Lagrange solvers.*

Note that both approaches to minimizing $\mathcal{J}$ are formally equivalent. When some aspect of the inverse problem is nonlinear, i.e., when either the model equations or the measurement functional is a nonlinear function of the state variables, direct minimization methods are always applicable. In contrast, the Euler-Lagrange solvers generally require one to consider a sequence of linear problems, which, idealy, will converge to the problem of interest. It is also worth noting that Euler-Lagrange solvers *do not* require one to evaluate $\mathcal{J}$; the importance of this distinction is highlighted in Appendix 4.3.

Bennett (1992) has made the distinction between *integrating* and *substituting* methods for solving time-dependent inverse problems. In the present context, integrating methods correspond to Euler-Lagrange solvers, and substituting methods correspond to direct minimization methods. However, it is possible to use both

model and adjoint integration steps as preconditioners within a direct minimization method (as in method J-CG2, below). Likewise, it is possible to use a substituting method as an Euler-Lagrange solver (as in method REP-CG, below, which is both a substituting and integrating method).

2.3.1. Euler-Lagrange Solvers

Elimination of λ between 2.41 and 2.42 results in the following system for u:

$$(L^T Q L + H W H^T) u = L^T Q f - H W m. \tag{2.47}$$

The solution of this system by direct methods (e.g., an LU decomposition) is impractical if N is large. Note that the Hessian of $\mathcal{J}$, which will be denoted by S, is the matrix $L^T Q L + H W H^T$ on the left-hand-side of equation 2.47. Thus, the solution of this system requires the construction and inversion of S; however, S^{-1} is the a posteriori covariance matrix of u. If one could create and inspect S^{-1}, one would have a complete description of the a posteriori errors (Thacker, 1989).

Because the dimension of the state space is so large that it is typically not feasible to create an $N \times N$ matrix, another direct method, the representer expansion, has proved very useful. This expansion reduces the number of unknowns from N to M by taking advantage of the fact that there are only M degrees of freedom in the inverse estimate of u (a complete discussion can be found in Wahba, 1990; Bennett, 1992; or Parker, 1994).

The representer expansion is the basis for an efficient solution method, provided that one can solve the model and adjoint model equations. To each measurement, there corresponds a "representer" r_i. In general, the representer is function, but here it is an $N \times 1$ vector. Each representer is obtained by solving the following system:

$$Lr_i = C\alpha_i \tag{2.48}$$

$$L^T\alpha_i = h_i. \tag{2.49}$$

Each of these M systems has the same form as the Euler-Lagrange system 2.41–2.42, except that the adjoint system 2.49 is decoupled from the forward system 2.48. The solution of the coupled Euler-Lagrange system 2.41–2.42 can now be obtained via the solution of M uncoupled systems.

Let R and A denote $N \times M$ matrices of representers and representer adjoints, respectively, then

$$LR = CA, \tag{2.50}$$

and

$$L^T A = H \tag{2.51}$$

are the systems which must be solved to obtain the representers; this amounts to M inversions of L and L^T (in time-dependent problems, these would be described as M forward-backward integrations). Assuming that the same amount of work is required to invert both L and L^T, the solution of the representer equations requires $2M$ model integrations, where *integration* refers to either a forward or an adjoint solve. The representer expansion for the solution itself is expressed as the sum of a first-guess field and a linear combination of representers:

$$u = u_{\text{fg}} + Rb, \tag{2.52}$$

where b is the $M \times 1$ vector of representer amplitudes, and the first-guess field solves

$$Lu_{\text{fg}} = f. \tag{2.53}$$

Substitution of the representer expansion 2.52 into 2.41 and 2.42 results in the following $M \times M$ system for b:

$$(W^{-1} + \mathcal{R})b = h, \tag{2.54}$$

where $\mathcal{R}$ is the $M \times M$ *representer matrix* (the matrix of measurements of the representers, $\mathcal{R} = H^T R$), and h is the $M \times 1$ vector $H^T u_{\text{fg}} - m$, the difference between measurements of the first-guess and the actual observations.

Provided that M is not too large, it is possible to perform the $2M$ model and adjoint integrations and solve the $M \times M$ system 2.54. If the representers are physically stored as R, then the solution to the inverse problem can be obtained as 2.52; however, this is unnecessary, and may be unmanageable if $M \times N$ is too large. Instead, one can eliminate u from the right-hand-side of 2.42 using 2.52; the resulting expression is in terms of u_{fg}, $\mathcal{R}$, and b, which are known. With 2.42 now decoupled from 2.41, solving for λ and u is straightforward. Thus, the total work consists of $2M + 3$ model integrations (1 integration for the first-guess, $2M$ integrations for the representers, and 2 integrations for the final decoupled system), and the solution of one $M \times M$ system (Bennett, 1992).

It is also possible to use an iterative solver for equation 2.54, as was suggested by Egbert et al. (1994). The product $\mathcal{R}\hat{b}$ can be obtained for any $M \times 1$ vector $\hat{b}$ by one sequence of forward and adjoint integrations, and the product $W^{-1}\hat{b}$ is easily constructed. The ability to create $(\mathcal{R} + W^{-1})\hat{b}$ and store one more $M \times 1$ vector are all that is needed to implement the conjugate gradient method (explained in the next section) to solve equation 2.54. In this context, the conjugate gradient solver is a direct minimization method applied to minimize $\phi(b) = \frac{1}{2}b^T(\mathcal{R} + W^{-1})b - b^T h$.

The convergence of the conjugate gradient solver for equation 2.54 depends on the condition number of $\mathcal{R} + W^{-1}$. For the two sample problems considered below (with $M = 662$ and $M = 1143$ measurements, respectively), it was possible to calculate the eigenvalue spectrum of the representer matrix and study the condi-

tioning in detail. The balance between model and data uncertainty was such that the condition number was roughly 10^4, and the conjugate gradient solver applied to 2.54 performed adequately without any preconditioning. In other circumstances it may be advantageous to precondition $\mathcal{R} + W^{-1}$ with $(\mathcal{R}_C + W^{-1})^{-1}$, where $\mathcal{R}_C$ is the representer matrix computed using a low-resolution version of the model, which would be inexpensive to compute (Egbert et al., 1994).

2.3.2. Direct Minimization Methods

Two minimization methods are compared in the following sections. Both methods are conjugate gradients solvers; however, they differ in the choice of preconditioning operators.

The conjugate gradient method (e.g., Luenberger, 1973) is a widely used iterative method for large-scale minimization. When $\mathcal{J}$ is a quadratic function of the state variables (as it is here), the conjugate gradient method has the important property of convergence in N steps. The method works by successively minimizing $\mathcal{J}$ over a sequence of linearly independent subspaces of the N-dimensional state space. Hence, after N steps, the global minimum of $\mathcal{J}$ is obtained.

Iterative descent methods have been applied to data assimilation problems in meteorology and oceanography, where they are commonly referred to as "variational data assimilation" (e.g., LeDimet and Talagrand, 1986) and "the adjoint method" (e.g., Tziperman and Thacker, 1989), respectively. Navon and Legler (1987) review a number of descent methods, including steepest descent, conjugate gradients, and quasi-Newton methods. Since Nazareth (1979) has shown the equivalence between quasi-Newton methods and the conjugate gradient method for quadratic $\mathcal{J}$ and exact arithmetic, only the conjugate gradient method is considered here.

The success of iterative methods is largely determined by the condition number of the Hessian of $\mathcal{J}$. Preconditioning methods seek a linear transformation of variables such that the new Hessian is close to the identity. An introduction to preconditioning methods can be found in Golub and VanLoan (1989).

Two preconditioning methods are attempted below. The first method is a simple rescaling of the state variables. The rescaling is done so that the diagonal elements of the rescaled Hessian are unity (Marotzke, 1992). The matrix representation of this preconditioner is simply a diagonal matrix equal to the square-root of the inverse of the Hessian diagonal.

The second preconditioner makes a change of variables using the model, L, and a square root of the weight, Q,

$$v = Q^{1/2}Lu. \tag{2.55}$$

The symbol $Q^{1/2}$ denotes any operator such that $Q = (Q^{1/2})^T Q^{1/2}$. In terms of v, the new penalty function is

$$\mathcal{J}(v) = v^T v + (H^T L^{-1} Q^{-1/2} v - m)^T W (H^T L^{-1} Q^{-1/2} v - m). \tag{2.56}$$

The Hessian of $\mathcal{J}$ with respect to v is

$$S_v = I + (H^T L^{-1} Q^{-1/2})^T W H^T L^{-1} Q^{-1/2}. \tag{2.57}$$

Note that S_v is equal to the identity plus a rank-M matrix, i.e.,

$$S_v = I + BB^T, \tag{2.58}$$

where $B^T = W^{1/2} H^T L^{-1} Q^{-1/2}$ is an $M \times N$ matrix. Thus, S_v has at most $M + 1$ distinct eigenvalues (Golub and VanLoan, 1989): the N eigenvalues of I are all unity, and BB^T has exactly M nonzero eigenvalues.

There are two reasons for using this preconditioner. First, since the transformed Hessian has at most $M+1$ distinct eigenvalues, as compared with N possible distinct eigenvalues of the original system, the conjugate gradient algorithm should converge in at most $M+1$ steps (Luenberger, 1973).

The second reason for using equation 2.55 as a preconditioner is suggested by the possibility that the condition number of the Hessian is determined by the unobservable part of the state space. Denote the untransformed Hessian by S_u, and recall that

$$S_u = L^T Q L + H W H^T. \tag{2.59}$$

Consider both pieces of the Hessian separately, and let

$$S_u^{\text{dyn}} = L^T Q L, \tag{2.60}$$

and

$$S_u^{\text{data}} = H W H^T. \tag{2.61}$$

S_u^{data} is at most of rank M; suppose that its eigenvalues are all equal to a constant, σ^{-2}, the inverse of the observational error. In contrast, since L is of rank N, and Q is positive-definite symmetric, S_u^{dyn} has a full compliment of N nonzero eigenvalues. It is plausible that S_u^{dyn} has some eigenvectors which are unobservable. Suppose ϕ is one such unobservable eigenvector, then, by definition, $H^T\phi = 0$, and ϕ is also an eigenvector of S_u. If ϕ is heavily penalized, which would be the case if $L\phi$ were dominated by small-scale features and the model weight Q were chosen specifically to penalize such structure, then the associated eigenvalue could be huge compared to σ^{-2}. Conceivably, such large eigenvalues, associated with the unobservable part of the state space, could be many orders of magnitude larger than the smallest eigenvalues of S_u, which are bounded from below by σ^{-2}.

In contrast, the unobservable eigenvectors of S_v will have eigenvalues equal to unity. It is difficult to predict much about the remaining, observable, eigenvectors. Inspection of equation 2.57 reveals that it may be best to think of this preconditioner as a transformation into the space of model residuals, out of the space of model states. The data terms in 2.56 can be regarded as measurements of the model residual.

2.3.3. Summary

Four solution procedures for the generalized inverse (system 2.24–2.40) are compared in the following two sections. The solution methods are as follows:

1. *REP* The representer expansion with a direct matrix solver for system 2.54.
2. *REP-CG* The representer expansion with a conjugate gradient solver for system 2.54.
3. *J-CG1* Conjugate gradient minimization of $\mathcal{J}$ preconditioned by rescaling.
4. *J-CG2* Conjugate gradient minimization of $\mathcal{J}$ preconditioned with equation 2.55.

The methods were compared in terms of the number of model and adjoint integrations or substitutions which must be carried out to reach a solution. For the present model, the operation counts for the integration and substitution procedures are not significantly different, so they are counted as the same amount of work (i.e., given u, it costs as much to evaluate Lu as it does to evaluate $L^{-1}u$). For comparison, the operation count for each solution method is summarized in Table 2.4. The one-time work for J-CG1 is an estimate of the (significant) number of substitutions

involved in computing the rescaling transformation; the amount of work depends on the operator L and the correlation scales of the forcing errors (Marotzke, 1992).

TABLE 2.4. Solution Methods

Method	Work per Step	One-Time Work	Total
REP	2	$3 + (M \times M$ solve)	$2M + 3$ $+(M \times M$ solve)
REP-CG	2	3	$2 \times N_{\text{step}} + 3$
J-CG1	2	800	$2 \times N_{\text{step}} + 800$
J-CG2	4	0	$4 \times N_{\text{step}}$

Note that it is necessary to invert the model operator in order to apply methods REP, REP-CG, and J-CG2. Using the terminology of Bennett (1992), these three methods rely on an *integration* step. Method J-CG1, in contrast, does not use the inverse of the model operator. Another distinction between the methods is that J-CG1 and J-CG2 are equally applicable to linear and nonlinear models alike, while representer-based methods would require the consideration of a sequence of linearized models in order to be applicable to a nonlinear inverse problem (e.g., Bennett and Thorburn, 1992).

The estimates in Table 2.4 are lower bounds on the amount of work per iteration step. In practice, the descent algorithm may require several (two to six) additional penalty and gradient evaluations. Nonetheless, iteration methods which converge in fewer than M steps may be a significant improvement over the direct representer expansion. The method which proves to be the "best" depends on the relative amount of work in the substitution versus the integration steps, and on the implementations of the covariance and weight operators.

2.4. Array Analysis I: Thermocline Depth Measurements

The machinery developed in the above sections is now applied to an observing array consisting of thermocline depth measurements in the North Pacific. The representer expansion is also used to study the a posteriori errors; it is concluded that the hydrographic data cause a negligible reduction in the Ekman pumping uncertainty. A much more accurate ocean model would be necessary for the hydrographic data to make a significant improvement in the surface boundary condition estimates.

The parameters in the inversion are summarized in Table 2.2, and the data locations are shown in Figure 2.3. The data consist of measurements of the 9.7°C isotherm depth, a proxy for the thermocline depth, taken from a North Pacific hydrographic data set (Reid and Mantyla, 1988).

The first-guess solution is determined by integrating the model with boundary conditions obtained from an objective analysis of the Reid-Mantyla data for the three z boundary conditions (at the top, bottom, and eastern boundaries), and by using the Ekman pumping velocity derived from the annually-averaged wind-stress data of Hellerman and Rosenstein (1983) for the top boundary condition on $\omega\bar{z}_\theta$.

The objective analysis of the Reid-Mantyla data set deserves some comment since it is used in each of the case studies below. Because objective analysis is a statistical estimation method, it is necessary to specify the first and second moments (the mean and the covariance) of the field which is to be estimated (Bretherton et al., 1976). For simplicity, the mean field was set equal to the horizontal average of the the observations, and the observational errors were assumed to be vertically uncorrelated. A bell-shaped covariance, or un-normalized Gaussian, was used for the horizontal analysis. The zonal and meridional e-folding scales of the

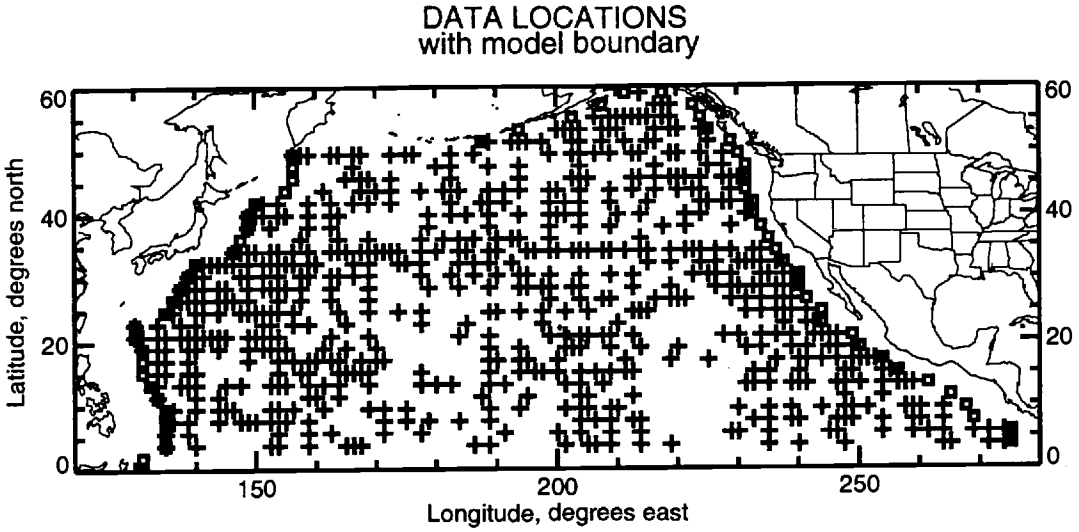

FIGURE 2.3. Data locations, "Thermocline Depth" experiment.

The 662 measurement locations used in the "Thermocline Depth" experiment are shown. The observations consist of the depth of the 9.6°C isotherm at each location. Squares indicate the zonal boundaries of the computational domain.

bell-shaped covariance were 2,600km and 1,800km, respectively (somewhat larger than used by Fukumori and Wunsch, 1991). These length scales were chosen after experimenting with a number of scales, and subjectively picking the scales which did not lead to "bulls-eyes" around clusters of data. The signal-to-noise ratio of the data, i.e., the ratio of the analysis covariance at zero lag to the data error variance, was assumed to be four. Because no obvious distinction between "signal" and "noise" is present in the observations, the objective analysis is regarded as an *ad hoc* smoothing procedure for the purpose of gridding the observations.

2.4.1. The Representers

It is informative to examine the structure of the representers to understand the predictive power of the model. It can be shown that the representer for a point measurement of z at $\mathbf{x}_i$ is the covariance of the state with $z(\mathbf{x}_i)$ under the hypothesis that the prior model is correct. By linearity, this prior state covariance (a representer) can be expressed as the sum of contributions from each source of model covariance. In other words, any representer for the planetary geostrophic model may be expanded as:

$$r_i = r_i^z + r_i^{z_E} + r_i^{z_T} + r_i^{z_B} + r_i^{w_T} + r_i^{w_B}, \tag{2.62}$$

where each term in the sum corresponds to each source of uncertainty. This decomposition is instructive since it makes explicit which control variables contribute most to the prior uncertainty of the state variable. A working heuristic is that the inverse solution will modify that control variable the most, which contributes most to the prior state covariance.

The most significant sources of prior state covariance are (in order) the surface Ekman pumping, the eastern boundary condition, and the interior forcing.

For a typical site in the middle of the domain, the prior state variance at the site ($3000m^2$) is comparable to the measurement error variance ($4000m^2$). This suggests that the data will explain roughly 50% of the prior state variance at the measurement locations, and that the surface Ekman pumping will be the control variable which is modified in order to fit the observations.

Figure 2.4 shows a representer for a point measurement near the middle of the domain. The three largest terms contributing to the sum (equation 2.62) are plotted in Figures 2.5 through 2.7. The shape of each representer component is a consequence of the correlations embodied in the dynamical model, as well as the spatial structure of the corresponding model forcing covariance. As the model dynamics consist of standing forced-dissipative Rossby waves, there is a strong zonal correlation in the spatial structure of each representer component. The vertical structure is primarily a consequence of the different zonal decay scales of the damped-baroclinic vertical modes.

2.4.2. Array Analysis

The observing array can be studied via an orthogonal decomposition of the representer matrix. The orthogonal decomposition (a Schur decomposition; Golub and Van Loan, 1989) diagonalizes the Hessian of the cost function with respect to the representer coefficients if the data covariance is diagonal, and it can be interpreted as an orthogonal decomposition of the prior state covariance at the measurement sites. A comparison of the eigenvalue spectrum of the representer matrix with the prior data variances shows how effective the data are at constraining the state. This analysis does not depend on the actual data values themselves, so the efficiency of

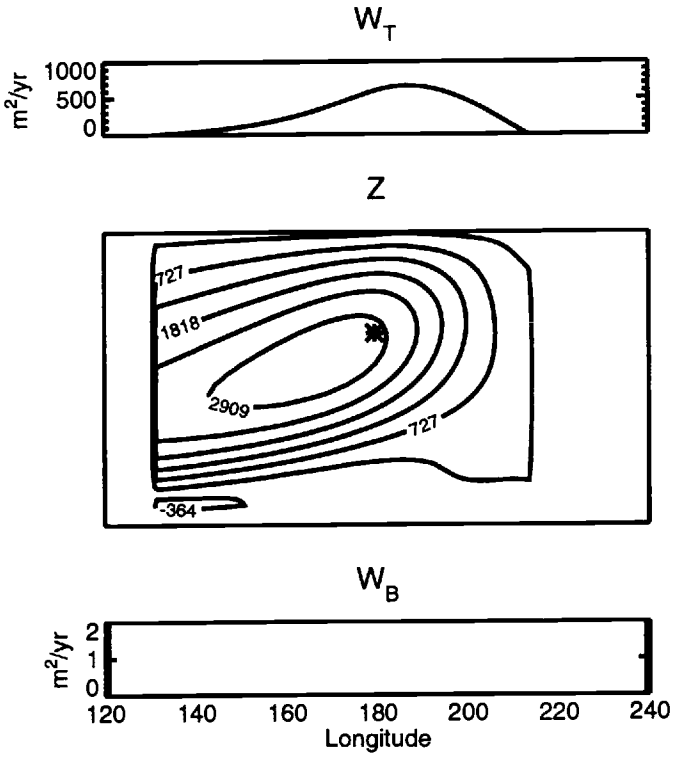

FIGURE 2.4. Total representer.

A zonal section of the representer for a point measurement is shown. The representer is the covariance of the state with the value of the state at the measurement site (marked *), under the assumption that the prior model error covariance (shown in Figures 2.1 and 2.2) is correct. The anisotropy of the representer is a consequence of the model dynamics.

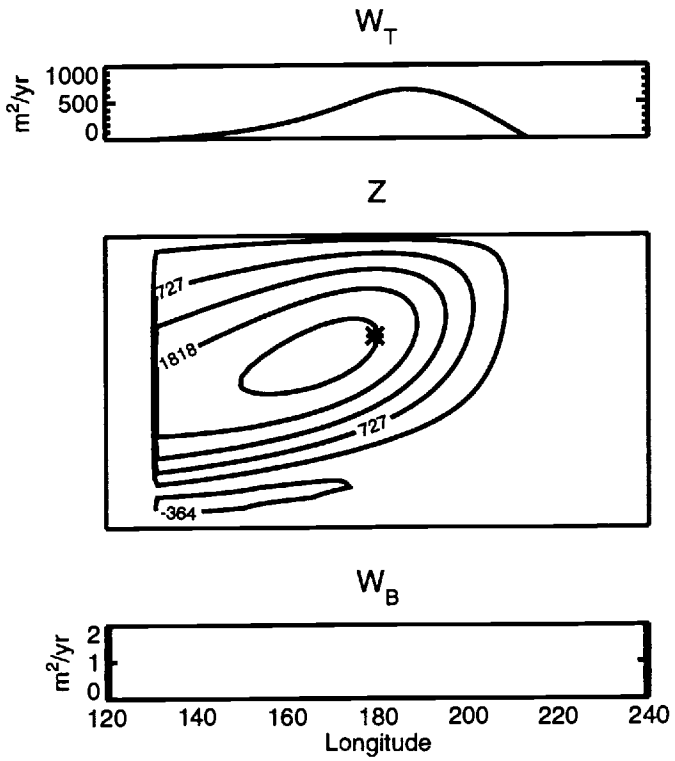

FIGURE 2.5. Surface Ekman pumping representer.

The component of the representer caused by surface Ekman pumping boundary condition covariance is shown. This is term $r_i^{w_T}$ in equation 2.62.

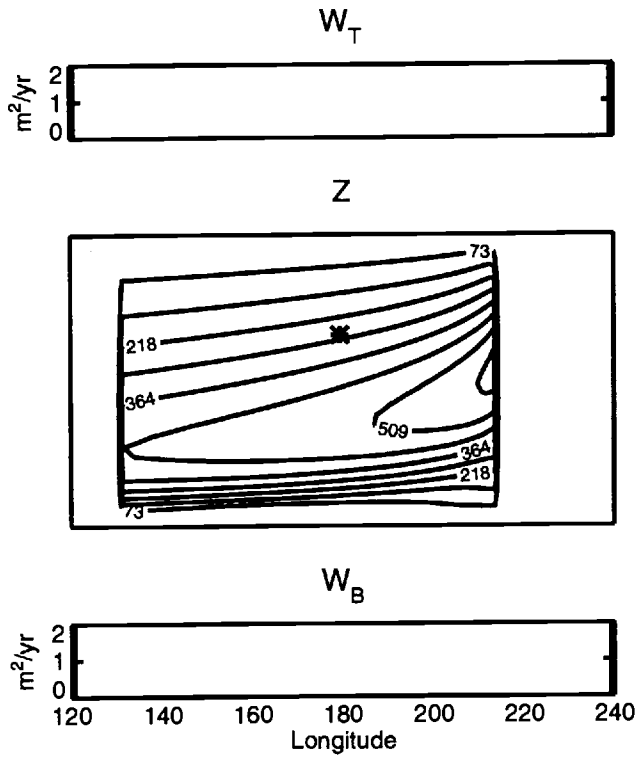

FIGURE 2.6. Eastern boundary condition representer.

The component of the representer caused by the eastern boundary condition covariance is shown (r_i^{zE} in equation 2.62).

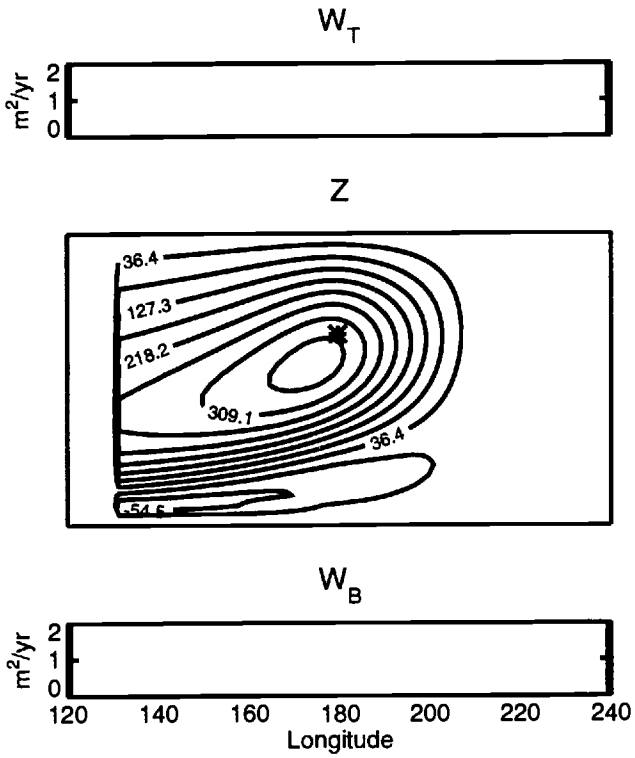

FIGURE 2.7. Interior forcing representer.

The component of the representer caused by interior (non-boundary condition) covariance is shown (r_i^z in equation 2.62).

the observing array can, in principle, be evaluated independently of the actual data collection program.

Substitution of the representer expansion (equation 2.52) into the penalty function (equation 2.43) yields an expression for the penalty function in terms of the representer coefficients:

$$\mathcal{J}(b) = b^T \mathcal{R} b + (\mathcal{R}b - m)^T W (\mathcal{R}b - m). \tag{2.63}$$

Let the $M \times M$ matrix Z denote the matrix of eigenvectors of $\mathcal{R}$, and let Λ denote the $M \times M$ diagonal matrix of eigenvalues of $\mathcal{R}$, then the orthogonal decomposition of $\mathcal{R}$ is

$$\mathcal{R} = Z \Lambda Z^T. \tag{2.64}$$

It is assumed that the diagonal entries of Λ are ordered $\lambda_1 \leq \lambda_2 \leq \ldots \leq \lambda_M$. This decomposition exists and is unique (up to a permutation of the eigenvalue ordering) since $\mathcal{R}$ is symmetric and positive-definite (Golub and VanLoan, 1989). Let $\hat{b}$ and $\hat{h}$ denote the projections of b and h onto the eigenvectors of $\mathcal{R}$:

$$\hat{b} = Z^T b, \tag{2.65}$$

and

$$\hat{h} = Z^T h. \tag{2.66}$$

Finally, the penalty function in terms of $\hat{b}$ is

$$\mathcal{J}(\hat{b}) = (\Lambda \hat{b})^T \Lambda^{-1} (\Lambda \hat{b}) + (\Lambda \hat{b} - \hat{h})^T Z^T W Z (\Lambda \hat{b} - \hat{h}). \tag{2.67}$$

If the prior data errors are uncorrelated and constant, i.e., $W = \sigma^{-2} I$, then $\mathcal{R}$ and W are simultaneously diagonable, and the penalty function Hessian (with respect to

$\hat{b}$) is diagonal. The penalty function is written so that $\hat{b}$ appears only in the product $\Lambda\hat{b}$, which has the same units as the measurements; therefore, the elements of Λ and W^{-1} are directly comparable.

A statistical interpretation of equation 2.67 is as follows. The prior model for $\Lambda\hat{b}$ states that

$$E[\Lambda\hat{b}] = 0, \tag{2.68}$$

and

$$E[\Lambda\hat{b}(\Lambda\hat{b})^T] = \Lambda, \tag{2.69}$$

where $E[*]$ denotes expected value. A little algebra shows that the posterior error covariance for $\Lambda\hat{b}$ is given by

$$\Lambda - \Lambda(Z^T W^{-1} Z + \Lambda)^{-1}\Lambda. \tag{2.70}$$

In essence, the explained covariance of the rotated and scaled representer coefficients is $\Lambda(Z^T W^{-1} Z + \Lambda)^{-1}\Lambda$.

Assuming that $W^{-1} = \sigma^2 I$, one can consider a number of limits regarding the size of the representer eigenvalues as compared to the prior data error variance σ. First, consider an eigenvector (representer mode) for which $\lambda_i \gg \sigma^2$. The prior modal uncertainty is much greater than the prior data uncertainty, so the posterior uncertainty for that mode is

$$\lambda_i - \lambda_i^2/(\sigma^2 + \lambda_i) \approx \sigma^2. \tag{2.71}$$

In other words, modes for which $\lambda_i \gg \sigma^2$ are well-constrained by the observations, and their posterior uncertainty is approximately σ^2. It is suggestive terminology to say that these modes are *interpolated* by the inverse solution.

The other extreme is represented by modes for which $\lambda_i \ll \sigma^2$. The observations cannot improve one's estimates for these modes because they are already determined by the prior model. In this case, the data explain an insignificant amount of the prior modal variance. One would say that these modes are *smoothed* by the inverse.

To summarize, the amplitudes of the modes for which $\lambda_i \ll \sigma^2$ cannot be estimated from the observing array. If an eigenvalue decomposition is actually used in the solution procedure for equation 2.54, it is possible to omit the component of the inverse solution associated with the modes having $\lambda_i \leq \sigma^2$ without adversely affecting the solution (Bennett, 1990). When the prior data errors are constant and uncorrelated, a plot displaying the diagonal elements of W^{-1} and Λ effectively summarizes the properties of the observing array.

Figure 2.8 compares the eigenvalue spectrum of $\mathcal{R}$ with the prior data variances. The figure indicates that the 662 observations provide a significant constraint on only about one-tenth as many modes. The high order (large λ_i) representer modes have large-scale, spatially coherent structure; thus, the inverse problem is stable in the sense that perturbations to an individual datum have little effect on the spatial structure of the solution.

The *solution-array-modes* are the physical fields associated with each representer mode (Bennett, 1990). They show what physical fields are actually constrained by the observations. For example, Figures 2.9 and 2.10 show the solution-array-mode corresponding to mode 662, the highest-order mode. Comparing λ_i with σ^2 indicates that the large-scale features present in this mode are well-determined by the array. Figures 2.11 and 2.12 show solution-array-mode number 600, for which $\lambda_i \approx \sigma^2$. As expected, this mode is composed of smaller-scale features than mode 662. It is reassuring that the spatial structure of the higher-order modes corresponds

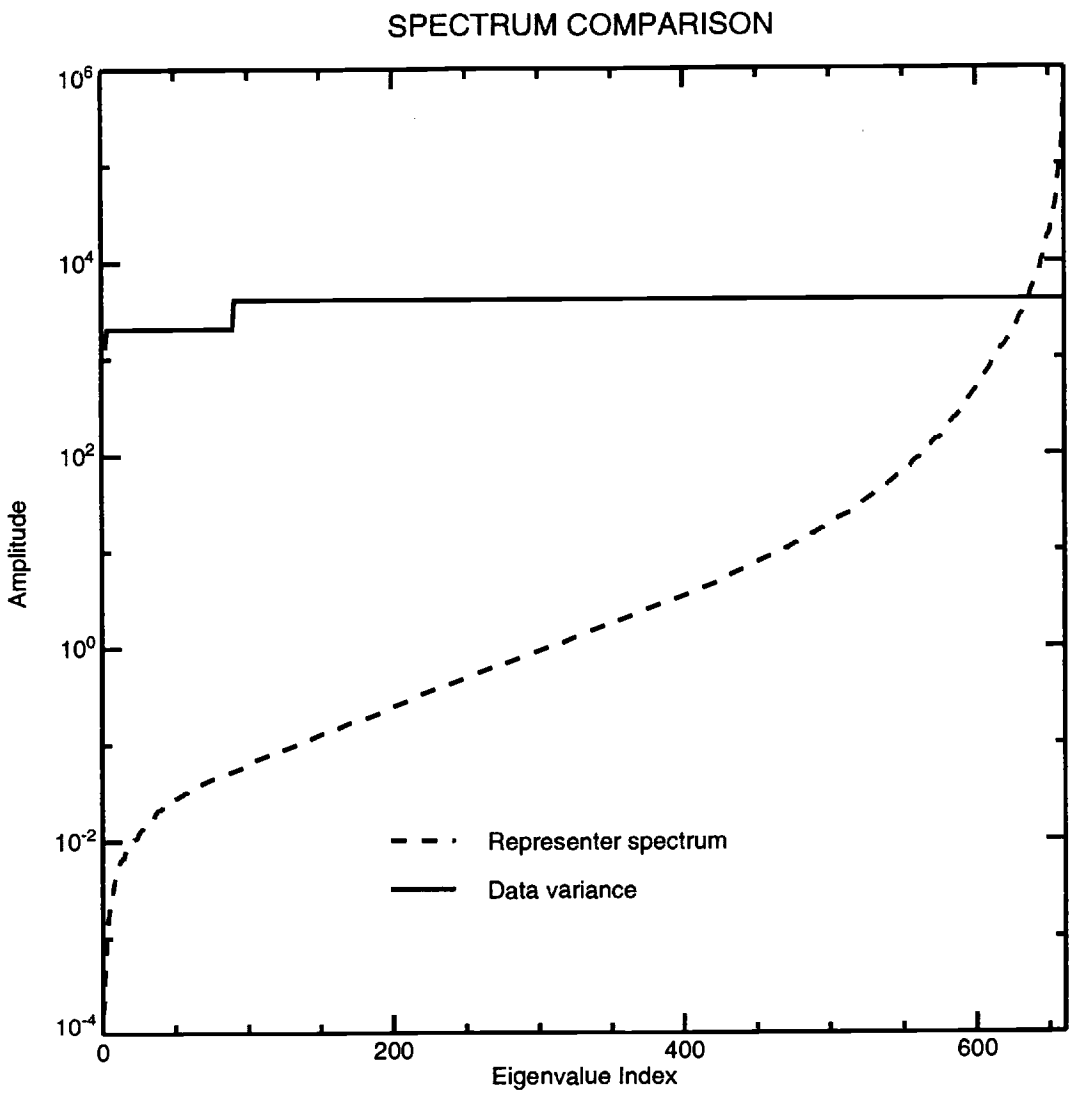

FIGURE 2.8. Representer spectrum, "Thermocline Depth".

The ordered eigenvalue spectrum, $\{\lambda_i\}_{i=1}^{M}$, of the representer matrix $\mathcal{R}$ is plotted as the dashed line. The ordered entries of the diagonal matrix W^{-1}, the observation error variances, are plotted as the solid line. The representer solution "interpolates" the observations with solution-array-modes for which $\lambda_i > W^{-1}$; the modes for which $\lambda_i < W^{-1}$ are "smoothed."

to the large-scale features which are normally thought of as defining the general circulation. If this were not the case, it would suggest that a redesign of the observing array (or a re-assessment of the prior error covariances) would be necessary for the observations to significantly improve upon the model.

2.4.3. Inverse Solution

Because of the relatively small dimension of this inverse problem, it is feasible to present a more extensive analysis than might be possible otherwise. The four solution methods listed in Table 2.4 are compared in this subsection, and the inverse solution and its errors are shown.

The four solution methods for obtaining the best-fit solution are compared in Figure 2.13. The least effective method is the diagonally preconditioned conjugate gradient method, J-CG1; no significant progress was made in the course of the minimization. In contrast, J-CG2, the conjugate gradient minimization preconditioned with the dynamics, converged quite rapidly. Fastest convergence was obtained with the REP-CG solver, which converged in roughly 1/20 the number of model integrations as the full representer calculation. It is emphasized that each of the solvers: REP, REP-CG, and J-CG2, obtained the identical (and unique) solution to within machine precision.

Figure 2.14 shows a section of isotherm depth across the middle of the subtropical gyre, and compares the inverse result with the measurements. As expected from the representer spectrum analysis above, the inverse solution fits the large scale features of the data, but it does not interpolate individual measurements. The total impact of the observations was to modify the first-guess by approximately 100m, the root-mean-square difference between the first-guess and the best-fit.

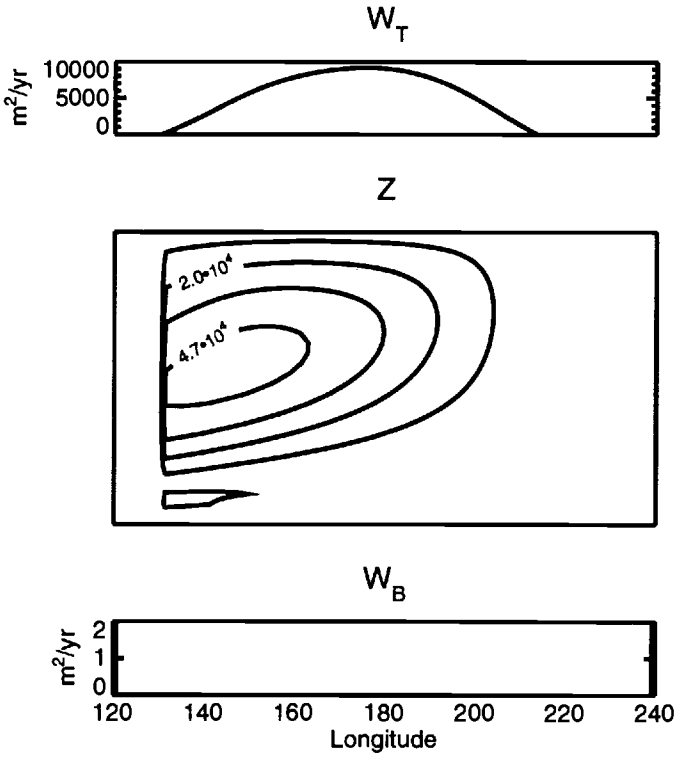

FIGURE 2.9. Solution-array-mode 622: zonal section.

The most significant solution-array-mode (SAM) is shown in zonal section. The representer spectrum indicates that it is large-scale features, such as are present in this mode, which are well-determined by the data.

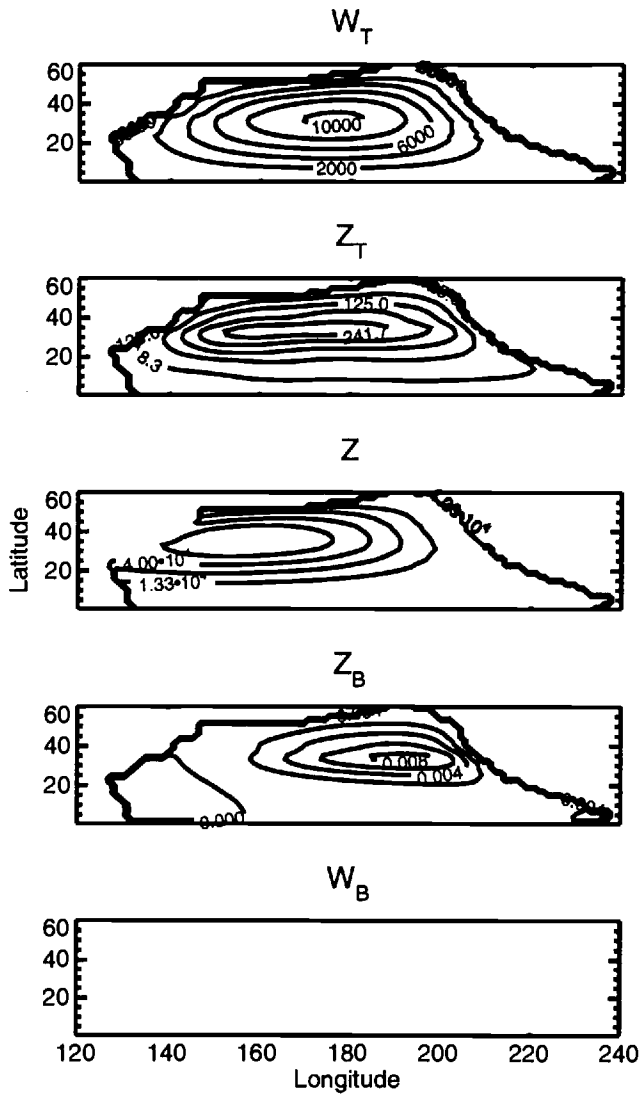

FIGURE 2.10. Solution-array-mode 622: plan view.

The most significant solution-array-mode (SAM) is shown in plan view. The middle panel entitled "Z" is the amplitude of the SAM on the 9.6°C isotherm.

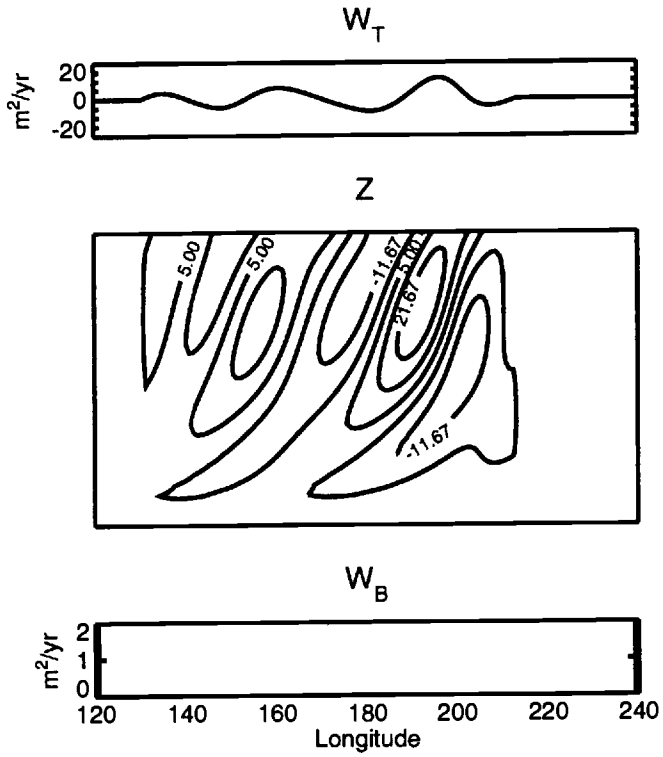

FIGURE 2.11. Solution-array-mode 600: zonal section.

A marginally significant solution-array-mode is shown in zonal section. The component of the observations which projects onto this mode is heavily smoothed, rather than interpolated, by the inverse solution.

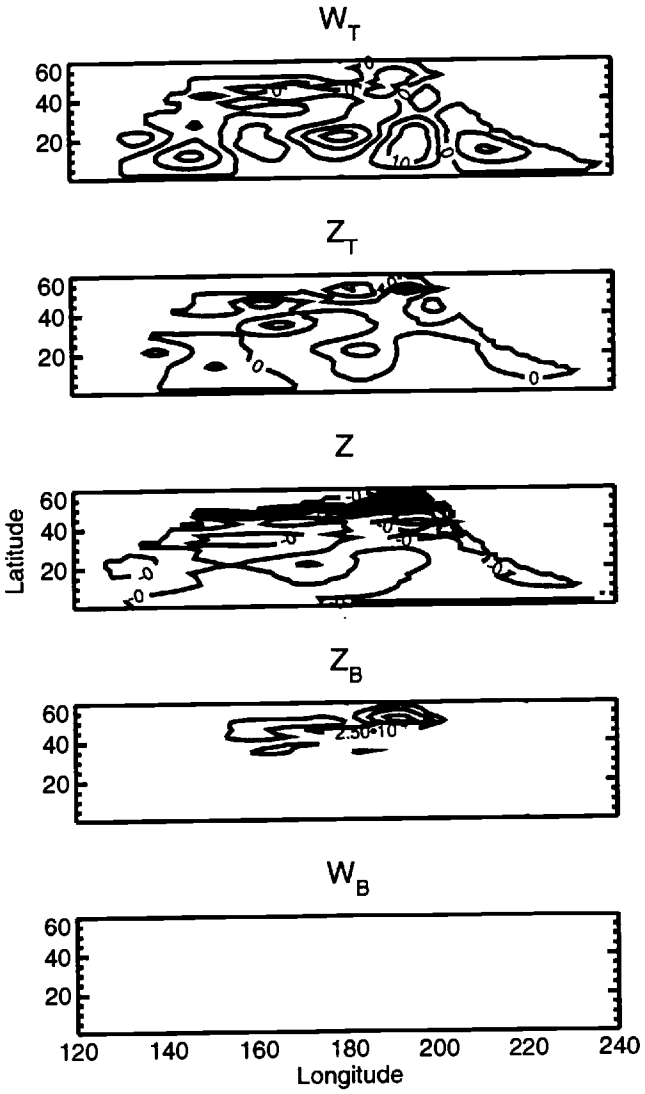

FIGURE 2.12. Solution-array-mode 600: plan view.

A marginally significant solution-array-mode is shown in plan view.

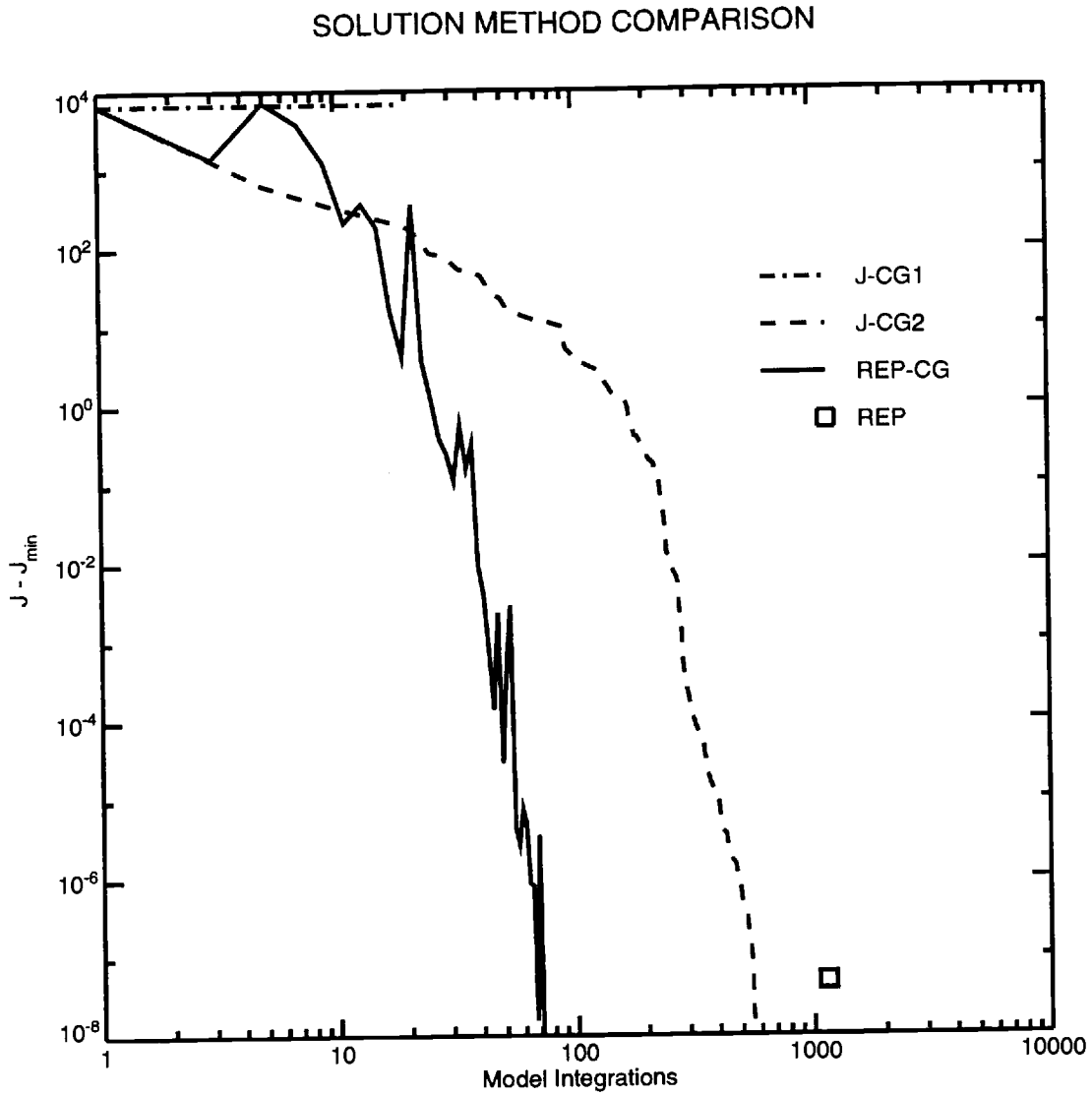

FIGURE 2.13. Solution method comparison, "Thermocline Depth".

The plot compares the relative efficiency of the solution procedures listed in Table 2.4. The x-axis measures the relative amount of work in units of model integrations, i.e., the number of times the model operator L is inverted. As mentioned in the text, model integrations and substitutions are equally expensive.

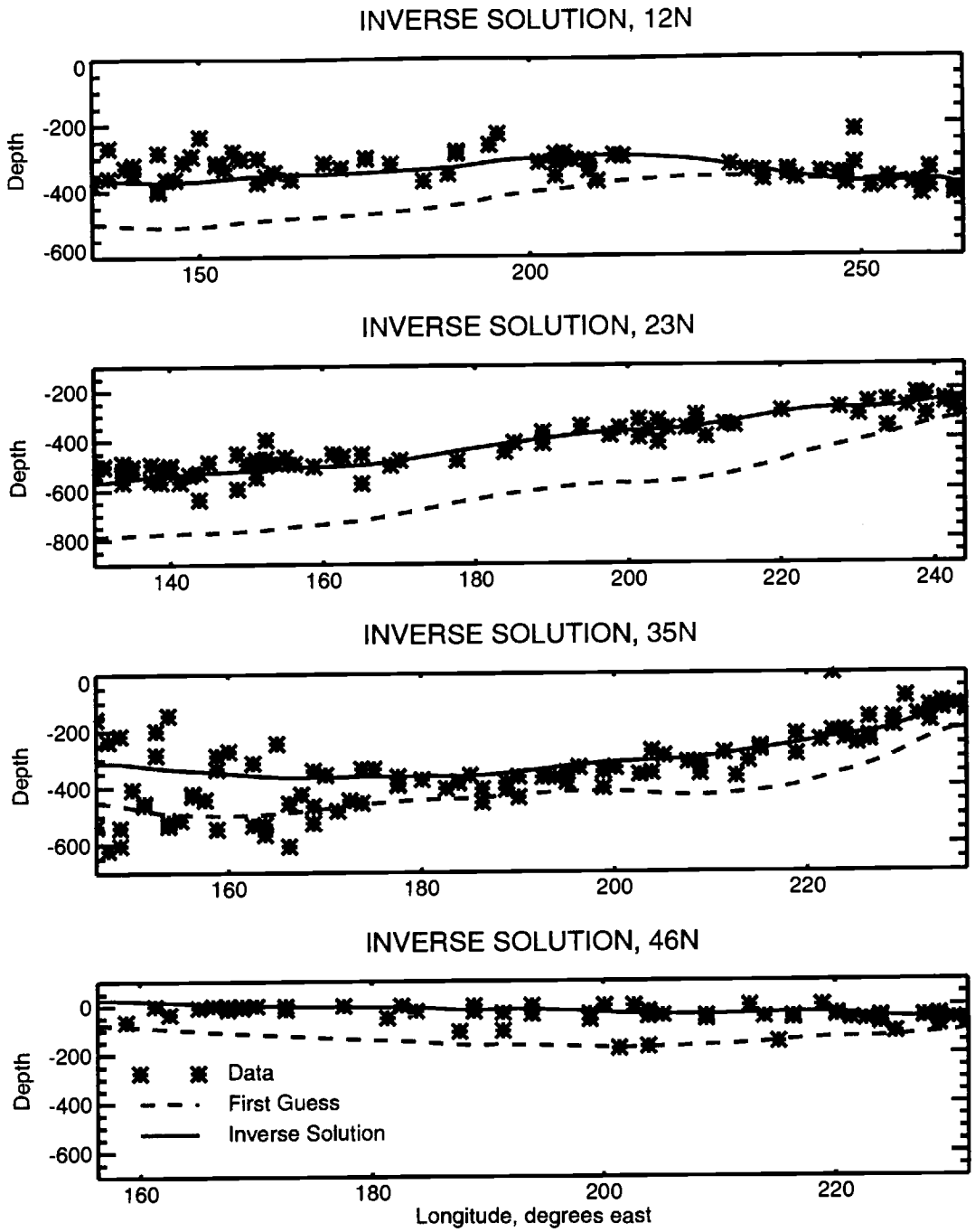

FIGURE 2.14. Inverse solution, "Thermocline Depth".

The inverse solution (solid line), data (asterisks), and first-guess solution (dashed line) are compared at four different latitudes.

The minimum penalty was shared disproportionately between the data misfit and the model residual, with the data misfit accounting for 88% of the final penalty. This is explained with Figure 2.15, which shows the magnitudes of the representer coefficients projected onto the representer array modes (the representer eigenvectors), and the contributions of the modes to $\mathcal{J}_{\text{dyn}}(u_{\text{min}})$. The representer coefficients projected roughly evenly onto the array modes; however, only the most significant modes, those modes for which $\lambda_i > \sigma^2$, contributed significantly to the minimum value of the penalty function.

Under the assumption that the prior error estimates are all correct (the null hypothesis), the minimum value of the penalty function is distributed like χ^2_M (Tarantola, 1987). Assuming that this is the case, the minimum value of the penalty function is a guide to the plausibility of the inverse solution. The minimum value of the penalty function was $\mathcal{J}(u_{\text{min}}) = 747$; for $M = 662$, the χ^2_M variable exceeds $\mathcal{J}(u_{\text{min}})$ with probability $p = 0.8\%$. It is typical for χ^2 variables to have p-values like 10^{-18} (Press et al., 1989) when the null hypothesis is *false*. Since we have only one realization of our χ^2 variable, the p-value of 0.8% is considered acceptable.

The minimum value of the penalty function suggests that the null hypothesis is plausible. Indeed, over the entire domain, the root-mean-square dynamical residual was only 8% of the root-mean-square of the diffusion term. The three dominant terms which contributed to the final dynamical penalty were the surface Ekman pumping, the eastern boundary condition, and the interior dynamics. Together the three terms accounted for roughly 40%, 35%, and 20%, of $\mathcal{J}_{\text{dyn}}(u_{\text{min}})$, respectively.

Posterior misfits in the surface Ekman pumping and eastern boundary conditions were roughly 3/2 their prior estimates. The other boundary conditions changed negligibly.

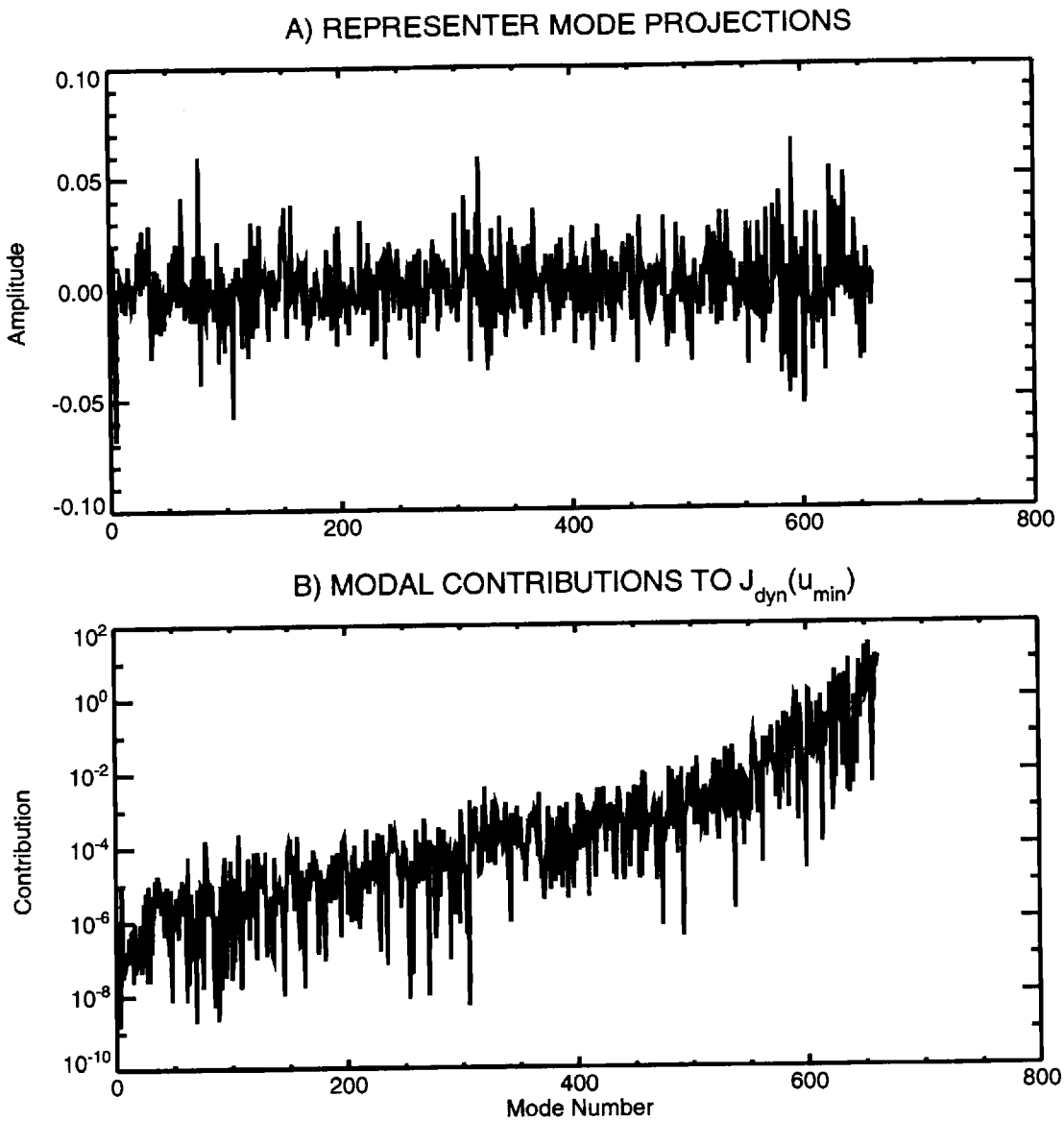

FIGURE 2.15. Representer projection.

A) In order to explain the relative contributions of the dynamics and the data to the minimum value of the penalty function, the projections of the representer coefficients onto the eigenvectors of the representer matrix are shown. The representer coefficients project relatively uniformly onto the modes. B) The contribution of each mode to $\mathcal{J}_{\text{dyn}}(u_{\text{min}})$ is shown. It is seen that only the modes associated with the largest eigenvalues contribute significantly to the penalty function.

When averaged over all of the observations, the *prior* root-mean-square data misfit was eight times larger than the expected misfit. The *posterior* root-mean-square misfit was 0.9 times the expected misfit. Figure 2.14 shows that the first-guess field agreed qualitatively with the data, but not quantitatively, and this was borne out by the prior penalty function. In contrast, the best-fit solution was as good a fit as was warranted by the data, given the prior estimate of the data errors.

A component of the posterior covariance is plotted in Figures 2.16 through 2.19. The figures show that the measurements significantly reduced the variance in the estimate of the state; however, the model forcing variance was not significantly reduced by the assimilation. Because thermocline depth is only weakly correlated with the boundary conditions (as is evident in Figure 2.4), only a modest reduction in boundary condition uncertainty was achieved. Another interpretation is that the model acts as a low-pass filter on the forcing and boundary conditions; hence, pointwise measurements of z constrain only the large-scale features of the model's inhomogeneities.

The fit to the data was achieved primarily through adjustments to the surface Ekman pumping boundary condition. This result was not unexpected, since the dominant term in equation 2.62 was associated with the surface Ekman pumping boundary condition.

2.5. Array Analysis II: A Zonal Section

A set of observations distributed zonally across the subtropical gyre is considered in this section. In this experiment, the depths of up to 13 separate isotherms were sampled at each station; in contrast, the depth of a single isotherm was considered in the previous section. Figure 2.20 shows the station locations and Table 2.5

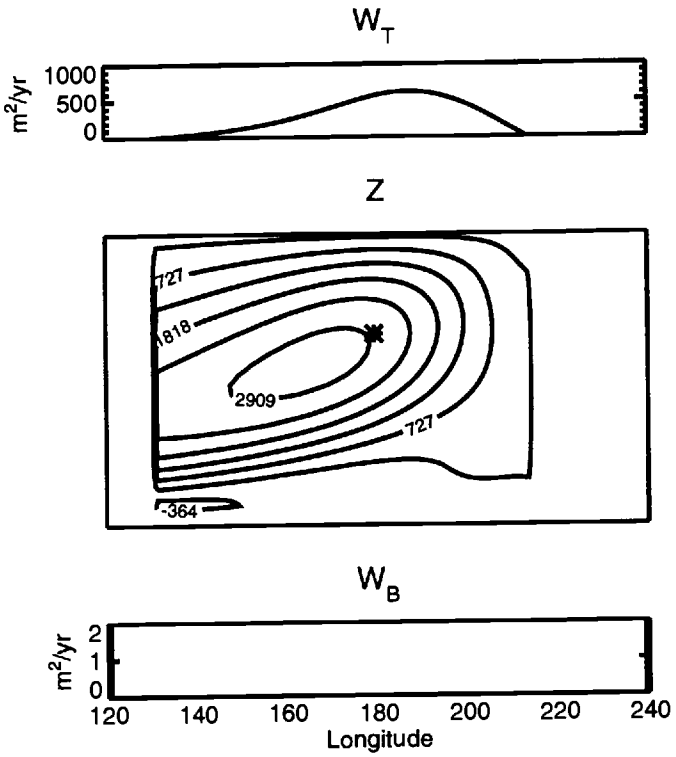

FIGURE 2.16. Explained state covariance.

The explained covariances of the state is shown. The panels show covariance of the fields with the point marked with the astericks (*). Comparing this figure with the prior state covariance (Figure 2.4) shows that the inverse was successful in explaining a large fraction of the state covariance.

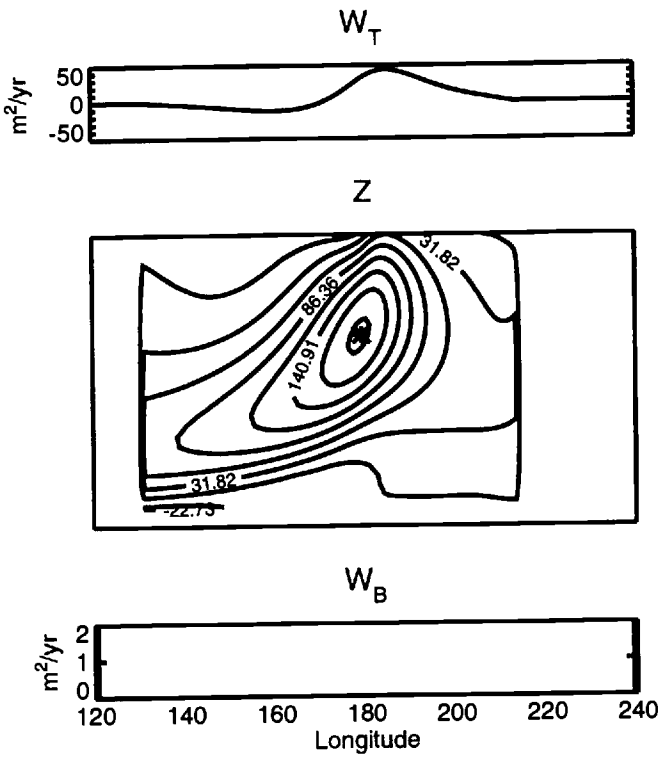

FIGURE 2.17. Final state covariance.

The posterior error covariance the state is shown. The field in this figure is the difference of the fields in Figures 2.4 and 2.16.

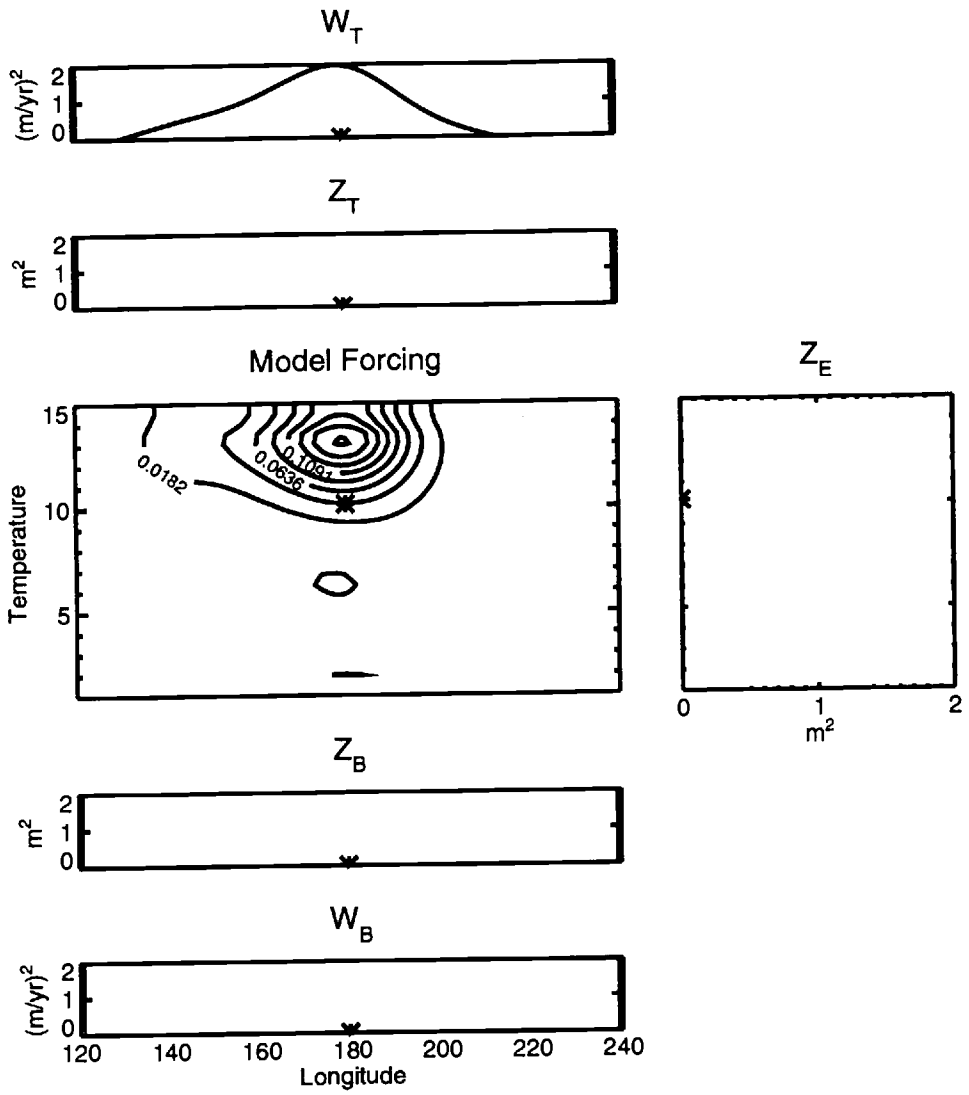

FIGURE 2.18. Explained forcing covariance.

The explained covariance of the model forcing is shown. The plots show covariances of the fields with the point marked with the astericks (*). Comparison with Figures 2.1 shows that the data is ineffective for explaining model forcing covariance.

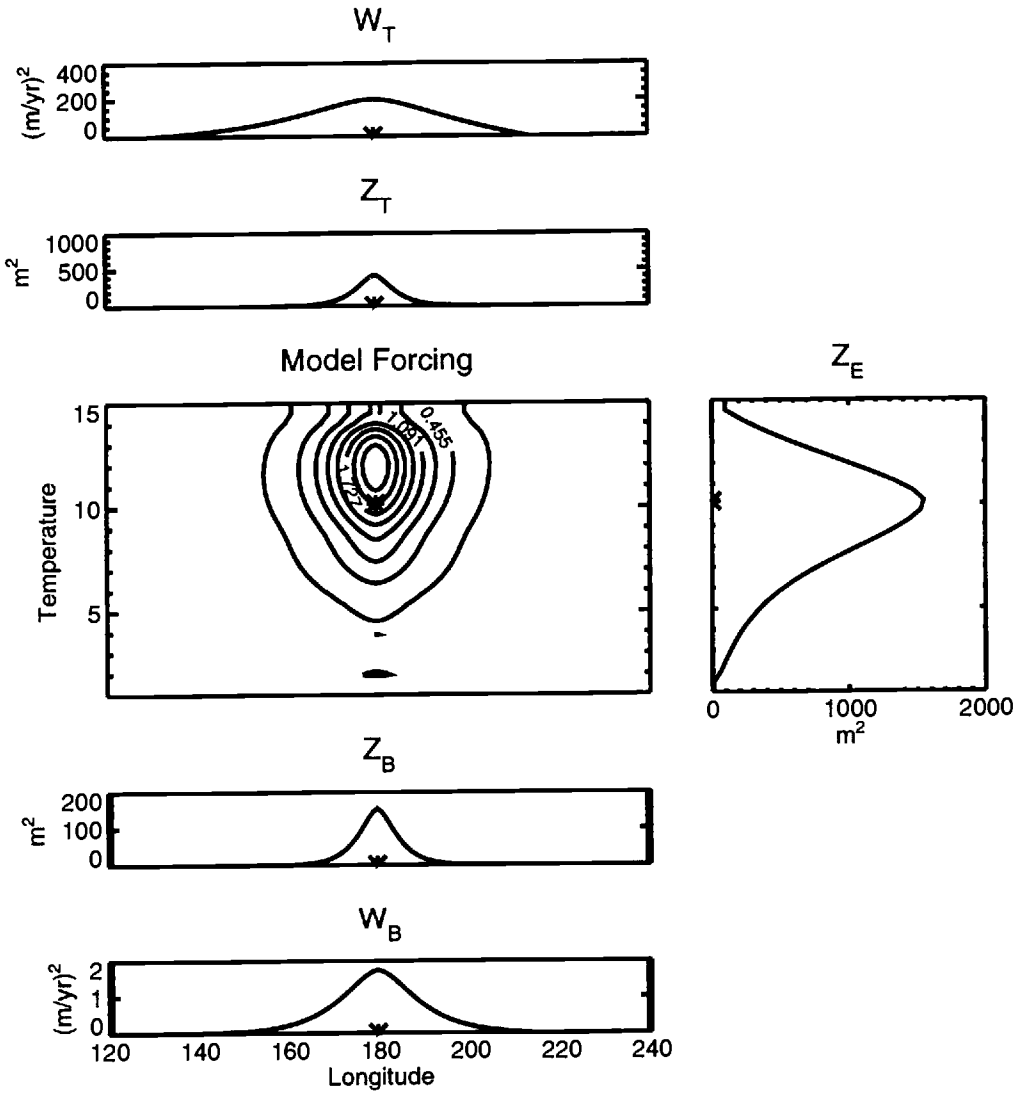

FIGURE 2.19. Final forcing covariance.

The posterior error covariance of the model forcing is shown.

lists the sampled isotherm depths. The total data set consisted of 1143 observations. Otherwise, the parameters for this inversion were identical to those used above (see Table 2.2).

TABLE 2.5. Prior Measurement Errors

Layer Temp., °C	Uncertainty, m
2.0	56
2.9	78
3.9	96
4.9	104
5.8	89
6.8	80
7.8	73
8.7	68
9.7	63
10.7	60
11.6	57
12.6	54
13.6	52

2.5.1. Array Analysis

The eigenvalue spectrum of the representer matrix is compared with the prior data error covariance in Figure 2.21. Once again, the observing array is redundant. Although the measurements contain a total of 1143 degrees of freedom, the model supports significant variance in only about 1/100 as many modes.

The prior data error variances for each layer are listed in Table 2.5; they span a greater range of values than in the previous section because of the differing spatial variance of each layer. Nonetheless, because of the steep slope of the representer matrix spectrum, it would be necessary to decrease the data error variances by more

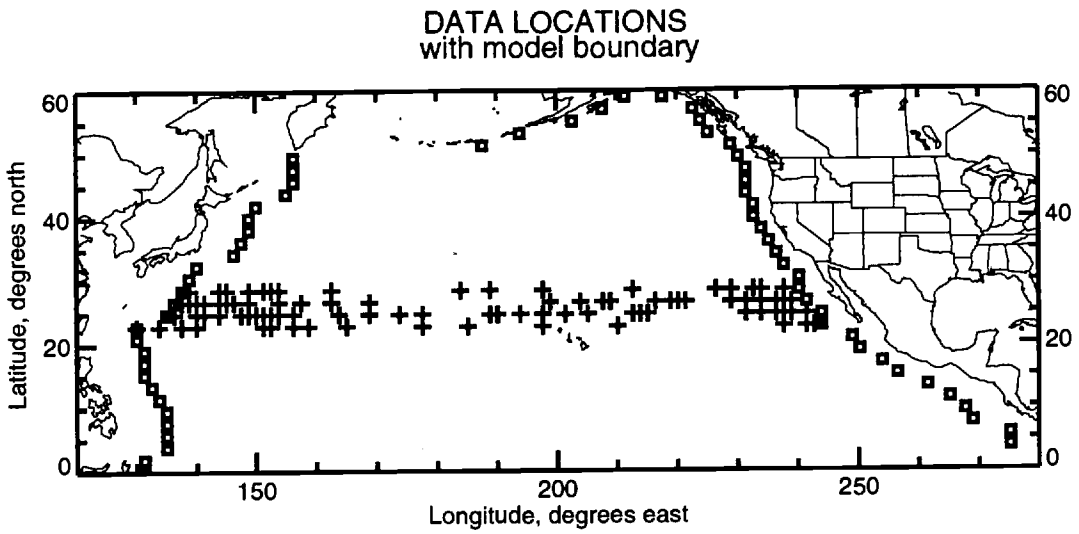

FIGURE 2.20. Data locations, "Zonal Section" experiment.

The sites of the "Zonal Section" station data are shown. At each location, as many as 13 isotherm depths are measured. There are a total of 1143 observations.

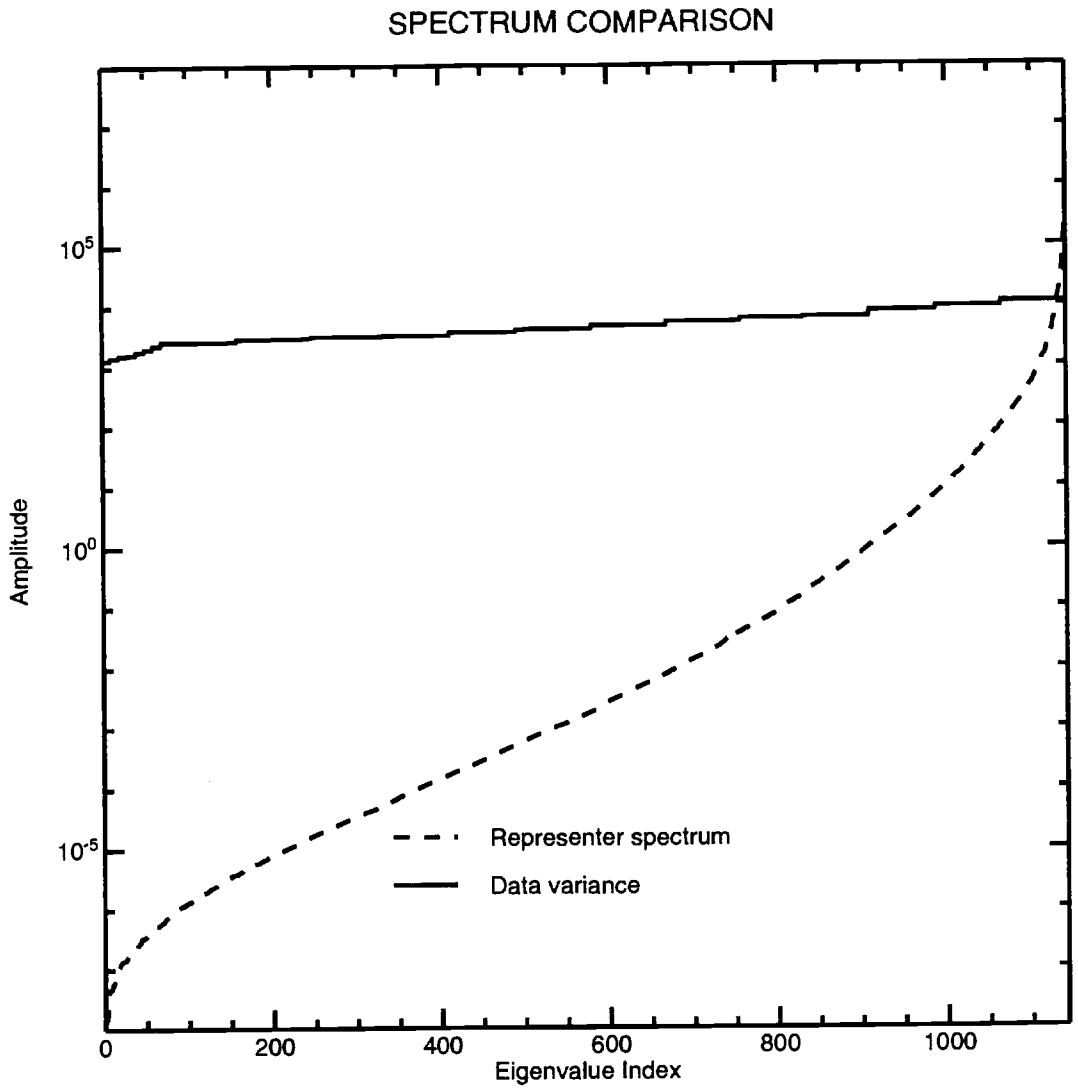

FIGURE 2.21. Representer spectrum, "Zonal Section".

The representer eigenvalue spectrum is shown with the dotted line. The solid line plots the diagonal entries of W^{-1}, the measurement error variance.

than an order of magnitude to cause a significant increase in the number of modes constrained by the data.

2.5.2. Inverse Solution

The four solution methods discussed in Section 2.3 are compared in Figure 2.22. Once again, REP-CG was the most efficient method, by roughly a factor of 8. The success of this method, without preconditioning, may have been a consequence of the particular eigenvalue spectrum for this problem, and it may not generalize to other inverse problems (see Luenberger, 1974, for a complete discussion of the convergence rate of the conjugate gradient method).

A section through the inverse solution is shown in Figure 2.23. A detailed analysis of the residuals showed insignificant differences from the "Thermocline Depth Measurement" array. The best-fit boundary condition residuals for the surface and eastern boundary were each roughly equal to the prior estimates in their uncertainties; the bottom boundary condition residuals were negligible. The root-mean-square interior model forcing residual was 7% of the root-mean-square mixing term, significantly smaller than its prior estimate of 20%.

The minimum value of the penalty function was 1300, which would be exceeded with $p = 0.0005$, or 0.05% probability if the prior error estimates are correct; although this p-value is small, the fit is still reasonably plausible since p is orders of magnitude larger than values typical for wrong null hypotheses. The minimum of the penalty was split between the data and dynamical residuals in the ratio 12:1. The model penalty was a sum of roughly equal contributions from errors in the interior model forcing, eastern boundary condition, and surface boundary conditions.

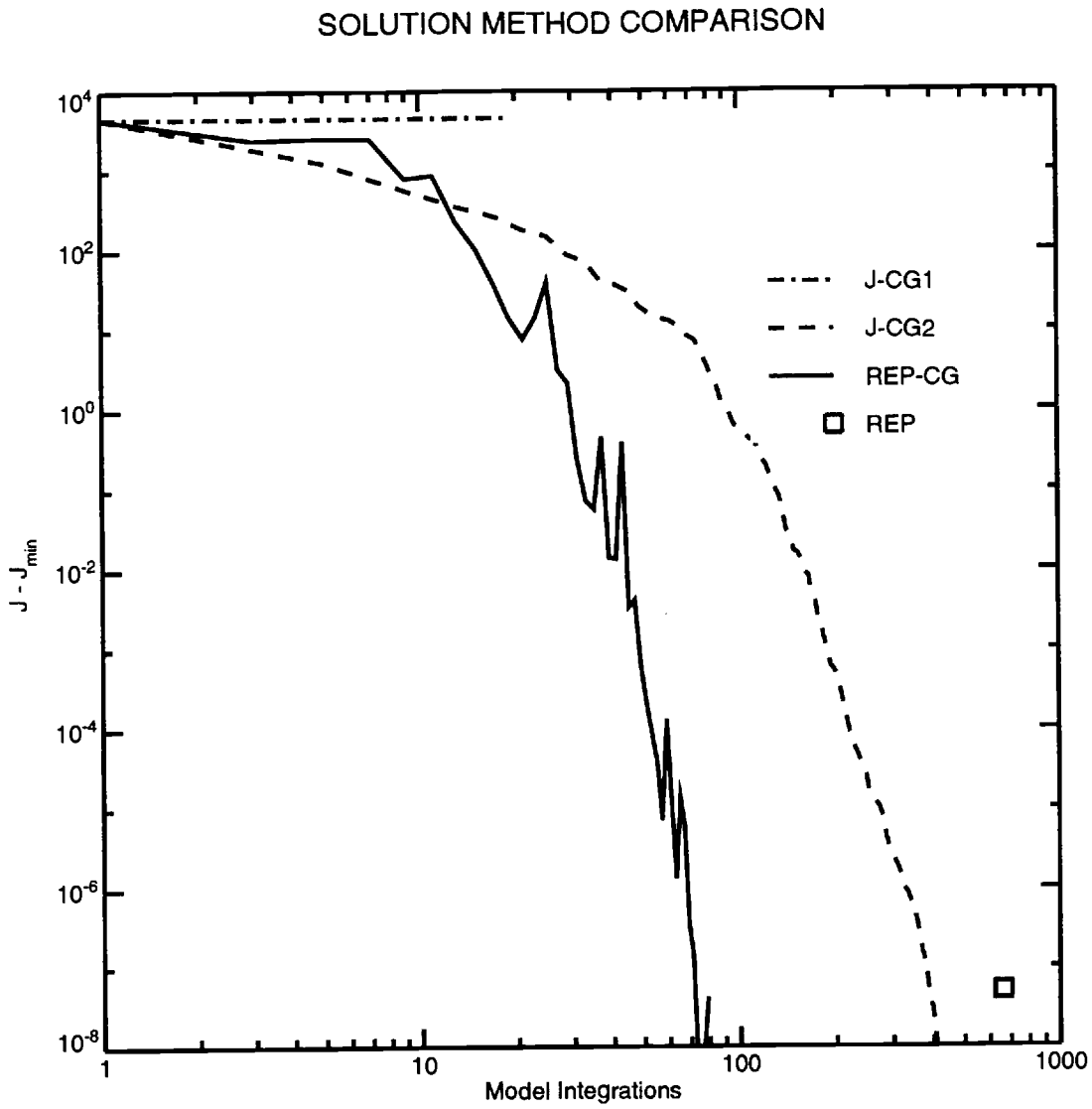

FIGURE 2.22. Solution method comparison, "Zonal Section".

As in Figure 2.13.

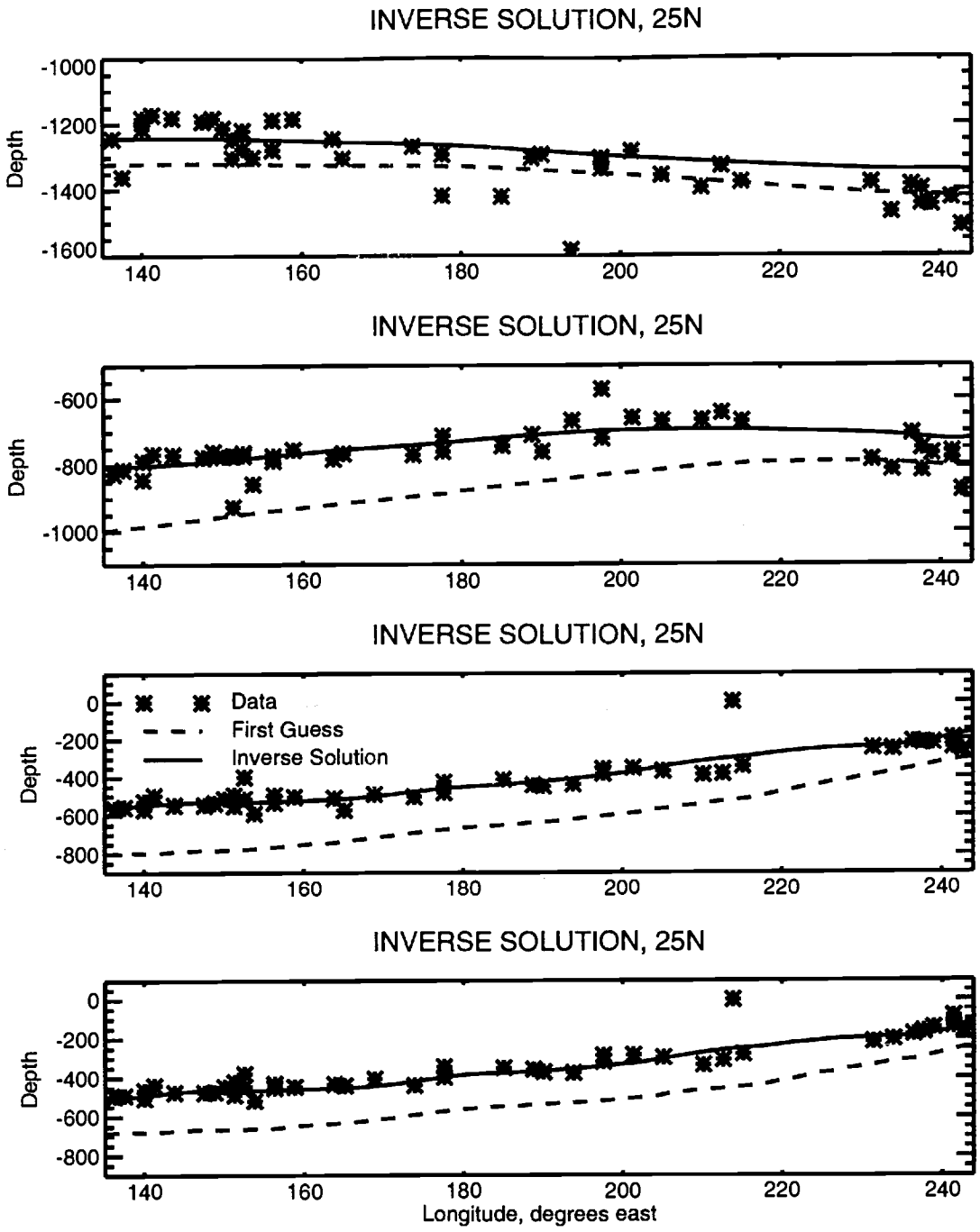

FIGURE 2.23. Inverse solution, "Zonal Section".

Sections of the inverse solution (solid line), data (asterisks), and first-guess solution (dashed line) are shown on four different isotherms.

Analysis of the a posteriori errors yielded results similar to those in the previous section. Hydrographic measurements are effective at explaining variance in the measured variable, but they are ineffective at reducing the model forcing and boundary condition uncertainties.

2.6. North Pacific Inverse

The entire North Pacific data set of Reid and Mantyla (1988) was assimilated in this experiment. The cast locations were the same as those plotted in Figure 2.3, and data were taken for the 13 isotherms listed in Table 2.5. The data set was comprised of 17,631 individual observations.

Because of the large number of observations, the most efficient solution method of those compared above was used, namely, REP-CG. Figure 2.24 shows the value of the penalty function over the course of the minimization. The solution method converged in 145 steps, a savings of more than two orders of magnitude over the direct representer solver, REP.

Figure 2.25 compares the inverse solution to the observations of the 9.7°C isotherm depth at several latitudes. As expected from the eigenvalue analyses above, the inverse solution heavily smoothed the observations. Nonetheless, the root-mean-square misfit between the observations and the best-fit solution is 94% of the prior data variance for this isotherm; thus, the inverse solution just fits the data. Assuming that $\mathcal{J}(u_{\min})$ is a χ^2_M variable once again indicated that the null hypothesis is plausible: the value of $\mathcal{J}(u_{\min})$ is at the $p = 52\%$ point of the cumulative χ^2_M distribution.

A further analysis of the penalty function and residuals yields insight into the plausibility of the model. The prior estimates for the errors and the root-

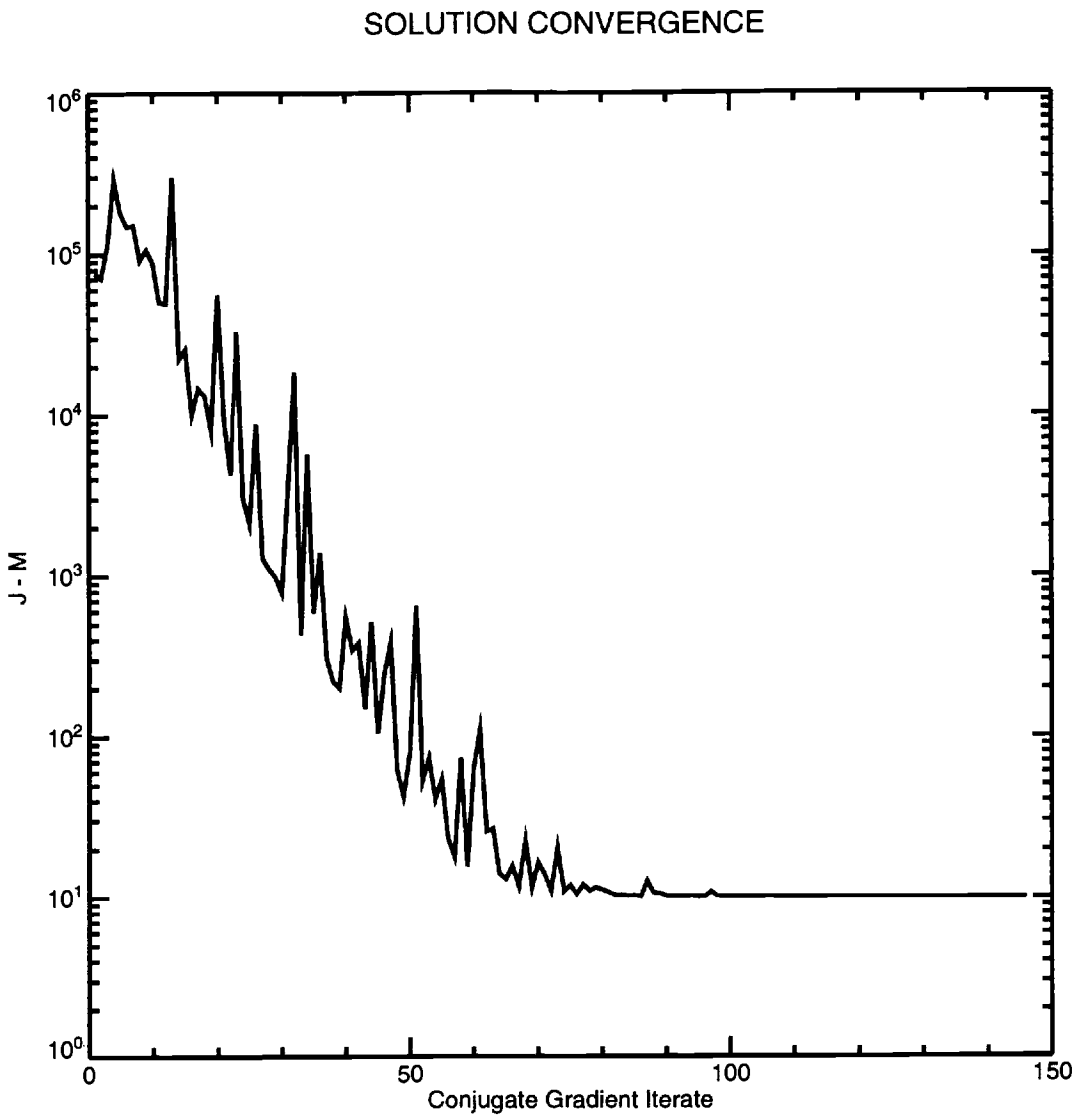

FIGURE 2.24. REP-CG minimization, "North Pacific Inverse".

The value of the penalty function during the progress of the solution procedure is shown. To accentuate the small changes in $\mathcal{J}$, which would otherwise not be visible, the value of M has been subtracted from the penalty function. Note that the reduction in $\mathcal{J}$ is not monotonic, as it would be with a direct minimization method.

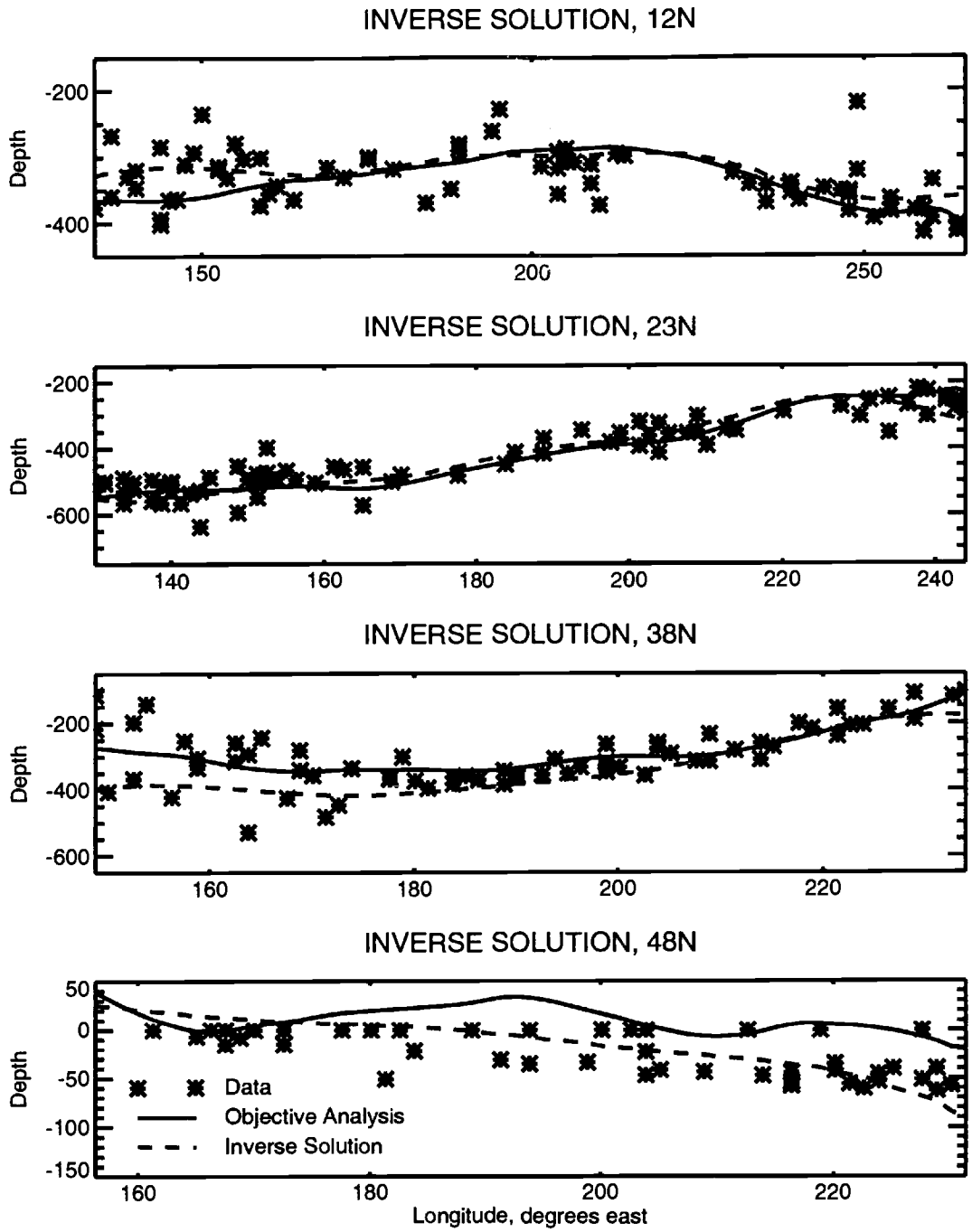

FIGURE 2.25. Inverse solution, "North Pacific Inverse".

As in Figures 2.14 and 2.23, the panels compare the inverse solution (solid line) with the observations (astericks); however, instead of showing the first guess solution, the objective-analysis is plotted as the dashed line. In each case, the 9.7°C isotherm depth is plotted.

mean-square errors in the inverse solution are compared in Table 2.6. Except for the bottom boundary conditions, the boundary condition misfits ranged from 170% to 260% of their prior estimates. Nonetheless, the contributions that these terms made to the penalty function were less than 50% of what one would expect if the mean-square misfit were equal to its prior estimate.

TABLE 2.6. Residuals, "North Pacific Inverse"

Field	Prior	Final	$\mathcal{J}$
z_{EB}, m	40.	69.	2.4×10^{2}
w_T, m/yr	15.	39.	4.1×10^{2}
z_T, m	21.	35.	5.5×10^{2}
w_B, m/yr	1.3	2.2×10^{-2}	5.6×10^{-3}
z_B, m	12.	3.5×10^{-2}	4.9×10^{-4}
data, m	150. (typical)	60. (typical)	1.6×10^{4}

This apparent contradiction may be resolved by understanding that the prior model error covariances define a hypothesis regarding the spatial structure of the model errors. The weighting functions appearing in the penalty function are the inverses of the prior covariances. Because the covariances must be sufficiently smooth to insure that the inverse solution is physically realizable (e.g., Bennett and Budgell, 1987), their inverses, the weighting functions, can be interpreted as "roughening" operators (see Appendix 4.3). The effect of these terms is to penalize the high-wavenumber, small-scale, component of the residuals. As listed in Table 2.6, the total variance of the boundary condition residuals was too large (by a factor of 1.7 to 2.6, depending on the boundary condition); however, the small contributions of these terms to the penalty function indicated that the residual variance was contained at large scales. In other words, it would appear that the prior estimates for the horizontal correlation scales were too small. Obviously, this discussion applies

to the upper and eastern boundary conditions; the bottom boundary conditions are inconsequential.

The interior term balance of the model is compared for the first-guess, objective-analysis, and inverse solutions in Table 2.7. The domain averaged root-mean-square values of the terms in the "thermocline equation" are compared. The "thermocline equation" is simply the planetary geostrophic system written in terms of z alone:

$$-\frac{\beta \overline{z}_\theta}{\mathrm{f}^2}\overline{b}_\theta \frac{1}{r_o \cos\phi}\frac{\partial z}{\partial \lambda} - \left(\frac{K_V}{\overline{z}_\theta^2} z_\theta\right)_{\theta\theta\theta} = \epsilon.$$

$$I \qquad II \qquad III \tag{2.72}$$

The terms in the thermocline equation may be interpreted as (I) advection of planetary vorticity, (II) vertical mixing of potential vorticity, and (III) the dynamical residual. The values listed in the table are in units of m/(yr $^\circ$C^2), which are, unfortunately not the most familiar. Nonetheless, the values indicate the relative significant of each term in the over-all balance. On average, the dynamical residual of the inverse solution is roughly 25% of the vertical mixing term, roughly equal to its prior estimate. In contrast, the objective-analysis field is completely out of balance with the dynamics.

TABLE 2.7. Term Balances, "North Pacific Inverse"

Field	I (advection)	II (mixing)	III (residual)
First-Guess	0.12	0.12	0.
Objective-Analysis	0.89	2.9	3.0
Inverse Solution	0.113	0.117	0.028

The objective-analysis and inverse solutions are compared in Figures 2.26 and 2.27. The fields are visually quite similar (as seen in Figure 2.26); however,

the inverse solution is a significantly better fit to the model equations (Figure 2.27). The visual similarity of the fields is somewhat deceptive, presumably one's eye can pick out only the dominant length scale; however, the penalty function "sees" the curvature and higher-order derivatives which determine the fit of the fields to the model.

A further test of the accuracy of the ocean model can be made by estimating the nonlinear divergence terms which were neglected when linearizing the continuity equation. Recall that the unapproximated continuity equation contains the term

$$\nabla \cdot [\mathbf{u}(\overline{z}_\theta + z_\theta)] = \overline{z}_\theta \nabla \cdot \mathbf{u} + z_\theta \nabla \cdot \mathbf{u} + \mathbf{u} \cdot \nabla z_\theta, \tag{2.73}$$

$$\qquad\qquad\qquad\qquad \text{I} \qquad \text{II} \qquad \text{III} \tag{2.74}$$

from which only the linear term (I) was retained (note that $\mathbf{u}$ is the total velocity because $\overline{\mathbf{u}} = 0$). Terms (II) and (III) were diagnosed from the inverse solution to assess the validity of the linear model. On average, the nonlinear divergence (II) is somewhat smaller than the linear divergence (I). In contrast, term (III) is larger than term (I) over most of the domain. Thus, the inadequacy of this linear model is revealed: the nonlinear convective term is no smaller than the linear divergence term. Figure 2.28 illustrates the term balance at a point in the middle of the domain.

2.7. Discussion

The experiments in this chapter demonstrated the efficacy of a particular solution method for the generalized inverse of this ocean model. An iterative solver based on the representer decomposition, REP-CG, proved to be the most efficient method. Similar, but not as impressive, results were obtained with a descent solver, which preconditioned with the inverse of the dynamical operators. In contrast to the

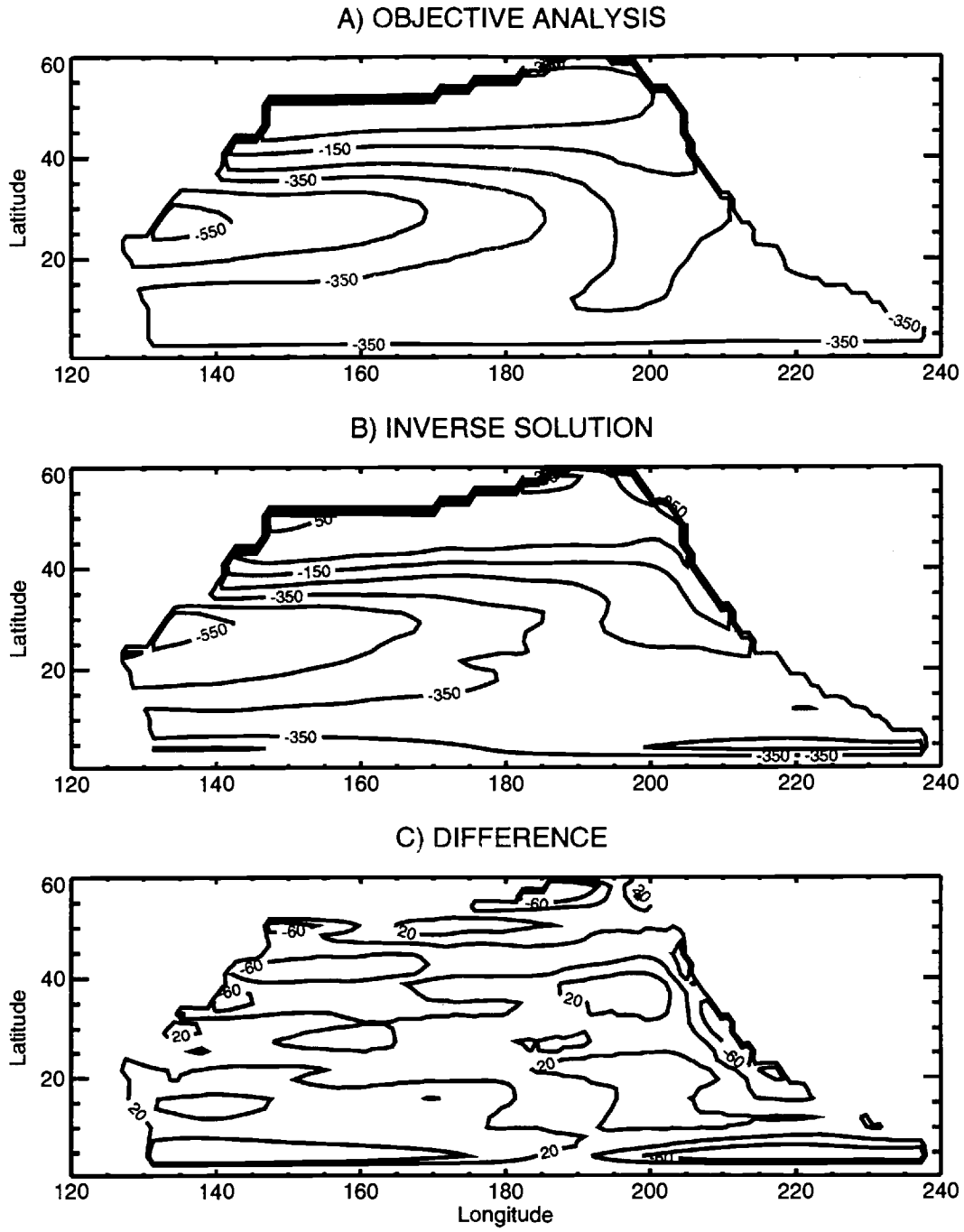

FIGURE 2.26. Solution comparison, "North Pacific Inverse".

A) The objective-analysis, B) inverse solution, and C) the difference of the two fields are shown (for the depth of the 9.7°C isotherm). Although the fields are visually similar, the dynamical residuals (shown in Figure 2.27) indicate that the inverse solution is much more dynamically consistent than the objective analysis.

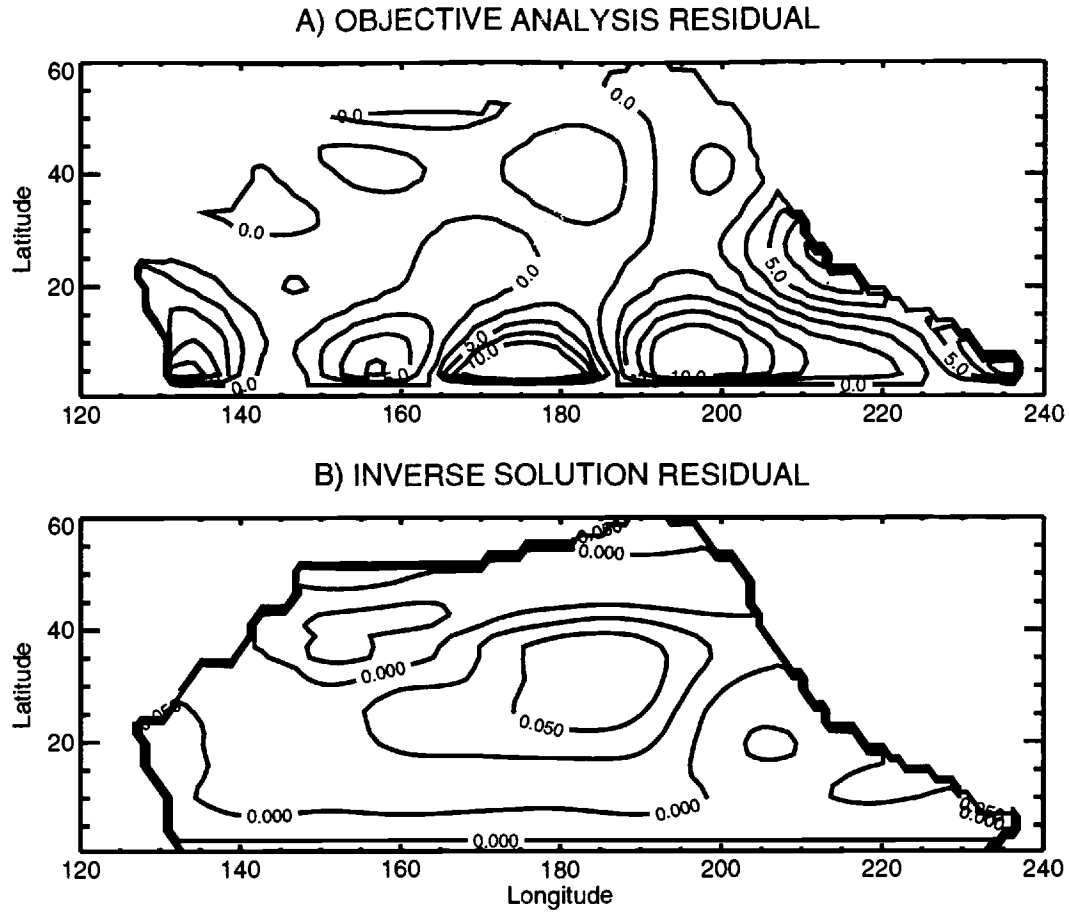

FIGURE 2.27. Residual comparison, "North Pacific Inverse".

The residual in the continuity equation is shown for A) the objective-analysis, and B) the inverse solution at the depth of the 9.7°C isotherm. The residual (units of m(yr °C)$^{-1}$) is orders of magnitude smaller in the inverse solution than in the objective-analysis.

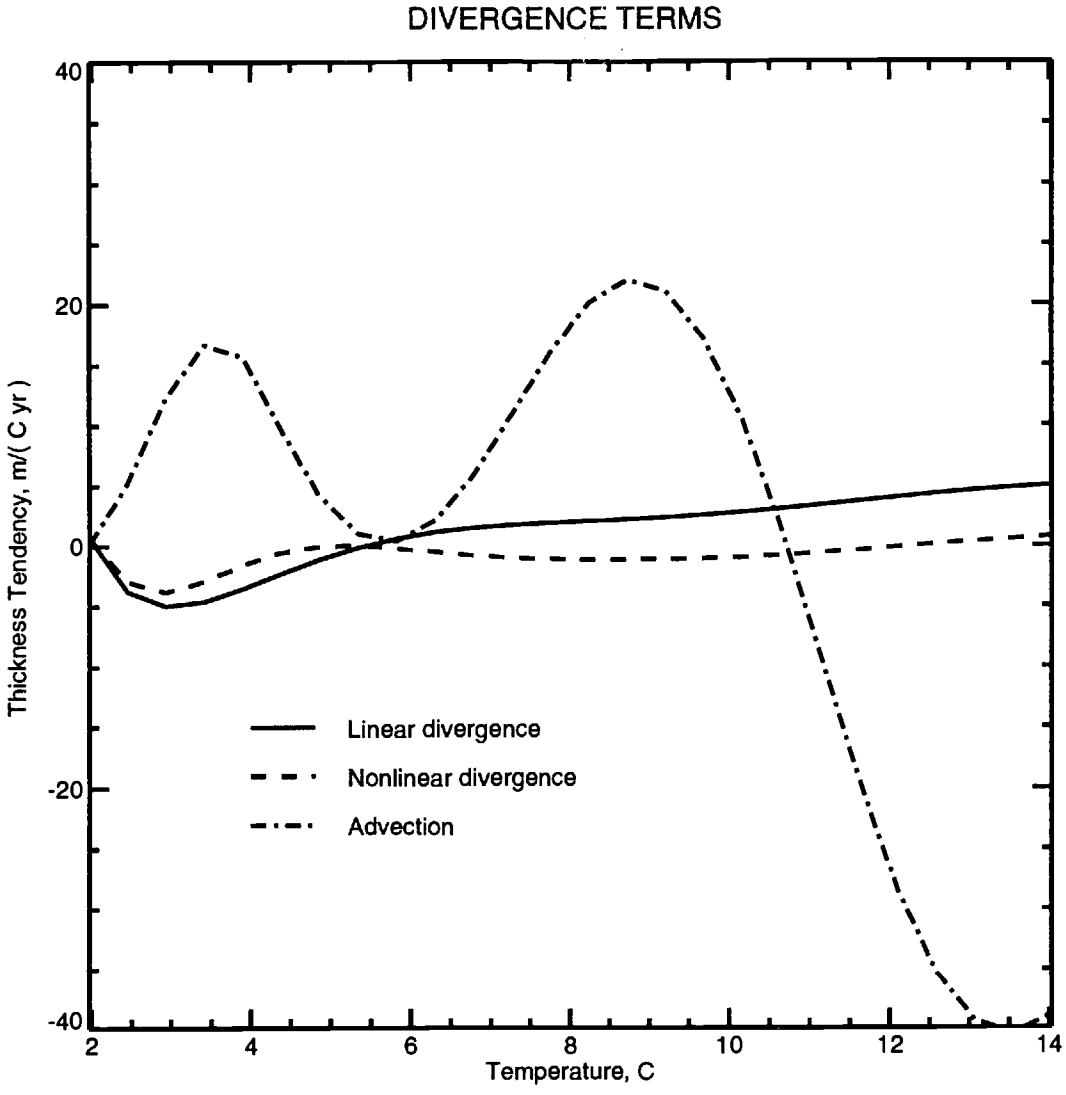

FIGURE 2.28. Nonlinear terms.

Three terms from the continuity equation are shown: (I) the linear divergence term retained in the model (solid line), (II) the nonlinear advection term (dashed-dot line), and (III) the nonlinear divergence term (dashed line).

direct method REP, one does not obtain a posteriori error information with either of the successful iterative solvers, REP-CG or J-CG2.

Although the prior error covariances are questionable, it is doubtful that any revision would significantly alter the present results. It is evident from Figures 2.8 and 2.21 that at least an order of magnitude increase in the prior model covariance, or an order of magnitude decrease in prior data covariance would be necessary to cause a significant increase in the number of modes constrained by the data. The generalized inverse is stable in the sense that an error in an individual datum does not strongly effect the final solution.

A large inverse calculation, which included approximately 18,000 observations, indicated that the linear planetary geostrophic system is an adequate explanation for the general circulation. The inverse solution was as close a fit to the data as was warranted by the prior data error. Inspection of the model residuals indicated that the prior correlation scales for the model forcing and boundary condition errors were too small. Given the stability of the inverse, i.e., the redundancy of the data relative to this model, cross-validation methods may prove useful for improving the prior error covariance parameterizations (Craven and Wahba, 1979).

In spite of the ability to fit the data, the linear dynamics of the present model are a serious liability. A diagnosis of the nonlinear terms from the final solution demonstrated that the assumption of linearity was not valid; however, this is no surprise, as an elementary comparison of the long-Rossby wave speeds to the advecting velocity scale suggested that the nonlinear convection terms could not be neglected. The linear model provided an opportunity to understand how the underlying physics, in which the westward propagation of Rossby waves is arrested by diabatic mixing, effects the inverse problem. Indeed, a consideration of the representers in Sections 2.4 and 2.5 suggests that careful modeling of the surface

mixed layer and the eastern boundary current will be necessary before hydrographic measurements can be effective at determining surface fluxes at any but the largest scales. Because the prior state variance is caused approximately equally by noise in the surface and eastern boundary conditions, it is imperative that the submodels for these regions be very accurate.

In spite of obvious limitations, the present calculations have demonstrated the feasibility of assimilating large data sets into ocean general circulation models using nondiagonal prior error covariances. Insofar as the posterior error covariances calculated from a linear model are applicable in a nonlinear setting, it is clear that hydrographic observations are ineffective at constraining the surface boundary conditions of a general circulation model.

3. DATA ASSIMILATION WITH A NONLINEAR PLANETARY GEOSTROPHIC MODEL

3.1. Introduction

The calculations of the previous chapter indicated that the linearized planetary geostrophic system is not an adequate model for the general circulation. Although the model was capable of fitting the observations, the validity of the linearization was not supported by the final results. This chapter describes an attempt to overcome the limitations of the linear system by using a nonlinear model based on the complete planetary geostrophic system.

In addition to the nonlinearity in the layer-thickness equation, which was neglected in Chapter 2, it is also necessary to include a number of other effects in order to model the general circulation. First, inspection of the temperature-salinity (θS) relation reveals that salinity is important in the dynamics of the sub-arctic region (Emery and Dewar, 1982). A proper consideration of salinity also demands an accounting of the air-sea fresh water flux, so a parameterization of the oceanic mixed-layer is necessary. The considerations in McDougall and Jackett (1988), regarding the dependence of the thermal expansion coefficient on pressure, suggest that the complete, nonlinear, equation of state should be used when calculating the buoyancy. Irregular bottom topography and open boundary conditions on the lateral boundaries also ought to be incorporated. Lastly, in order for the model to support a western boundary current, some parameterization of the Reynolds stress should be included. All of these processes were included in the model described below.

Having specified the model, the next task was to formulate the inverse problem. As in Chapter 2, a quadratic control (least-squares) formulation was used. The most general formulation would have involved admitting errors in each of the dynamical equations and boundary conditions defining the model. Instead, an incremental approach was taken in which errors were admitted in the steady heat and salt conservation equations, and in the boundary conditions. This will be discussed in more detail below; however, the intent was to make a tractable inverse problem which would be an extension of the work by Tziperman et al. (1992b and 1992c).

The data for the inverse calculation included both boundary (air-sea flux) and interior (hydrographic) observations. The surface flux observations were taken from gridded climatologies (Hellerman and Rosenstein, 1983; Oberhuber, 1988), and the hydrographic data were based on Reid and Mantyla (1988). It was assumed that each type of measurement contained error.

Next, it was necessary to specify a solution method for the inverse problem. As was emphasized in Chapter 2, the representer expansion is an ideal method for solving inverse problems when there exists an efficient means of inverting the model system. Also, the representer expansion is applicable only to linear systems; extensions of the representer expansion for nonlinear systems are discussed in Bennett and Thorburn (1992) and Hagelberg (1992). The application of these extensions of the representer expansion to the present nonlinear model would have required a solver for the linearized planetary geostrophic system. Attempts to solve the steady planetary geostrophic system using the accelerated time-stepping procedure described in Bryan and Lewis (1979) were too computationally demanding; therefore, solution methods based on the representer expansion were not attempted. Because of the applicability of direct minimization methods, as defined in Chapter 2, to both linear

and nonlinear systems, it was decided to use a descent method to solve the inverse problem.

The last important consideration was a method for estimating the posterior errors of the inverse solution. Because of the nonlinearity in the model, substituting methods appeared ideal for computing the posterior errors. However, because preliminary attempts to compute the posterior errors using importance sampling (methods based on Metropolis et al., 1953 and Duane et al., 1987) were unsuccessful, no posterior error estimates are reported below. The importance sampling methods failed to give accurate results because of the large serial correlations from one Monte Carlo trial to the next (see Ferrenberg et al. 1991 for a more complete discussion of the sources of error in Monte Carlo calculations).

To summarize, an attempt was made to assimilate hydrographic data into a nonlinear planetary geostrophic model. The goal of the assimilation was to obtain an estimate of the time-averaged circulation of the North Pacific, along with an estimate of the air-sea fluxes necessary to drive the circulation. The ocean model and inverse formulation are presented in Sections 3.2 and 3.3, and Section 3.4 reviews the sources of data and error estimates which were used in the inverse calculations. Section 3.5 summarizes a number of preliminary calculations which assessed the efficacy of the descent and preconditioning methods, and which demonstrated the importance of the system's nonlinearity. Lastly, Section 3.6 concludes the nonlinear calculations with an attempt to estimate the circulation, hydrography, and air-sea fluxes of the North Pacific.

3.2. The Model

The planetary geostrophic equations, which are the basis for the present inverse calculation, are distinguished from the more familiar primitive equations by the neglect of the acceleration terms in the horizontal momentum equations (e.g. Pedlosky, 1979). As a consequence, the momentum equations form a set of diagnostic relations for the velocity field.

As in Chapter 2, spherical-polar coordinates are used, with latitude λ, longitude ϕ, and potential temperature θ, the local vertical coordinate. The total velocity vector is defined as (u, v, ω), and the along-isotherm (adiabatic) velocity vector is denoted $\mathbf{u} = (u, v)$. The thermodynamic state variables are potential temperature θ, salinity $S(\lambda, \phi, \theta)$, and (approximate) pressure $p = -\rho_o g z(\lambda, \phi, \theta)$. Buoyancy, $\rho g/\rho_o$, is denoted by b, and it is determined from the International Equation of State for Seawater (UNESCO, 1983). B is a Bernoulli function which is related to pressure, buoyancy, and z by $B = p/\rho_o + bz$, and f is the Coriolis parameter. The operators ∇ and $\nabla\cdot$ are, respectively, the horizontal gradient and divergence operators in spherical polar coordinates.

Before stating the equations, it is necessary to explain a number of assumptions. First, the Boussinesq approximation is made; thus the continuity equation states that volume (not mass) is conserved. Second, when using potential temperature as a vertical coordinate, the pressure gradient term is split into two terms. The new term is proportional to the buoyancy gradient along the isothermal surfaces. To minimize the spurious effects caused by truncation error acting through this term, a reference buoyancy profile (which depends on z alone) is subtracted from the full buoyancy (Phillips, 1957). Third, the rigid-lid approximation is made; thus, the barotropic and baroclinic velocity fields are decoupled. Lastly, it is as-

sumed that the equations are derived via thickness-weighted Reynolds averages (Van Mieghem, 1952); therefore, no Reynolds fluxes appear in the continuity equation. The Reynolds flux parameterizations which do appear in the momentum, salt, and energy equations are discussed below, after the equations are presented.

The steady planetary geostrophic system is as follows:

(the horizontal momentum equations)

$$\mathrm{f}\hat{k} \times \mathbf{u} = -\nabla B + z\nabla b + (F^{\tau})_{\theta}/z_{\theta} + \frac{A_H}{z_{\theta}}\nabla \cdot z_{\theta}\nabla \mathbf{u}, \tag{3.1}$$

(hydrostatic balance)

$$B_{\theta} = b_{\theta} z, \tag{3.2}$$

(the continuity equation)

$$\nabla \cdot (\mathbf{u} z_{\theta}) + (\omega z_{\theta})_{\theta} = 0, \tag{3.3}$$

(the salt conservation equation)

$$\nabla \cdot (\mathbf{u} z_{\theta} S) + (\omega z_{\theta} S)_{\theta} = \nabla \cdot (z_{\theta} K_H \nabla S) + \left(\frac{K_V}{z_{\theta}} S_{\theta} + F^S \right)_{\theta}, \tag{3.4}$$

and (the heat equation)

$$\omega z_{\theta} = \left(\frac{K_V}{z_{\theta}} + F^Q \right)_{\theta}. \tag{3.5}$$

Let D denote the lateral extent of the oceanic domain, and ∂D the boundary of D. With θ_T and θ_B as the top and bottom temperatures, respectively, the entire domain is $D \times [\theta_B, \theta_T]$. Boundary conditions are no-slip and no-normal-flow on ∂D, i.e., $\mathbf{u} = 0$ on lateral boundaries. At the bottom and top surfaces, the no-normal-flow condition is applied:

$$\mathbf{u} \cdot \nabla \theta = \omega, \tag{3.6}$$

on $\theta = \theta_T$ and $\theta = \theta_B$.

Modeling the oceanic mixed-layer is not trivial. Some provisions must be made for the *ventilation* of layers at the ocean surface, where *ventilation* refers to the modification of a layer's properties via air-sea fluxes of heat, fresh water, and momentum. This is a problem with a long history, and it is not easily resolved.

The approach taken here is straightforward. The vertical Reynolds fluxes near the ocean surface are parameterized with a simple functional form as a function of depth. The functional form (a decaying exponential) is monotonic and scaled so that its value at the surface is equal to the imposed air-sea flux. The vertical component of the horizontal Reynolds flux is

$$F^{\tau} = \frac{\tau_{\text{wind}}}{\rho_o} \exp(\mu z), \tag{3.7}$$

where τ_{wind} is the wind stress vector. The vertical salt flux is

$$F^{S} = -\frac{F}{S_o} \exp(\mu z), \tag{3.8}$$

where F is the net fresh water flux (precipitation minus evaporation). The vertical heat flux is

$$F^{Q} = \frac{Q}{\rho_o \mathrm{C_p}} \exp(\mu z), \tag{3.9}$$

where Q is the air-sea heat flux, positive into the ocean. Values of the constants are, $\mu^{-1} = 50\text{m}$, $\rho_o = 1025\text{kg m}^{-3}$, $S_o = 35\text{psu}$, and $\mathrm{C_p} = 4200\text{J (°C kg)}^{-1}$. The wind stress, fresh water flux, and heat flux are prescribed functions of latitude and longitude.

The are other approaches to treating the surface boundary conditions in layer models. In the original work of Bleck (1973), layers intersected the model boundary, and ω was specifed directly. In order to avoid difficulties with approximating the momentum equation at outcropping boundaries, subsequent models

(e.g., Bleck, 1974) did not permit the layers to intersect the boundary, they did, however, allow the layers to become infinitesimally thin. Oceanographic versions of these models incorporate the surface fluxes in a manner similar to that which is used here (Bleck et al., 1989). The most recent approach involves using a hybrid vertical coordinate, which avoids the problem of outcropping altogether (Gerdes, 1993a). Each approach has its advantages, and there does not appear to be a consensus on which is the best approach. The method used here was chosen because it is computationally simple, and the because the vertical fluxes are continuous and differentiable functions of the model's state variables. The latter point is crucial to the implementation of a gradient descent method in the solution procedure.

In the oceanic interior, away from the surface, Reynolds fluxes are modeled with Fickian diffusion. The effect of unresolved time-dependent motions is represented by these terms. Away from the surface, the turbulent vertical flux of momentum is neglected. It is assumed that the diffusivity tensors are diagonal in the present coordinates: K_H and A_H are the lateral (adiabatic) diffusivities of salt and momentum; K_V is the vertical diffusivity of both heat and salt. Heating caused by the mixing of salt is neglected (Gregg, 1984). As discussed in DeSzoeke and Bennett (1993), K_V is equal to a turbulent Cox number times the molecular diffusivity. Here, K_V is taken as $0.1\text{cm}^2/\text{s}$ (Ledwell et al., 1993). The value used for the horizontal mixing coefficients is $2 \times 10^4 \text{m}^2/\text{s}$, just sufficient for the barotropic western boundary current to be resolved in the numerical model (Munk, 1950); this value is comparable to that estimated from large-scale oceanographic measurements (Sverdrup et al., 1942; Needler and Heath, 1975), but an order of magnitude larger than that estimated from the dispersal of neutrally buoyant floats (Freeland et al., 1975).

Note that the value of the vertical diffusivity is one-tenth that used in the previous, linear model. In the linearization used in Chapter 2, the three pieces

of information defining the mean state cannot be specified independently: L_{TC}, the thermocline depth scale; $\overline{w}$, the mean upwelling rate; and K_V, the vertical diffusivity. The canonical value of $10^{-4}\mathrm{m}^2/\mathrm{s}$ (Munk, 1966) was used in Chapter 2 because it is consistent with both the (observed) thermocline length scale, and with the estimates of the global deepwater production rate. The smaller value of the vertical diffusivity, which is used in this chapter, was chosen in an attempt to improve the quantitative validity of the ocean model.

The inverse problem in the next section is posed in terms of the baroclinic and barotropic components of the flow. The split into barotropic and baroclinic components is motivated by the observation that the barotropic flow field is very sensitive to vortex stretching caused by cross-isobath flow, the so-called "JEBAR" effect (an acronym for *J*oint *E*ffect of *B*aroclinicity *A*nd *R*elief; Sarkisyan, 1977). For our purposes, the baroclinic-barotropic split decouples the nonlocally forced barotropic velocity field from the locally forced baroclinic velocity field. That is, given the buoyancy, wind stress, and bottom topography, the barotropic velocity field is governed by a singularly perturbed hyperbolic equation (the singular perturbation is the elliptic frictional term); the time-like characteristics of this equation follow the isopleths of f/H. In contrast, the baroclinic velocity is governed by a local relationship between buoyancy and the velocity field, namely, thermal wind. The singular perturbation provided by the elliptic frictional term is neglected in the baroclinic momentum equations because the model resolution is insufficient to resolve the baroclinic boundary layer thickness, which is of order $(A_H/f)^{1/2}$. The barotropic-baroclinic split is often used in rigid-lid primitive-equation models (Cox, 1984; Semtner, 1986) in order to decouple the faster barotropic waves from the slower baroclinic waves.

Let Ψ denote the streamfunction for the vertically averaged (barotropic) flow. By taking the curl of the vertically averaged momentum equations, it can be shown that Ψ satisfies the following equation:

$$J(\Psi, \frac{\mathrm{f}}{H}) = J\left(\int_{\theta_B}^{\theta_T} bzz_\theta d\theta, \frac{1}{H}\right) + \mathrm{curl}\left(\frac{\tau_{\mathrm{wind}}}{\rho_o H}\right) + A_H \nabla \cdot \frac{1}{H}\nabla^2 \nabla\Psi, \qquad (3.10)$$

where small frictional terms proportional to $\nabla H/H$ have been neglected. The notation $J(a,b) = (a_\phi b_\lambda - a_\lambda b_\phi)/(r_o^2 \cos\phi)$ denotes the Jacobian of the two-dimensional fields a and b. The no-normal-flow and no-slip boundary conditions on $\mathbf{u}$ take the form of boundary conditions on Ψ and $\nabla\Psi \cdot \mathbf{n}$ ($\mathbf{n}$ is the outer-normal unit vector). The equation governing the baroclinic flow is simply the full momentum equation (3.1), minus its vertical average.

3.3. Cost Function, Adjoint Model, and Minimization Algorithm

As mentioned above, the inverse problem is solved using a minimization method, as opposed to using an Euler-Lagrange solver. This approach is taken because of its applicability to linear and nonlinear problems alike.

The cost function, which is specified below, quantifies the disagreement among a set of constraints provided by the ocean model, surface flux data, and hydrographic measurements. Descent methods, which are used to minimize the cost function, require the cost function gradient with respect to the state variables, and the gradient is computed efficiently using the adjoint of the tangent-linearization of the model (Talagrand and Courtier, 1987).

The over-riding goal of this study is to understand the relative roles of advection and diffusion in the maintenance of the thermocline. The observation by Iselin (1939) of the remarkable similarity between the θS relation of the winter sea-surface and the θS relation of the thermocline water suggests that the general

circulation is largely adiabatic. Similarly, the success of the Luyten, Pedlosky, and Stommel (1983) adiabatic model at describing the qualitative features of the thermocline is impressive. We have sought to quantify these notions, by asking: does there exist a set of hydrographic fields which are simultaneously consistent with both the advection-diffusion equations for heat and salt *and* the hydrographic observations? In addition, the surface forcing fields, which provide the boundary conditions for the advection-diffusion equations, are known to be highly uncertain. Hence, it was decided to focus on these points by admitting errors in the air-sea flux data, the energy equation, the steady continuity equation, and the steady salt conservation equation. Additionally, errors are admitted in the no-normal-flow condition at the bottom.

The general form of the cost function considered below is

$$\mathcal{J} = \mathcal{J}_{\text{dyn}} + \mathcal{J}_{\text{bc}} + \mathcal{J}_{\text{data}}, \tag{3.11}$$

where $\mathcal{J}_{\text{dyn}}$, $\mathcal{J}_{\text{bc}}$, and $\mathcal{J}_{\text{data}}$ are each functions of the state variables. $\mathcal{J}_{\text{dyn}}$ measures the misfit in the model equations, $\mathcal{J}_{\text{bc}}$ measures the misfit in the surface boundary conditions, and $\mathcal{J}_{\text{data}}$ measures the misfit of the observations. The state variables consist of the set $(z, \Psi, \omega, S, Q, F, \tau_{\text{wind}})$, defined on pages 77-79.

$\mathcal{J}_{\text{dyn}}$ is expressed in terms of residuals in the continuity, salt, heat, and streamfunction equations. The residuals $(\epsilon, \eta, \gamma, \chi)$ are defined as follows:

$$\nabla \cdot (\mathbf{u} z_\theta) + (\omega z_\theta)_\theta = \epsilon, \tag{3.12}$$

$$\nabla \cdot (\mathbf{u} z_\theta S) + (\omega z_\theta S)_\theta = \nabla \cdot (z_\theta K_H \nabla S) + \left(\frac{K_V}{z_\theta} S_\theta + F^S \right)_\theta + \eta, \tag{3.13}$$

$$\omega z_\theta = \left(\frac{K_V}{z_\theta} + F^Q \right)_\theta + \gamma, \tag{3.14}$$

and

$$J(\Psi, \frac{\mathrm{f}}{H}) = J\left(\int_{\theta_B}^{\theta_T} bzz_\theta d\theta, \frac{1}{H}\right) + \mathrm{curl}\left(\frac{\tau_{\mathrm{wind}}}{\rho_o H}\right) \tag{3.15}$$

$$+A_H \nabla \cdot \frac{1}{H} \nabla^2 \nabla \Psi + \chi. \tag{3.16}$$

Thus, $\mathcal{J}_{\mathrm{dyn}}$ is

$$\mathcal{J}_{\mathrm{dyn}} = \epsilon \circ_3 W^\epsilon \circ_3 \epsilon + \eta \circ_3 W^\eta \circ_3 \eta \tag{3.17}$$

$$+\gamma \circ_3 W^\gamma \circ_3 \gamma + \chi \circ_2 W^\chi \circ_2 \chi, \tag{3.18}$$

where W^ϵ, W^η, W^γ, and W^χ are symmetric positive definite weighting functions (it is tacitly assumed that the errors are uncorrelated between the equations). The subscripted $\circ$ symbols denote inner products (integrals) which are defined in Appendix 4.3.

The boundary condition residuals are summed as

$$\mathcal{J}_{\mathrm{bc}} = (Q - Q^{\mathrm{obs}}) \circ_2 W^Q \circ_2 (Q - Q^{\mathrm{obs}}) \tag{3.19}$$

$$+(F - F^{\mathrm{obs}}) \circ_2 W^F \circ_2 (F - F^{\mathrm{obs}}) \tag{3.20}$$

$$+(\tau_{\mathrm{wind}} - \tau_{\mathrm{wind}}^{\mathrm{obs}}) \circ_2 W^\tau \circ_2 (\tau_{\mathrm{wind}} - \tau_{\mathrm{wind}}^{\mathrm{obs}}). \tag{3.21}$$

Superscript *obs* refers to the observed value of the particular state variable and W^Q, W^F, and W^τ are the corresponding weighting functions.

The interior hydrographic data consist entirely of observations of isotherm depth and salinity, i.e.

$$\mathcal{J}_{\mathrm{data}} = \sum_{i=1}^{M} (z(\mathbf{x}_i) - z_i^{\mathrm{obs}})^2 w_i^z + \sum_{i=1}^{M} (S(\mathbf{x}_i) - S_i^{\mathrm{obs}})^2 w_i^S, \tag{3.22}$$

where $\mathbf{x}_i = (\lambda_i, \phi_i, \theta_i)$ is the location of the i^{th} measurement; w_i^z and w_i^S weight the observations. It is tacitly assumed that the observational errors are uncorrelated.

In the language of control theory, $(z, \Psi, \omega, S, Q, F, \tau_{\text{wind}})$ comprises the set of state variables. If we let $Q_{\text{res}} = Q - Q^{\text{obs}}$, $F_{\text{res}} = F - F^{\text{obs}}$, and $\tau_{\text{res}} = \tau_{\text{wind}} - \tau_{\text{wind}}^{\text{obs}}$, then $(\epsilon, \eta, \gamma, \chi, Q_{\text{res}}, F_{\text{res}}, \tau_{\text{res}})$ comprises the set of control variables.

The weighting functions determine the relative importance of the different constraints, and the degree of smoothness sought for the inverse solution. Formally, each is the inverse of a corresponding prior error covariance. The prior error covariances are discussed in Section 3.5, below.

The cost function was minimized using the BFGS (Broyden-Fletcher--Goldfarb-Shanno) method, as recommended by Navon and Legler (1987). This method performs a conjugate gradient search, preconditioned by a rank-2 approximation to the inverse Hessian (Gill et al., 1981). The preconditioning in the BFGS method is in addition to the preconditioning discussed below. The BFGS algorithm has some specific advantages when minimizing a non-quadratic function (i.e., when the model is nonlinear), and when finite-precision arithmetic is used; namely, the method defaults towards a steepest descent search. In accordance with the considerations in Shanno (1985), a restart condition was used to guarantee the convergence of the BFGS method (without periodically resetting the search direction to the direction of steepest descent, it is possible for the algorithm to converge to a non-extremal point when applied to a non-quadratic cost function). Numerical experiments confirmed the superiority of the BFGS versus the conjugate gradient algorithm for the cases considered below.

Preconditioners for the descent method were based on the discussion in Golub and VanLoan (1989) regarding preconditioning iterative solvers on massively parallel computers. In essence, the preconditioners are polynomials of local spatial averaging operators which were intended be approximate inverses of the differential operators appearing in the penalty function. Local averaging operators were used in order

to take advantage of the particular architecture of the CM-5 and CM-200 Connection Machines, on which it is desirable to minimize interprocessor communications, especially on the CM-200.

The numerical implementation of the model is presented in detail in Appendix 4.3. For a summary, Table 3.1 lists the basic facts concerning the numerical model.

TABLE 3.1. Numerical Model Parameters

Parameter	Value
D, model domain	North Pacific, 3° to 60°N 111°E to 70°W
$\Delta\lambda$, zonal resolution	1°
$\Delta\phi$, meridional resolution	1°
$\Delta\theta$, vertical resolution	0.5°C (below 4.5°C), 1.5°C (above 4.5°C)
nx, zonal grid–points	180
ny, meridional grid–points	60
n, vertical grid–points	20
θ_B, bottom temperature	1.5°C
θ_T, top temperature	22.5°C

3.4. Preliminary Calculations

There are two main problems which can confound large-dimensional minimization problems, such as is considered here. The difficulties are: 1) the nonconvexity of the cost function, caused by the model's nonlinearity, and 2) the poor conditioning of the Hessian of the cost function.

The first of these issues, the nonconvexity of the cost function, can cause the cost function to have local minima. Thus, assuming that the descent method is successful at reaching a minimum, the state at the minimum may depend on the

starting guess for the descent process. Even if the cost function does *not* contain local minima, to the extent that the cost function is not quadratic in the state variable, the conjugate gradient search directions will lose the optimality conditions which make the conjugate gradient procedure so advantageous as a minimization method.

The second issue, the poor conditioning of the Hessian, can cause the descent procedure to converge very slowly. The condition number of the Hessian is related to the ratio of the maximum and minimum curvatures of the cost function surface. In a poorly conditioned problem, the cost function surface has directions in which the cost function changes very gradually, and other directions in which the cost function changes very rapidly. It is suggestive to say that the cost function surface has very narrow "valleys" when the condition number is large; however, the "valleys" exist in a multi-dimensional space

It should be emphasized that once the dimension of the state space increases beyond three or four, it becomes increasingly difficult to visualize the global structure of the cost function surface. At best, one can only build up a local picture of the surface in some reduced-dimensional space.

A number of preliminary calculations were performed using various simplifications of the planetary geostrophic system. The calculations, which were performed at reduced model resolution ($3^\circ \times 3^\circ$ and 5 vertical layers), were intended to provide a test-bed for developing the appropriate preconditioners and for exploring the significance of the model's nonlinearity.

The experiments consisted of minimizing the penalty function with respect of one set of state variables at a time. For example, in one experiment z, ω, Ψ, S, Q, and F were held constant, while the cost function was minimized with respect to variations in τ.

It was found that the minimization algorithm was successful and efficient when the penalty function was a function of the surface fluxes (Q, F, τ) and the diabatic velocity ω. The minimization algorithm was much less efficient for the z, S, and Ψ fields. Numerous experiments were conducted to improve the minimization algorithm for these fields, two of which are discussed below.

3.4.1. Preconditioning: Ψ

In this experiment, all of the state variables except for Ψ were held constant, and the BFGS method was used to solve the equation for streamfunction for the barotropic flow. Note that, since the streamfunction equation is linear in Ψ, the penalty function is a quadratic function of the Ψ field; therefore, the BFGS method is equivalent to the conjugate gradient method (Nazareth, 1979). This experiment is reported in order to explain how the preconditioning operators were chosen. In the interest of brevity, no figures are presented for this preliminary calculation.

The penalty function is

$$\mathcal{J}(\Psi) = \chi \circ_2 W^{\chi} \circ_2 \chi + (\Psi - \Psi_{\mathrm{bc}}) \circ_{\partial D} W^{\Psi} \circ_{\partial D} (\Psi - \Psi_{\mathrm{bc}}), \tag{3.23}$$

where, as above, χ is the residual in the streamfunction equation:

$$J\left(\Psi, \frac{\mathrm{f}}{H}\right) - J\left(\int_{\theta_B}^{\theta_T} bzz_\theta d\theta, \frac{1}{H}\right) - \mathrm{curl}\left(\frac{\tau_{\mathrm{wind}}}{\rho_o H}\right) - A_H \nabla \cdot \frac{1}{H} \nabla^2 \nabla \Psi = \chi. \tag{3.24}$$

Recall, from Appendix 4.3, that $\circ_2$ and $\circ_{\partial D}$ denote inner products over the horizontal domain and its boundary, respectively. The inhomogeneities in the equation, which depend on τ_{wind}, z, b, H, and Ψ_{bc}, were all held constant (the normal derivative of Ψ was set to zero on the boundary). The task was then to solve a well-posed linear elliptic equation in two dimensions. Note that the equation is a singularly perturbed hyperbolic equation since the friction term is small compared with the

planetary vorticity advection term outside of the boundary currents. The weights were chosen to be "diagonal," i.e., the inner product of a weight with a field was just multiplication by a scalar:

$$W^{\chi} \circ_2 = \left(10 \text{ m/yr } \frac{\mathrm{f}}{H}\right)^{-2}, \tag{3.25}$$

and

$$W^{\Psi} \circ_{\partial D} = (0.5 \times 10^6 \mathrm{m}^3/\mathrm{s})^{-2}. \tag{3.26}$$

Preconditioning took place in two steps. In the first step, a diagonal operator was applied which rescaled and nondimensionalized the state variable. The second step involved applying a local averaging operator to invert, approximately, the dynamical operators. Let $L\Psi$ denote the finite-difference form of the linear operator on Ψ:

$$J(\Psi, \frac{\mathrm{f}}{H}) - A_H \nabla \cdot \frac{1}{H} \nabla^2 \nabla \Psi. \tag{3.27}$$

Preconditioning operators, denoted D and P, were sought such that the product PDL was approximately the identity.

The rescaling operator D was determined by computing the diagonal elements of the Hessian of $\mathcal{J}$ with respect to Ψ. Recall that the Hessian S is the matrix of second derivatives of $\mathcal{J}$ with respect to Ψ; for the finite-difference model, the diagonal elements of S were computed by successively perturbing elements of Ψ and computing $S \circ_2 \chi = \frac{1}{\epsilon}[\nabla_\Psi \mathcal{J}(\Psi + \epsilon\chi) - \nabla_\Psi \mathcal{J}(\Psi)]$ for unit vectors χ, and scalar ϵ (Marotzke, 1991). D was set equal to the reciprocal of the square-root of the diagonal of S. Analysis of the finite-difference expression for $L\Psi$ shows that

$$D_{i,j} \approx \left[\left(\frac{\beta_j}{H\Delta x} + \frac{4A_H}{H\Delta x^4}\right)^2 W^{\chi}\right]^{-1/2}, \tag{3.28}$$

where it is assumed that the zonal and meridional resolutions are equal, and small terms related to the curvature of the coordinate system have been neglected. For the weighting functions given above, a scale for Ψ of roughly 0.5Sv is obtained at 45°N.

Because of the spatial variation in β, as well as the presence of boundary conditions, the Hessian diagonal is inhomogeneous (spatially variable). However, in all of the cases studied, the minimization was more efficient if a homogeneous, or heavily smoothed preconditioner were used instead. Thus, in all of the calculations below, the rescaling preconditioner D was set equal to the inverse of the root-mean-square of the diagonal elements of S.

Preconditioning by rescaling with D had a dramatic effect on the convergence rate of the minimization algorithm. For Ψ, the rescaled system had a convergence rate three orders of magnitude larger than the un-scaled system.

The preconditioning operator P was chosen as follows. Without preconditioning, it was observed that the BFGS search directions (note that each "search direction" is a field) became progressively "rougher" as the search proceeded. At each step, the BFGS search direction can be expressed as a polynomial of the dynamical and weighting operators acting on the initial guess field (e.g., Luenberger, 1973); in other words, each search direction is a linear combination of high-order derivatives of the initial guess field. Hence, the "roughness" of the search directions is not surprising. In order to smooth the search directions, and accelerate the convergence of the large-scale features of the state, the preconditioner was chosen to be an iterated local averaging operator.

Specifically, in the experiments reported below, P was set equal to P_o^s: a 5-point weighted averaging operator, P_o, iterated s-times. The optimal number of

iterations, s, was determined separately for each field by experimentation. In every case, s between 2 and 5 was found to be optimal.

For the streamfunction equation, $s = 2$ was found to be the optimum number of iterations. The convergence rate (averaged over the first 20 BFGS iterations) was a convex function of s, with $s = 5$ having the same convergence rate as $s = 0$. Preconditioning with $s = 2$ improved the convergence rate by 18%.

In summary, the calculations below were preconditioned as follows. For each field, there was an operator D which rescaled the field so that the diagonal elements of the Hessian were approximately unity. Then, an averaging operator was applied to invert, approximately, the differential operators appearing in the penalty function.

3.4.2. Nonlinearity: z

In this set of experiments, z alone was allowed to vary, and the penalty function only penalized the misfit in the continuity equation. That is,

$$\mathcal{J}(z) = \epsilon \circ_3 W^{\epsilon} \circ_3 \epsilon, \tag{3.29}$$

where

$$\epsilon = \nabla \cdot (\mathbf{u} z_\theta) + (\omega z_\theta)_\theta. \tag{3.30}$$

It should be remembered that $\mathbf{u}$ depends implicity on z through hydrostatic balance and the momentum equations. No boundary conditions on z are needed since there is no normal flow on the boundaries.

To investigate whether the descent method would be capable of reconstructing a known solution to this (nonlinear) system, an "identical twin" experiment was performed in which the true solution outcropped. Because the model equations are

nonlinear, there was no guarantee that the descent method would be able to obtain the solution successfully.

The true solution was specified in the following manner. A field $z = z_{\text{true}}$, which outcropped, was chosen as the true solution, then the diabatic component of the vertical velocity, $\omega(z_{\text{true}})_\theta$, was diagnosed from the continuity equation. Henceforth, $\omega(z_{\text{true}})_\theta$ was treated as an independent quantity and held constant. Thus, the residual ϵ reduced to

$$\epsilon = \nabla \cdot (\mathbf{u} z_\theta) + (\overline{w})_\theta, \tag{3.31}$$

where $\overline{w} = \omega(z_{\text{true}})_\theta$, was held constant through the minimization.

The weight used in the penalty function was more complicated than for Ψ in the previous example. Since the momentum equations are approximately geostrophic, the gradient of z must be finite; therefore, the z field must be differentiable. A linear analysis shows that the penalty on the divergence of $\mathbf{u} z_\theta$ does not guarantee that z is differentiable.[1] To guarantee the smoothness of the solution, the weight was chosen to be the operator

$$W^\epsilon \circ_3 = \frac{\mathcal{N}_\epsilon}{\sigma_\epsilon} \left(1 + L^4 \nabla^2 \nabla^2\right) \frac{1}{\sigma_\epsilon}, \tag{3.32}$$

where L, the lateral correlation scale is 500km, and σ_ϵ^2 is a scalar equal to 1% of the horizontally averaged spatial variance of $(\overline{w})_\theta$ within each layer. The correspondence between weighting functions and weighting operators is discussed in detail in Appendix 4.3. Let us note here that because the expression $(\epsilon \circ_3 W^\epsilon \circ_3 \epsilon)$ is

---

[1]The linear analysis involves expressing z as a sum of vertical modes, each of which obeys a hyperbolic equation in two dimensions. The penalty on the divergence of $\mathbf{u} z_\theta$ insures that each mode is differentiable along its characteristic direction; however, the sum of modes need not be differentiable in any direction.

finite, ϵ has square-integrable second derivatives, which is adequate to insure that z is continuously differentiable. The coefficient $\mathcal{N}_\epsilon$ in equation (3.32) is a normalizing coefficient, which is determined by the condition that the correlation at zero lag be unity (see Appendix 4.3).

For this penalty function, the descent method failed to reconstruct the true solution after 1000 steps (at which time the penalty decreased by less than one part in 10^4 per step). In order to explain the cause of the difficulty, the value of the penalty function is plotted along sections of the state space in Figure 3.1. Because of the high dimension of the state space, it is difficult to visualize the global structure of the penalty function; the figure shows the value of the penalty function along lines in state space parameterized as follows:

$$z = \alpha z_{\text{start}} + (1 - \alpha) z_{\text{end}}, \tag{3.33}$$

$$z = \alpha z_{\text{end}} + (1 - \alpha) z_{\text{true}}, \tag{3.34}$$

$$z = \alpha z_{\text{true}} + (1 - \alpha) z_{\text{start}}, \tag{3.35}$$

for α in the interval $[0, 1]$. The fields z_{start} and z_{end} denote the starting and ending points in the descent calculation. Note that z_{start}, z_{end} and z_{true} define the vertices of a triangle in state space; however, in Figure 3.1 they are plotted consecutively along the abscissa.

It is evident that there is a large ridge between the true minimum and the minimum obtained by the descent procedure; the ridge is "large" in the sense that the value of $\mathcal{J}$ at the ridge's peak is two orders of magnitude larger than $\mathcal{J}(z_{\text{end}})$. Because the penalty function is not convex, there may be local minima. The state z_{end} is presumably located nearby one such minimum.

In a realistic inverse problem, there would be data constraints in the penalty function, so the problem with non-convexity may not be as severe in the full cal-

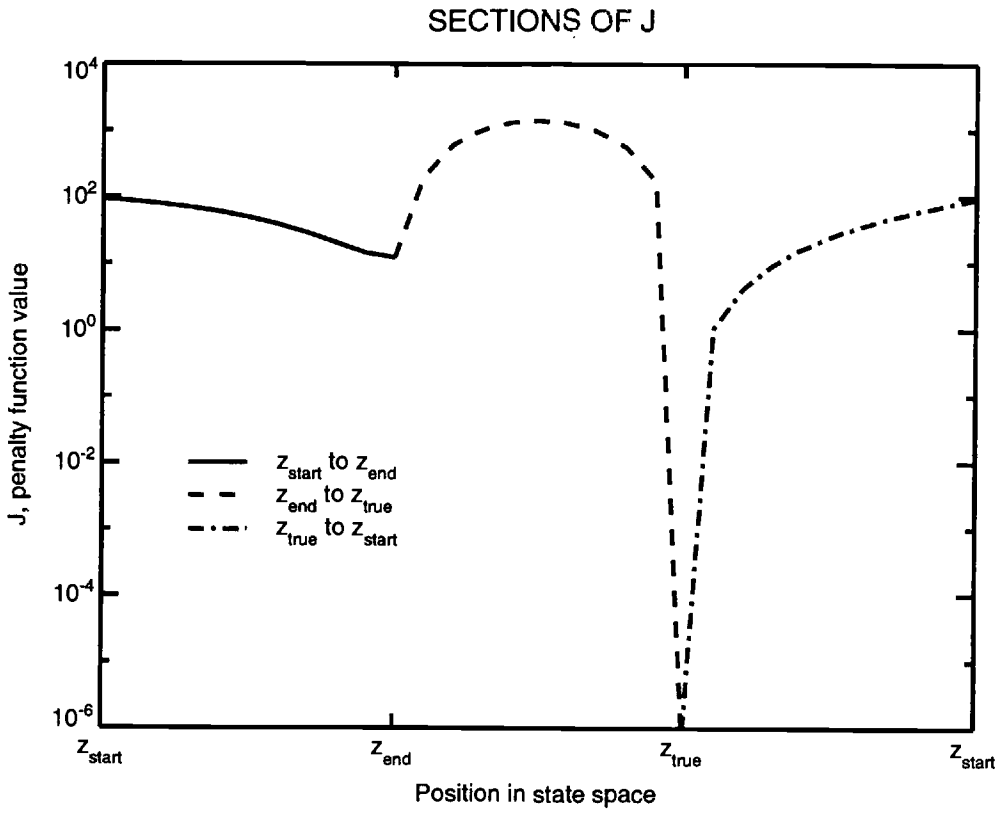

FIGURE 3.1. Penalty Function Sections.

To demonstrate the non-convexity of the penalty function used in Section 3.4.2, the panel shows the value of the penalty function along three sections in state space. Because the state variable, $z(\lambda, \phi, \theta)$, is a three-dimensional field, it is difficult to visualize the global structure of the penalty function, so sections along one-dimensional paths are plotted. The plot shows that between the end state of the minimization, z_{end}, and the true minimum of the penalty function, z_{true}, there is a large "ridge" which separates the two "valleys" in which z_{end} and z_{true} lie.

culations. In an effort to test this idea, an observation (of the true solution) was added at every fifth model grid point in the horizontal; the prior measurement error was set equal to the spatial variance of the layer depth (averaged horizontally). It was found that the penalty function decreased more rapidly than without the data and that convergence was to the true solution.

3.4.3. Summary

The main conclusion from these experiments is that the nonlinearity of the planetary geostrophic system may make the cost function non-convex. Since the cost function is defined on a high-dimensional space, there is no practical means of determining if the final state of the descent algorithm has reached a local or a global minimum. The non-convexity in the demonstration problem suggests that cost functions of interest do have local minima.

The experiments also highlighted the importance that data constraints were likely to play in the inversion. The experiments in which z alone was permitted to vary were unsuccessful without the added data constraints. The nonlinearity of the continuity equation appeared to vitiate the success of the descent algorithm. The added data increased the contribution to the gradient associated with the linear terms and aided in the convergence to the correct solution.

It may have been fortuitous, but in none of the preliminary calculations did the subsurface layers intersect. This suggested that it would be unnecessary to append to the penalty function an inequality constraint guaranteeing that the layer thicknesses remain positive definite; however, this proved to be incorrect: see below.

3.5. Final Experiment: North Pacific Inverse

Rather than continue with optimizing and improving the descent method, it was decided to proceed to the minimization using all of the state variables and constraints.

3.5.1. Data and Weights

Data sources for the inversion were as follows. The surface heat and fresh water flux data were taken from Oberhuber (1988), and the source of wind stress data was Hellerman and Rosenstein (1983). In both cases, the annually averaged values for the North Pacific ocean were used. Bilinear interpolation followed by convolution with an isotropic two-dimensional Gaussian (200km length scale) was used to transfer the climatological fields to the model grid; the Gaussian smoothing was performed to smooth out grid-scale noise which was apparent when computing the wind-stress curl. The hydrographic data were derived from the deep station data of Reid and Mantyla (1988). As discussed in Chapter 2, the temperature, salinity, and pressure data were interpolated with cubic splines and converted to observations of depth and salinity on isothermal levels. The bottom topography was obtained by smoothing the ETOPO5 (1988) data with an isotropic 500km Gaussian filter and then subsampling onto the model grid. The model domain extended from 3°N to 60°N and the land-sea boundaries were taken as the 1500m isobath in the ETOPO5 data (median filtered over 1° squares).

There are insufficient observations to completely specify the covariance for each control variable, the best that can be done is to propose a variance and correlation scale based on an educated guess regarding the sources of error. The full covariances (real functions of two space indices, i.e., 6 independent variables) are

never used in the computations; only their functional inverses, the weighting functions, are used. As detailed in Appendix 4.3, the inner products of weighting functions with state variables can be implemented as differential operators acting on the state variables. The relationships among covariances, weighting functions, and weight operators is briefly reviewed in Appendix 4.3; see McIntosh (1990) for more oceanographically relevant examples. The hypothesized covariances are completely determined by the magnitude of the variance and by the horizontal and vertical correlation length scales (the vertical "length" scale is measured in °C). The length scales determine the half-power point of the one-dimensional power spectra of the respective covariances.

The following subsections discuss the sources of error and the error variance scales upon which the weighting functions were based.

3.5.1.1. model equations

The momentum equations were imposed as exact constraints in the inversion. This was done for two reasons. First, by keeping the equations exact, the present formulation was more directly comparable to the contemporary work of Tziperman et al. (1992b and 1992c) than would have otherwise been the case. Second, outside of the western boundary current, and away from the equator, geostrophic momentum balance is believed to be quite accurate on scales larger than an internal Rossby radius (Bryden, 1980). For a 10cm/s velocity scale, and a length scale of 100km, the Rossby number is approximately 10^{-2} at midlatitudes. In addition, preliminary experiments showed that the descent procedure converged very slowly if errors were admitted in the momentum equations. For all of these reasons, the momentum equations were retained as exact constraints.

Error in the steady continuity equation may be caused by truncation error in the numerical model or by the spatial averaging implicit in defining the model quantities. There is also the possibility that the planetary geostrophic equations do not have a steady solution. Tziperman et al. (1992a) point out that that the vast majority of the data, on which our knowledge of the general circulation is based, were collected within the last 25 years or so; therefore, it is unreasonable to expect the observations to constrain any temporal changes in the circulation on a time scale longer than the time span over which observations were made. After much experimentation with the weight for this equation, it was decided base the weight on an error variance equal to 1% of the misfit (horizontally averaged mean-square) in the continuity equation, as computed from an objective-analysis of the observations. If the misfit in this equation is ascribed to temporal variation of the fields (e.g., a secular trend in isotherm depths), it corresponds, approximately, to a 15 year e-folding time-scale in the main thermocline.

The weights in the salt advection-diffusion equation and the heat equation were derived similarly. An objective-analysis of the observations was substituted into the the equations, and 1% of the misfit was selected as the uncertainty. The uncertainties for the continuity, salt, and heat equations are listed in Table 3.2.

TABLE 3.2. Dynamical Error Scales

Uncertainty in	Symbol	Typical value
Continuity equation	σ_ϵ	5 m/(yr °C)
Salt conservation equation	σ_η	35psu $\times$ σ_ϵ
Thermodynamic equation	σ_γ	15 m/yr
Streamfunction equation	σ_χ	10 m/yr $\times \frac{\mathrm{f}}{H}$

Error in the streamfunction equation was attributed to uncertainty in the no-normal-flow boundary condition at the ocean bottom. The model equations written

above (3.1-3.5) apply to spatially averaged quantities, so there is an implicit spatial averaging of the nonlinearity in the bottom no-normal-flow boundary condition. As discussed in Bogden (1991), there is an analogy between the omitted spatial average in the bottom boundary condition and the Reynolds stress terms in the momentum equations. Unresolved spatial scales in the flow and bottom topography could have a cumulative effect, a phenomenon which has been recognized in the atmospheric science modeling community (Wallace et al., 1983). The Ψ equation weight was based on an uncertainty corresponding to an erroneous vortex stretching of 10m/yr. For comparison, a typical value of the wind-driven Ekman pumping out of the mixed layer is 50m/yr in the subtropics. A deep horizontal velocity of 1cm/s up a typical large-scale oceanic bottom slope (5×10^{-6}) would create a 150m/yr vertical velocity.

3.5.1.2. surface fluxes

Errors in the surface flux data have numerous causes. The Comprehensive Ocean-Atmosphere Data Set (hereafter COADS, Woodruff et al., 1987; Oberhuber, 1988) was the source of the heat and fresh water flux data, while wind-stress data were taken from Hellerman and Rosenstein (1983). The air-sea fluxes in both of these sources were derived by applying bulk parameterizations to large archives of "marine reports," i.e., observations of air temperature, sea state, etc., largely from commercial vessels. An exception to this is the precipitation data in Oberhuber (1988) which was used to compute the fresh water flux; it is based on an earlier compilation of land and island station data (Shea, 1986; as cited by Oberhuber).

Bunker (1976) and Weare (1989) discuss the sources of error in air-sea fluxes computed from marine report archives such as COADS. Errors may be classified as either systematic or random. In the present context, a "systematic" error refers to an

error which does not decrease when observations are temporally averaged. All of the fundamental marine observations are contaminated by random error; however, over most of the North Pacific, there are enough observations so that the random error of a temporal average (i.e., the climatological mean) is negligible compared with the systematic error of the average. Unfortunately, systematic errors in the sea-surface temperature and air temperature measurements are likely to be a significant source of error. Their cumulative effect on the latent heat flux is estimated to be $28 W/m^2$ (Weare, 1989), which is comparable to the annually averaged heat flux over much of the subtropical North Pacific.

Systematic errors may also be introduced by the bulk parameterizations, which were used to convert the fundamental marine observations to air-sea fluxes. In principle, since the bulk formulae are empirical relations, any systematic errors ought to already have been absorbed into a calibration "offset;" however, marine observations are typically made under conditions different from those under which the bulk formulae were derived. Weare (1989) estimated a systematic uncertainty of $21 W/m^2$ in the bulk parameterization of the latent heat flux, which is caused by uncertainty in the value of the turbulent exchange coefficient. Isemer and Hasse (1991) considered the consequences of systematic error in the formula which is used to convert the Beaufort sea state (the variable most frequently reported in the marine reports) to wind speed. They find that the revised, corrected, Beaufort conversion formula results in annually averaged wind-stress and heat flux values which are, on average, approximately $3. \times 10^{-2} N/m^2$ and $27 W/m^2$ larger than those predicted using the un-revised Beaufort conversion scale. This corresponds to an error of approximately 20% in wind stress magnitude.

In summary, there are likely to be significant systematic and spatially inhomogeneous errors in the surface flux climatologies. The relevant surface flux errors

are summarized in Table 3.3. Although the dominant source of uncertainty in the heat flux is the latent heating, the contributions from the net solar and infra-red radiances, and the sensible heat exchange were included in the uncertainty estimate for Q in the Table. The fresh water flux uncertainty was determined by converting the latent heat flux uncertainty of Weare (1989) into an evaporation water flux. The fresh water flux is also contaminated by errors in the precipitation field; however, away from the intertropical convergence zone, the uncertainty in the precipitation estimate is negligible in comparison to the uncertainty in evaporation (Dorman and Bourke, 1979).

TABLE 3.3. Data Uncertainties

Uncertainty in	Symbol	Typical Value
Wind stress	σ_τ	3×10^{-2}N/m^2
Heat flux	σ_Q	36W/m^2
Fresh water flux	σ_F	0.45m/yr
Isotherm depth	σ_z	150 m
Salinity	σ_S	0.05 psu

It is difficult to quantify the spatial structure of the surface flux errors. The errors caused by the bulk parameterizations and un-revised Beaufort conversion scale are likely to be correlated on the same scales as the atmospheric circulation itself. Also, it is possible that the errors are correlated along shipping lanes, if vessels of different nationalities use different measurement practices. For this inverse calculation, it was assumed that the surface flux error covariances are homogeneous and isotropic with a 500km correlation scale. Also, the errors were assumed to be uncorrelated between the different fluxes. The precise functional forms of the covariances and weighting functions are described in Appendix 4.3. The prior error parameterizations could be improved; however, it was judged that a more precise

parameterization of the errors would not be warranted until after the flux fields are revised in accordance with the corrected Beaufort conversion scale, as recommended by Isemer and Hasse (1991).

3.5.1.3. hydrographic observations

The hydrographic observations were weighted by considering the spatial and temporal variability of hydrographic data in the domain. First, the National Oceanographic Data Center (NODC) archive of station data was used to determine the mean and variance of isotherm depth and salinity within $10^\circ \times 10^\circ$ squares in the North Pacific.[2] The variance field was then interpolated onto the model grid, and smoothed with a $20^\circ \times 20^\circ$ box-car filter. This averaging smoothed out spatial inhomogeneity in the variance; the spatial inhomogeneity is primarily a consequence of variability in coastal water mass properties. Finally, the reciprocal of this variance was used to weight the hydrographic observations in the Reid-Mantyla (1988) data set. The larger NODC data set was used to obtain the statistics of the hydrographic data, while the smaller Reid-Mantyla data set was used for the actual observations because of the greater degree of quality control applied to the Reid-Mantyla cast data. Typical values for the hydrographic data errors are listed in Table 3.3.

---

[2]Two steps were taken for quality control: observations were excluded with two passes of a three-standard-deviation filter, and casts were rejected if their deepest observations did not rank in NODC's highest quality category.

3.5.2. Descent Calculation

The initial state in the descent calculation was as follows. The surface fluxes τ, Q, and F were each set equal to their observed values, and the diabatic velocity, ω, was set to zero. The z and S fields were set equal to an objective analysis of their respective observations. The streamfunction for the barotropic transport, Ψ, was set to zero. Thus, the initial value of penalty was a consequence of residuals in the thermodynamic, continuity, salt-conservation, and barotropic vorticity equations; the data penalty was negligible initially.

In order to facilitate the convergence of the large-scale adjustments to the fields, an initial minimization was performed on a coarse grid. In this case, 5500 minimization steps were performed on a model running at 1/3 the standard horizontal resolution.

Figure 3.2 shows the value of the penalty function over the course of the minimization. The jump in the penalty function value at iteration 5500 was caused by the interpolation onto the fine, $1^o \times 1^o$, resolution grid.

The other jumps in the penalty were caused by the removal of layer intersections in the solution: it was found that negative layer thicknesses did arise in the descent calculation. A constrained minimization algorithm was implemented (Luenberger, 1973; section 11.6, the reduced gradient method); however, periodically resetting the layer depths to a feasible (positive layer thickness) state was more efficient than the constrained minimization procedure. The jumps at step numbers 500, 6000, and 7000 were caused by resetting the layer depths to a feasible configuration.

Table 3.4 shows the components of the cost function before and after the fine-grid minimization (at steps 5500 and 8000). The total penalty function was

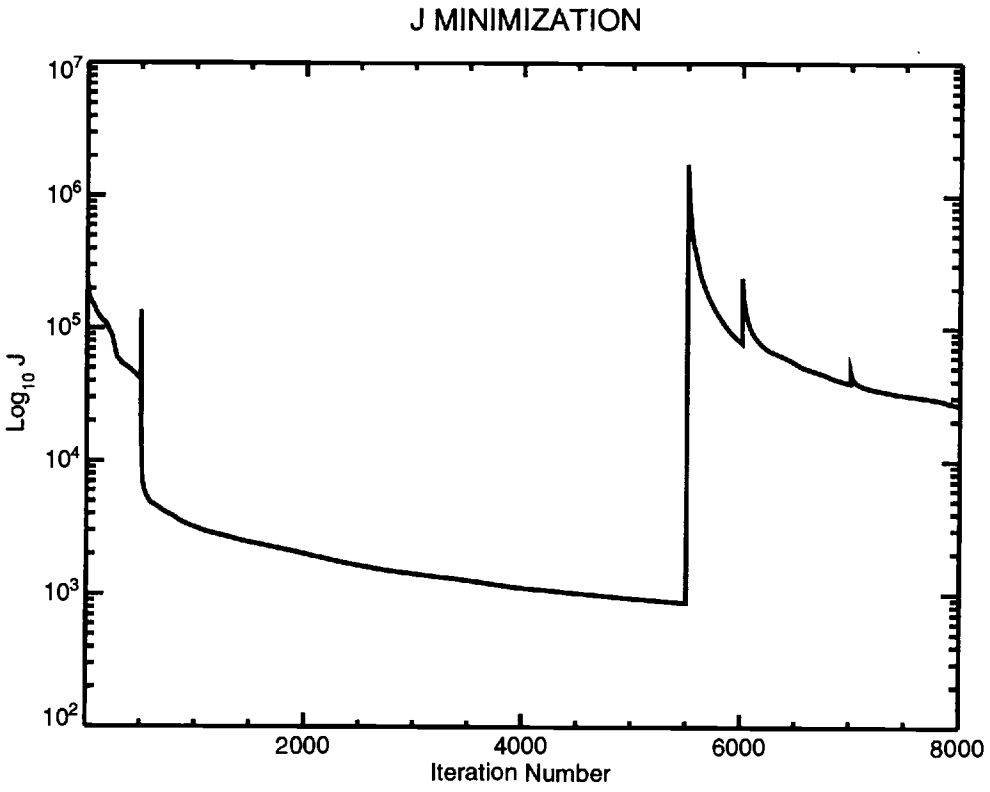

FIGURE 3.2. $\mathcal{J}$ Minimization.

The plot shows the progress of the nonlinear minimization reported in Section 3.5. Iterations 1-5500 took place with a coarse-resolution version of the model. The solution was then interpolated to the full model resolution, and the descent procedure continued until iterate 8000. The discontinuous jumps in the value of the penalty function (at iterates 500, 6000, and 7000) occurred when the z-field was adjusted to remove intersecting layers.

reduced by approximately 2 orders of magnitude. At the end of the run, the single largest contribution to the penalty was the layer depth data term.

TABLE 3.4. Penalty Function Components

Component	Starting Value	Ending Value
$\mathcal{J}_\epsilon$	7.4×10^5	1.5×10^3
$\mathcal{J}_\eta$	7.2×10^5	1.4×10^3
$\mathcal{J}_\gamma$	4.4×10^2	4.6×10^2
$\mathcal{J}_\chi$	4.3×10^6	8.7×10^2
$\mathcal{J}_{\text{z data}}$	2.5×10^5	1.8×10^4
$\mathcal{J}_{\text{S data}}$	2.1×10^3	2.5×10^3
$\mathcal{J}_\tau$	3.3×10^1	1.2×10^2
$\mathcal{J}_F$	1.7×10^2	1.8×10^2
$\mathcal{J}_Q$	1.4×10^3	5.4×10^2
$\mathcal{J}_\Psi$	6.9×10^2	1.0×10^2
$\mathcal{J}$ (total)	5.9×10^6	2.6×10^4

There is no evidence to suggest that convergence to a minimum was achieved after 8000 steps. Nonetheless, since the fractional decrease in $\mathcal{J}$ at the final step was approximately 4×10^{-5}, it was decided to terminate the experiment and see what could be learned from the results.

First, consider the surface flux fields before and after the minimization. Overall, the surface fluxes were reduced in magnitude by roughly a factor of two. Figure 3.3 compares the initial and final and heat flux fields: the magnitude of the heat flux was reduced almost everywhere. The same reduction in magnitude was also seen in both the fresh water flux and the wind stress. Because of the uniformity of the reductions, and because of the spatial structure present in the heat flux field (which indicates a conditioning problem), the state found by the minimization is unrealistic. In particular, the large values of sea-to-air heat exchange over the western boundary current were strongly reduced.

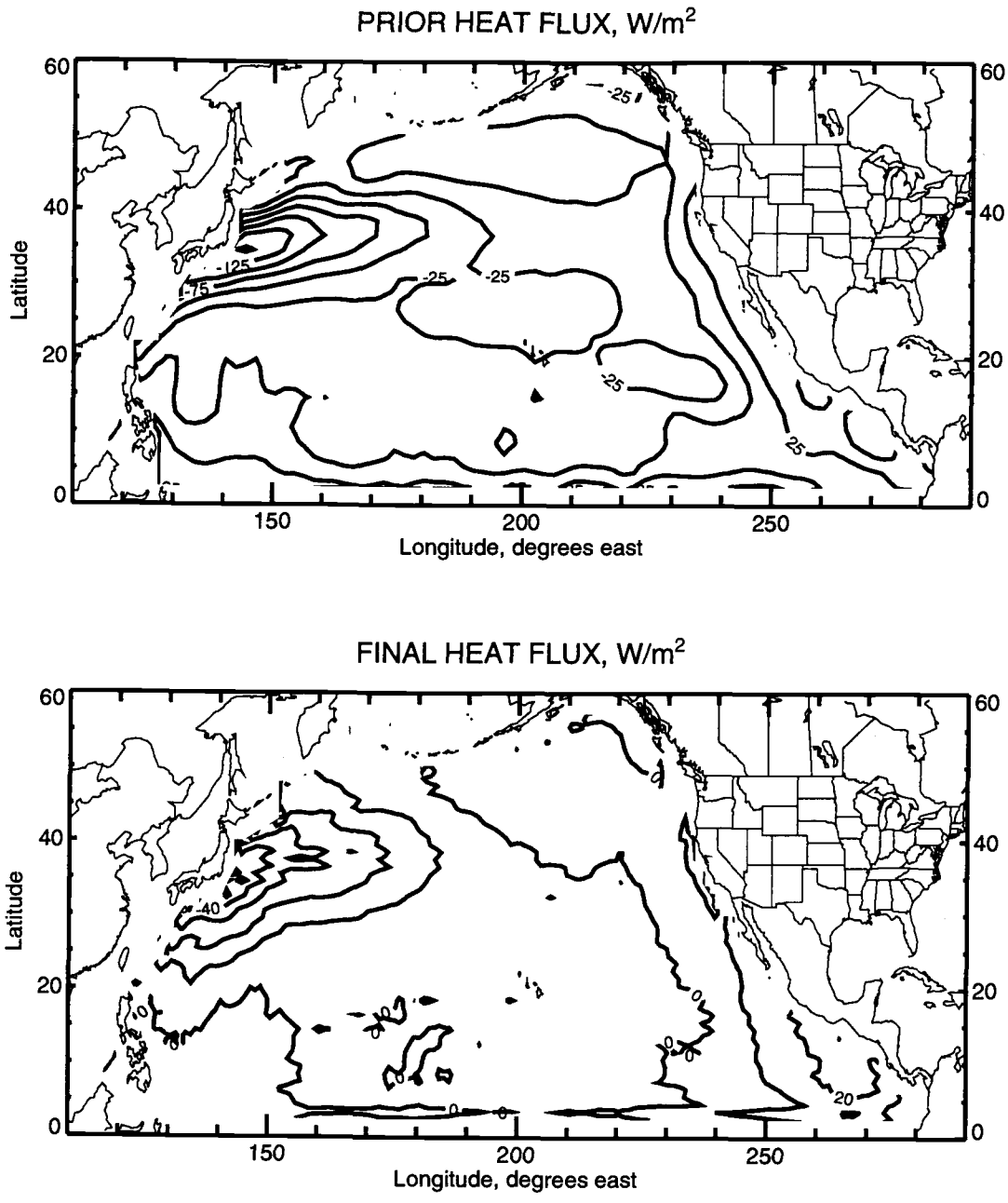

FIGURE 3.3. Surface Heat Flux.

The upper panel shows the Oberhuber (1988) heat flux estimate which was used as boundary condition data. The lower panel shows the heat flux estimate after the minimization. The magnitude of the heat flux was greatly reduced, especially over the western boundary current region.

Figure 3.4 shows the term balance for the heat equation (3.14) at (150°E, 32°N), roughly the center of the heat flux maximum in the Kuroshio extension. The curves are labeled I, II, III, and IV corresponding to the terms as follows:

$$\underset{\text{I}}{\omega z_\theta} = \underset{\text{II}}{\left(\frac{K_V}{z_\theta}\right)_\theta} + \underset{\text{III}}{F^Q_\theta} + \underset{\text{IV}}{\gamma}. \tag{3.36}$$

It can be seen that the diabatic component of the vertical velocity (term I) is incapable of balancing the imposed heat flux divergence (term III) at the ocean surface (deeper in the water, term I is too large). In the surface layer, we should expect that F^Q_θ, the divergence of the vertical Reynolds heat flux, would be balanced by ωz_θ, the diabatic component of the vertical velocity. In fact, ωz_θ is too small above the 20°C isotherm, and too large below that level, to balance the prescribed heat flux divergence.

Inspection of the term balance in the continuity equation (3.12), Figure 3.5, reveals a good balance, i.e., a small residual. The terms are labelled I, II, III, and IV as follows:

$$\underset{\text{I}}{\mathbf{u}\cdot\nabla z_\theta} + \underset{\text{II}}{z_\theta \nabla\cdot\mathbf{u}} + \underset{\text{III}}{(\omega z_\theta)_\theta} = \underset{\text{IV}}{\epsilon}. \tag{3.37}$$

The ωz_θ field in Figure 3.4 is evidently a consequence of the horizontal divergence in the upper layers, and advection in the deeper layers. In other words, because of the small residual (IV), term III balances term II in the upper layers; while term III balances term I on the deeper layers.

The term balance in equation 3.37 reveals that the diabatic velocity, ωz_θ, is determined primarily by the continuity equation: the diabatic velocity is essentially just the wind-driven Ekman pumping. However, the balance from equation 3.36

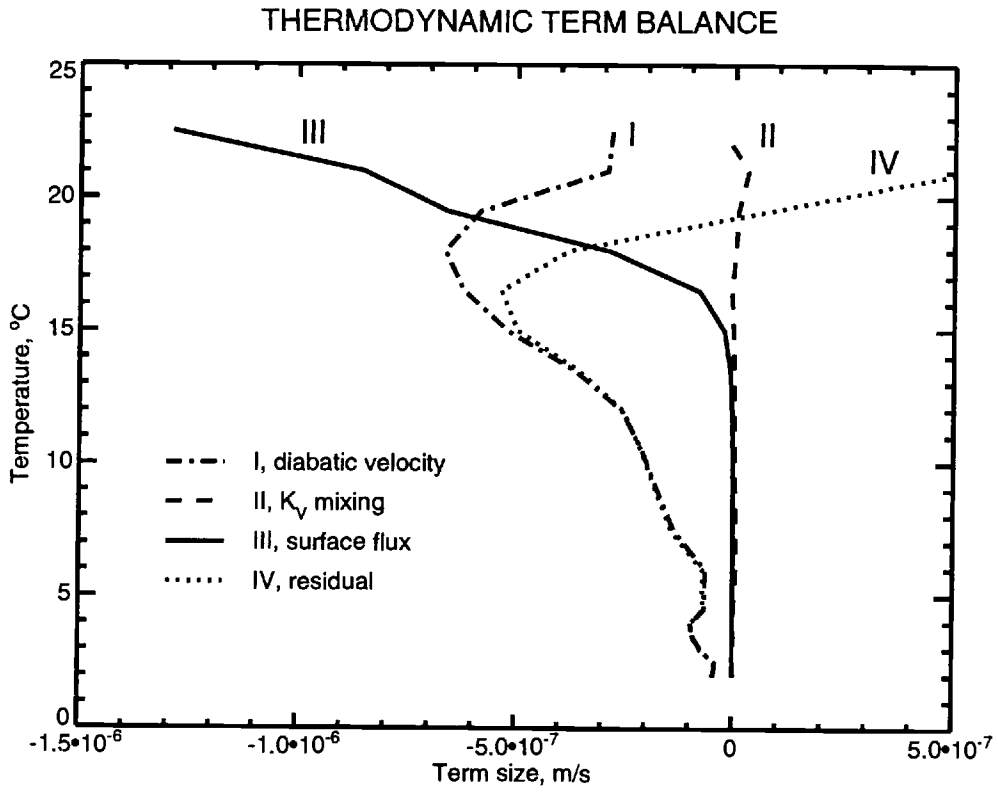

FIGURE 3.4. Thermodynamic Term Balance: 150°E, 32°N.

The sizes of the terms in the thermodynamic equation are plotted. The imbalance is evident.

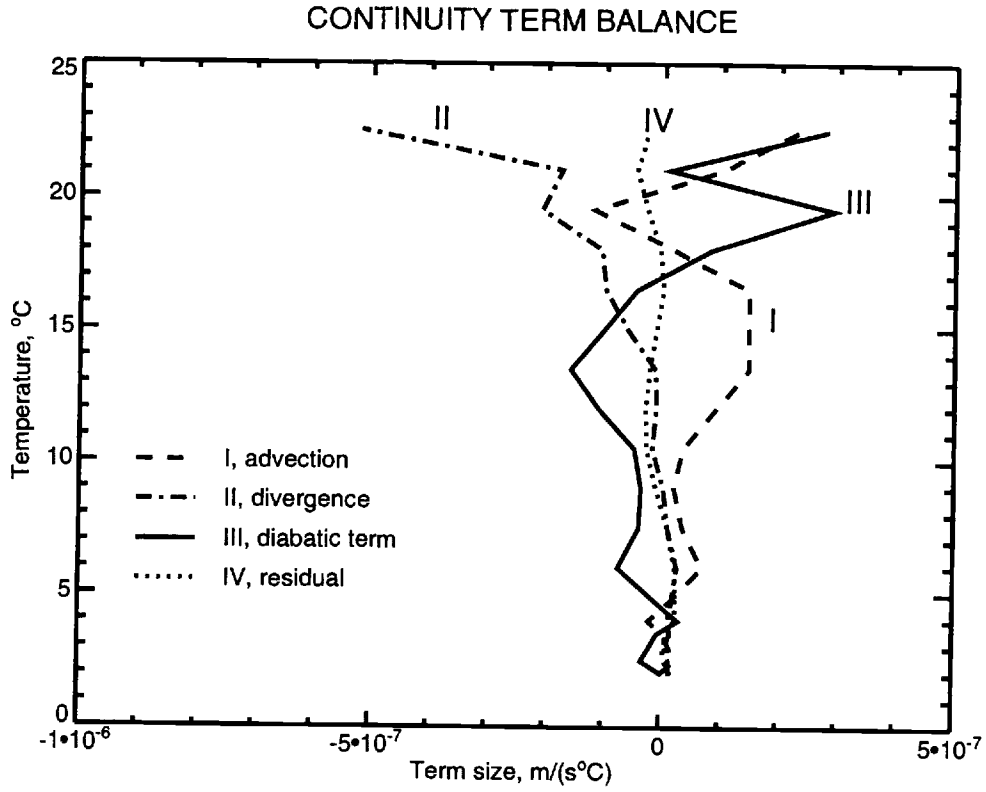

FIGURE 3.5. Continuity Term Balance: 150°E, 32°N.

The sizes of the terms in the continuity equation are plotted. The residual (IV) is small compared to the divergence of the diabatic velocity (III).

reveals that this diabatic velocity is insufficient to balance the heat removed from the upper layers. In other words, it would appear that the wind-driven Ekman pumping is insufficient to balance the heat lost from the surface layers. Another explanation for the term balance is that the model's parameterizations of the surface heat and momentum fluxes may be incompatible, or they may simply be poor representations of the vertical Reynolds fluxes.

Elsewhere in the domain, a similar phenomenon occurs. The diabatic velocity is generally consistent with the continuity equation; however, it is decoupled from the thermodynamic balance. In order to affect a thermodynamic balance, the descent procedure has reduced the value of the surface heat flux. Analogous considerations apply to the surface salt balance: the over-all magnitude of the freshwater flux was too large relative to the diabatic salt flux, therefore, the former was reduced.

The wind-stress magnitude was also decreased (Figures 3.6 and 3.7). This is surprising, one would have expected it to increase in order to reconcile the thermodynamic balance by increasing the Ekman layer divergence. In fact, the zonal component of the wind-stress does intensify slightly over the western boundary current region (130°E, 24°N), where the Ekman drift transports warm water shoreward (compare Figure 3.6B with Figure 3.10).

The streamfunction (Figure 3.8) would suggest a barotropic flow that is much wider and more sluggish than that predicted from the wind-stress and Munk (1950) boundary layer theory. The wide boundary layer is a consequence of the relatively large residual in the barotropic vorticity equation at this stage in the minimization. Figure 3.9 shows the term balance in the barotropic vorticity equation across the subtropical gyre.

The above remarks regarding the surface flux fields indicate that the continuity equation is largely controlling how the fields adjust in the minimization. The

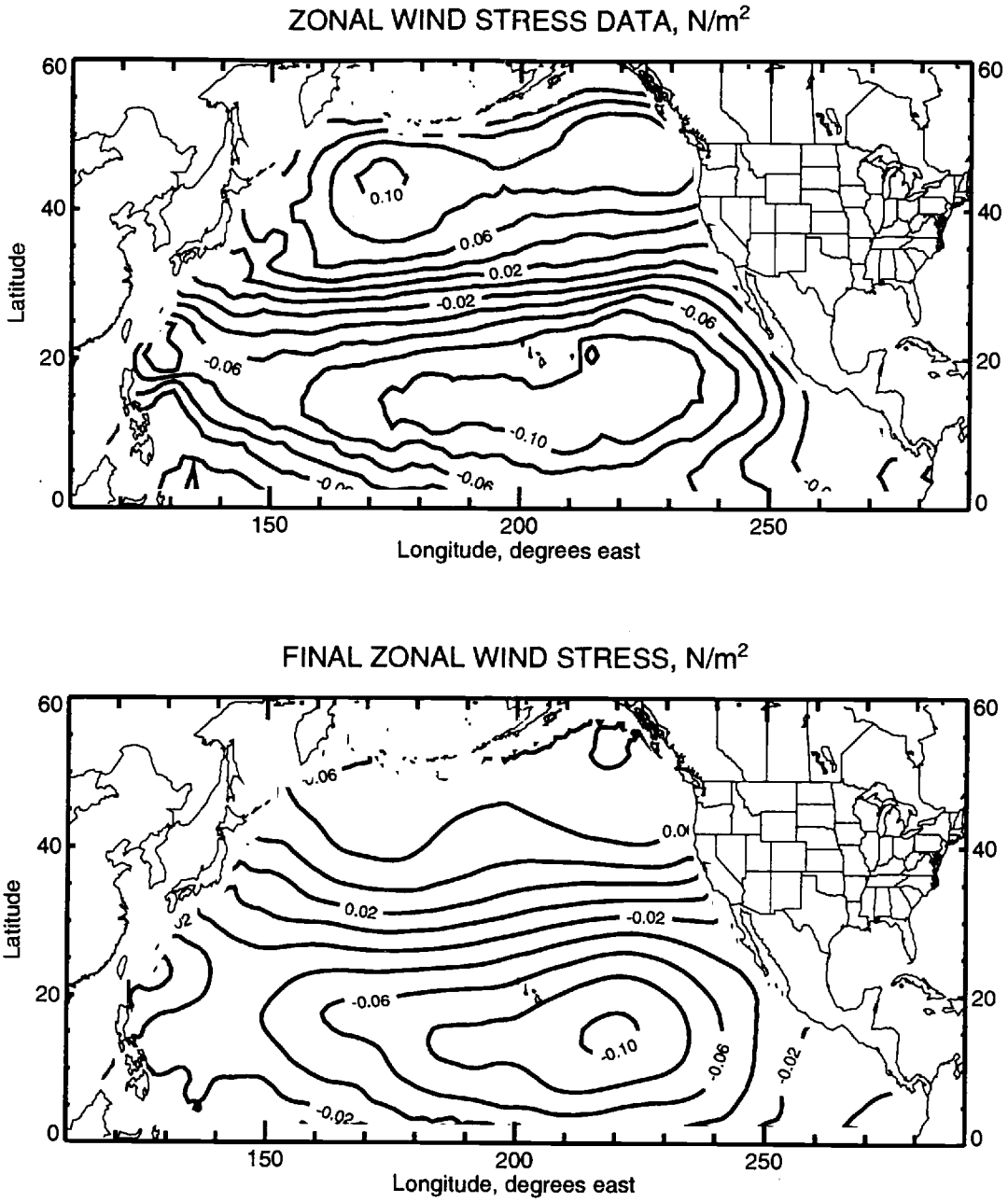

FIGURE 3.6. Zonal Wind Stress.

The zonal wind stress component was uniformly reduced in the descent procedure. The upper panel shows the wind stress data (Hellerman and Rosenstein, 1983), and the lower panel shows the estimated wind stress.

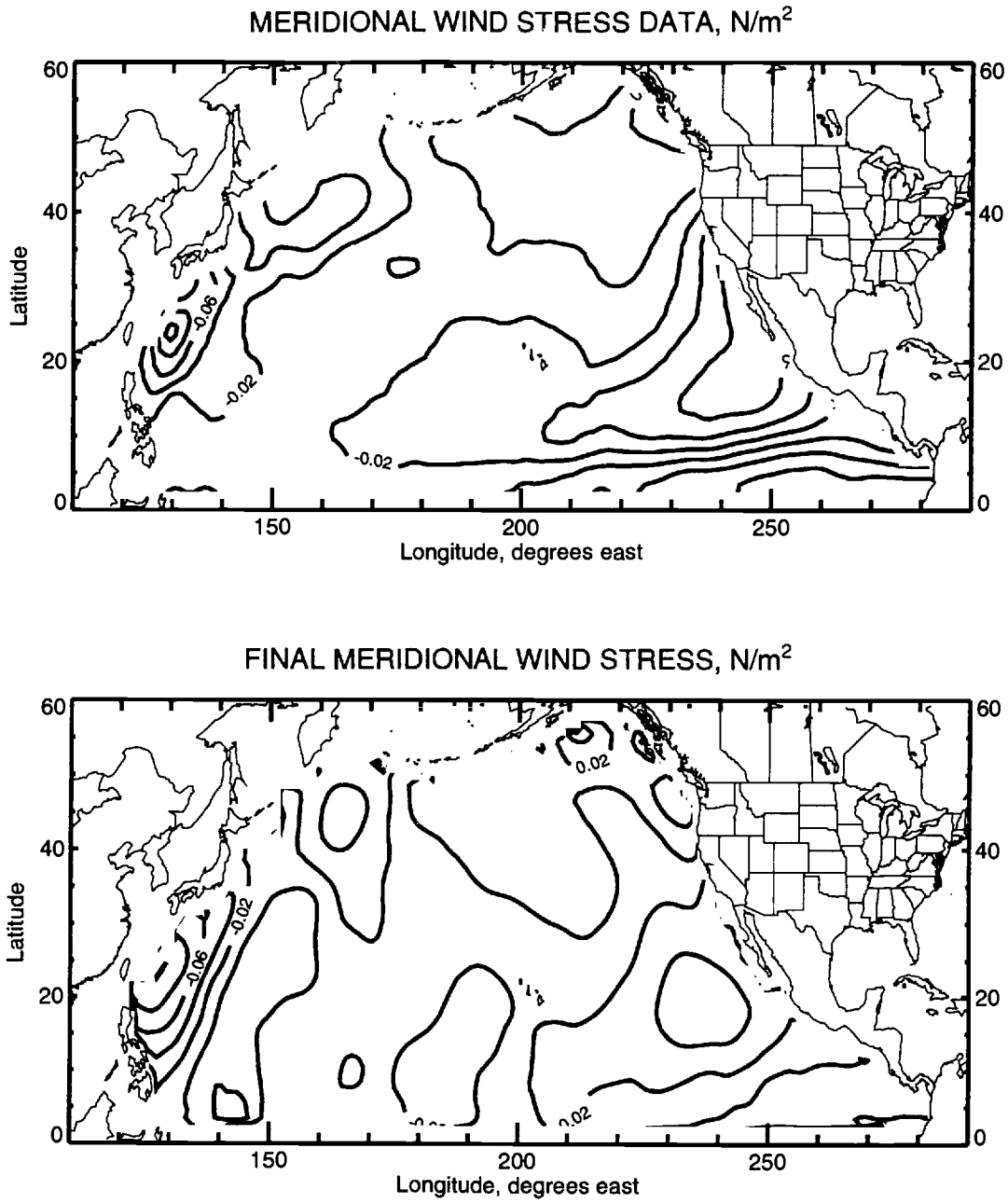

FIGURE 3.7. Meridional Wind Stress.

See Figure 3.6.

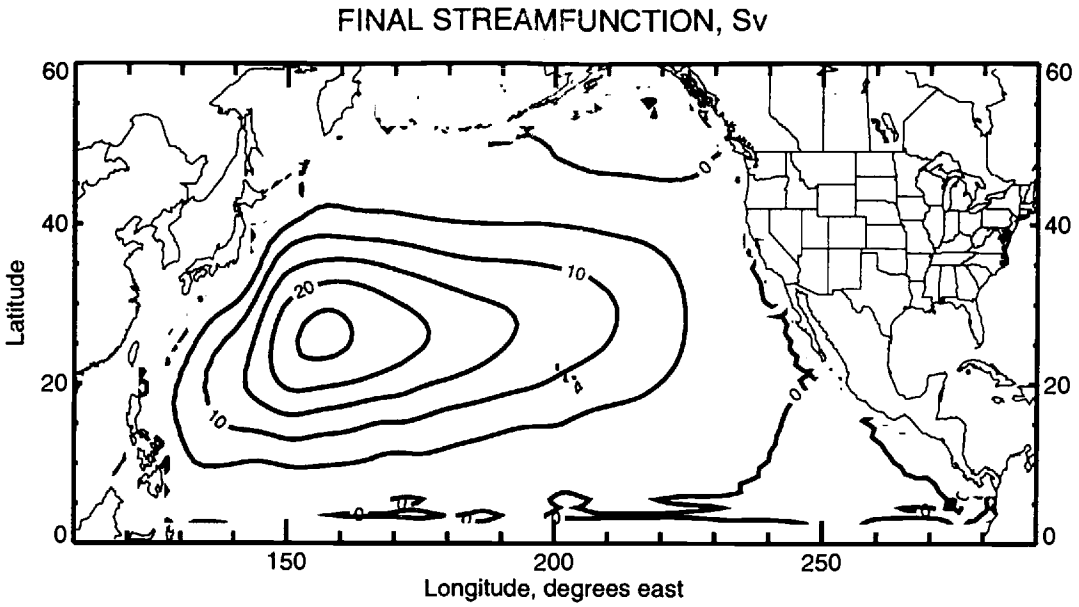

FIGURE 3.8. Final Streamfunction.

The streamfunction for the barotropic flow is plotted. The width of the western boundary current is too large for a Munk (1950) layer. It is a consequence of the residual in the barotropic vorticity equation.

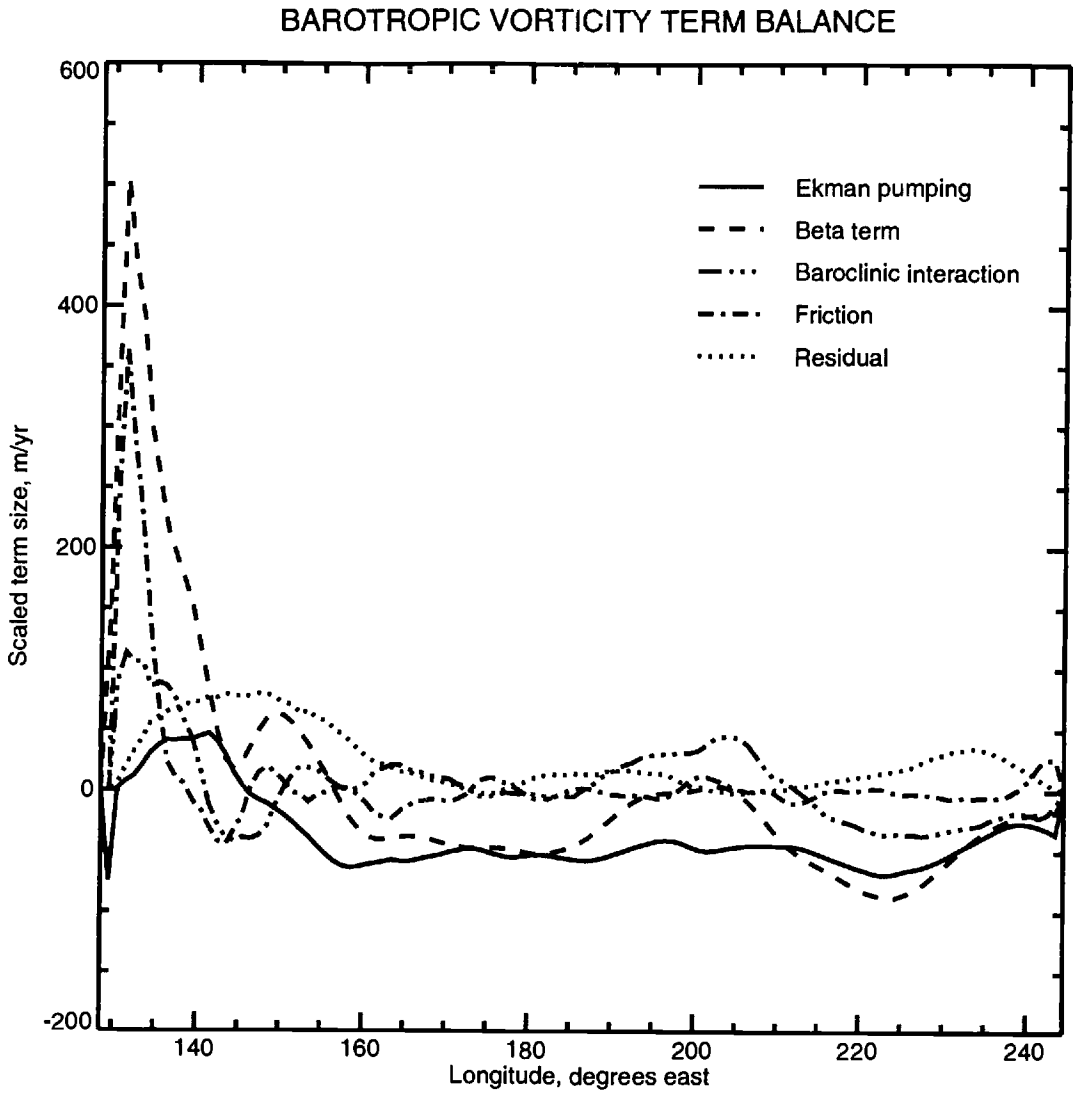

FIGURE 3.9. Barotropic Vorticity Term Balance: 24°N.

The term balance shows that the barotropic vorticity equation is roughly in balance across the subtropical gyre. The intensification of the flow in the western boundary current is a Munk (1950) balance between the "beta term" (advection of planetary vorticity) and friction only within a narrow boundary layer. Just outside of the boundary layer, the beta term is unbalanced and contributes to the residual.

continuity equation is acting as such a strong constraint (compared to the thermodynamic and data constraints), that the state is being biased towards a sluggish and thermodynamically inactive state in order to reduce the penalty function. In other words, the state is being adjusted towards a state of rest in order to minimize (trivially) the penalty associated with the continuity equation.

In order to quantify the control of the continuity equation on the minimization, consider the components of the gradient of $\mathcal{J}$ with respect to each state variable. For example, $\nabla_z \mathcal{J}$, the gradient of $\mathcal{J}$ with respect to the z state variable, is composed of terms caused by the variation of z in the following terms:

1. the barotropic vorticity equation: $\nabla_z^{\chi} \mathcal{J}$,
2. the continuity equation: $\nabla_z^{\epsilon} \mathcal{J}$,
3. the salt conservation equation: $\nabla_z^{\eta} \mathcal{J}$,
4. the thermodynamic equation: $\nabla_z^{\gamma} \mathcal{J}$, and
5. the data terms: $\nabla_z^{\text{data}} \mathcal{J}$.

The symbol "$\nabla_a^b \mathcal{J}$" denotes "the gradient of $\mathcal{J}$ with respect to a associated with equation b." Thus, the total gradient with respect to z is the sum of contributions caused by each constraint:

$$\nabla_z \mathcal{J} = \nabla_z^{\chi} \mathcal{J} + \nabla_z^{\epsilon} \mathcal{J} + \nabla_z^{\eta} \mathcal{J} + \nabla_z^{\gamma} \mathcal{J} + \nabla_z^{\text{data}} \mathcal{J} \tag{3.38}$$

(the superscript on the ∇ refers to the symbols used in equations 3.1-3.5, above).

Tables 3.5 and 3.6 show the root-mean-square (averaged over the computational domain) values of each gradient component. For example, one can see that the wind-stress is being controlled by the continuity equation:

$$|\nabla_\tau^{\epsilon} \mathcal{J}| \gg |\nabla_\tau^{\chi} \mathcal{J}|, \tag{3.39}$$

TABLE 3.5. Gradient Components

Gradient	Component	Value (rms)
$\nabla_\tau \mathcal{J}$:		
	$\nabla_\tau^\epsilon \mathcal{J}$	1.5×10^{6}
	$\nabla_\tau^\eta \mathcal{J}$	1.4×10^{6}
	$\nabla_\tau^\chi \mathcal{J}$	5.2×10^{4}
	$\nabla_\tau^{\text{data}} \mathcal{J}$	2.4×10^{4}
$\nabla_Q \mathcal{J}$:		
	$\nabla_Q^{\text{data}} \mathcal{J}$	1.4×10^{5}
	$\nabla_Q^\gamma \mathcal{J}$	9.3×10^{4}
$\nabla_F \mathcal{J}$:		
	$\nabla_F^{\text{data}} \mathcal{J}$	2.0×10^{5}
	$\nabla_F^\eta \mathcal{J}$	6.4×10^{4}
$\nabla_z \mathcal{J}$:		
	$\nabla_z^\eta \mathcal{J}$	5.6
	$\nabla_z^\epsilon \mathcal{J}$	4.7
	$\nabla_z^\chi \mathcal{J}$	1.3×10^{-1}
	$\nabla_z^\gamma \mathcal{J}$	8.9×10^{-2}
	$\nabla_z^{\text{data}} \mathcal{J}$	5.3×10^{-2}

and

$$|\nabla_\tau^\epsilon \mathcal{J}| \gg |\nabla_\tau^{\text{obs}} \mathcal{J}|. \tag{3.40}$$

Similarly, S, z, and ω are being controlled by the continuity equation (the salt conservation equation provides little independent information in this formulation). To reiterate: the minimization has found a set of fields which are mutually consistent with the continuity equation.

The initial and final layer depth fields are plotted for a few layers in Figures 3.10 through 3.13. In large part, the layer interfaces have been smoothed and shallowed. Below the thermocline, the most noteworthy features are the undulations in the deepest layer thickness (Figure 3.13). The bottom topography is shown

TABLE 3.6. Gradient Components (continued)

Gradient	Component	Value (rms)
$\nabla_S \mathcal{J}$:		
	$\nabla_S^{\eta} \mathcal{J}$	7.9×10^{2}
	$\nabla_S^{\epsilon} \mathcal{J}$	5.6×10^{2}
	$\nabla_S^{\chi} \mathcal{J}$	2.4×10^{1}
	$\nabla_S^{\text{data}} \mathcal{J}$	1.1×10^{1}
$\nabla_\Psi \mathcal{J}$:		
	$\nabla_\Psi^{\chi} \mathcal{J}$	4.1×10^{-5}
	$\nabla_\Psi^{\epsilon} \mathcal{J}$	2.9×10^{-6}
	$\nabla_\Psi^{\eta} \mathcal{J}$	2.3×10^{-6}
$\nabla_\omega \mathcal{J}$:		
	$\nabla_\omega^{\epsilon} \mathcal{J}$	6.0×10^{6}
	$\nabla_\omega^{\eta} \mathcal{J}$	5.8×10^{6}
	$\nabla_\omega^{\gamma} \mathcal{J}$	1.1×10^{5}

in Figure 3.14 to emphasize that it is not obviously related to changes in the 2°C isotherm depth.

Changes in the deepest isotherm depth are found in areas of strong cross-isobath flow. As shown in Figure 3.15, at 20°N, the region of largest change is located on both flanks of the Izu ridge at approximately 140°E. Inspection of the term balance in the continuity equation reveals that the advection term, $\mathbf{u} \cdot \nabla z_\theta$, and the divergence term, $z_\theta \nabla \cdot \mathbf{u}$, are large and nearly cancel in this region. If it is assumed that the best-fit solution is in a state of baroclinic adjustment (i.e., if the cross-isobath flows are nearly zero; Anderson and Killworth, 1977), then the minimization procedure may be passing through a transient state involving local nonlinear balances between the advection and divergence in the deepest layer. The nonlinear nature of these balances may significantly slow the minimization process.

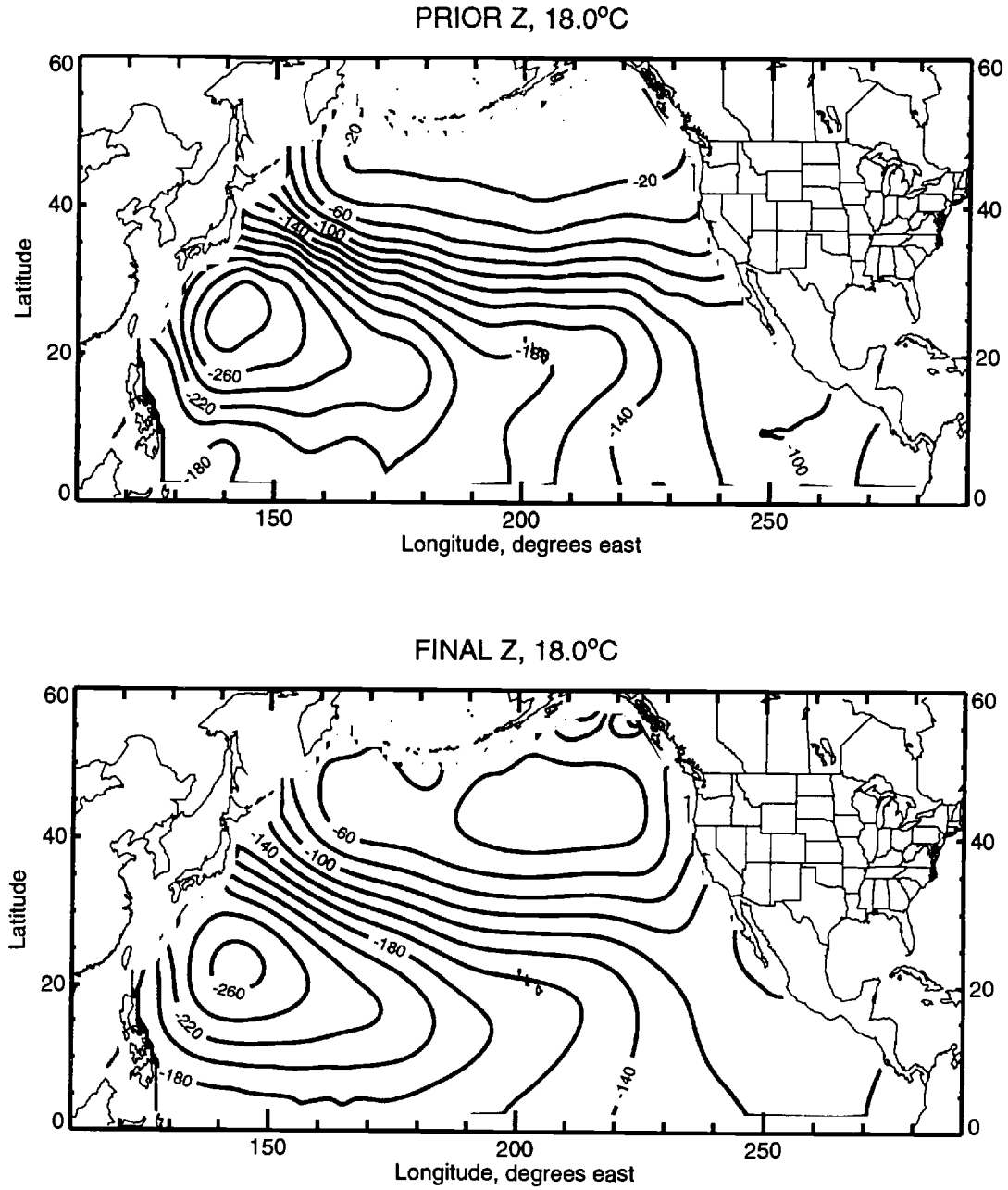

FIGURE 3.10. 18.0°C Isotherm Depth.

The prior and final depths of the 18.0°C isotherm are shown. The contour levels are identical in both panels. Over-all, the layer depth has been smoothed, and its gradient is reduced.

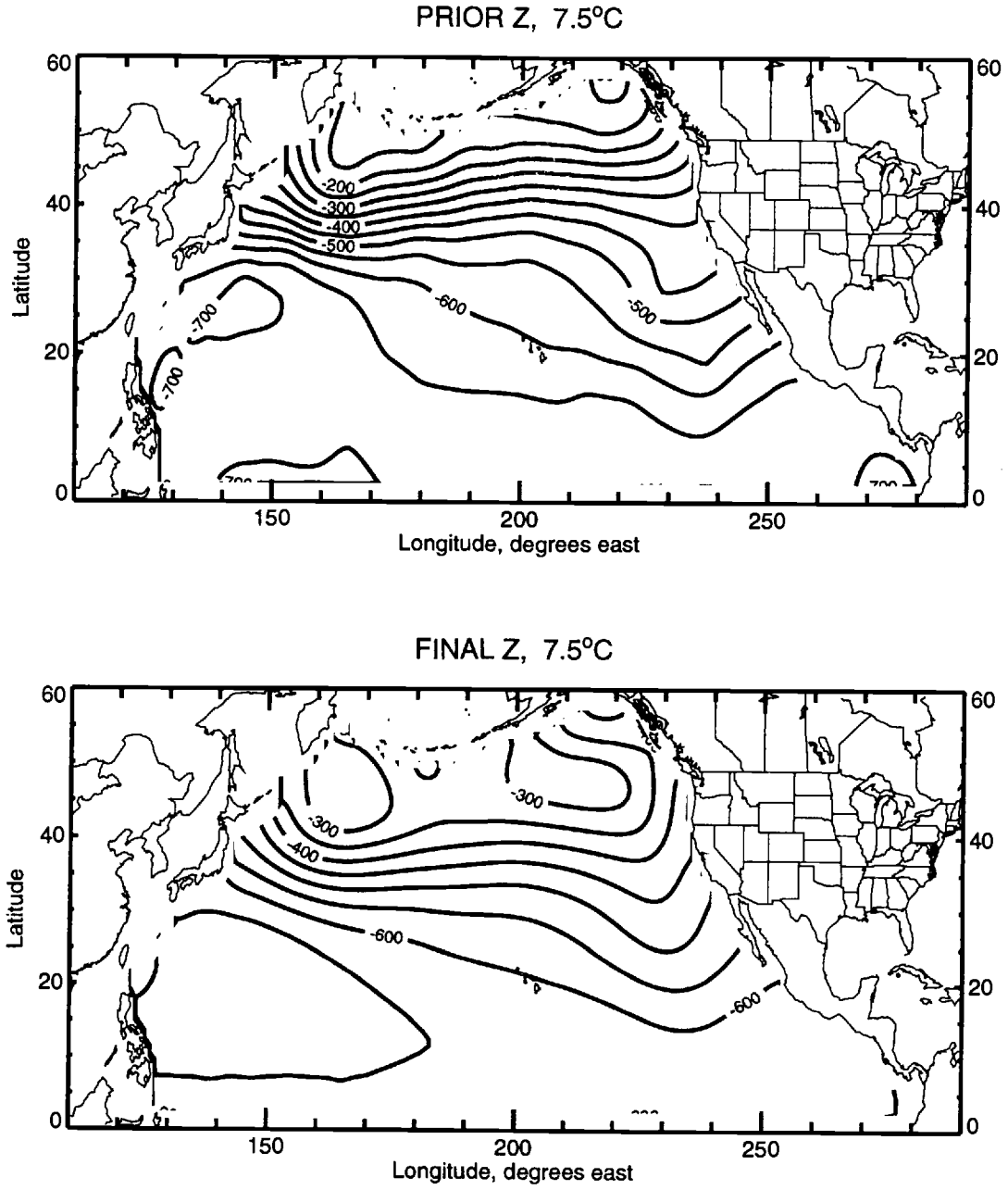

FIGURE 3.11. 7.5°C Isotherm Depth.

The prior and final depths of the 7.5°C isotherm are shown.

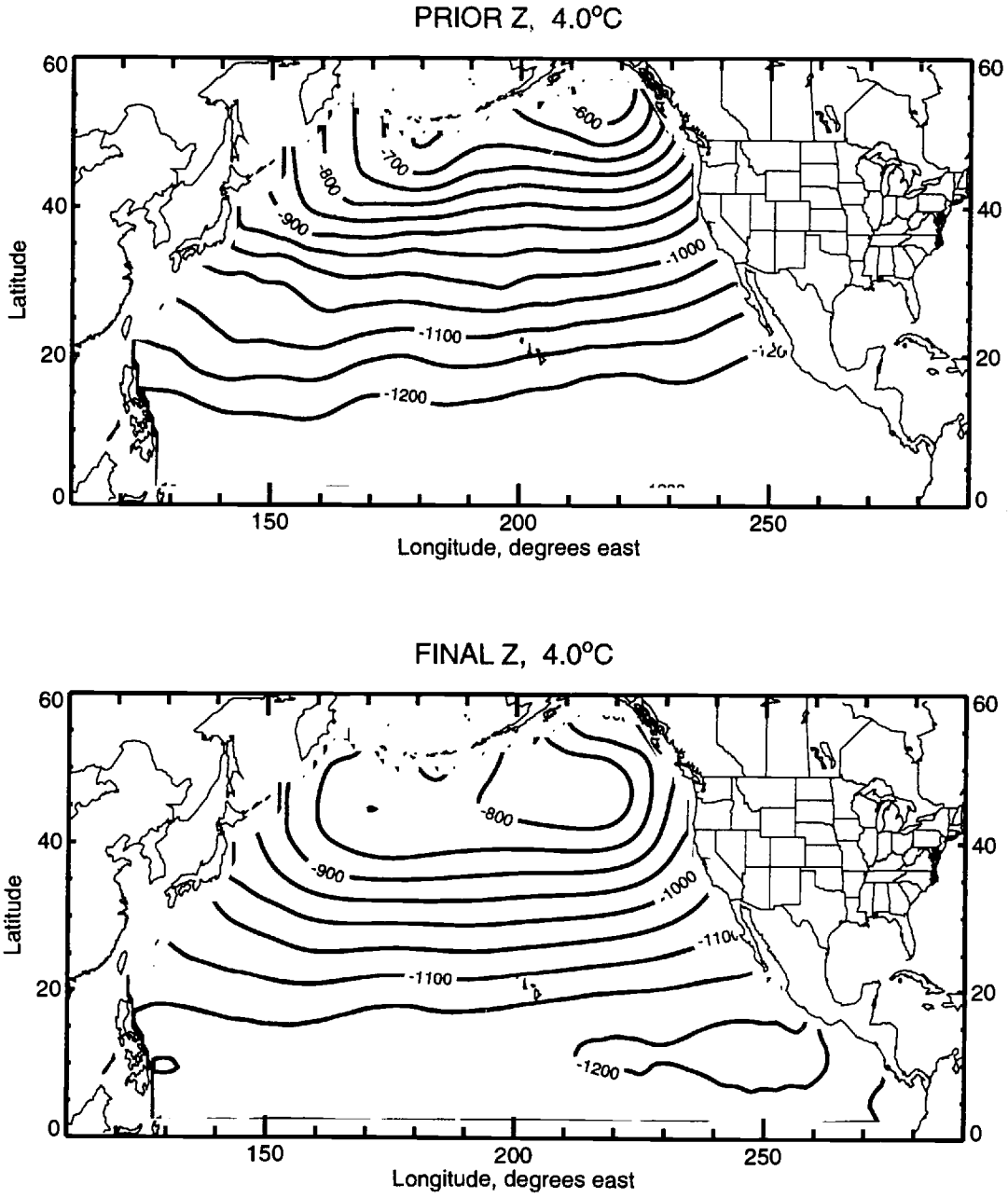

FIGURE 3.12. 4.0°C Isotherm Depth.

The prior and final depths of the 4.0°C isotherm are shown.

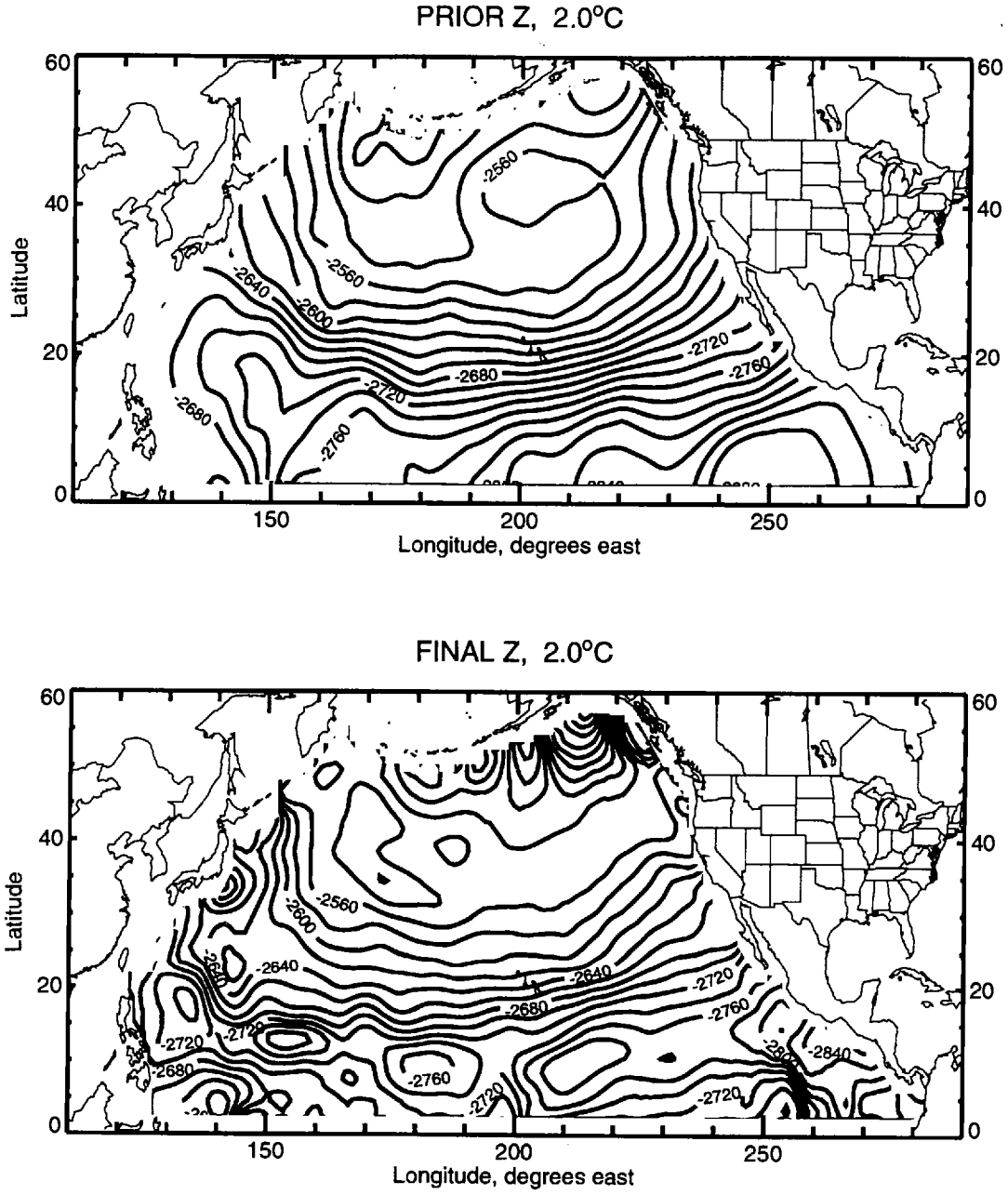

FIGURE 3.13. 2.0°C Isotherm Depth.

The prior and final depths of the 2.0°C isotherm are shown.

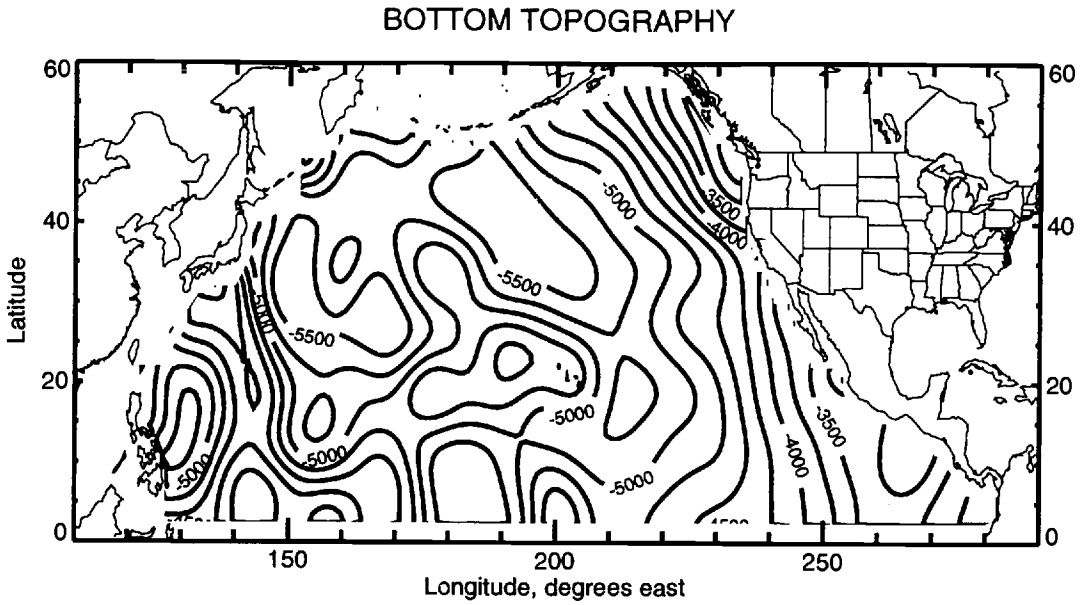

FIGURE 3.14. Bottom Topography.

The bottom topography used in the model is shown for reference.

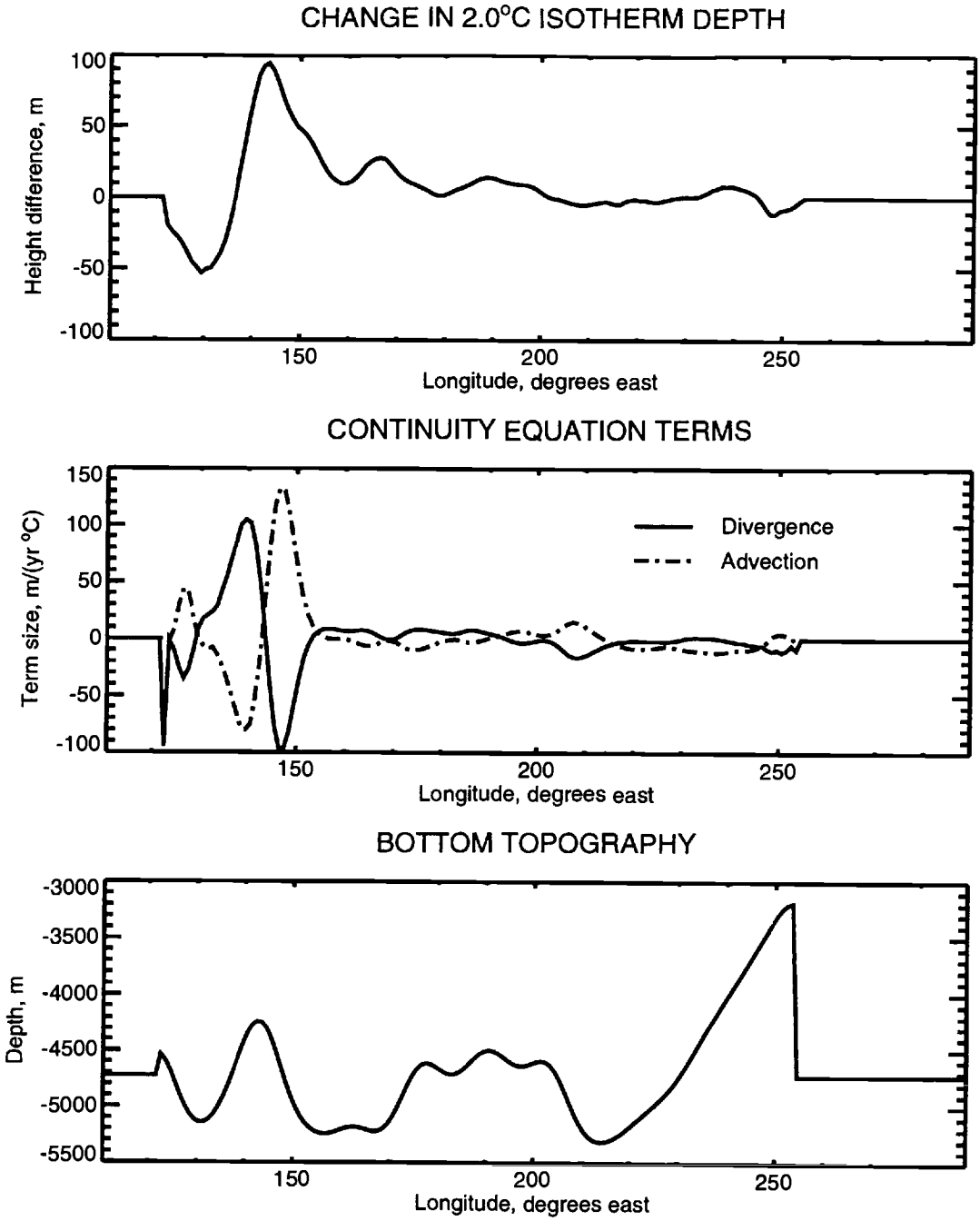

FIGURE 3.15. Changes in Isotherm Depth.

Large changes in the 2.0°C isotherm depth are associated with regions of large cross-isobath flow. The three panels show sections of their respective fields at 24°N. During the minimization, the largest changes in the deep isotherm depth (top panel) occurred in regions of large cross-isobath flow (advection term in the middle panel). For reference, the bottom panel shows the bottom topography at this latitude.

3.6. Conclusion

The above discussion has highlighted a number of points regarding the results of the minimization:

1. The dominant term in the heat equation is the residual. Evidently, the solution is controlled by the continuity equation.

2. The surface flux fields have been reduced to unrealistic values.

3. There is no real evidence that a minimum has been achieved.

There are several possibilities at this stage:

First, we could accept the solution as a valid minimum of $\mathcal{J}$. Based on the implausible surface flux fields and the heat equation balance, a new parameterization of the mixed-layer is necessary. Changes to the heat, salt, or momentum fluxes in the upper ocean are all candidates for improvement.

Another possibility is that the state may be trapped in a local minimum because of the nonlinearity in the ocean model. Hence, the unrealistic surface fluxes and heat equation balances are a consequence of the particular initial guess for the minimization. Even if the state is not trapped at a local extremum, it may be caught in a circuitous path on its way to an extremum. Unfortunately, without some global view of the penalty function in state space, it is impossible to determine if this is the case.

Lastly, it may be that the condition number of the cost function Hessian is so large that the state is gradually moving towards the global minimum by edging down a very narrow multi-dimensional valley. The preconditioning may have been inadequate. A simplified analysis (see Appendix B.2.7), which assumed that the domain was a constant depth beta-plane, suggested that the condition number may

have been as large as 10^9. Given the importance of nonlinear term balances in the model, more precise condition number estimates were not attempted.

4. CONCLUSIONS

4.1. Discussion

The planetary geostrophic equations, which are derived by neglecting horizontal inertia in the more familiar primitive equations, have provided the basis for two studies of the general circulation of the North Pacific. In both cases, an estimate for the circulation was sought which approximately satisfied the model equations, and which was in agreement with observations. Because the problem of estimating the general circulation from both model and observational constraints is overdetermined, inverse methods were used.

In the first set of calculations (Chapter 2), a *linearized* planetary geostrophic system was used to study the conditioning of the generalized inverse, and to explore a number of solution methods for solving this system. Two solution methods based on the representer expansion were compared with two descent methods, and the most efficient method proved to be a conjugate gradient solver for the representer coefficients. Of the two descent methods, the one which preconditioned with the inverse of the model operators was far superior to the method which preconditioned with a re-scaling of the variables.

Among the solution procedures which were compared in Chapter 2, only the direct solver based on the representer expansion (REP) provided information concerning the posterior errors. For two relatively small calculations, involving 662 and 1153 observations, respectively, it was shown that hydrographic measurements are of little utility for improving estimates of the model's boundary conditions. For example, less than one percent of the surface Ekman pumping boundary condition

variance was explained in the inversions. In contrast, the inverse explained roughly 50% of the variance in the isotherm depth measurements. An orthogonal decomposition of the representer matrix showed that the observing array was capable of explaining significant variance only for basin-scale phenomena. Note that these statements are facts regarding the structure of the inverse problem (as defined by the model, observational array, and prior error covariances); they are not a consequence of the solution method or the particular data values.

In Chapter 3, an attempt was made to assimilate data into a more realistic, nonlinear model of the North Pacific. A descent method was used to directly minimize the penalty function that defined the inverse problem; this approach was taken because of its applicability to linear and nonlinear problems alike.

Because of the slow convergence rate of the descent algorithm, it was impossible to conclude that the global minimum of the cost function was obtained. The slow convergence rate may have been a result of the poorly conditioned nature of the problem, or it may have been a consequence of the nonconvexity of the penalty function (caused by the model's nonlinearities). The huge dimension of the state space makes it difficult to obtain a global view of the penalty function; without this, one cannot determine whether poor conditioning or nonlinearity was the source of the difficulty.

A study of the residuals in the results of the descent calculation revealed a decoupling of the mixed-layer flow from the deeper flows. Whether this was a consequence of the mixed-layer parameterization, or an artifact of the descent procedure (caused, for instance, by the state being trapped in a local minimum) cannot be determined. The final state achieved by descent was unrealistic: the mixed-layer decoupling resulted in air-sea fluxes which were reduced by roughly a factor of two over most of the domain.

4.2. Comparisons with Other Work

The climatology estimated in Section 2.6 of Chapter 2, the "North Pacific Inverse," has already been compared with an objective analysis of the same data. The isotherm depths are visually quite similar; however, the "North Pacific Inverse" estimate is much more consistent with the dynamical model than the plain (dynamically un-informed) objective analysis. Comparison with another climatology, e.g., the Levitus atlas (1982), should yield similar results. The inverse solution is dynamically consistent with regard to the linear model that formed the basis for the calculation; relative to the complete nonlinear dynamics, the "North Pacific Inverse" is likely to be as inconsistent as any other climatology.

Results similar to those in Chapter 3 were obtained by Tziperman et al. (1992b and 1992c) in their attempts to estimate the North Atlantic circulation. The time-stepping procedure (and the forward-backward temporal integrations) used in their papers (and as extended in Marotzke and Wunsch, 1992) can be viewed as an approximation to the dynamical preconditioner used in method J-CG2 in Chapter 2. If it had been feasible to extend their time-stepping procedure sufficiently to reach a steady-state solution with the linearized form of their forward-backward solvers, they would have achieved perfect dynamical preconditioning in the spirit of Chapter 2. However, the solution method used by Marotzke and Wunsch (1992) is computationally intensive: counting each model substitution as one unit of work (as in Chapter 2), their descent procedure executed roughly $N/2$ model substitutions in order to reach a solution, where $N \approx 85,000$ was the total number of temperature and salinity state variables. Even for this relatively low-dimensional steady problem, there is room for improvement in the solution method.

Marotzke and Wunsch (1992) have questioned the need for further time-independent general circulation inverse studies. Their conclusion is based on the observation that their inverse estimate for the time-averaged circulation of the North Atlantic tends towards winter conditions. In other words, in order to produce the necessary water masses, the inverse estimate is biased towards the extreme conditions under which the water masses are produced. Their experience suggests that a model for the general circulation must eventually include the seasonal cycle. More fundamentally, the real issue concerns how well both spatial and temporal Reynolds averages can be parameterized. Compared with the studies based on the GFDL model (e.g., Tziperman et al., 1992b and c; and Marotzke and Wunsch, 1992), we have much less experience with the layer model used in Chapter 3; nonetheless, an analysis of the residuals indicated that the parameterizations of the heat, salt, and momentum fluxes in the mixed-layer were inadequate or incompatible in the model used here.

One of the original motivations for assimilating data into a general circulation model was to solve the "spin-up" or initialization problem for general circulation models (e.g., Tziperman et al., 1992a). The desire was to obtain a steady-state solution of the general circulation model for initializing prognostic model runs, and for model testing (by comparing the steady-state solution with observations). At present, general circulation models are time-stepped for hundreds, and sometimes thousands of years to spin-up the circulation.

From the discussion of solution methods in Chapter 2, it is evident that a solution to the initialization problem should be regarded as a prerequisite to solving the data assimilation problem, and not vice versa. The inverse, or data assimilation problem requires the solution of two systems, the "forward" model and the "adjoint" model, which together form the Euler-Lagrange equations for the extremum of the

penalty function. Thus, one must solve two sets of equations, each of which is of complexity comparable to the spin-up problem. The linear algebraic equivalent of the problem under discussion would be to solve the matrix system

$$Ax = b \tag{4.1}$$

by minimizing the penalty function

$$\mathcal{J}(x) = (Ax - b)^T(Ax - b) + (x - \overline{x})^T W(x - \overline{x}), \tag{4.2}$$

where $\overline{x}$ is an estimate of the solution to equation 4.1, and W is a positive-definite symmetric weighting matrix. The minimization of this penalty function is equivalent to the solution of the Euler-Lagrange system for the extremum of $\mathcal{J}$:

$$\begin{aligned} Ax &= b + \lambda \\ A^T\lambda &= -W(x - \overline{x}). \end{aligned} \tag{4.3}$$

Thus, using the inverse model to solve the spin-up problem is formally twice as difficult as solving the spin-up problem alone. If the weighting matrix W is zero, i.e., if one has no estimate of the solution, the inverse formulation squares the condition number of the original system. This is a well-known problem associated with solving the so-called "normal equations" for linear least-squares problems (Golub and VanLoan, 1989).

4.3. Suggestions for Further Research

The working plan for the synthesis phase of WOCE (the World Ocean Circulation Experiment), as presented by Church et al. (1995), is a measured approach to a very difficult problem, namely, the design and testing of models for predicting climate change. As the report points out (p. 17), there is no clear plan regarding

how to proceed once the data collection phase of WOCE has ended. Tentatively, the plan is to produce a number of analysis products which differ in the degree of post-collection processing: from quality controlled data collections, to large data "syntheses," in which inverse methods are used to produce high level data products.

Given the WOCE goal of constructing a model for predicting climate change, it is understood that a necessary first step is to construct a model which reproduces the present state of the ocean. Therefore, it is first necessary to define what is meant by the "present state of the ocean." In other words, what is it we wish to explain with the model? For the purpose of this discussion: we wish to explain the spatial variance of the temporally averaged hydrographic fields.

This problem definition is not particularly exhaustive or original, but it provides an explicit starting point for conceptualizing the synthesis phase of WOCE. Also, it is clear that the problem definition is still incomplete: the ocean's hydrographic fields contain spatial variance which is observable on all length scales, but on which length scales do we wish to explain variance? Furthermore, the estimates of the temporal mean are necessarily made from a finite number of measurements which themselves contain error: how much of the spatial variance is "signal" and how much is "noise"? The work described in this thesis has been one step towards the goal of doing a WOCE-like synthesis. Thus, the suggestions for further research are couched in this framework.

It is recommended that the synthesis phase of WOCE proceed by developing the generalized inverse of a global ocean model. The generalized inverse is defined so that its solution consists of a set of fields which are constrained by both the model and the observations, in a least-squares sense. The tasks of "data synthesis" and "model testing" can both be carried out in the framework provided by statistical

estimation and inverse theory: the solution of the generalized inverse is the data synthesis, while an analysis of the residuals affords a test of the model.

For this discussion, let us focus on determining the present state of the ocean as defined by the annually averaged hydrographic fields. To "test a model" then means to explain the spatial variance of the hydrographic fields with a model, i.e., to fit the observations with a model. Obviously, neither too tight nor too loose of a fit is warranted since any observation measures the annually averaged part of the circulation plus a temporally variable part. The temporally variable part can be estimated from the observations themselves by empirically estimating various sample statistics such as the space-time mean, variance, and correlation scale (e.g., Levitus, 1982; Wyrtki and Ulrich, 1982). An alternate approach would use high-resolution time-dependent models to estimate these statistics; however, the statistics would be only as good as the model (and its forcing functions). This approach would be feasible if the time-scales of the forcing and state variability were short enough to be measured directly so that the time-dependent model could be verified.

Having decided on how close of a fit is warranted, one must choose the model's control variables. In other words, it is necessary to specify what parameters are appropriate to alter in order to produce a fit. This topic deserves serious consideration. The natural choice for the control parameters are the model's inhomogeneities, e.g., the air-sea fluxes. If these are chosen as the control variables, then it is possible to estimate the errors in these through intensive observation, or through an intercomparison of climatologies (e.g., Böning et al., 1991). If the control parameters are intended to represent subgrid-scale phenomena, it is much more difficult to estimate their uncertainty since the fluxes depend on both the underlying phenomena and the model resolution; it seems that the best one can do is to estimate a magnitude and a length scale for the unresolved phenomena by

appealing to data compilations such as Dickson (1983). Finally, it may be that one wishes to regard variables such as the turbulent diffusivity as control parameters, which makes the inverse problem nonlinear, even if the model dynamics are linear (e.g., Smedstad and O'Brien, 1991).

When there are no good estimates for the uncertainty of a control parameter, it seems wise to proceed in two directions simultaneously. First, the model can be linearized and a representer analysis performed. Array analyses like those presented in Chapter 2 are helpful in prioritizing future modeling and observational efforts. In the examples of Chapter 2, it was shown that the eastern boundary conditions and vertical diffusivity must be known much more accurately than at present in order for the inverse calculation to improve the surface flux estimates significantly. This conclusion is based on a relatively simple model which is linearized about a state of no horizontal motion.

The second direction for research consists of using cross-validation methods to improve the parameterizations of the prior errors. The basic idea of these methods is to minimize the fitting error of the inverse solution as a function of the error parameterizations. The error of the inverse solution is estimated using bootstrap methods: data are withheld from the inverse calculation, and then compared with the solution (Craven and Wahba, 1979; Efron and Gong, 1983).

If these methods are to be applied to the WOCE goal of creating a "global snapshot," representative of the oceanic state as averaged over the last decade, it will require the construction of a global model for the steady circulation. Such models already exist; however, the present means for obtaining their solution involves time-stepping the model to steady state. As the thermodynamic equilibration time for the global ocean is on the order of 1000 years, present solution methods are inadequate for a realistic calculation of the kind envisioned here, which would require 10's, if not

100's or 1000's of model solutions. Thus, the next logical step is the development of efficient solvers for the steady-state of a general circulation model. Nonlinearity may prevent the model from even having a steady solution, in which case a solver for the quasi-steady-state would itself be a generalized inverse. Another possibility is that nonlinear instabilities may make the steady solution unstable.

Such a solver, if it is developed, might use techniques similar to those used for implicitly time-stepping general circulation models (Oberhuber, 1993). Other promising approaches include extending the time-step acceleration procedure in Bryan and Lewis (1979), or generalizing the preconditioned conjugate gradient solver in Dukowicz et al. (1993). Finding the steady or quasi-steady circulation is difficult because the governing equations form a three-dimensional nonlinear elliptic system. The nonlinear part of the equation is hyperbolic, and the elliptic part is essentially a singular perturbation added to the hyperbolic system. It is irregular bottom topography which makes the equations non-separable. The search for efficient solution methods for these kinds of partial differential equations is an active area of research within the applied mathematics community: multigrid methods appear to be the most promising approach (e.g., Adams et al., 1992) See Vuik et al. (1995) for a recent comparison of state-of-the-art multigrid and iterative methods.

Once a solver for the steady, or quasi-steady, circulation is in place, the development of a solver for the discrete adjoint system is relatively straightforward, in principle. Then, any of the methods in Chapter 2 would be applicable, as follows.

Essentially, we can regard the nonlinear planetary geostrophic model as a system of the form

$$\mathbf{N}(u) = f, \tag{4.4}$$

where $\mathbf{N}$ is a nonlinear vector-valued function of the state vector u, and f represents all of the model's inhomogeneities. Let u be an $N \times 1$ vector, and assume that the observations, which we wish to fit, are given as the $M \times 1$ vector d:

$$d = H^T u. \tag{4.5}$$

The Euler-Lagrange equations for the generalized inverse of the system 4.4-4.5 are:

$$\mathbf{N}(u) = f + C\lambda$$

$$\left(\frac{\partial \mathbf{N}(u)}{\partial u}\right)^T \lambda = -HW(H^T u - d), \tag{4.6}$$

where C is the prior covariance of the uncertainty in equation 4.4, and W is the inverse of the covariance of the uncertainty in equation 4.5. As in Chapter 2, standard matrix notation is used. H is $N \times M$, C is $N \times N$, and W is $M \times M$.

The recommendation made above, that solvers for the tangent-linearization of the planetary geostrophic model and its adjoint be developed, amounts to finding the operator

$$\left(\frac{\partial \mathbf{N}(u)}{\partial u}\right)^{-1} \tag{4.7}$$

and its transpose. If efficient algorithms for these inverses can be found, then the following linearization of 4.6 may be implemented:

$$\left(\frac{\partial \mathbf{N}(u^{n-1})}{\partial u}\right) u^n = f - \mathbf{N}(u^{n-1}) + \left(\frac{\partial \mathbf{N}(u^{n-1})}{\partial u}\right) u^{n-1} + C\lambda^n$$

$$\left(\frac{\partial \mathbf{N}(u^{n-1})}{\partial u}\right)^T \lambda^n = -HW(H^T u^n - d). \tag{4.8}$$

Provided that the tangent-linear model is well-posed, the above system 4.8 is amenable to solution via the representer expansion. Additionally, with solvers for

the tangent-linear system and it adjoint, one would have ideal preconditioners for a direct minimization method analogous to the J-CG2 solver of Chapter 2.

Several studies have found that the sequence of iterates produced by tangent-linearizations such as 4.8 may not converge (Bennett and Thorburn, 1992; Evensen, 1992; Hagelberg, 1992). Essentially, the problem can be traced to terms in the tangent-linear model equations which act as sources of energy for u^n, driven by u^{n-1}. These terms arise because conservation properties of the nonlinear equation $\mathbf{N}(u)$ are not inherited by its linearization. Bennett and Thorburn (1992) and Hagelberg (1992) have shown that linear *approximations* (rather than *linearizations*) of $\mathbf{N}(u)$ can lead to convergent approximations of the nonlinear Euler-Lagrange system 4.6. Another approach is the "creeping algorithm" (Parker, 1994). Rather than taking u^n as the solution of 4.8, one takes

$$u^n = \alpha u^* + (1-\alpha)u^{n-1}, \tag{4.9}$$

where u^* solves 4.8. For $\alpha = 1$, the algorithm is unchanged, but for $0 < \alpha < 1$, one reduces the "distance" between consecutive linearizations. It may be shown that, for α sufficiently small (but greater than zero), the creeping algorithm is guaranteed to converge (provided the tangent-linear system is well-posed).

For the specific production of WOCE Level 3c data products, which are intended to be dynamically consistent syntheses of WOCE data (Church et al., 1995), a provisional set of data and model weights should be defined. So long as the covariances (which are inverses of the corresponding weights) are smooth enough, where "enough" is in accordance with the considerations in Bennett and McIntosh (1982), their precise forms should be immaterial. Review papers on the air-sea exchanges (e.g., Schmitt, 1994; Weare, 1989; Isemer and Hasse, 1991) can provide some guidance for specifying the covariances of the air-sea fluxes. Particular attention should

be paid to areas of intense air-sea exchange because of their importance in setting extreme water mass properties. The observational errors should be straightforward to estimate, except for large areas of the Southern Ocean which are poorly sampled.

The model errors are much more difficult to estimate. Nonetheless, it is the values for these errors which define what it means to "test a model." Some quantities, such as the eddy stresses, may be estimated from compilations of current meter data. Similarly, tracer release experiments (Ledwell et al., 1993) or direct microstructure measurements (Moum, 1992) may someday be distributed widely enough for estimating turbulent diffusivities and their uncertainties. Determining the uncertainty of surface boundary layer parameterizations is more difficult; an analysis of long-term weather station data would be helpful, as would be short-term, time-dependent, data assimilation experiments.

As a practical step to accelerate the development of solvers for the generalized inverse of global ocean models, *it is recommended that the data synthesis and modeling efforts of WOCE be tightly coordinated.* So long as least-squares formulations continue to dominate inverse studies of the general circulation, the computational adjoints of the forward models will need to be developed. Because of the similarity of the forward and adjoint codes, it is helpful if solvers for both systems can be developed simultaneously. Efficient solvers for the quasi-steady circulation are needed especially, in order to carry out the data synthesis for the general circulation.

Lastly, *it is recommended that the surface fluxes be recomputed using the most up-to-date data sources and bulk formulae.* Improving the air-sea fluxes is already a goal of WOCE, and I can only re-iterate the importance of accurate air-sea fluxes for understanding the general circulation. The calculations reported in Chapter 2 serve to emphasize that hydrographic observations alone are insufficient to improve our estimates of the air-sea flux fields significantly. Hall and Bryden (1982), for

example, have shown that a complete zonal section of hydrographic data effectively constrains the net meridional heat transport (which is related to the areal average of the heat flux, assuming steady state); however, such sections offer little information about the heat flux at a particular location. Revision of the surface flux estimates should be considered *the* top priority.

5. BIBLIOGRAPHY

Adams, J. C., Garcia, R., Gross, B., Hack, J., Haidvogel, D., and Pizzo, V. (1992). Applications of multigrid software in the atmospheric sciences. *Mon. Wea. Rev.*, 120:1447–1458.

Anderson, D. and Killworth, P. (1977). Spin-up of a stratified ocean, with topography. *Deep Sea Res.*, 22:583–596.

Anderson, D. and Willebrand, J., editors (1989). *Oceanic Circulation Models: Combining Data and Dynamics.* Kluwer Academic Publications, Amsterdam.

Anderson, E., Bai, Z., Bischof, C., Demmel, J., J.R., J. D., Croz, J. D., Greenbaum, A., Hammarling, S., McKenney, A., Ostrouchov, S., and Sorensen, D. (1992). *LAPACK User's Guide.* SIAM Publications, Philadelphia.

Arakawa, A. (1988). Finite-difference methods in climate modelling. In *Physically-Based Modelling and Simulation of Climate and Climatic Change, Part 1*, pages 79–168. Kluwer Academic Publications, Boston.

Arakawa, A. and Lamb, V. (1977). Computational design of the basic dynamical processes of the ucla general circulation model. In *Methods in Computational Physics*, volume 17, pages 174–264. Academic Press, New York.

Beckman, A. and Haidvogel, D. (1993). Numerical simulation of flow around a tall isolated seamount. Part I: problem formulation and model accuracy. *J. Phys. Oceanogr.*, 23:1736–1753.

Bengtsson, L., Ghil, M., and Kallen, E. (1981). *Dynamic Meteorology: Data Assimilation Methods.* Springer-Verlag, New York.

Bennett, A. (1990). Inverse methods for assessing ship-of-opportunity networks and estimating circulation and winds from tropical expendable bathythermograph data. *J. Geophys. Res.*, 95:16111–16148.

Bennett, A. (1992). *Inverse Methods in Physical Oceanography.* Cambridge University Press, New York, first edition.

Bennett, A. and Budgell, W. (1987). Ocean data assimilation and the Kalman filter: spatial regularity. *J. Phys. Oceanogr.*, 17:1583–1601.

Bennett, A. and McIntosh, P. (1982). Open ocean modeling as an inverse problem: tidal theory. *J. Phys. Oceanogr.*, 12:1004–1018.

Bennett, A. and Thorburn, M. (1992). The generalized inverse of a nonlinear quasi-geostrophic ocean circulation model. *J. Phys. Oceanogr.*, 22:213–230.

Bleck, R. (1973). Numerical forecasting experiments based on conservation of potential vorticity on isentropic surfaces. *J. Appl. Meteor.*, 12:737–752.

Bleck, R. (1978). Finite-difference equations in generalized vertical coordinates Part I: total energy conservation. *Beitrage zur Physik der Atmosphere*, 51:360–372.

Bleck, R., Hanson, H., Hu, D., and Kraus, E. (1989). Mixed layer-thermocline interaction in a three-dimensional isopycnic coordinate model. *J. Phys. Oceanogr.*, 19:1417–1439.

Bogden, P. (1991). *The North Atlantic circulation: combining simplified dynamics with hydrographic data.* PhD thesis, U.C. San Diego, Scripps Inst. of Oceanography, La Jolla.

Boning, C.W., R. D. and Isemer, H.-J. (1991). Monthly mean wind stress and Sverdrup transports in the North Atlantic: a comparison of the Hellerman-Rosenstein and Isemer-Hasse climatologies. *J. Phys. Oceanogr.*, 21:221–235.

Bretherton, F., Davis, R., and Fandry, C. (1976). A technique for objective analysis and design of oceanographic experiments applied to MODE-73. *Deep Sea Res.*, 23:559–582.

Bryan, K. and Lewis, L. (1979). A water mass model of the world ocean. *J. Geophys. Res.*, 84:2503–2517.

Bryden, H. (1980). Geostrophic vorticity balance in midocean. *J. Geophys. Res.*, 85:2825–2828.

Bunker, A. (1976). Computations of surface energy flux and annual air–sea interaction cycles of the North Atlantic ocean. *Mon. Wea. Rev.*, 104:1122–1140.

Church, J., Owens, W., and Gould, W. (1995). A strategy for the synthesis phase of the World Ocean Circulation Experiment – WOCE. Planning memo for the March, 1995 meeting of the WCRP JSC.

Colin deVerdiere, A. (1988). Buoyancy driven planetary flows. *J. Mar. Res.*, 46:215–265.

Colin deVerdiere, A. (1989). On the interaction of wind and buoyancy driven flows. *J. Mar. Res.*, 47:595–633.

Cox, M. (1984). A primitive equation, 3-dimensional model of the ocean. GFDL Ocean Group Technical Report 1, NOAA Geophys. Fluid Dyn. Lab., Princeton University.

Craven, P. and Wahba, G. (1979). Smoothing noisy data with spline functions: estimating the correct degree of smoothing by the method of generalized cross-validation. *Numer. Math.*, 31:377–403.

Daley, R. (1991). *Atmospheric Data Analysis.* Cambridge University Press, New York.

Davis, R. (1978). On estimating velocity from hydrographic data. *J. Geophys. Res.*, 83:5507–5509.

Desaubies, Y., Tarantola, A., and Zinn-Justin, J., editors (1990). *Oceanographic and Geophysical Tomography.* North-Holland, New York.

DeSzoeke, R. and Bennett, A. (1993). Microstructure fluxes across density surfaces. *J. Phys. Oceanogr.*, 23:2254–2264.

Dickson, R. (1983). Global summaries and intercomparisons: flow statistics from long-term current meter moorings. In *Eddies in Marine Science*, pages 278–329. Springer-Verlag, New York.

Dorman, C. and Bourke, R. (1979). Precipitation over the Pacific Ocean, 30°S to 60°N. *Mon. Wea. Rev.*, 107:896–910.

Duane, S., Kennedy, A., Pendleton, B., and Roweth, D. (1987). Hybrid Monte Carlo. *Phys. Let. B*, 195:216–222.

Dukowicz, J., Smith, R., and Malone, R. (1993). A reformulation and implementation of the Bryan-Cox-Semtner ocean model on the Connection Machine. *J. Atm. and Oc. Tech.*, 10(2):195–208.

Efron, B. and Gong, G. (1983). A leisurely look at the bootstrap, the jackknife and cross-validation. *Amer. Stat.*, 37:36–48.

Egbert, G., Bennett, A., and Foreman, M. (1994). TOPEX/POSEIDON tides estimated using a global inverse model. *J. Geophys. Res.*, 99:24821–24852.

Emery, W. and Dewar, J. (1982). Mean temperature–salinity, salinity–depth and temperature–depth curves for the North Atlantic and North Pacific. *Prog. Oceanog.*, 11:219–305.

ETOPO5 (1988). Orography data set: global 5' by 5' resolution. NCAR Data Services, Boulder.

Ferrenberg, A., Landau, D., and Binder, K. (1991). Statistical and systematic errors in Monte Carlo sampling. *J. Stat. Phys.*, 63:867–882.

Flierl, G. and McWilliams, J. (1977). On the sampling requirements for measuring moments of eddy variability. *J. Mar. Res.*, 35(4):797–820.

Freeland, H., Rhines, P., and Rossby, T. (1975). Statistical observations of the trajectories of neutrally buoyant floats in the North Atlantic. *J. Mar. Res.*, 33(383-404).

Fujio, S. and Imasoto, N. (1991). Diagnostic calculation for circulation and water mass movement in the deep Pacific. *J. Geophys. Res.*, 96:759–774.

Fukumori, I. and Wunsch, C. (1991). Efficient representation of the North Atlantic hydrographic and chemical distributions. *Prog. Oceanog.*, 27:111–195.

Gerdes, R. (1993a). A primitive equation ocean circulation model using a generalized vertical coordinate transformation, 1, description and testing of the model. *J. Geophys. Res.*, 98:14683–14702.

Ghil, M. (1989). Meteorological data assimilation for oceanographers. Part I: Description and theoretical framework. *Dyn. Atm. and Oceans*, 13:171–218.

Ghil, M., Cohn, S., Tavantzis, J., Bube, K., and Isaacson, E. (1981). Application of estimation theory to numerical weather prediction. In *Dynamic Meteorology: Data Assimilation Methods I*, pages 139–224. Springer-Verlag, New York.

Ghil, M. and Malanotte-Rizzoli, P. (1991). Data assimilation in meteorology and oceanography. *Advances in Geophysics*, 33:141–266.

Gill, P., Murray, W., and Wright, M. (1981). *Practical Optimization.* Academic Press, New York.

Golub, G. and Van Loan, C. (1989). *Matrix Computations.* Johns Hopkins University Press, Baltimore, second edition.

Gregg, M. (1984). Entropy generation in the ocean by small-scale mixing. *J. Phys. Oceanogr.*, 14:688–711.

Gregg, M. (1987). Diapycnal mixing in the thermocline: A review. *J. Geophys. Res.*, 92:5249–5286.

Hagelberg, C. (1992). *Existence of a Solution to a Variational Data Assimilation Method in Two-dimensional Hydrodynamics.* PhD thesis, Department of Mathematics, Oregon State University, Corvallis.

Haney, R. (1991). On the pressure gradient force over steep topography in sigma coordinate ocean models. *J. Phys. Oceanogr.*, 21:610–619.

Hasselmann, K. (1982). An ocean circulation model for climate variability studies. *Prog. Oceanog.*, 11:69–92.

Hellerman, S. and Rosenstein, M. (1983). Normal monthly wind stress over the world ocean with error estimates. *J. Phys. Oceanogr.*, 13:1093–1104.

Iselin, C. (1939). The influence of vertical and lateral turbulence on the characteristics of the waters at mid-depths. *Transactions of the American Geophysical Union*, 20:414–417.

Isemer, H. and Hasse, L. (1991). The Scientific Beaufort Equivalent Scale: effects on wind statistics and climatological air–sea flux estimates in the North Atlantic Ocean. *J. Climate*, 4:819–836.

Krauss, W. (1993). Ekman drift in homogeneous water. *J. Geophys. Res.*, 98(C11):20187–20209.

Lanczos, C. (1961). *Linear Differential Operators.* Van Nostrand, New York.

LeDimet, F.-X. and Talagrand, O. (1986). Variational algorithms for analysis and assimilation of meteorological observations: theoretical aspects. *Tellus*, 38A:97–110.

Ledwell, J., Watson, A., and Law, C. (1993). Evidence for slow mixing across the pycnocline from an open-ocean tracer-release experiment. *Nature*, 364:701–703.

Levitus, S. (1982). Climatological atlas of the world ocean. NOAA Prof. Pap. 13, U.S. Govt. Print. Office, Washington, D.C.

Lighthill, M. (1958). *Introduction to Fourier Analysis and Generalized Functions.* Cambridge University Press, New York.

Luenberger, D. G. (1973). *Introduction to Linear and Nonlinear Programming.* Addison-Wesley Publishing Co., Inc., Menlo Park.

Luyten, J., Pedlosky, J., and Stommel, H. (1983). The ventilated thermocline. *J. Phys. Oceanogr.*, 13:292–309.

Maier-Reimer, E. and Hasselmann, K. (1987). Transport and storage of CO_2 in the ocean. An inorganic ocean-circulation carbon cycle model. *J. Climate*, 2:63–90.

Marotzke, J. (1992). The role of integration time in determining a steady state through data assimilation. *J. Phys. Oceanogr.*, 22(12):1556–1566.

Marotzke, J. and Wunsch, C. (1992). Finding the steady state of a general circulation model through data assimilation: application to the North Atlantic ocean. *J. Geophys. Res.*, 98:20149–20168.

McDougall, T. and Jackett, D. (1988). On the helical nature of neutral trajectories in the ocean. *Prog. Oceanog.*, 20:153–183.

McIntosh, P. (1990). Oceanographic data interpolation: objective analysis and splines. *J. Geophys. Res.*, 95:13529–13541.

Mesinger, F. (1982). On the convergence and error problems of the calculation of the pressure gradient force in sigma coordinate models. *Geophys. Astrophys. Fluid Dynamics*, 19:105–117.

Metropolis, N., Rosenbluth, M., Rosenbluth, A., Teller, E., and Teller, J. (1953). Equation of state calculations by fast computing machines. *J. Chem. Phys.*, 21:1087–1092.

Miller, R. and Ghil, M. (1990). Data assimilation in strongly nonlinear current systems. *Proc. Int. Symp. Assimil. Obs. Meteorl. Oceanogr.*, pages 93–98.

Monin, A. and Yaglom, A. (1965). *Statistical Fluid Mechanics*, volume 1. MIT Press, Cambridge, MA.

Moum, J., Herbert, D., Paulson, C., and Caldwell, D. (1992). Turbulence and internal waves at the equator. Part I: Statistics from towed thermistors and a microstructure profiler. *J. Phys. Oceanogr.*, 22:1330–1345.

Munk, W. (1950). On the wind-driven ocean circulation. *J. Meteorol.*, 7:79–93.

Munk, W. (1966). Abyssal recipes. *Deep Sea Res.*, 13:707–730.

National Research Council (1991). *Four-Dimensional Model Assimilation of Data, a strategy for the Earth system sciences.* National Academy Press, Washington, D.C.

National Research Council (1993). *Statistics and Physical Oceanograohy.* National Academy Press, Washington, D.C.

Navon, I. and Legler, D. (1987). Conjugate-gradient methods for large-scale minimization in meteorology. *Mon. Wea. Rev.*, 115:1479–1502.

Navon, I., Zou, X., Berger, M., Phua, P., Schlick, T., and LeDimet, F. (1992b). Testing for reliability and robustness of optimization codes for large scale optimization problems. In et al., K. P., editor, *Optimization Techniques and Applications, Vol 1*, pages 445–480. World Scientific Publishing Co., New York.

Nazareth, L. (1979). A relationship between the BFGS and conjugate gradient algorithms and its implications for new algorithms. *SIAM J. Numer. Anal.*, 16(4):794–800.

Needler, G. and Heath, R. (1975). Diffusion coefficients calculated from the mediterranean salinity anomaly in the North Atlantic ocean. *J. Phys. Oceanogr.*, 5:173–182.

Oberhuber, J. (1988). An atlas based on the "COADS" data set: the budgets of heat, buoyancy and turbulent kinetic energy at the surface of the global ocean. Technical Report 15, Max-Plank-Institute for Meteorology.

Oberhuber, J. (1993). Simulation of the Atlantic circulation with a coupled sea ice-mixed layer-isopycnal general circulation model. Part I: Model description. *J. Phys. Oceanogr.*, 23:808–829.

Olbers, D.J., M. W. and Willebrand, J. (1985). The inference of North Atlantic circulation patterns from climatological hydrographic data. *Rev. Geophys. and Space Phys.*, 23:313–356.

Parker, R. L. (1994). *Geophysical Inverse Theory.* Princeton University Press, Princeton.

Pedlosky, J. (1979). *Geophysical Fluid Dynamics.* Springer-Verlag, New York.

Pedlosky, J. (1992). The baroclinic structure of the abyssal circulation. *J. Phys. Oceanogr.*, 22:652–659.

Phillips, N. (1957). A coordinate system having some special advantages for numerical forcasting. *J. Meteor.*, 14:184–185.

Pickard, G. and Emery, W. (1982). *Descriptive Physical Oceanography.* Pergammon Press, Elmsford, fourth edition.

Press, W., Flannery, B., Teukolsky, S., and Vetterling, W. (1989). *Numerical Recipes. Fortran version.* Cambridge University Press, New York.

Reid, J. and Mantyla, A. (1988). *Deep Station Data.* NCAR Data Services, National Center for Atmospheric Research, Boulder.

Roemmich, D. (1983). Optimal estimation of hydrographic station data and derived fields. *J. Phys. Oceanogr.*, 13:1544–1549.

Roemmich, D. and McCallister, T. (1989). Large scale circulation of the North Pacific ocean. *Prog. Oceanog.*, 22:171–204.

Sarkisyan, A. (1977). The diagnostic calculation of a large–scale oceanic circulation. In E.D. Goldberg, I.N. McCave, J. O. and Steele, J., editors, *The Sea*, volume 6, pages 363–458. John Wiley, New York.

Sarmiento, J. and Bryan, K. (1982). An ocean transport model for the North Atlantic. *J. Geophys. Res.*, 87:394–408.

Schmitt, R., Bogden, P., and Dorman, C. (1989). Evaporation minus precipitation and density fluxes for the north atlantic. *J. Phys. Oceanogr.*, 19:1208–1221.

Schmitt, R. W. (1994). The ocean freshwater cycle. Technical report, JSC Ocean Observing System Development Panel, Texas A&M University, College Station.

Semtner, A. (1986). Finite-difference formulation of a world ocean model. In *Advanced Physical Oceanographic Numerical Modelling*, pages 187–202. Reidel, New York.

Shanno, D. (1985). Globally convergent conjugate-gradient algorithms. *Math. Program.*, 33:61–67.

Smedstad, O. and O'Brien, J. (1991). Variational data assimilation and parameter estimation in an equatorial Pacific Ocean model. *Prog. Oceanog.*, 26:179–241.

Smolarkiewicz, P. (1983). A simple positive definite advection scheme with small implicit diffusion. *Mon. Wea. Rev.*, 111:479–486.

Stommel, H. and Schott, F. (1977). The beta spiral and the determination of the absolute velocity field from hydrographic station data. *Deep Sea Res.*, 24:325–329.

Sverdrup, H., Johnson, M., and Fleming, R. (1942). *The Oceans: Their Physics, Chemistry and General Biology.* Prentice-Hall, Englewood Cliffs, N.J.

Talagrand, O. and Courtier, P. (1987). Variational assimilation of meteorological observations with the adjoint vorticity equation I, theory. *Quart. J. Royal Met. Soc.*, 113:1311–1328.

Talley, L. (1984). Meridional heat transport in the Pacific ocean. *J. Phys. Oceanogr.*, 14:231–24.

Tarantola, A. (1987). *Inverse Problem Theory.* Elsevier, Amsterdam.

Thacker, W. (1989). The role of the Hessian matrix in fitting models to measurements. *J. Geophys. Res.*, 94:6177–6196.

Thepaut, J.-N. and Courtier, P. (1991). Four-dimensional variational data assimilation using the adjoint of a multilevel primitive-equation model. *Quart. J. Royal Met. Soc.*, 117:1225–1254.

Thiebaux, H. and Pedder, M. (1987). *Spatial Objective Analysis: with applications in atmospheric science.* Academic Press, San Diego.

Tziperman, E. (1988). Calculating the time-mean oceanic general circulation and mixing coefficients from hydrographic data. *J. Phys. Oceanogr.*, 18:519–52.

Tziperman, E. and Thacker, W. (1989). An optimal-control/adjoint-equation approach to studying the oceanic general circulation. *J. Phys. Oceanogr.*, 19:1471–1485.

Tziperman, E., Thacker, W., and Bryan, K. (1992a). Computing the steady state oceanic circulation using an optimization approach. *Dyn. Atm. and Oceans*, 16:379–403.

Tziperman, E., Thacker, W., Long, R., and Hwang, S.-M. (1992b). Oceanic data analysis using a general circulation model. Part I: Simulations. *J. Phys. Oceanogr.*, 22:1434–1457.

Tziperman, E., Thacker, W., Long, R., Hwang, S.-M., and Rintoul, S. (1992c). Oceanic data analysis using a general circulation model. Part II: A North Atlantic model. *J. Phys. Oceanogr.*, 22:1458–1485.

UNESCO (1983). Algorithms for computation of fundamental properties of seawater. Technical Report 44, UNESCO/SCOR/ICES/IAPSO Joint Panel on Oceanographic Tables and Standards.

U.S. WOCE (1989). *U.S. WOCE Implementation Report.* Number 1. U.S. WOCE Office, College Station.

Van Mieghem, J. (1952). Energy conversions in the atmosphere on the scale of the general circulation. *Tellus*, 4:334–351.

Vuik, C., Wesseling, P., and Zeng, S. (1995). Krylov subspace and multigrid methods applied to the incompressible Navier-Stokes equations. In *Seventh Copper Mountain Conference on Multigrid Methods*, pages 1–17. NASA, Hampton, VA.

Wahba, G. (1990). *Spline Models for Observational Data.* SIAM publications, Philadelphia.

Wallace, J., Tibaldi, S., and Simmons, A. (1983). Reduction of systematic forecast errors in the ECMWF model through the introduction of an envelope orography. *Quart. J. Royal Met. Soc.*, 109:683–717.

Warren, B. (1983). Why is no deep water formed in the North Pacific? *J. Mar. Res.*, 41:327–347.

Weare, B. (1989). Uncertainties in estimates of surface heat fluxes derived from marine reports over the tropical and subtropical oceans. *Tellus*, 41A:357–370.

Woodruff, S., Slutz, R., Jenne, R., and Steurer, P. (1987). A comprehensive ocean–atmosphere data set. *Bull. Amer. Met. Soc.*, 68:1239–1250.

Wunsch, C. (1978). The North Atlantic general circulation west of 50°W determined by inverse methods. *Rev. Geophys. and Space Phys.*, 16:583–620.

Wyrtki, K. and Uhrich, L. (1982). On the accuracy of heat storage calculations. *J. Phys. Oceanogr.*, 12:1411–1416.

APPENDICES

APPENDIX A. The Euler-Lagrange System for the Linearized Planetary Geostrophic Model

The equations for the generalized inverse of the linear planetary geostrophic model considered in Chapter 2 are derived in this Appendix. Recall that the state variables consist of the following functions of longitude, latitude, and temperature (λ, ϕ, θ):

1. $\mathbf{u}$ the horizontal (adiabatic) velocity vector (u, v),
2. ω the diabatic "velocity" $D\theta/Dt$,
3. z the isotherm depth,
4. B the Bernoulli function.

Error is admitted in each of the equations defining the linear planetary geostrophic system (equations 2.5 through 2.14). For reference, the symbols used to denote prior covariance functions for each equation are listed in Table 5.1. It is tacitly assumed that the errors are normally distributed and uncorrelated between the equations.

The generalized inverse of the linearized planetary geostrophic system 2.5-2.14 is defined as the set of $\mathbf{u}$, ω, z, and B fields which minimize the quadratic penalty function,

$$\begin{aligned}\mathcal{J}(\mathbf{u}, \omega, z, B) = \quad & \mathcal{J}_{\text{dyn}}(\mathbf{u}, \omega, z, B) + \mathcal{J}_{\text{bc}}(\mathbf{u}, \omega, z, B) \\ & + \mathcal{J}_{\text{data}}(\mathbf{u}, \omega, z, B) + \mathcal{J}_{\text{bc}'}(\mathbf{u}, \omega, z, B). \qquad \text{(A1)}\end{aligned}$$

Each term in the penalty function is expressed in terms of inner products over the domain and its boundaries. Subscripted $\circ$ symbols are used to denote these inner products as follows:

TABLE 5.1. Error Covariances

Symbol	Uncertainty in
C^u	zonal momentum equation
C^v	meridional momentum equation
C^B	hydrostatic balance
C^z	continuity equation
C^{z_B}	bottom isotherm depth
C^{z_T}	top isotherm depth
C^{w_B}	bottom Ekman pumping
C^{w_T}	top Ekman pumping
C^{B_E}	bottom-eastern boundary B
C^{z_E}	eastern boundary z
σ_i^2	z measurement at $\mathbf{x}_i$

$$C \circ_3 \mu = \int_D \int_{\theta_B}^{\theta_T} C(\lambda, \phi, \theta; \xi, \eta, \vartheta) \mu(\xi, \eta, \vartheta) r_o^2 \cos(\eta) d\xi d\eta d\vartheta,$$

$$C \circ_2 \mu = \int_D C(\lambda, \phi; \xi, \eta) \mu(\xi, \eta) r_o^2 \cos(\eta) d\xi d\eta,$$

$$C \circ_{2E} \mu = \int_{\phi_S}^{\phi_N} \int_{\theta_B}^{\theta_T} C(\phi, \theta; \eta, \vartheta) \mu(\eta, \vartheta) r_o d\eta d\vartheta,$$

$$C \circ_{1E} \mu = \int_{\phi_S}^{\phi_N} C(\phi; \eta) \mu(\eta) r_o d\eta. \tag{A2}$$

Each term in the sum defining the penalty function (A1) is quadratic in the model residuals, and weighted with the appropriate weighting function. The weighting functions are denoted W^*, corresponding to the covariances listed in Table 5.1, where the * indicates any of the super-scripts on the C variables. For example, C^u denotes the error covariance in the zonal momentum equation; the weighting function W^u is defined as the functional inverse of C^u by the relation

$$W^u \circ_3 C^u \circ_3 \mu = \mu \tag{A3}$$

for all test functions μ defined on the three-dimensional domain. Appendix 4.3, Section B.1.2, discusses the correspondence between weighting functions and covariances in more detail.

$\mathcal{J}_{\text{dyn}}$ is the penalty caused by the misfit in the interior dynamics:

$$\begin{aligned}
\mathcal{J}_{\text{dyn}} = & \left(-\mathrm{f}v + \frac{1}{r_{\text{o}}\cos\phi}\frac{\partial B}{\partial\lambda}\right) \circ_3 W^u \circ_3 \left(-\mathrm{f}v + \frac{1}{r_{\text{o}}\cos\phi}\frac{\partial B}{\partial\lambda}\right) \\
& + \left(\mathrm{f}u + \frac{1}{r_{\text{o}}}\frac{\partial B}{\partial\phi}\right) \circ_3 W^v \circ_3 \left(\mathrm{f}u + \frac{1}{r_{\text{o}}}\frac{\partial B}{\partial\phi}\right) \\
& + \left(\overline{b}_\theta z - B_\theta\right) \circ_3 W^B \circ_3 \left(\overline{b}_\theta z - B_\theta\right) \\
& + \left\{\frac{1}{r_o\cos\phi}\left[\frac{\partial u\overline{z}_\theta}{\partial\lambda} + \frac{\partial(v\overline{z}_\theta\cos\phi)}{\partial\phi}\right] + (\omega\overline{z}_\theta)_\theta\right\} \\
& \circ_3 W^z \circ_3 \left\{\frac{1}{r_o\cos\phi}\left[\frac{\partial u\overline{z}_\theta}{\partial\lambda} + \frac{\partial(v\overline{z}_\theta\cos\phi)}{\partial\phi}\right] + (\omega\overline{z}_\theta)_\theta\right\} \\
& + \left(\omega\overline{z}_\theta + \left(\frac{K_V}{\overline{z}_\theta^2}z_\theta\right)_\theta\right) \circ_3 W^\omega \circ_3 \left(\omega\overline{z}_\theta + \left(\frac{K_V}{\overline{z}_\theta^2}z_\theta\right)_\theta\right). \qquad \text{(A4)}
\end{aligned}$$

$\mathcal{J}_{\text{bc}}$ is the penalty caused by the misfit in the prescribed boundary conditions:

$$\begin{aligned}
\mathcal{J}_{\text{bc}} = & \ (z - z_B) \circ_2 W^{z_B} \circ_2 (z - z_B) \\
& + (\omega\overline{z}_\theta - w_B) \circ_2 W^{w_B} \circ_2 (\omega\overline{z}_\theta - w_B) \\
& + (z - z_T) \circ_2 W^{z_T} \circ_2 (z - z_T) \\
& + (\omega\overline{z}_\theta - w_T) \circ_2 W^{w_T} \circ_2 (\omega\overline{z}_\theta - w_T) \\
& + (z - z_E) \circ_{2E} W^{z_E} \circ_{2E} (z - z_E) \\
& + (B - B_E) \circ_{1E} W^{B_E} \circ_{1E} (B - B_E). \qquad \text{(A5)}
\end{aligned}$$

$\mathcal{J}_{\text{data}}$ is the penalty caused by the data misfit:

$$\mathcal{J}_{\text{data}} = \sum_{i=1}^{M} w_i \left(\mathcal{L}_i \circ_3 (\mathbf{u}, \omega, z, B) - m_i\right)^2, \qquad \text{(A6)}$$

in which it is tacitly assumed that the data errors are uncorrelated. In general, the measurement functional is the inner product of a vector of functions, $\mathcal{L}_i = (\mathcal{L}_i^u, \mathcal{L}_i^v, \mathcal{L}_i^\omega, \mathcal{L}_i^z, \mathcal{L}_i^B)$, with the state variables, $(\mathbf{u}, \omega, z, B)$. The inner product of the measurement function with the state is written as

$$\begin{aligned}\mathcal{L}_i \circ_3 (\mathbf{u}, \omega, z, B) = \quad & \mathcal{L}_i^u \circ_3 u + \mathcal{L}_i^v \circ_3 v \\ & + \mathcal{L}_i^\omega \circ_3 \omega + \mathcal{L}_i^z \circ_3 z \\ & + \mathcal{L}_i^B \circ_3 B. \end{aligned} \tag{A7}$$

Note that the vector function $\mathcal{L}_i$ is a function of the independent variables (λ, ϕ, θ).

In order to solve the forward equations, there are certain relations between the state variables which must hold on the boundaries. A well-posed forward problem must satisfy these consistency conditions because the boundaries are characteristic surfaces. These relations are hydrostatic balance and the momentum equation normal to the boundary, on the boundary. For the generalized inverse of this system, let $\mathcal{J}_{\mathrm{bc}'}$ be the penalty caused by misfits in the consistency conditions on the boundaries:

$$\begin{aligned}\mathcal{J}_{\mathrm{bc}'} = \quad & \left(\overline{b}_\theta z - B_\theta\right) \circ_{2E} W^{B'} \circ_{2E} \left(\overline{b}_\theta z - B_\theta\right) \\ & + \left(\mathbf{fu} \cdot \mathbf{n} + \frac{\partial B}{\partial s}\right) \circ_{2E} W^{\mu'} \circ_{2E} \left(\mathbf{fu} \cdot \mathbf{n} + \frac{\partial B}{\partial s}\right). \end{aligned} \tag{A8}$$

The vector $\mathbf{n}$ denotes the outer-normal unit vector on the boundary, and s parameterizes the length tangential to the boundary.

The fields which minimize $\mathcal{J}$ are the solution of the following Euler-Lagrange system A9-A15. The model equations, which define the adjoint variables, are:

$$-\mathrm{f}v = -\frac{1}{r_o \cos\phi} \frac{\partial B}{\partial \lambda} + C^u \circ_3 \mu$$

$$\mathrm{f}u = -\frac{1}{r_o}\frac{\partial B}{\partial \phi} + C^v \circ_3 \nu$$

$$\overline{b}_\theta z = B_\theta + C^B \circ_3 \alpha$$

$$\frac{1}{r_o \cos\phi}\left[\frac{\partial u \overline{z}_\theta}{\partial \lambda} + \frac{\partial (v \overline{z}_\theta \cos\phi)}{\partial \phi}\right] = -(\omega \overline{z}_\theta)_\theta + C^z \circ_3 \epsilon$$

$$\omega \overline{z}_\theta = -\left(\frac{K_V}{\overline{z}_\theta^2} z_\theta\right)_\theta + C^\omega \circ_3 \gamma, \tag{A9}$$

with boundary conditions at θ_B, the bottom isotherm,

$$\begin{aligned} z &= z_B - C^{z_B} \circ_2 \frac{K_V}{\overline{z}_\theta^2}\gamma_\theta, \\ \omega \overline{z}_\theta &= w_B - C^{w_B} \circ_2 \epsilon, \end{aligned} \tag{A10}$$

at θ_T, the top isotherm,

$$\begin{aligned} z &= z_T + C^{z_T} \circ_2 \frac{K_V}{\overline{z}_\theta^2}\gamma_\theta, \\ \omega \overline{z}_\theta &= w_T + C^{w_T} \circ_2 \epsilon, \end{aligned} \tag{A11}$$

and at the eastern boundary, $\lambda = \lambda_E$,

$$z = z_E - C^{z_E} \circ_{2E} \overline{b}_\theta \int_\theta^{\theta_T} \epsilon \frac{\beta}{\mathrm{f}^2} \overline{z}_\vartheta(1,0) \cdot \mathbf{n} d\vartheta,$$

$$B(\lambda_E, \theta_B) = B_E - C^{B_E} \circ_{1E} \int_{\theta_B}^{\theta_T} \epsilon \frac{\beta}{\mathrm{f}^2} \overline{z}_\theta(1,0) \cdot \mathbf{n} d\theta. \tag{A12}$$

The so-called "adjoint" equations are:

$$\mathrm{f}\nu - \overline{z}_\theta \frac{1}{r_o \cos\phi}\frac{\partial \epsilon}{\partial \lambda} = -\mathcal{L}_i^u \sum_{i=1}^{M} w_i \left(\mathcal{L}_i \circ_3 (\mathbf{u}, \omega, z, B) - m_i\right)$$

$$-\mathrm{f}\mu - \overline{z}_\theta \frac{1}{r_o}\frac{\partial \epsilon}{\partial \phi} = -\mathcal{L}_i^v \sum_{i=1}^{M} w_i \left(\mathcal{L}_i \circ_3 (\mathbf{u}, \omega, z, B) - m_i\right)$$

$$-\overline{z}_\theta \epsilon_\theta + \overline{z}_\theta \gamma = -\mathcal{L}_i^\omega \sum_{i=1}^{M} w_i \left(\mathcal{L}_i \circ_3 (\mathbf{u}, \omega, z, B) - m_i \right)$$

$$-\nabla \cdot \underline{\mu} + \alpha_\theta = -\mathcal{L}_i^B \sum_{i=1}^{M} w_i \left(\mathcal{L}_i \circ_3 (\mathbf{u}, \omega, z, B) - m_i \right)$$

$$\overline{b}_\theta \alpha + \left(\frac{K_V}{\overline{z}_\theta^2} \gamma_\theta \right)_\theta = -\mathcal{L}_i^z \sum_{i=1}^{M} w_i \left(\mathcal{L}_i \circ_3 (\mathbf{u}, \omega, z, B) - m_i \right), \tag{A13}$$

with homogeneous boundary conditions at θ_B and θ_T,

$$\begin{aligned} \alpha &= 0, \\ \gamma &= 0, \end{aligned} \tag{A14}$$

and at the western boundary,

$$\epsilon = 0. \tag{A15}$$

The symbol $\underline{\mu}$ denotes the vector field (μ, ν).

In the main text, it was assumed that the errors in the momentum equations, hydrostatic balance, and the heat equation are negligible. Furthermore, only measurements of z were considered.

Since the momentum, hydrostatic, and heat equations are now exact relations, their contribution to the penalty function is zero. To enforce these constraints, the equations are appended to the penalty function using Lagrange multipliers. Let two times $\underline{\mu}$, α, and γ be the Lagrange multipliers for the momentum, hydrostatic, and heat equations, respectively. As above, ϵ is still the (weighted) residual of the continuity equation. Under these circumstances, the Euler-Lagrange system simplifies to the following:

$$-\mathrm{f}v = -\frac{1}{r_o \cos\phi} \frac{\partial B}{\partial \lambda}$$

$$\mathrm{f}u = -\frac{1}{r_o}\frac{\partial B}{\partial \phi}$$

$$\bar{b}_\theta z = B_\theta$$

$$\frac{1}{r_o \cos\phi}\left[\frac{\partial u \bar{z}_\theta}{\partial \lambda} + \frac{\partial (v \bar{z}_\theta \cos\phi)}{\partial \phi}\right] = -(\omega \bar{z}_\theta)_\theta + C^z \circ_3 \epsilon$$

$$\omega \bar{z}_\theta = -\left(\frac{K_V}{\bar{z}_\theta^2} z_\theta\right)_\theta, \tag{A16}$$

with boundary conditions at θ_B, the bottom isotherm,

$$\begin{aligned} z &= z_B - C^{z_B} \circ_2 \frac{K_V}{\bar{z}_\theta^2}\epsilon_{\theta\theta}, \\ \omega \bar{z}_\theta &= w_B - C^{w_B} \circ_2 \epsilon, \end{aligned} \tag{A17}$$

at θ_T, the top isotherm,

$$\begin{aligned} z &= z_T - C^{z_T} \circ_2 \frac{K_V}{\bar{z}_\theta^2}\epsilon_{\theta\theta}, \\ \omega \bar{z}_\theta &= w_T - C^{w_T} \circ_2 \epsilon, \end{aligned} \tag{A18}$$

and at the eastern boundary, $\lambda = \lambda_E$,

$$z = z_E - C^{z_E} \circ_{2E} \bar{b}_\theta \int_\theta^{\theta_T} \epsilon \frac{\beta}{\mathrm{f}^2} \bar{z}_\vartheta(1,0) \cdot \mathbf{n} d\vartheta, \tag{A19}$$

$$B(\lambda_E, \theta_B) = B_E - C^{B_E} \circ_{1E} \int_{\theta_B}^{\theta_T} \epsilon \frac{\beta}{\mathrm{f}^2} \bar{z}_\theta(1,0) \cdot \mathbf{n} d\theta. \tag{A20}$$

The adjoint equations are:

$$\mathrm{f}\nu - \bar{z}_\theta \frac{1}{r_o \cos\phi}\frac{\partial \epsilon}{\partial \lambda} = 0 \tag{A21}$$

$$-\mathrm{f}\mu - \bar{z}_\theta \frac{1}{r_o}\frac{\partial \epsilon}{\partial \phi} = 0 \tag{A22}$$

$$-\epsilon_\theta + \gamma = 0$$

$$-\frac{1}{r_o \cos\phi}\left[\frac{\partial \mu}{\partial \lambda} + \frac{\partial(\nu \cos\phi)}{\partial \phi}\right] + \alpha_\theta = 0 \tag{A23}$$

$$\bar{b}_\theta \alpha + \left(\frac{K_V}{\overline{z}_\theta^2}\gamma_\theta\right)_\theta = -\mathcal{L}_i^z \sum_{i=1}^{M} w_i \left(\mathcal{L}_i^z \circ_3 z - m_i\right), \tag{A24}$$

with homogeneous boundary conditions at θ_B and θ_T,

$$\begin{aligned} \alpha &= 0, \\ \gamma &= 0, \end{aligned} \tag{A25}$$

and at the western boundary,

$$\epsilon = 0. \tag{A26}$$

It may be shown that measurements of z make no impact on the eastern boundary condition for B. To see this, vertically integrate the adjoint divergence equation, A23, and eliminate μ and ν with A21 and A22. One finds that

$$\int_{\theta_B}^{\theta_T} \epsilon \frac{\beta}{\mathrm{f}^2} \overline{z}_\theta d\theta = 0. \tag{A27}$$

Inspection of equation A20 shows that the eastern boundary condition for B is not affected by z measurements.

APPENDIX B. Numerical Methods

B.1. The Linear Planetary Geostrophic System

This section describes the numerical methods used to perform the calculations described in Chapter 2.

B.1.1. Model Discretization

The linear planetary geostrophic model was solved by manipulating the equations to eliminate all but $z(\lambda, \phi, \theta)$ to form a parabolic thermocline equation, with the time-like characteristics pointing zonally westward (Pedlosky, 1992). The thermocline equation was discretized using second-order centered differences in the vertical, and the time-like discretization was implicit. Thus, the thermocline equation was solved by inverting one penta-diagonal $n \times n$ system for each latitude, and integrating westward.

In order to carry out the calculations described in Chapter 2, the thermocline equation and its adjoint were solved numerically as the discretized forward equation and its finite-difference adjoint. The latter is an adjoint with respect to the discretized inner product for spherical-polar geometry, including discretized integrals over the boundary of the domain.

B.1.2. The Relationship Between Covariance Functions, Weighting Functions, and Weight Operators

definitions

Let $\epsilon(\mathbf{x})$ denote a random field defined on the domain D, and let $\mathbf{x} \in D$ label a point in D. The covariance of ϵ is denoted with $C^{\epsilon}(\mathbf{x}, \mathbf{y})$. Assuming that the expected value of ϵ is zero, the covariance of ϵ is defined as

$$C^{\epsilon}(\mathbf{x}, \mathbf{y}) = E[\epsilon(\mathbf{x})\epsilon(\mathbf{y})], \tag{B1}$$

where $E[*]$ denotes the expected value.

Each weighting function which appears in the penalty function corresponds to the functional inverse of its respective covariance. That is, the weighting function $W^{\epsilon}(\mathbf{x}, \mathbf{y})$, corresponding to the covariance function $C^{\epsilon}(\mathbf{x}, \mathbf{y})$, is defined by the relation

$$\int_D C^{\epsilon}(\mathbf{x}, \mathbf{y}) \int_D W^{\epsilon}(\mathbf{y}, \mathbf{z})\phi(\mathbf{z})d\mathbf{z}d\mathbf{y} = \phi(\mathbf{x}), \tag{B2}$$

or, equivalently,

$$\int_D W^{\epsilon}(\mathbf{x}, \mathbf{y}) \int_D C^{\epsilon}(\mathbf{y}, \mathbf{z})\phi(\mathbf{z})d\mathbf{z}d\mathbf{y} = \phi(\mathbf{x}), \tag{B3}$$

for all test functions ϕ defined on the domain D.

In each of the calculations presented in the text, it was assumed that the prior covariances were of the form

$$C^{\epsilon}(\mathbf{x}, \mathbf{y}) = \sigma_{\epsilon}(\mathbf{x})\sigma_{\epsilon}(\mathbf{y})c^{\epsilon}(\mathbf{x}, \mathbf{y}). \tag{B4}$$

The functions $\sigma_{\epsilon}(\mathbf{x})$ and $c^{\epsilon}(\mathbf{x}, \mathbf{y})$ are the standard deviation and correlation functions, respectively, of the field ϵ. It was also assumed that the correlation functions were separable in spherical polar coordinates:

$$c^{\epsilon}(\mathbf{x_1}, \mathbf{x_2}) = c^{\epsilon}_{\text{zon}}(\lambda_1, \lambda_2) c^{\epsilon}_{\text{mer}}(\phi_1, \phi_2) c^{\epsilon}_{\text{vert}}(\theta_1, \theta_2), \tag{B5}$$

where $\mathbf{x_i} = (\lambda_i, \phi_i, \theta_i)$. Furthermore, each one-dimensional correlation function was assumed to be homogeneous and isotropic, i.e., each is a function of the absolute value of the difference in its arguments. Although it was assumed that the correlation functions were all homogeneous and separable, the prior correlations of the state variables were non-separable, anisotropic, and inhomogeneous (as illustrated in Figure 2.4), owing to the constraints provided by the planetary geostrophic dynamics.

Thus, to each source of error, there corresponds a standard deviation, and a set of correlation functions.

The standard deviation of each error is discussed in the text and listed in Tables 2.2, 2.5, 3.2, and 3.3. Note that, in the Tables, the only information regarding the correlation functions are the correlation length scales. The functional form of each correlation function was determined by the spatial regularity considerations discussed in Bennett and Budgell (1987). Briefly, the linearized planetary geostrophic system was analyzed and the minimum asymptotic (high-wavenumber) spectral roll-off rates of the error fields were determined to insure that the physical fields (i.e., solutions of the planetary geostrophic system) would be physically realizable. By "physically realizable," it is meant that the physical fields should not contain any delta function singularities, which would make the fields unrealistic from a physical point of view.

For the linearized planetary geostrophic system, a sufficient condition for the physical realizability of the solutions is that the Fourier transforms of the one-dimensional correlation functions decay like k^{-4}, where k is the one-dimensional wavenumber. Weaker conditions are possible for this system; however, k^{-4} has some specific advantages for the numerical implementation, which are discussed

below. Therefore, the asymptotic spectral roll-off rate for each one-dimensional correlation function was chosen to be k^{-4}.

In order to evaluate the penalty function, it is necessary to evaluate integrals of the form

$$\int_D W^\epsilon(\mathbf{x},\mathbf{y})\phi(\mathbf{y})d\mathbf{y}. \tag{B6}$$

For brevity, integrals of this type are denoted as $W^\epsilon \circ_D \phi$, similar to the notation used in the text and defined in Appendix 4.3.

The operation count for the approximation of integrals, such as B6, on an N-point finite-difference lattice is $O(N^2)$. The $O(x)$ notation is used to denote a number, y, such that the limit y/x is nonzero and finite as $x \to \infty$. If each integral had been implemented as such a sum, none of the inverse calculations presented in the text would have been feasible (the linear model in Chapter 2 had $N \approx 6 \times 10^4$, and the nonlinear model in Chapter 3 had $N \approx 5 \times 10^5$).

Instead, the integrals were written in a special form, in which $W^\epsilon \circ_D \phi$ was represented as the action of a differential operator on the field ϕ. By re-writing the inner product as the action of a differential operator, it was possible to evaluate $W^\epsilon \circ_D \phi$ in $O(N)$ operations, a huge savings over an $O(N^2)$ implementation.

The following example should help to clarify these ideas for those readers who are unfamiliar with this material. A one-dimensional example is worked out in detail.

example

Consider a random field $\epsilon(x)$, defined for all real x. Although it would seem logical to begin by defining the covariance of ϵ, it is more relevant to the numerical implementation (discussed below) if we start from the differential operator which

defines the weight. This point of view is similar to that taken by McIntosh (1990) in discussing the correspondence between smoothing splines and objective analysis.

Define the inner product of the weighting function $W^\epsilon(x,y)$ with the test function $\phi(x)$ as

$$\begin{aligned} W^\epsilon \circ_D \phi &\equiv \int_{-\infty}^{+\infty} W^\epsilon(x,y)\phi(y)dy \\ &= \frac{\mathcal{N}}{\sigma_\epsilon(x)}\left[1 + L^4\frac{\partial^4}{\partial x^4}\right]\frac{\phi(x)}{\sigma_\epsilon(x)}. \end{aligned} \tag{B7}$$

The factor $\mathcal{N}$ is a normalizing constant, which will insure that the correlation at zero separation is unity. We shall show that σ_ϵ is the standard deviation of ϵ and L is equal to a correlation length scale of ϵ.

To find the covariance corresponding to this weight, consider the definition relating the weight to the covariance, equation B2. Substituting the expression B7 into B2 yields

$$\int_{-\infty}^{+\infty} C^\epsilon(x,y)\frac{\mathcal{N}}{\sigma_\epsilon(y)}\left[1 + L^4\frac{\partial^4}{\partial y^4}\right]\frac{\phi(y)}{\sigma_\epsilon(y)}dy = \int_{-\infty}^{+\infty}\delta(y-x)\phi(y)dy, \tag{B8}$$

where the Dirac delta function $\delta(x)$ has also been used. Next, assume that $C^\epsilon(x,y)$, $C^\epsilon_y(x,y)$, $C^\epsilon_{yy}(x,y)$, and $C^\epsilon_{yyy}(x,y)$ go to zero as $|y|$ goes to infinity, and integrate by parts. Since equation B8 must hold for all test functions ϕ, $C^\epsilon(x,y)$ satisfies the following:

$$\frac{1}{\sigma_\epsilon(y)}\left[1 + L^4\frac{\partial^4}{\partial y^4}\right]\left(\frac{\mathcal{N}C^\epsilon(x,y)}{\sigma_\epsilon(y)}\right) = \delta(y-x). \tag{B9}$$

The solution of this equation is straightforward and yields

$$C^\epsilon(x,y) = \frac{L}{2\sqrt{2}\mathcal{N}}\sigma_\epsilon(x)\sigma_\epsilon(y)\exp\left(-\frac{|x-y|}{\sqrt{2}L}\right)\cos\left(\frac{x-y}{\sqrt{2}L}\right). \tag{B10}$$

For unit correlation at zero separation, the normalizing coefficient is

$$\mathcal{N} = \frac{2\sqrt{2}}{L}. \tag{B11}$$

If $\sigma_\epsilon(x)$ is a constant, one can take the Fourier transform of equation B9 to obtain

$$\hat{C}^\epsilon(k,l) = \frac{\sigma_\epsilon^2}{\mathcal{N}} \frac{1}{1+L^4k^4}\delta(k+l), \tag{B12}$$

where the two-dimensional Fourier transform is defined by

$$\hat{C}^\epsilon(k,l) = \frac{1}{2\pi}\int_{-\infty}^{\infty}\int_{-\infty}^{\infty} C^\epsilon(x,y)e^{ikx}e^{ily}dxdy. \tag{B13}$$

It is evident from equation B12 that the asymptotic spectral roll-off rate of C^ϵ is k^{-4}. Furthermore, the correlation scale L is equal to the inverse of the wavenumber at the half-power point of the Fourier transform of C^ϵ.

numerical implementation

The numerical implementation of the weights was based on the observation that differential operators can be approximated by finite-difference operators, which are local in space. That is, the inner product of a weight with a field was computed by applying a finite-difference operator to the field. Rather than costing $O(N^2)$ floating point operations (flops) per inner product, the finite-difference implementation used only $O(N)$ flops.

In the linear calculations of Chapter 2, both descent and representer methods were used. Therefore, it was necessary to implement both inner products, $W^\epsilon \circ_D \phi$ and $C^\epsilon \circ_D \phi$. The weights were implemented as the finite-difference approximation to

$$\begin{aligned} W^\epsilon \circ_D \phi = {} & \frac{\mathcal{N}}{\sigma_\epsilon(\mathbf{x})}\left(1 - L_{\mathrm{H}}^2\frac{\partial^2}{r_o\partial\lambda^2}\right)\left(1 - L_{\mathrm{H}}^2\frac{\partial^2}{r_o\partial\phi^2}\right)\left(1 - L_{\mathrm{V}}^2\frac{\partial^2}{\partial\theta^2}\right) \\ & \times \left(1 - L_{\mathrm{V}}^2\frac{\partial^2}{\partial\theta^2}\right)\left(1 - L_{\mathrm{H}}^2\frac{\partial^2}{r_o\partial\phi^2}\right)\left(1 - L_{\mathrm{H}}^2\frac{\partial^2}{r_o\partial\lambda^2}\right)\frac{\phi(\mathbf{x})}{\sigma_\epsilon(\mathbf{x})}, \end{aligned} \tag{B14}$$

which, in finite-difference form, is the product of three tridiagonal systems:

$$W^{\epsilon} \circ_D \phi = \frac{\mathcal{N}}{\sigma_{\epsilon}(\mathbf{x})} T_{\text{zon}} T_{\text{mer}} T_{\text{vert}}^2 T_{\text{mer}} T_{\text{zon}} \frac{\phi(\mathbf{x})}{\sigma_{\epsilon}(\mathbf{x})}. \tag{B15}$$

T_{zon}, T_{mer}, and T_{vert} are the finite-difference approximations of the corresponding differential operators in the zonal, meridional and vertical directions in expression B14. The symmetry of equation B15 guarantees that the resulting product is symmetric and positive-definite.

The operator inverse of $W^{\epsilon} \circ_D \phi$, which is $C^{\epsilon} \circ_D \phi$, was computed efficiently through the solution of a sequence of tridiagonal systems. All of the linear algebra was performed using the LAPACK software library (Anderson et al., 1992).

The condition determining the normalizing coefficient is that the correlation at zero lag be unity. To illustrate how $\mathcal{N}$ was determined for the numerical calculations, consider the implementation of the weight in the one-dimensional example, above (section B.1.2). To make the example relevant, restrict the domain to $x \in [0, N\Delta x]$, where Δx is the grid resolution. The second-order accurate discretization of the weight operator is

$$(W \circ \phi)_i = \frac{\mathcal{N}}{\sigma_i} \left[1 + L^4 (\delta_i^2)^2\right] \frac{\phi_i}{\sigma_i} \tag{B16}$$

for all $i \in [1, N-1]$. The symbol δ_i^2 denotes the second-derivative operator on the one-dimensional finite-difference grid:

$$\delta_i^2 \phi = \frac{\phi_{i+1} - 2\phi_i + \phi_{i-1}}{(\Delta x)^2}, \tag{B17}$$

with Dirichlet boundary conditions on ϕ:

$$\begin{aligned} \phi_0 &= 0, \\ \phi_N &= 0. \end{aligned} \tag{B18}$$

Define the discrete Fourier transform on this domain with

$$\hat{\phi}_k = \sum_{j=0}^{N-1} \phi_j e^{\frac{2\pi i}{N} kj} \tag{B19}$$

for integer k. The inverse transform is defined as

$$\phi_j = \frac{1}{N} \sum_{k=0}^{N-1} \hat{\phi}_k e^{-\frac{2\pi i}{N} kj}. \tag{B20}$$

Recall that $C(x,y) = \sigma(x)\sigma(y)c(x,y)$, where the correlation function satisfies $c(x,x) = 1$. A straightforward calculation shows that the Fourier transform of c is

$$\hat{c}_{k\ l} = \frac{N}{\mathcal{N}} \left[1 + \left(\frac{\sqrt{2}L}{\Delta x} \right)^4 (1 - \cos 2\pi l/N)^2 \right]^{-1} \delta_{l\ -m}, \tag{B21}$$

where $\delta_{p\ q}$ is the Kronecker delta. Transforming back into physical space, and using the fact that $c_{k\ k} = 1$, reveals that the normalizing coefficient is

$$\mathcal{N} = \frac{1}{N} \sum_{l=0}^{N-1} \left[1 + \left(\frac{\sqrt{2}L}{\Delta x} \right)^4 (1 - \cos 2\pi l/N)^2 \right]^{-1}. \tag{B22}$$

summary

This section has been a detailed discussion of the implementation of the non-diagonal covariances used in the text. This implementation was possible because of the correspondence between a weighting *operator* and a weighting *function.* Given the variance, correlation length scales, and the asymptotic spectral form of the covariance function, the weighting operator was implemented as the finite-difference approximation to the appropriate differential operator. Because the weighting operator was separable and local in space, its functional inverse (the covariance) could be determined through the solution of a sequence of tridiagonal problems.

Note that the inner product of a covariance function with a field is a smoothing operation. Conversely, the inner product of a weighting function with a field

is a *roughening* operation. Thus, the differential operators corresponding to the weighting functions may be referred to as "roughening operators."

The bell-shaped, or un-normalized Gaussian, correlation function, which is commonly used in objective analysis (e.g., Roemmich, 1983), was intentionally not used in this study. The bell-shaped correlation is very smooth, it is infinitely differentiable; however, it is not invertible. To be precise, the inverse of a bell-shaped covariance is a roughening operator of such severity that its domain excludes almost all functions. If bell-shaped covariances are used, the penalty function cannot, in general, be summed.

The development of the above implementation scheme was inspired by the approach of Egbert et al. (1994), in which the convolution of a bell-shaped covariance with a field, ϕ, was implemented by time-stepping a heat equation using ϕ as the initial condition.[1] The time-stepping method can be regarded as the iteration of a local finite-difference operator on the field, in precisely the same form as equation B15.

B.1.3. Numerical Convergence

Because the representer equations involve the response of the model/adjoint equations to delta function forcing, it is not evident a priori that the solutions obtained from finite-difference approximations will be accurate. A 2×2 representer matrix for measurements at two widely separated sites was used to test for numerical

---

[1]Note that in Egbert et al. (1994), a representer based solver was used for their inverse problem. Because the representer algorithm does not require the use of weighting functions, the non-invertability of the bell-shaped covariance was not an issue for their calculations. Indeed, this can be regarded as a major advantage of the Euler-Lagrange solvers over the direct minimization methods.

convergence. The resolution in each direction was halved until the representer matrix changed by less than 1%. This resolution was taken as the working resolution for the calculations. Note that this resolution entirely depends on the model dynamics *and* on the length scales of the covariance operators used in the calculation. Had diagonal weights been used in the dynamics, the numerical solution would not have converged because of the presence of delta-function singularities in the solution.

B.1.4. Numerical Correctness

It is notoriously difficult to create sufficiently bug-free code for descent computations with realistic ocean models (Navon et al., 1992b). If the forward and adjoint operators are not the precise finite-difference adjoints of one another, the gradient calculations for the descent computations will be in error. If the finite-difference codes are derived from the continuous forward and adjoint equations, the "continuous-adjoint" and "finite-difference-adjoint" gradients should differ only at the level of truncation error; nonetheless, this difference can create havoc for descent methods. It is unfortunate that descent methods are exceedingly sensitive to the details of the state variables at the level of truncation error. Nonetheless, to create correct and consistent solvers, it is necessary that the adjoint and forward operators be adjoint to machine precision.

The adjoint properties were checked in two ways. For each operator L and its adjoint L^*, the adjoint property was checked directly,

$$(Lu) \circ v - u \circ_* (L^* v) = 0.0, \tag{B23}$$

where 0.0 denotes zero at machine precision, and u and v were randomly chosen vectors. The appropriate inner products, which depend on the domain and range of the operator in question, are denoted with the $\circ$ and $\circ_*$ symbols. This test is

a check on the individual operators; however, it is still possible to make a mistake when preconditioning or convolving the fields with the weight operators. These properties were checked by computing the Gateaux derivative in the direction of the gradient. From the definition of the derivative, the following limit must hold (Thepaut and Courtier, 1991):

$$\lim_{\alpha \to 0} \frac{\mathcal{J}(u + \alpha\xi) - \mathcal{J}(u)}{\alpha < \xi, \xi >} = 1.0, \tag{B24}$$

where $\xi = \nabla_u \mathcal{J}(u)$. This too was checked to machine precision.

To insure the consistency of the representer calculations with the descent calculations, the following identity was also checked in Chapter 2 (to machine precision):

$$\mathcal{J}(u_{\min}) = b^T \mathcal{R} b + b^T \mathcal{R} W \mathcal{R} b. \tag{B25}$$

This check insures that the direct sum of $\mathcal{J}$ at the minimum agrees with the representer sum. This property will fail if any of the following occur:

1. The covariances and weights are not self-adjoint.
2. The covariances and weights are not operator inverses.
3. The forward and adjoint finite-difference operators are not finite-difference adjoints.
4. The forward and adjoint finite-different solvers are not operator inverses of the finite-difference forward and adjoint operators.

No test can definitively reveal the absence of programming errors, but the dependence of this test on so many properties makes it unlikely that an error would escape undetected.

B.2. The Nonlinear Planetary Geostrophic System

This section describes the numerical implementation of the model used in Chapter 3.

B.2.1. Numerical Grid and Difference Operators

An Arakawa A-grid (Arakawa and Lamb, 1977) was used to position the variables laterally in spherical-polar coordinates. Boundary conditions were derived by assuming that the physical boundary exists midway between grid-points at the border of the computational domain.

The variables were positioned vertically on a "Lorenz" grid (Arakawa, 1988). In this scheme, the water column is divided into a stack of layers in which horizontal velocity, Bernoulli function, and layer thickness are defined. The diabatic velocity, salinity, and depth are specified at the layer interfaces. By convention, the layers are numbered from 1 to N going up the water column, and the layer interfaces range from 1/2 (the bottom) to $N - 1/2$.

Wherever possible, second-order centered finite-differences were used to discretize the equations. Finite difference operators were defined in terms of standard differencing and averaging operators. For any variable Φ defined on the grid, the operators $\delta_a \Phi$ and $\overline{\Phi}^a$ are defined by

$$\delta_a \Phi_i = \frac{\Phi_{i+1/2} - \Phi_{i-1/2}}{\Delta a_i}, \tag{B26}$$

and

$$\overline{\Phi_i}^a = \frac{\Phi_{i+1/2} + \Phi_{i-1/2}}{2}, \tag{B27}$$

where the subscript i denotes whichever index corresponds to the a coordinate, and $\Delta a_i = a_{i+1/2} - a_{i-1/2}$. A vertical averaging operator is also used in the model, it is defined by

$$I^{\theta}(\Phi)_{ij} = \frac{1}{H_{ij}} \sum_{k=1}^{N} \Phi_{ijk} \delta_{\theta} z_{ij(k-1/2)} \Delta\theta_k. \tag{B28}$$

The bottom depth, H_{ij}, is equal to $-z_{ij1/2}$.

Letting r_o denote the radius of the Earth, the components of the gradient are

$$\delta_{\lambda}\Phi_{ij} = \frac{\Phi_{i+1/2\ j} - \Phi_{i-1/2\ j}}{r_o \cos\phi_j \Delta\lambda}, \tag{B29}$$

and

$$\delta_{\phi}\Phi_{ij} = \frac{\Phi_{i\ j+1/2} - \Phi_{i\ j-1/2}}{r_o \Delta\lambda}. \tag{B30}$$

The gradient, divergence, and curl operators are defined with

$$\nabla\Phi = \left(\delta_{\lambda}\overline{\Phi}^{\lambda}, \delta_{\phi}\overline{\Phi}^{\phi}\right), \tag{B31}$$

$$\nabla \cdot \mathbf{U} = \delta_{\lambda}\overline{U}^{\lambda} + \frac{1}{\cos\phi}\delta_{\phi}(\cos\phi\overline{V}^{\phi}), \tag{B32}$$

and

$$\mathrm{curl}\mathbf{U} = \delta_{\lambda}\overline{V}^{\lambda} - \frac{1}{\cos\phi}\delta_{\phi}(\cos\phi\overline{U}^{\phi}), \tag{B33}$$

for any scalar field, Φ, and vector field, $\mathbf{U} = (U, V)$.

B.2.2. Governing Equations

The discretized horizontal momentum equations are,

$$\mathrm{f}\hat{\mathbf{k}} \times \mathbf{u} = -\nabla B + \overline{z}^{\theta}\nabla b + \delta_{\theta}\mathbf{F}^{\tau}/\delta_{\theta}z + \frac{A_H}{\delta_{\theta}z}\nabla \cdot \delta_{\theta}z\nabla\mathbf{u}, \tag{B34}$$

where $\hat{\mathbf{k}}$ is unit vector directed in the vertical direction and the subscripts $\{i, j, k\}$ are implied. The vertical momentum equation (hydrostatic balance) is discretized as

$$\delta_{\theta}B = z\delta_{\theta}b. \tag{B35}$$

Since ω never appears alone, but only in the combination ωz_{θ}, we let $w = \omega z_{\theta}$, and carry this at layer interfaces. Physically, w is the diabatic component of $\frac{Dz}{Dt}$, the vertical velocity. The layer-thickness equation (conservation of volume) is,

$$\nabla \cdot (\mathbf{u}\delta_{\theta}z) + \delta_{\theta}w = 0, \tag{B36}$$

and the thermodynamic equation is

$$w = \delta_{\theta}\left(\frac{K_V}{\delta_{\theta}z} + F^{Q}\right). \tag{B37}$$

The salt conservation equation is

$$\nabla \cdot (\mathbf{u}S\delta_{\theta}z) + \delta_{\theta}(w\overline{S}^{\theta}) = \nabla \cdot (K_H\delta_{\theta}z\nabla S) + \delta_{\theta}\left(\frac{K_V}{\delta_{\theta}z}\delta_{\theta}S + F^{S}\right). \tag{B38}$$

Finally, the equation for the perturbation buoyancy is

$$b = \frac{g}{\rho_{\mathrm{o}}}(\rho(\theta, S, \overline{z}^{\theta}) - \rho(\Theta(\overline{z}^{\theta}), S_{\mathrm{o}}, \overline{z}^{\theta})). \tag{B39}$$

The discrete streamfunction equation was obtained by vertically averaging the horizontal momentum equation (B34) with the I^{θ} operator (B28), and then applying the finite-difference curl operator.

B.2.3. Reynolds Fluxes

As written above, the Reynolds fluxes are written in two forms depending on their origin. The terms F^{τ}, F^{Q}, and F^{S} are the vertical (diabatic) Reynolds fluxes caused by the turbulent exchange of momentum, heat, and freshwater, respectively, across the air-sea interface. The other Reynolds fluxes are caused by turbulent motion in the ocean interior and are represented in terms of the large-scale property gradients and turbulent diffusivities; these are the terms proportional to A_H, K_H and K_V above. Each of these terms is discussed separately in this section.

One of the principal difficulties in using a model with a Lagrangian vertical coordinate is the treatment of surface and bottom boundary conditions. In this model, the surface and bottom are material surfaces along which potential temperature is constant. The representation of the surface mixed layer is contained in the definitions of the vertical Reynolds fluxes F^{τ}, F^{Q}, and F^{S}. The philosophy taken here is that the detailed vertical structure of the mixed layer is inconsequential to the general circulation (for caveats see Krauss, 1993), and each of these Reynolds fluxes is given a simple vertical structure consisting of exponential decay with a 50m e-folding scale. Other parameterizations of the mixed layer would have been possible (e.g., Bleck et al., 1989); however, the intended use of the model in an inverse calculation made it highly desirable to use a parameterization which was a continuously differentiable function of the layer interface depths. The specific forms of these terms are as follows: the Ekman layer body force is discretized in total,

$$(\delta_\theta \mathbf{F}^{\tau}/\delta_\theta z)_{ijk} = (\tau_{\text{wind}})_{ij} \exp(\mu \bar{z}^{\theta}_{ij(k-1/2)}) \left(\sum_{k=1}^{N} \exp(\mu \bar{z}^{\theta}_{ij(k-1/2)}) \delta_\theta z_{ij(k-1/2)} \right)^{-1} . \quad \text{(B40)}$$

This peculiar-looking discretization insures two things: 1) that the vertically integrated Ekman transport is correct, and 2) that the Ekman layer velocity is monotonically decreasing with depth. The Reynolds flux for surface heating is

$$F^Q_{ijk} = \frac{Q_{ij}}{\rho_o C_p} \exp(\mu(\overline{z}^{\theta}_{ij(k-1/2)} - \overline{z}^{\theta}_{ij(N-1/2)})), \tag{B41}$$

and the Reynolds salt flux is

$$F^S_{ijk} = \frac{F_{ij}}{S_o} \exp(\mu z_{ijk}). \tag{B42}$$

Values of the constants are, $\mu^{-1} = 50\text{m}$, $\rho_o = 1025\text{km m}^{-3}$, $S_o = 35\text{psu}$, and $C_p = 4200\text{J (°C kg)}^{-1}$.

The terms for turbulent mixing of heat and salt down their mean gradients are standard (e.g., DeSzoeke and Bennett, 1993). Since both temperature and salinity are active tracers, a simple Fick's Law closure such as this is not formally justified (Ch. 10 of Monin and Yaglom, 1965). Values of the turbulent diffusion coefficients were $K_V = 10^{-5}\text{m}^2/\text{s}$ and $K_H = 2 \times 10^4\text{m}^2/\text{s}$.

B.2.4. Boundary Conditions

The solution method for these equations involves splitting the velocity field into a vertical average and a remainder. As a consequence of the Boussinesq and rigid-lid approximations, a streamfunction exists for the vertically integrated volume transport. The no-slip and no-normal-flow conditions on the velocity field become boundary conditions on the streamfunction. On each connected portion of the closed boundaries, the streamfunction is constant and its derivative normal to the boundary vanishes. The computational boundary conditions across a solid boundary at a point indexed by i are

$$\overline{\Psi_i}^x = C, \tag{B43}$$

and

$$\delta_x \Psi_i = 0, \tag{B44}$$

where Ψ denotes streamfunction, and C is its constant value on the boundary segment. The second-order accurate boundary condition at a rigid boundary is simply $\Psi_{i-1/2} = \Psi_{i+1/2} = C$.

On open boundaries, the streamfunction and its normal derivative must be specified. The computational boundary conditions permit free choice of $\Psi_{i-1/2}$ and $\Psi_{i+1/2}$ across an open boundary. For simplicity, the experiments of Chapter 3 were all conducted in a closed domain.

A second consequence of the rigid-lid approximation is that no boundary conditions on the Bernoulli function, B, are needed. At lateral boundaries, the gradients of B and buoyancy, b, in the momentum equations are approximated with one-sided differences.

A reflection condition is used to provide computational boundary conditions for the horizontal divergence operator at closed boundaries. This guarantees global conservation of volume and salt for each layer in the absence of diabatic mixing and air-sea exchange.

The ocean surface and bottom are material surfaces. For computational purposes they are also stationary isothermal surfaces, so an insulating condition is applied in the form of $\omega = 0$.

B.2.5. Weighting Functions

The discussion of Section B.1.2 concerning the correspondence between covariances, weighting functions, and weighting operators applies to the nonlinear planetary geostrophic model as well. In contrast to the linear experiments in Chapter 2, the nonlinear calculations of Chapter 3 were based on descent methods alone.

Therefore, it was not necessary to compute the inner product of a covariance with a field for the experiments in Chapter 3.

The weights used in Chapter 3 were chosen to insure that the residual fields would have square-integrable second derivatives. Each inner product of a weighting function with a field was implemented as a differential operator acting on the corresponding field. For example, the inner product of W^ϵ with the three-dimensional field $\epsilon(\mathbf{x})$ was defined as

$$W^\epsilon \circ_D \epsilon = \frac{\mathcal{N}_\epsilon}{\sigma_\epsilon(\mathbf{x})} \left(1 + L_{\text{corr}}^4 \nabla^2 \nabla^2 + \Theta^4 \frac{\partial^4}{\partial \theta^4} \right) \frac{\epsilon(\mathbf{x})}{\sigma_\epsilon(\mathbf{x})}, \tag{B45}$$

where $\sigma_\epsilon^2(\mathbf{x})$ is the variance of ϵ, and $\mathcal{N}_\epsilon$ is a normalizing coefficient. L_{corr} is the horizontal correlation length scale, and Θ is a vertical correlation *temperature* scale.

Let c denote the correlation function of the covariance corresponding to the weighting operator in equation B45. As a consequence of the irregular domain shape, the function c is not separable, and the expression for the normalizing coefficient is not as simple as in equation B22 in Section B.1.2. The correct expression for the normalizing coefficient would involve a sum of the eigenvalues of the finite-difference Laplacian in spherical polar coordinates for the irregular computational domain. Rather than carry out this computation, the normalizing coefficients in Chapter 3 were computed by approximating the computational domain with a rectangular domain in cartesian coordinates. Therefore, the correlation at zero separation was not precisely unity; however, a synthesis of the exact correlation, for a test problem, indicated that the errors in this approximation should be less than 10%.

B.2.6. Numerical Correctness

In order to implement the descent methods described in Chapter 3, it was necessary to construct the finite-difference adjoint to the tangent linearization of

the finite-difference model. Once again, the adjoint was defined with respect to the discretized form of the standard inner product in spherical polar coordinates (including boundary conditions).

The numerical correctness of the adjoint code was tested by directly checking the adjoint property for each linearized model operator and its adjoint (as in equation B23). Furthermore, the full adjoint code, which is used to compute the gradient of the cost function, was checked by computing the Gateaux derivative in the direction of the gradient (equation B24). A further check of the minimization and gradient software was accomplished by performing a line-minimization in a randomly chosen direction, and then checking that the gradient at the minimum was perpendicular to the search direction.

B.2.7. Discussion

With any numerical model, a number of decisions must be made about the representation of the continuous equations with respect to the issues of global vs. local accuracy, and conservation laws or symmetries obeyed by the continuous equations. This subsection addresses a number of these issues in the context of the model described above.

pressure-gradient split

The pressure gradient force is split between the two terms ∇B and $\overline{z}^{\theta}\nabla b$ in this system. Figure 5.1 illustrates the contribution of these two terms to the zonal pressure gradient for a typical point in the middle of the North Pacific. It is clear that these terms are relatively large and tend to cancel over much of the water column. A similar split in the pressure gradient force has been studied in sigma-coordinate models (Mesinger, 1982; Haney, 1991; Beckmann & Haidvogel, 1993).

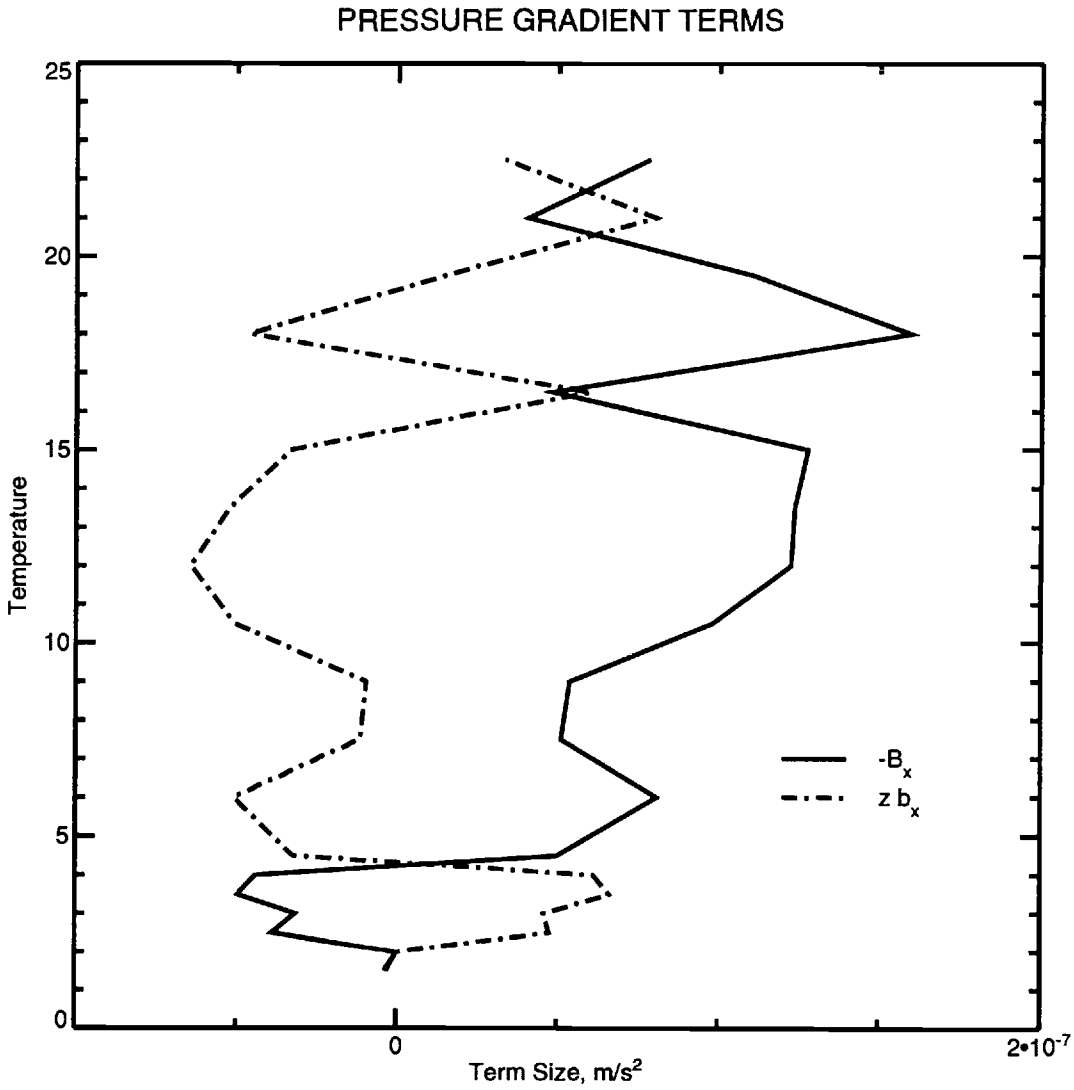

FIGURE 5.1. Pressure Gradient Terms.

The two terms comprising the zonal pressure gradient are shown for a typical point in the middle of the computational domain: I) $-B_x$, II) zb_x.

One consequence of truncation in the pressure-gradient split is that a buoyancy field which is a function of depth alone can give rise to erroneous currents. Imagine a configuration of layer depths and salinities which are arranged so that no horizontal gradients of buoyancy exist. The exact solution of the continuous equations has zero baroclinic velocity; however, because of vertical and horizontal truncation error, the numerical representation generates currents. The present situation is somewhat different from that in sigma coordinate models since the slope of the coordinate surfaces does not depend directly on the bottom slope; nonetheless, the errors can still be significant.

Following Phillips (1957), a reference profile of buoyancy was subtracted from the total buoyancy; the symbols B and b used above denote perturbation Bernoulli function and buoyancy. The reference profile is given by

$$b_{\text{ref}} = \frac{g}{\rho_o}\rho(\Theta(\overline{z}^{\theta}), S_o, \overline{z}^{\theta})), \tag{B46}$$

where the reference potential temperature profile $\Theta(z)$, was an exponential function with a 750m e-folding scale. It can be shown that subtracting this reference profile from the buoyancy does not affect the velocity field in the continuous formulation of the model. In contrast, the velocity field of the numerical model *is* significantly altered by removing the reference profile.

coordinate intersection

Coordinate intersection can be problematic for layer models in a number of different ways. First, in time dependent models the layer surfaces can intersect and produce negative layer thickness; this can be overcome by the judicious use of positive-definite advection schemes (e.g., Smolarkiewicz, 1983). Second, some provisions must be made for computing pressure gradients at the boundary where the coordinate surfaces intersect the top or bottom material boundary; obviously

sigma coordinates hold the advantage for this problem, but many approaches are possible when a Lagrangian coordinate is used (Bleck, 1974). Third, the vertical coordinate may be strongly coupled to thermodynamic processes at the ocean surface (Bleck et al., 1989).

Since the model described here was intended for use in a steady (time independent) inverse calculation, the problem of layer intersection is somewhat different from that in a time dependent model. Negative layer thicknesses are unphysical, but since the constraint of positive layer thicknesses is a convex constraint, standard methods can be used to insure that the layer thicknesses remain non-negative in the inverse problem.

The top and bottom layer interfaces of this model coincide with the oceanic surface and bottom. The reason for treating the top and bottom this way was to avoid complicated extrapolation formulae for calculating the velocity on the material surfaces (Bleck, 1974); implementations of such extrapolations would use "if-then" statements, which would make the penalty function non-differentiable with respect to the layer depths. Since layers never intersect either the top or bottom surfaces, the gradient of the Bernoulli function is always well-defined.

cross-isobath flow

As stated in Chapter 3, the vertically integrated vorticity equation contains a vortex stretching source term from the cross-isobath baroclinic flow. If the buoyancy is a function of z alone, or if the bottom is flat, then this vortex stretching source term is identically zero in the continuous formulation of the model.

In the finite-difference form of the model, the vertically integrated vorticity equation is derived by summing over the thickness-weighted momentum equations vertically, and then applying the finite-difference curl operator to the equations.

Because of truncation error in the horizontal finite-difference operators, the following equality is not satisfied:

$$\nabla \times \xi \nabla \eta = \nabla \xi \times \nabla \eta, \tag{B47}$$

where ξ and η are any two fields defined on the horizontal grid. A consequence of this error is that the baroclinic vortex stretching term in the barotropic vorticity equation is nonzero in the above mentioned cases, i.e., when the bottom is flat and when the buoyancy is a function of z alone. This is an error in the net bottom pressure torque.

Following Arakawa and Lamb (1977), prognostic atmospheric models are usually designed to eliminate this spurious source of vorticity (Arakawa, 1988). The recent work of Beckmann and Haidvogel (1993) showed that there may be a trade-off between local accuracy and global conservation in such schemes; they tested two "vertically integrated pressure gradient"-conserving schemes in a sigma coordinate model, and found that both methods performed worse than the original, non-conserving, pressure gradient formulation.

In order to asses the quantitative level of truncation error in the model, two experiments were conducted in which the continuous formulation of the model predicted zero barotropic (depth integrated) flow. In both experiments, the erroneous barotropic flows were a small fraction of what would be caused by the wind-stress curl.

baroclinic boundary layers

As discussed in Pedlosky (1969), and further in Pedlosky (1979), baroclinic boundary layers have a structure which differs from the barotropic boundary layer structure. The important point is that the vertically averaged flow has a particular boundary layer structure, a Munk (1950) layer in the present model, while the

the flow at any particular depth need not have the same boundary layer width. In particular, the baroclinic boundary layer can be narrower than the barotropic boundary layer.

The numerical grid is not fine enough to permit the frictional term to significantly enter the baroclinic momentum balance. The baroclinic boundary layer scales like

$$L_{\mathrm{bc}} = \left(\frac{A_H}{\mathrm{f}}\right)^{1/2}, \tag{B48}$$

and north of approximately 10°N, L_{bc} is less than the resolution of the finite-difference grid. Therefore, the frictional balance is not obtained on the grid. Consequently, the baroclinic velocity was calculated by not including the lateral friction term.

To verify that the frictional term could be safely excluded in the baroclinic momentum equations, numerical experiments were conducted by solving the elliptic equation for the (unapproximated) baroclinic velocities. A comparison of the true velocity field with the approximated baroclinic velocity field showed that the frictional terms could be neglected outside of a several degree band centered on the equator. Based on these considerations, the frictional terms were excluded from the baroclinic momentum equations in the experiments reported in Chapter 3.

bottom topography

Previous investigators (e.g., Sarkisyan, 1977; Sarmiento and Bryan, 1982; and Fujio and Imasoto, 1991) have found that it is difficult to produce realistic estimates of ocean circulation when hydrographic data is used to estimate the cross-isobath baroclinic flow. Small inaccuracies in the the alignment of the topographic gradient relative to the cross-isobath baroclinic flow can generate vortex stretching which is much larger than the wind-driven Ekman pumping. The origin of the unrealistic flow

is attributed to uncertainty in the large-scale hydrographic fields, and to uncertainty in the bottom topography.

The boundary condition of no-normal-flow should hold point-wise at the ocean bottom; however, the equations for the large-scale flow are valid only on certain length scales. Bogden (1991) pointed out that the no-normal-flow boundary condition on the large-scale flow contains an implicit spatial average over non-linear terms. In analogy with the conventional Reynolds averages, the product of spatially averaged fields may differ from the spatial average of the product.

A similar problem has been appreciated for some time in the meteorological community. Wallace et al. (1983) observed systematic errors in geopotential height predictions in an operational weather prediction model. Based on the hypothesis that the small-scale (unresolved) circulations act as a cap over small-scale topographic variations, Wallace et al. (1983) experimented with "envelope" orography. They were able to significantly reduce systematic model errors, thus supporting the contention that the large-scale flow only "feels" the tops of the large-scale topography.

Small-scale, topographically trapped, circulations in the atmosphere are different from those in the ocean, owing to the absence of latent energy exchanges within the latter. In the present model, the topography was smoothed by convolving the original topography with a two-dimensional Gaussian filter with a 500km length scale.

APPENDIX C. Condition Number Estimates

C.1. Introduction

This Appendix presents the technical material concerning the condition number estimates alluded to in the text. While this material may be too detailed for the general reader, it is hoped that the methods used herein will prove helpful to others wishing to extend upon the calculations in Chapters 2 and 3. The methods used in this appendix are all based on the analysis found in Pedlosky (1992), in which solutions of the linearized planetary geostrophic system are constructed by using a modal decomposition in the vertical.

The equivocal results of the descent calculations in Chapter 3 suggest a closer look at the conditioning of the system. The "conditioning" of the penalty function is determined by the condition number, defined as the ratio of the largest eigenvalue to the smallest eigenvalue, of the Hessian of the penalty function. Recall that the Hessian is the matrix of second derivatives of the cost function, with respect to the state variables.

For example, if $\mathbf{u}$ denotes the (vector) state variable, and $\mathcal{J}(\mathbf{u})$ denotes the cost function, then

$$S(\mathbf{u}) = \frac{\partial^2 \mathcal{J}}{\partial \mathbf{u} \partial \mathbf{u}^T}(\mathbf{u}) \tag{C1}$$

is the Hessian of $\mathcal{J}$. The Hessian defines a family of multidimensional ellipsoids in the state space, the surfaces of which are normal to the cost function gradient at the point $\mathbf{u}$. Note that if the cost function is quadratic in $\mathbf{u}$, then the Hessian is independent of $\mathbf{u}$, and the ellipsoids defined by the Hessian coincide with isopleths

of the cost function surface. The condition number of the Hessian can be interpreted as the ratio of the lengths of the major and minor axes of the ellipses defined by the Hessian.

As mentioned in Chapter 2, the condition number of the Hessian controls the convergence rate of the descent algorithm. This is generally true, whether the underlying descent method is steepest descent, conjugate gradient, or a secant method (Luenberger, 1974). The condition number measures the narrowness of the steepest "valley" on the penalty function surface. Like S itself, if the penalty function is quadratic in $\mathbf{u}$, the condition number is independent of $\mathbf{u}$; otherwise, it may vary as a function of $\mathbf{u}$, even becoming negative or infinite if the penalty function is not convex.

To illustrate these concepts, Figure 5.2 shows examples of penalty functions when $\mathbf{u}$ is a two-dimensional vector. As the dimension of $\mathbf{u}$ increases beyond two or three, it is increasingly difficult to visualize the penalty function surface, but no qualitatively different phenomena occur. The figure shows four cases: a well conditioned, a poorly conditioned, a non-convex, and a non-convex, poorly conditioned penalty function. For each case, a vector pointing in the steepest descent direction is also plotted. When the Hessian is ill-conditioned or non-constant, the plots show that the steepest descent direction is not necessarily directed towards the global minimum of the penalty function.

In this appendix, an estimate is made of the condition number of the Hessian of the penalty function from Chapter 3, Section 3.5. The condition number estimates are based on a linearized planetary geostrophic model. The model domain is approximated by a rectangular β-plane of constant depth. As a consequence of the constant depth assumption, the baroclinic and barotropic dynamics are completely decoupled; thus, they are considered separately in the condition number estimates.

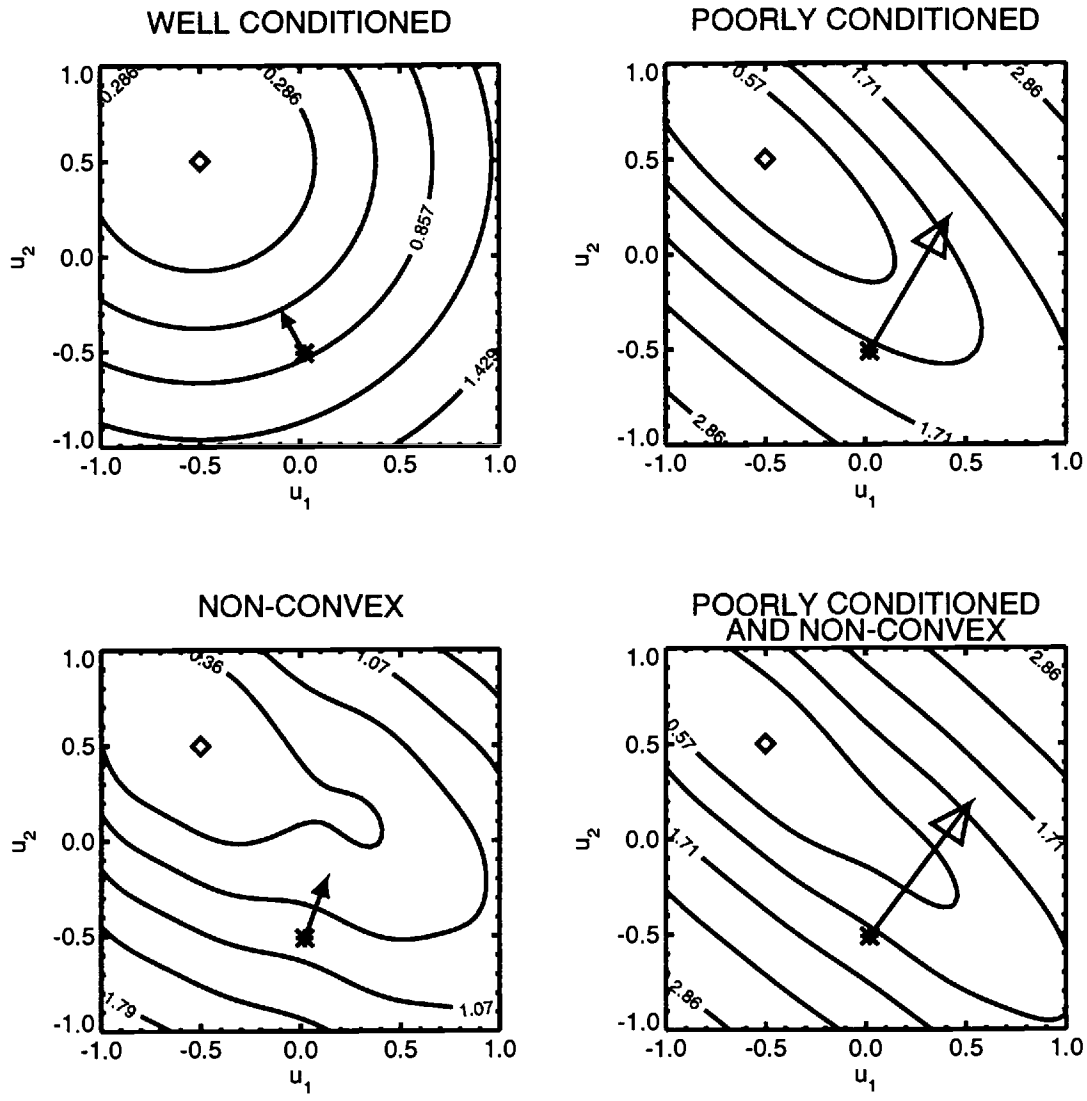

FIGURE 5.2. Conditioning example.

The panels contour four different penalty functions to illustrate the effects of poor conditioning and non-convexity of the penalty function.
Well conditioned: $\mathcal{J}(u_1, u_2) = (u_1 + 0.5)^2 + (u_2 - 0.5)^2 + 1$. Poorly conditioned: $\mathcal{J}(u_1, u_2) = (u_1 + 0.5)^2 + (u_2 - 0.5)^2 + 5(u_1 + u_2)^2 + 1$. Non-convex: $\mathcal{J}(u_1, u_2) = (u_1 \cos(3(u_1 + 0.5)) + 0.5)^2 + (u_2 - 0.5)^2 + (u_1 + u_2)^2 + 1$. Non-convex and poorly conditioned: $\mathcal{J}(u_1, u_2) = (u_1 \cos(3(u_1 + 0.5)) + 0.5)^2 + (u_2 - 0.5)^2 + 5(u_1 + u_2)^2 + 1$. The global minimum is indicated with the diamond in each panel, and the steepest descent direction at the point marked with the astericks is shown with the arrow.

The next section presents a condition number calculation for a simple model in one space dimension. The example is presented in detail to illustrate the methods which are used in Sections C.3 and C.4.

C.2. One-Dimensional Example

Consider the model provided by the steady linear advection equation on the interval $[0, L]$:

$$u_x = 0, \tag{C2}$$

and

$$u(0) = 0, \tag{C3}$$

where $u(x)$ is a continuous, differentiable, real-valued function of $x \in [0, L]$. For the inverse problem, assume that there exists a single measurement of u at the point $\overline{x} \in [0, L]$, i.e.,

$$u(\overline{x}) = \overline{u} \tag{C4}$$

is observed.

We wish to pose the inverse problem to obtain the maximum likelihood estimate of u when error is admitted in equations C2 through C4. Assume that errors in C2, the model, have zero mean and covariance $C(x, y)$, for $x, y \in [0, L]$. Assume that the error in C3, the boundary condition, has zero mean and variance σ_0^2. Assume that the error in C4, the datum, has zero mean and variance σ^2. Assuming that the errors are normally distributed, and uncorrelated between the model, boundary conditions, and datum, the maximum likelihood estimate for u minimizes the penalty function

$$\mathcal{J}(u) = \int_0^L u_x \int_0^L W(x,y) u_y dx\, dy + \frac{u^2(0)}{\sigma_0^2} + \frac{(u(\overline{x}) - \overline{u})^2}{\sigma^2}. \tag{C5}$$

The weighting function $W(x,y)$ is the functional inverse of the covariance $C(x,y)$, as per the discussion in Appendix 4.3.

A finite-difference approximation to the penalty function C5 is

$$\mathcal{J}(u) = \sum_{n=0}^{N-1} \frac{u_{n+1} - u_n}{\Delta x} \sum_{m=0}^{N-1} W(x_n, x_m) \frac{u_{m+1} - u_m}{\Delta x} \Delta x\, \Delta x + \frac{u_0^2}{\sigma_0^2} + \frac{(u_M - \overline{u})^2}{\sigma^2} \tag{C6}$$

where $\Delta x = L/N$, $x_n = n\Delta x$, and $\overline{x} = M\Delta x$. The Δx terms in C6 obviously cancel; however, they are retained to emphasize the discretization of the integrals in C5. For convenience, we shall use the notational convention that summation occurs over repeated indices. Using this convention, define $\mathcal{J}_{\text{dyn}}$, $\mathcal{J}_{\text{b.c.}}$, and $\mathcal{J}_{\text{data}}$ as follows:

$$\mathcal{J}_{\text{dyn}} = (u_{n+1} - u_n) W(x_n, x_m) (u_{m+1} - u_m), \tag{C7}$$

$$\mathcal{J}_{\text{b.c.}} = \frac{u_0^2}{\sigma_0^2}, \tag{C8}$$

and

$$\mathcal{J}_{\text{data}} = \frac{(u_M - \overline{u})^2}{\sigma^2}, \tag{C9}$$

so that $\mathcal{J} = \mathcal{J}_{\text{dyn}} + \mathcal{J}_{\text{b.c.}} + \mathcal{J}_{\text{data}}$.

To determine the condition number of the Hessian of $\mathcal{J}$, diagonalize $\mathcal{J}_{\text{dyn}}$ by transforming from u to $\hat{u}$ with

$$\hat{u}_k = u_j \exp(\frac{2\pi i}{N} jk), \tag{C10}$$

i.e., Fourier transform u (recall the summation convention). The inverse transform is defined by

$$u_j = \frac{1}{N}\hat{u}_k \exp(-\frac{2\pi i}{N}jk). \tag{C11}$$

Note that j and k range from 0 to $N-1$; the letter i denotes $\sqrt{-1}$.

Let S denote the Hessian of $\mathcal{J}(u)$, and let $\hat{S}$ denote the Hessian of $\mathcal{J}(\hat{u})$. For any matrix A, let $(A)_{n\ m}$ denote the entry at the m^{th} column and n^{th} row of A. The $N \times N$ matrices S and $\hat{S}$ are related by

$$(\hat{S})_{n\ m} = \frac{1}{N}(P)^T_{n\ k}(S)_{k\ l}(P)_{l\ m}, \tag{C12}$$

where P is an orthogonal matrix, $(P)_{j\ k} = N^{-1/2}\exp(-\frac{2\pi i}{N}jk)$, and superscript ^{T} denotes Hermitian transpose. Thus, the eigenvalues of $\hat{S}$ are equal to the eigenvalues of S divided by N, and the condition number, which is the ratio of eigenvalues, is the same for each matrix. In other words, the transformation of the Hessian affected by Fourier transforming the state variable does not alter the conditioning of the penalty function. Therefore, the analysis may proceed by considering the eigenvalues of $\hat{S}$.

Define $\hat{S}_{\text{dyn}}$, $\hat{S}_{\text{b.c.}}$, and $\hat{S}_{\text{data}}$ to be the components of the Hessian in correspondence with C7 through C9. Differentiating the components of $\mathcal{J}(\hat{u})$ twice with respect to $\hat{u}$ yields:

$$(\hat{S}_{\text{dyn}})_{n\ m} = \frac{4}{N}\hat{w}_n(1-\cos\frac{2\pi n}{N})\delta_{n\ m}, \tag{C13}$$

$$(\hat{S}_{\text{b.c.}})_{n\ m} = \frac{2}{\sigma_0^2 N^2}, \tag{C14}$$

$$(\hat{S}_{\text{data}})_{n\ m} = \frac{2}{\sigma^2 N^2}\exp(\frac{2\pi i}{N}Mm)\exp(-\frac{2\pi i}{N}Mn). \tag{C15}$$

To obtain the above, it was assumed that the Fourier transform of W is $\hat{W}_{kl} = \hat{w}_k\delta_{k\ -l}$, i.e., the weighting function is homogeneous. $\delta_{n\ m}$ is the Kronecker delta, equal to 1 if n equals m, and zero otherwise.

To estimate the condition number of $\hat{S}$, note the following:

1. $\hat{S}_{\text{dyn}}$ is diagonal, hence its eigenvalues can be read off.

2. $\hat{S}_{\text{b.c.}}$ is a rank-1 matrix, i.e.,

$$\hat{S}_{\text{b.c.}} = \frac{2}{\sigma_0^2 N^2} z z^T, \tag{C16}$$

where z is the $N \times 1$ vector $(1 \ldots 1)^T$.

3. $\hat{S}_{\text{data}}$ is a rank-1 matrix, i.e.,

$$\hat{S}_{\text{data}} = \frac{2}{\sigma^2 N^2} z z^T, \tag{C17}$$

where z is the $N \times 1$ vector with elements $z_n = \exp(-\frac{2\pi i}{N} M n)$, and $0 \leq n,\ M \leq N-1$. Note that superscript ^{T} denotes the Hermitian transpose.

Theorem 8.6.2 of Golub and VanLoan (1989, p.462) can be used to bound the eigenvalues of systems of the form $A = D + \rho z z^T$, where D is an $N \times N$ diagonal matrix, ρ is a scalar, and z is an $N \times 1$ vector. Essentially, the theorem states an *interleaving* property for the eigenvalues of A. Let d_i and λ_i denote the i^{th} ordered eigenvalues of D and A, respectively, where $d_0 < d_1 < \ldots < d_{N-1}$ and $\lambda_0 \leq \lambda_1 \leq \ldots \leq \lambda_{N-1}$. For $\rho > 0$, the following relation between the d_i and λ_i is obtained:

1. for $i = 0, \ldots, N-2$:

$$d_i < \lambda_i < d_{i+1}, \tag{C18}$$

2. for $i = N-1$:

$$d_i < \lambda_i < d_i + \rho z^T z. \tag{C19}$$

Based on this relationship it is possible to put the following bounds on the condition number κ of A:

$$\frac{d_{N-1}}{d_1} \leq \kappa \leq \frac{d_{N-1} + \rho z^T z}{d_0}. \tag{C20}$$

The theorem requires that the N eigenvalues of D be distinct; we shall assume that this is the case for $\hat{S}_{\text{dyn}}$.

Let $\hat{S}_{\text{dyn}}$ be the diagonal matrix D mentioned in the theorem. It is evident from C13 that $d_0 = 0$; therefore, the upper bound on κ in equation C20 is infinite. An improved lower bound on λ_0 is necessary.

Before improving the lower bound on λ_0, it is instructive to consider the lower bound on κ, namely, d_{N-1}/d_1. This lower bound on the condition number is determined entirely by $\hat{S}_{\text{dyn}}$. Based on equation C13, we have the following bound:

$$\frac{\hat{w}_{N/2}}{\hat{w}_1} \frac{2}{(1 - \cos(2\pi/N))} \leq \kappa, \tag{C21}$$

or, for large N,

$$\frac{\hat{w}_{N/2}}{\hat{w}_1} \frac{N^2}{2\pi^2} \leq \kappa. \tag{C22}$$

It has been assumed that $\hat{w}_k$, the transformed weighting function, is maximum at $k = N/2$ (the two-gridpoint wave).

Let κ_- denote the lower bound on κ. Evidently, κ_- is the product of two terms, $\kappa_- = \kappa_w \kappa_d$:

1. $\kappa_w = \frac{\hat{w}_{N/2}}{\hat{w}_1}$ This term is a consequence of the spectral form of the weighting function. If it is assumed that the spectral form of the prior model covariance is proportional to k^{-p} for large k, then κ_w is proportional to N^p. Thus, as the spectral roll-off rate of the model covariance is increased, the condition number becomes worse.

2. $\kappa_d = \frac{2}{(1-\cos(2\pi/N))}$ This term is a consequence of the differential operator appearing in the dynamical model, namely $\partial/\partial x$. As shown in equation C22, for large N, κ_w is proportional to N^2.

This interpretation of κ_- is applied to the linear planetary geostrophic system in sections C.3 and C.4, below. Note that κ_- is a *lower* bound on the condition number, and it is independent of the constraints provided by the boundary conditions or data.

A trivial extension of the above-mentioned theorem results in a lower bound on λ_0 (hence, an upper bound on κ), as follows. It is proved in Golub and Van-Loan (1989) that the eigenvalues of $D + \rho z z^T$ satisfy $f(\lambda) = 0$, where the function $f(\lambda)$ is given by

$$f(\lambda) = 1 + \rho \sum_{i=0}^{N-1} \frac{|z_i|^2}{d_i - \lambda}. \tag{C23}$$

Note that f is monotone between its poles, and recall that $d_0 = 0$ and $|z_i|^2 = 1$ in the present example calculation. For $\lambda \in (0, d_1)$ the function f_u, given by

$$f_u(\lambda) = 1 - \frac{\rho}{\lambda} + \frac{(N-1)\rho}{d_1 - \lambda}, \tag{C24}$$

is an upper bound on f. Because both f and f_u are monotone in the interval $(0, d_1)$, and $f_u(\lambda) \geq f(\lambda)$, we have the following inequality:

$$0 \leq \lambda_- \leq \lambda_0 \leq d_1. \tag{C25}$$

$\lambda_- \in (0, d_1)$ is the smallest root of f_u, namely,

$$\lambda_- = \frac{d_2 + N\rho}{2} \left[1 - \left(1 - \frac{4\rho d_2}{(d_2 + N\rho)^2} \right)^{1/2} \right]. \tag{C26}$$

For clarity, Figure 5.3 shows the relationship between $f(\lambda)$ and $f_u(\lambda)$.

Let κ_+ denote the upper bound on κ, $\kappa_+ = (d_{N-1} + \rho z^T z)/\lambda_1$. It is possible to derive asymptotic expressions for λ_- and κ_+ if the number of grid-points N is

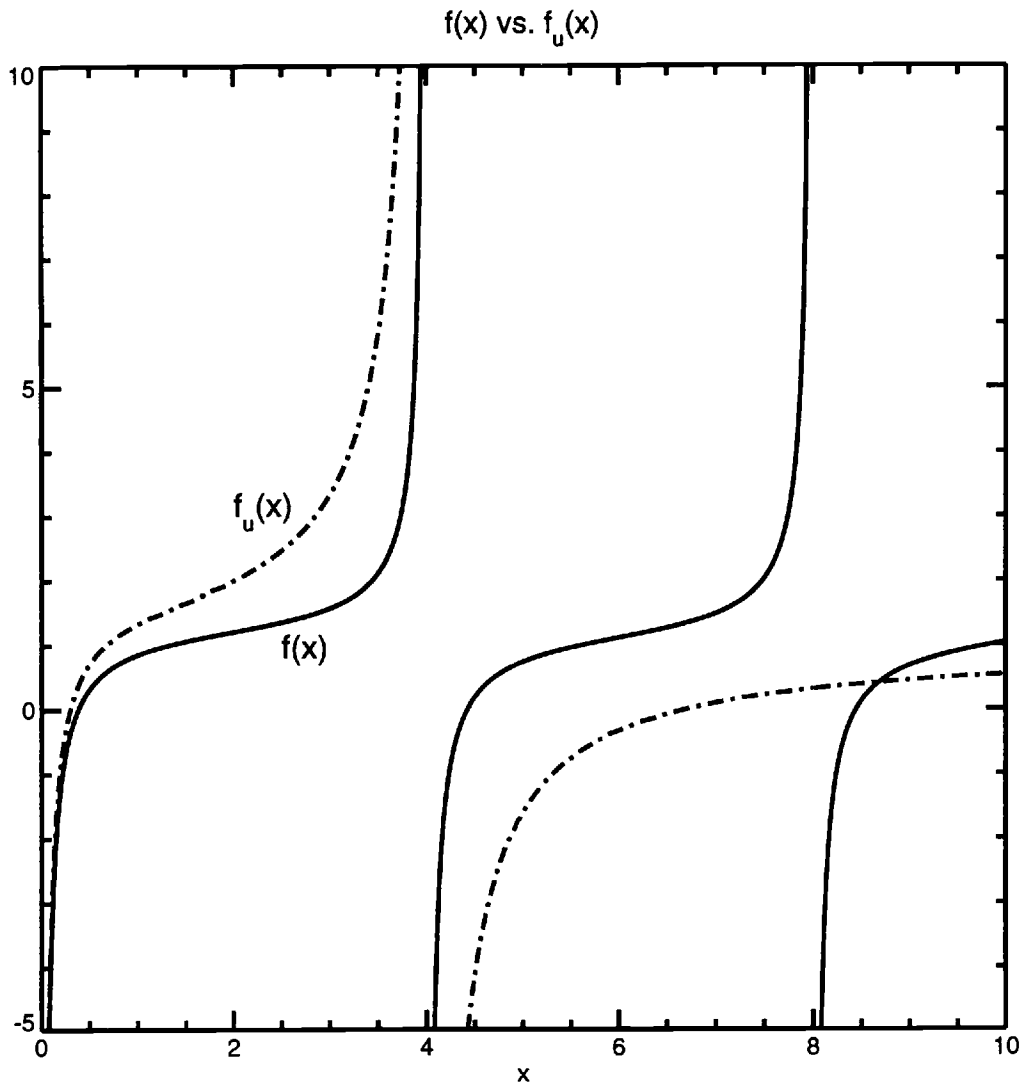

FIGURE 5.3. Eigenvalue Bound.

The functions f and f_u are compared (equations C23 and C24). In this example, $d_1 = 4$ and $d_2 = 8$. It can be seen that $f_u(x)$ has the desired property, namely, $f_u(x) \geq f(x)$ for $x \in (0, d_1)$.

large. The notation $y = O(x)$ will be used to indicate that the limit y/x is nonzero and finite as $x \to \infty$. For large N, a consistent asymptotic expression for λ_- is

$$\lambda_- = d_1 N^{-1}[1 + O(N^{-1})]. \tag{C27}$$

It is interesting to note that this expression is independent of ρ to lowest order. The $O(N^{-1})$ term is proportional to Nd_1/ρ.

With this bound on the smallest eigenvalue of the system $A = D + \rho zz^T$, the following upper bound on the condition number of A is obtained, asymptotic for large N:

$$\kappa_+ = N[\kappa_- + N\rho/d_1][1 + O(N^{-1})]. \tag{C28}$$

Note that it has been assumed that $|z_i|^2 = 1$ and $d_0 = 0$.

The expression (C28) for κ_+ is in terms of N, κ_-, and the ratio $N\rho/d_1$. Let us evaluate this expression to estimate the condition number of $\hat{S}_{\text{dyn}} + \hat{S}_{\text{b.c.}}$, a diagonal plus rank-one matrix. A little algebra, with careful book-keeping of powers of N, reveals that

$$N\rho/d_1 \cong \frac{\sigma_{\text{dyn}}^2 L L_{\text{corr}}}{\sigma_0^2} \frac{1}{(2\pi)^2} N^2, \tag{C29}$$

which is an $O(N^2)$ number for reasonable choices of the prior model and boundary condition variances (L_{corr} is the correlation length scale of the model forcing covariance). From equation C22, it is evident that $\kappa_- = O(N^{2+p})$, where p is the asymptotic spectral roll-off rate of the prior model forcing covariance. Thus, for large N,

$$\kappa_+ \cong N\kappa_-. \tag{C30}$$

The condition number estimate for $\hat{S}_{\text{dyn}} + \hat{S}_{\text{data}}$ is identical.

We may summarize the asymptotic bounds from equations C22 and C30 as

$$\kappa_- \leq \kappa \leq N\kappa_-, \tag{C31}$$

where $\kappa_- = N^2\hat{w}_{N/2}/(4\pi^2\hat{w}_1)$. Although these bounds are not very tight, and they are only asymptotic for large N, they do clarify what aspects of the inverse problem determine the conditioning of the penalty function.

To conclude, for this relatively simple one-dimensional example, it is possible to obtain upper and lower bounds on the condition number. The lower bound is determined independently of the boundary conditions or data, and it is obtained by a diagonalization of S_{dyn}. An upper bound on the condition number of S, which accounts for either the boundary conditions or the datum, is simply N times the lower bound. Given that N is large, the upper bound is not especially useful; therefore, no attempt was made to find an upper bound which accounted for both the boundary conditions and datum.

In the following sections, only the lower bound on the condition number is computed. The nonzero eigenvalues of the appropriate operators are estimated by considering the dimensions of the domain and the grid resolution.

C.3. Barotropic Equation

In this section, the condition number of the Hessian associated with the barotropic vorticity equation is estimated. It is assumed that the model domain can be approximated with a constant depth, doubly periodic β-plane. As in the above condition number estimates, it is assumed that the weighting function is homogeneous. With these assumptions it is possible to diagonalize the Hessian associated with the barotropic vorticity equation and read off its eigenvalues.

Recall the barotropic vorticity equation (3.10), from Section 3.2. Neglecting the terms which do not depend on Ψ, the barotropic vorticity equation is

$$\Psi_x \frac{\beta}{H} = A_H \nabla \cdot \frac{1}{H} \nabla^2 \nabla \Psi. \tag{C32}$$

As in Section 3.2, Ψ is the streamfunction for the barotropic transport, β is the planetary vorticity gradient, A_H is the lateral friction coefficient, and H is the bottom depth. As in Chapter 3, define the residual of C32 as

$$\Psi_x \frac{\beta}{H} - A_H \nabla \cdot \frac{1}{H} \nabla^2 \nabla \Psi = \chi; \tag{C33}$$

therefore, the contribution of the barotropic vorticity equation to the penalty function is

$$\mathcal{J}_{\text{dyn}}(\Psi) = \chi \circ_2 W^\chi \circ_2 \chi. \tag{C34}$$

The symbol $\circ_2$ denotes the inner product over the computational domain, and W^χ is the weighting function for this equation.

Let N_x and N_y denote the number of gridpoints in the zonal and meridional directions, respectively, and let $L_x = N_x \Delta x$ and $L_y = N_x \Delta y$ denote the physical dimensions of the domain. As above, it is possible to diagonalize the Hessian by Fourier transforming the streamfunction Ψ and the weighting function W^χ. The method is identical to that used in the one-dimensional example; however, now the transforms are two-dimensional. In terms of the numerical and physical parameters, the lower bound on the condition number of the Hessian is

$$\begin{aligned} \kappa_- \cong & \left[1 + \left(\frac{L_{\text{corr}}}{2\Delta x} \right)^4 \left(1 + \left(\frac{\Delta x}{\Delta y} \right)^4 \right) \right] \\ & \times \left(\frac{N_x}{2} \right)^2 \left[1 + \left(\frac{L_{\text{Munk}}}{2\Delta x} \right)^6 \left(1 + \left(\frac{\Delta x}{\Delta y} \right)^2 \right)^4 \right]. \end{aligned} \tag{C35}$$

L_{corr} is defined as the correlation length scale of the prior error covariance for the vorticity equation (the inverse of the wavenumber at the half-power point of the error covariance power spectrum). L_{Munk} is 2π times the length scale for a Munk (1950) western boundary current:

$$L_{\text{Munk}} = 2\pi \left(\frac{A_H}{\beta} \right)^{1/3}. \tag{C36}$$

Note that equation C35 is an approximation in which terms proportional to L_{Munk}/L_x have been neglected.

The expression for κ_- (C35) is the product of two dimensionless expressions:

1. $\left[1 + \left(\frac{L_{\text{corr}}}{2\Delta x}\right)^4 \left(1 + \left(\frac{\Delta x}{\Delta y}\right)^4\right)\right]$ This term is a consequence of the weighting function. It is assumed that $W^\chi \circ_2 \chi$ is proportional to $[1 + L_{\text{corr}}^4 \nabla^2 \nabla^2]\chi$.
2. $\left(\frac{N_x}{2}\right)^2 \left[1 + \left(\frac{L_{\text{Munk}}}{2\Delta x}\right)^6 \left(1 + \left(\frac{N_y}{N_x}\right)^2\right)^4\right]$ This term is a consequence of the differential operators in the streamfunction equation.

Using the estimates appropriate to the calculations in Chapter 3, namely, that the correlation scale is five times the model resolution, and the Munk boundary current length scale is equal to the model resolution, we obtain

$$\kappa_- \cong 10^6. \tag{C37}$$

Notice that as the correlation scale becomes larger, $L_{\text{corr}}/\Delta x$ increases, and the conditioning of the system becomes worse. Thus, attempts to increase the smoothness of the inverse solution (by increasing the correlation scale) will increase the condition number of the system. This result is intuitively reasonable: as the correlation scale of the errors becomes larger, the model equations become less linearly independent at adjacent gridpoints.

C.4. Baroclinic Equation

It is possible to estimate the condition number of the Hessian associated with the baroclinic dynamics by following the same general procedure as above: one makes a modal expansion in the vertical, and Fourier transforms in the horizontal. In order for this procedure to succeed in diagonalizing the Hessian, we must once again assume that the domain is a rectangular β-plane of constant depth.

As in Chapter 3, we are interested in the case when errors are admitted in the continuity and heat equations. For simplicity, salinity is neglected and the mean profile, $\overline{z}_\theta$, is taken to be constant. The ocean depth is given by $H = \theta_o \overline{z}_\theta$, where $\theta_o = \theta_T - \theta_B$.

Assume that the prior model forcing covariance is homogeneous and separable. Let k and l be horizontal wavenumbers, and let integer m index the vertical modes. After making the Fourier/modal expansion, the Hessian matrix is block diagonal with the following two-by-two blocks arranged on the diagonal:

$$S_{k\ l\ m} = L^T_{k\ l\ m} Q_{k\ l\ m} L_{k\ l\ m}, \tag{C38}$$

where ^{T} denotes Hermitian transpose. The spectral forms of the model operator and weight are defined as

$$L_{k\ l\ m} = \begin{pmatrix} c_p^{(m)} \frac{m\pi}{\theta_o} ik & \frac{m\pi}{\theta_o} \\ -\frac{K_V}{\overline{z}_\theta^2} \left(\frac{m\pi}{\theta_o}\right)^2 & 1 \end{pmatrix}, \tag{C39}$$

and

$$Q_{k\ l\ m} = \begin{pmatrix} \hat{W}^\epsilon_{k\ l\ m} & 0 \\ 0 & \hat{W}^\gamma_{k\ l\ m} \end{pmatrix}, \tag{C40}$$

respectively. The hat ($\hat{}$) denotes the transform of a variable; otherwise, the notation is identical to that used in Chapter 3. The phase speed of the m^{th}-mode baroclinic Rossby wave is

$$c_p^{(m)} = \frac{\beta}{\mathrm{f}^2}\frac{\bar{b}_\theta}{\bar{z}_\theta}\frac{H^2}{m^2\pi^2}. \tag{C41}$$

The barotropic mode corresponds to $m = 0$. Because of the importance of lateral friction to the barotropic dyanmics, the barotropic mode was considered separately in the previous section. Henceforth, the modes for which $m > 0$ are considered.

As mentioned, the Hessian S is block diagonal, with the two-by-two blocks $S_{k\ l\ m}$ arranged along the diagonal. Therefore, the maximum and minimum eigenvalues of S, which determine its condition number, are given by

$$\lambda_{\max} = \max_{k\ l\ m} \lambda^+_{k\ l\ m}, \tag{C42}$$

and

$$\lambda_{\min} = \min_{k\ l\ m} \lambda^-_{k\ l\ m}, \tag{C43}$$

where $\lambda^+_{k\ l\ m}$ and $\lambda^-_{k\ l\ m}$ are, respectively, the maximum and minimum eigenvalues of the two-by-two matrix $S_{k\ l\ m}$. Given the physical and numerical parameters of the planetary geostrophic model used in Chapter 3, the eigenvalues of $S_{k\ l\ m}$ can be computed.

The eigenvalues of $S_{k\ l\ m}$ are monotonic functions of wavenumbers k and l; therefore, the eigenvalues can be extremized with respect to these parameters. The functional dependence of the eigenvalues on the vertical mode number m is more complicated. Figure 5.4 plots the maximum and minimum eigenvalues of $S_{k\ l\ m}$ as a function of m. We seek the maximum and minimum eigenvalues over the set of possible k, l, and m; the eigenvalues in the plot have already been extremized with respect to k and l.

The minimum value of $\lambda^-_{k\ l\ m}$ is approximately 10^{-18}, and the maximum value of $\lambda^+_{k\ l\ m}$ is approximately 10^5. Thus, a *lower* bound on the condition number of the

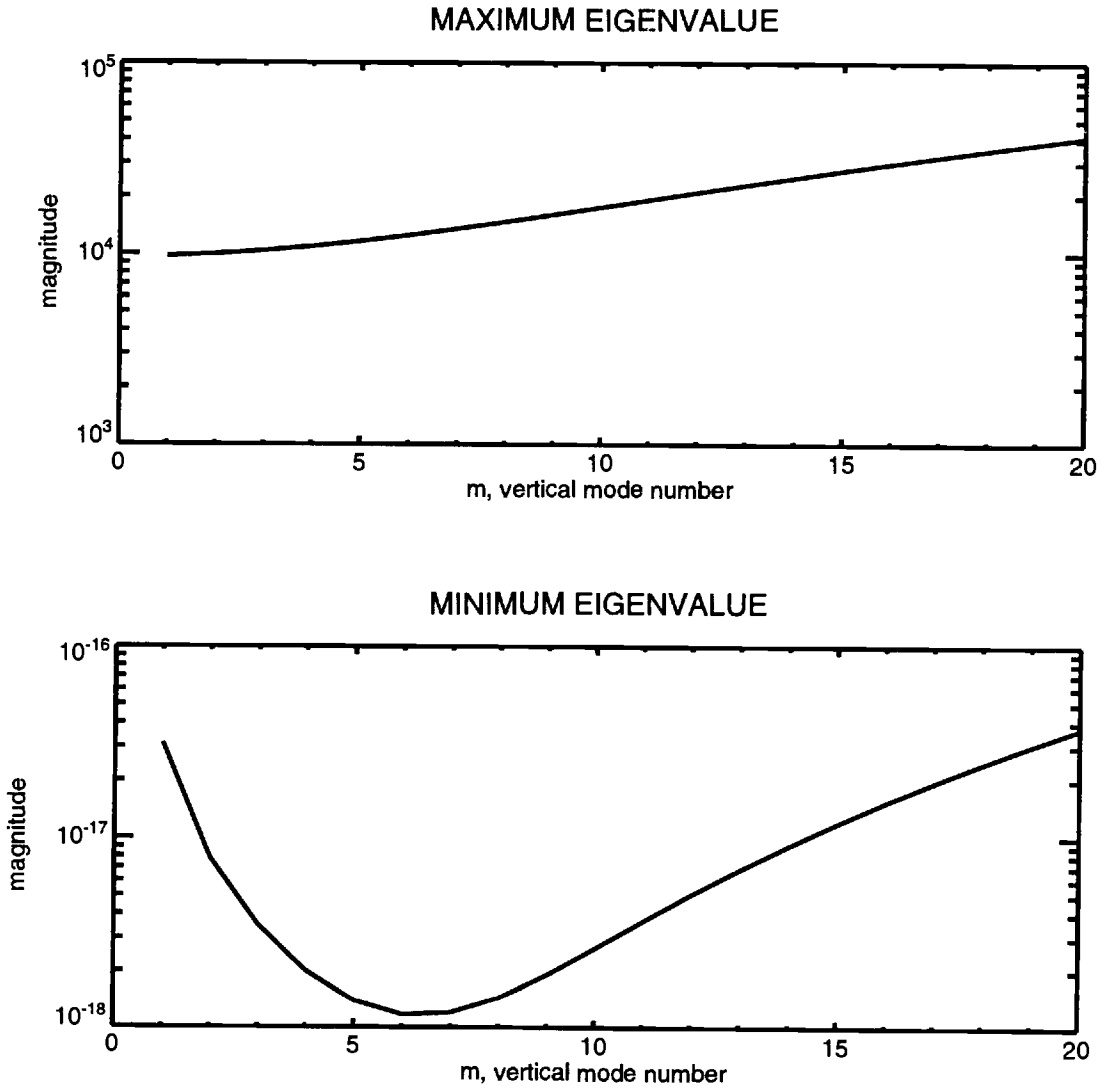

FIGURE 5.4. Hessian Eigenvalues.

The maximum and minimum eigenvalues of the Hessian for the baroclinic equations are plotted. The maximum eigenvalue occurs for $m = 20$, and the minimum eigevalue has $m = 6$. The condition number of the non-preconditioned Hessian is approximately 10^{23}.

Hessian is 10^{23}! This number is larger than the working range for double precision arithmetic on a 64 bit machine, which is approximately 10^{19}, and hence the penalty function with Hessian S *cannot* be minimized on such a machine.

In the calculations reported in Chapter 3, preconditioning operators were used which: 1) rescaled, and 2) spatially averaged the state variables. The rescaling operation had the single largest effect on the convergence rate of the descent calculation, and it is relatively easy to estimate the impact of the rescaling operator on the Hessian. In Figure 5.5 are plotted the maximum and minimum eigenvalues of $S' = DSD$, where D is a diagonal rescaling matrix. The rescaling matrix was determined so that the largest element of the rescaled Hessian was unity.

The *lower* bound on condition number of the rescaled system is approximately 10^9. This is an enormous improvement over the original system, and it is consistent with the finding that non-preconditioned descent methods could make no progress on the penalty function proposed in 3.5 of Chapter 3.

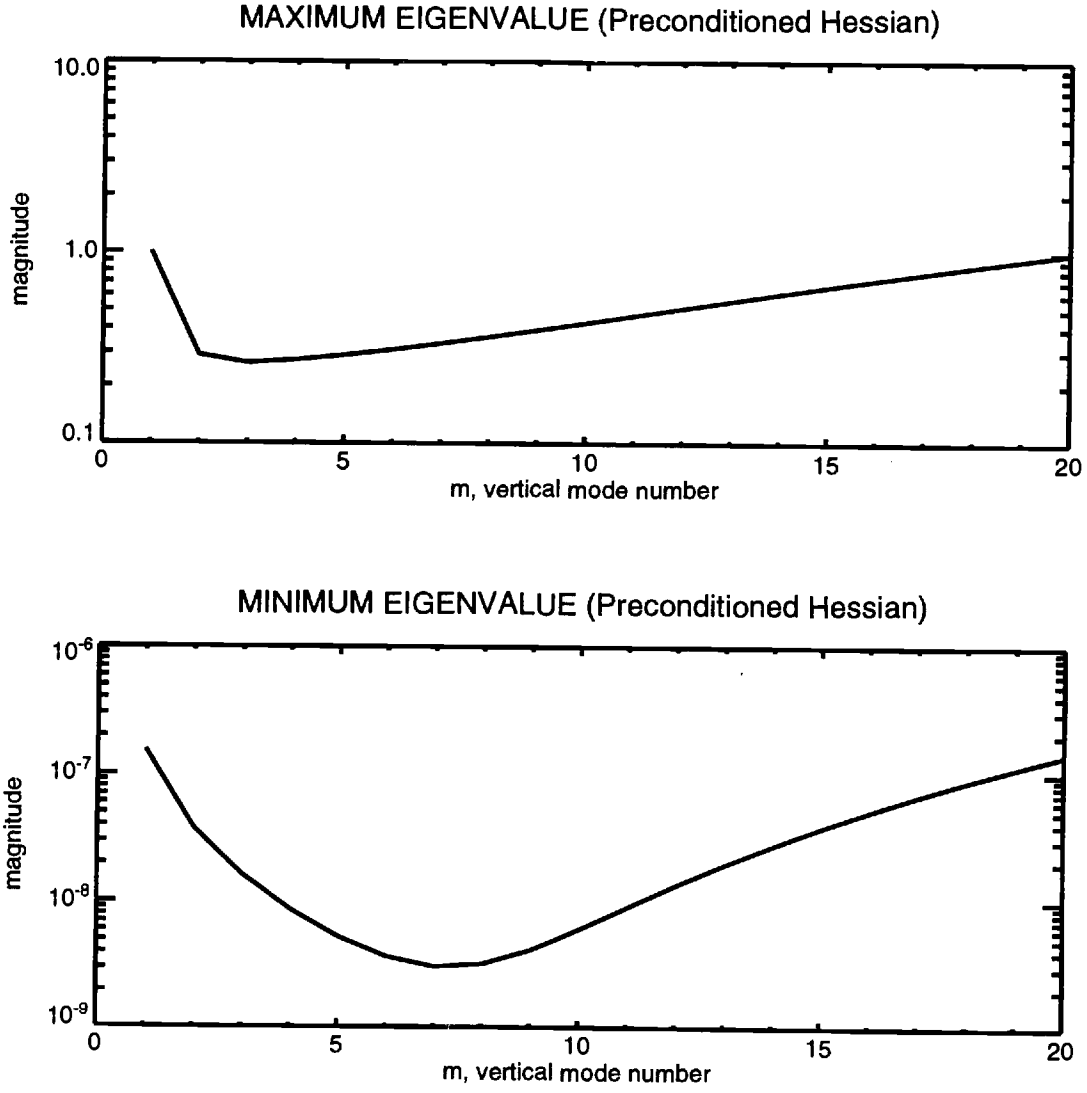

FIGURE 5.5. Preconditioned Hessian Eigenvalues.

The maximum and minimum eigenvalues of the preconditioned Hessian are plotted. The preconditioner was chosen to rescale the state variables (z and $\omega\overline{z}_\theta$) to make the largest entry in the Hessian unity. With this preconditioner, the condition number of the Hessian is approximately 10^9.